UNDERSTANDING MICROSEISMICITY BEHAVIOR AND THEIR RESPONSE TO EARTH PROCESSES BY IMPROVING EARTHQUAKE CATALOGS

A Dissertation
Presented to
The Academic Faculty

by

Qiushi Zhai

In Partial Fulfillment
of the Requirements for the Degree
Doctor of Philosophy in the
School of Earth and Atmospheric Sciences

Georgia Institute of Technology
August 2022

UNDERSTANDING MICROSEISMICITY BEHAVIOR AND THEIR RESPONSE TO EARTH PROCESSES BY IMPROVING EARTHQUAKE CATALOGS

Approved by:

Dr. Zhigang Peng, Advisor
School of Earth and Atmospheric Sciences
Georgia Institute of Technology

Dr. Sheng Dai
School of Civil and Environmental Engineering
Georgia Institute of Technology

Dr. Andrew Newman
School of Earth and Atmospheric Sciences
Georgia Institute of Technology

Dr. Shimon Wdowinski
Department of Earth and Environment
Florida International University

Dr. Felix Herrmann
School of Earth and Atmospheric Sciences
Georgia Institute of Technology

Date Approved: June 30, 2022

ACKNOWLEDGEMENTS

I would like to thank my advisor Dr. Zhigang Peng for his support, patience, and guidance in doctoral research during the past five years. He always provides valuable and timely advice that guides me to learn how to propose and solve scientific problems independently and how to collaborate with others, and then present the results professionally in conference meetings or peer-reviewed journals. His extensive knowledge and experience help me to learn how to evaluate my own and others' work critically. He also provides valuable advice and opportunities for my future career in academia. Without his support and advice, I would not have learned so much and be able to defend my Ph.D. thesis.

I would also like to thank all the members of my defense committee and qualifying exam committee for their kind support and valuable comments, including Dr. Andrew Newman, Dr. Felix Herrmann, Dr. Sheng Dai, Dr. Shimon Wdowinski, Dr. Taka Ito, and Dr. Alexander Robel. I would like to give my thanks to my collaborators Dr. Ya-Ju Hsu, Dr. Yih-Min Wu, Dr. Yanbin Wang, Dr. Makoto Matsubara, Dr. Kazushige Obara, Dr. Tim Officer, Dr. Jesse Williams, Dr. Jake Walter, Dr. Liang Zhao, Dr. Lihua Fang, and Dr. Ming Zhao. I would also like to thank colleagues and friends I met at Georgia Tech, including Dr. Lijun Zhu, Dr. Zefeng Li, Dr. Dongdong Yao, Dr. Chenyu Li, Miguel Neves, Dr. Clara Daniels, Lindsay Chuang, Chen Zhou, Dr. Zijian Li, Dr. Biao Wan, Mingyu Ji, Kai Hu, and many others.

Finally, I would like to especially thank my parents and my wife Yan Yang for their support and faith in me.

TABLE OF CONTENTS

LIST OF TABLES

LIST OF FIGURES

LIST OF SYMBOLS AND ABBREVIATIONS

AE	Acoustic Emission
CBAM	Convolutional Block Attention Module
CC	Cross Correlation
CEA	China Earthquake Administration
CNN	Convolutional Neural Network
CWB	Central Weather Bureau
CWBSN	Central Weather Bureau Seismic Network
EQ	Earthquake
ETAS	Epidemic Type Aftershock Sequence
FM	Focal Mechanism
GBP	Guided Backpropagation
Grad-CAM	Gradient-weighted Class Activation Mapping
Guided Grad-CAM	Guided Backpropagation Gradient-weighted Class Activation Mapping
Hi-net	High-Sensitivity Seismograph Network
HLEQ	Hualien earthquake
IDEQ	Intermediate Depth Earthquake
JMA	Japan Meteorological Agency
JSEQ	Jiashian earthquake
M	Magnitude
MAD	Median Absolute Deviation
MAXC	MAXimum Curvature
Mc	Magnitude of completeness
MFT	Matched Filter Technique
MJEQ	Mingjian earthquake
NIED	National Research Institute for Earth Science and Disaster Resilience
NPC	Network for Polarity Classification
ODIN	Out-of-DIstribution detector for Neural networks
OGS	Oklahoma Geological Survey
RAM	Random Access Memory
SCSN	Southern California Seismic Network
SNR	Signal to Noise Ratio
SSE	Slow Slip Event
TOEQ	Tohoku-Oki earthquake

SUMMARY

Natural earthquakes occur on faults ranging from 0 to 700 km beneath Earth's surface in different tectonic settings, such as along major subduction zones in Japan and the arc-continent collisional environment in Taiwan. Recent studies suggest that earthquake activities can be affected by various Earth processes, including extreme weather events on the Earth's surface, large earthquakes, water/snow/glacier loading and unloading, erosion and sedimentation, etc. The Gutenberg–Richter magnitude-frequency statistics suggest that the number of earthquakes decays as a power law with the increase of earthquake magnitude, which means most earthquakes are of small magnitudes, i.e., microseismicity. Studying the behavior of microseismicity and their response to the Earth's surface process can help us to better understand fault structures at depth as well as the physics of earthquake nucleation, and to mitigate seismic as well as other natural hazards. However, the understanding of microseismicity may be limited by the incompleteness of standard earthquake catalogs, especially during the noisy period following extreme weather events and large earthquakes. During my Ph.D. study, I have developed/applied machine-learning and template-matching tools to improve earthquake catalogs by detecting microearthquakes and calculating their focal mechanisms. Based on the improved high-resolution catalogs, I then perform a detailed analysis of the microseismicity behavior and their response to Earth processes. Specifically, I build a deep-learning Network for Polarity Classification (NPC) to automatically determine P-wave first-motion polarity. The outputs of NPC can directly be used to build focal mechanism catalogs for several times more microearthquakes than those listed in the

standard catalogs. Next, I use template-matching and deep-learning methods to build a more complete earthquake catalog in Taiwan before and after the 2009 typhoon Morakot, which brought the highest rainfall in southern Taiwan in the past 60 years and triggered numerous landslides. I then use the new catalog to investigate the impact of this wet typhoon on microseismicity. I observe no other significant seismicity changes that can be attributed to surface changes induced by typhoon Morakot, but a clear reduction in seismicity rate near the typhoon's low-pressure eye center in northeastern Taiwan during the typhoon passed by. I also relocate earthquakes in this new catalog and use it to study the spatiotemporal variations of mainshock-aftershock sequences and the subsurface faults structure in Taiwan. Last, I perform a systematic detection of intermediate-depth earthquakes (IDEQs) in the Japan subduction zone using the template-matching technique. I obtain a more complete IDEQ catalog before and after the 2011 magnitude (M) 9 Tohoku-Oki earthquake (TOEQ) and ten M5+ IDEQ mainshocks in Japan. The newly built template-matching catalog does not show any significant increase in IDEQs in the two months prior to TOEQ. But following the TOEQ, I find a significant increase in the rate of IDEQs in both upper and lower planes of the double seismic zone beneath 70 km depth. These results suggest that like seismic activity at shallow depth, IDEQs in the double seismic zone also respond to stress perturbations generated by the 2011 M9 TOEQ, highlighting a sustained seismic hazard associated with these intraslab events in the next decades.

CHAPTER 1. INTRODUCTION

1.1 Earthquakes and Their Responses to Earth Processes

Natural earthquakes occur on geological faults between 0-700 km beneath Earth's surface in different tectonic settings, such as along major subduction zones in Japan and the arc-continent collisional environment in Taiwan. The sudden release of elastic energy during the fault slip generates seismic waves that can be recorded by seismic stations. These seismic recordings form the basis for many subdisciplines in observational seismology (Stein and Wysession, 2003). These include seismic tomography from local or teleseismic earthquakes and ambient noises (e.g., Zhang and Thurber, 2006; Yao and van der Hilst, 2009), high-resolution earthquake relocation (e.g., Waldhauser and Ellsworth, 2000), large earthquake rupture back projection (e.g., Ishii et al., 2005), nonvolcanic deep tremor observation (e.g., Obara, 2002), and statistical behaviors of earthquake sequences (e.g., Kanamori and Brodsky, 2004; Ogata, 2017). While some studies directly use continuous waveforms such as deep tectonic tremor and ambient noise tomography, others (e.g., statistical seismology) require an earthquake catalog (i.e., a list of earthquake information that includes origin time, location, and magnitude) that is complete to the smallest-magnitude event possible.

Recent studies have shown that the timings of earthquakes can be affected by various Earth processes, including large earthquakes at nearby and remote distances (e.g., Stein, 1999; Hill and Prejean, 2015; Delbridge et al., 2017), water/snow/glacier loading and unloading (e.g., Thorson, 1996; Heki, 2001; Johnson et al., 2017a; Hsu et al., 2020), sedimentation and erosion (e.g., Maniatis et al., 2009; Calais et al., 2010; Steer et al., 2014),

variations in atmospheric pressures (e.g., Gao et al., 2000; Liu et al., 2009; Lin, 2013; Hsu et al., 2015; Meng et al., 2018), and extreme weather events on the Earth's surface (e.g., Roth et al., 1992; Hainzl et al., 2006; Husen et al., 2007; Steer et al., 2020). Studying earthquake behaviors and their responses to the various Earth processes can help us to better understand fault structures at depth (e.g., Sibson, 1982; Eberhart-Phillips and Michael, 1993; Ben-Zion and Sammis, 2003) and the physics of earthquake nucleation (e.g., Dieterich, 1992; Dieterich, 1994), and to assess, forecast, and mitigate seismic and other natural hazards (e.g., Reasenberg and Jones, 1989; Gerstenberger et al., 2005), as well as their cascading effects.

1.2 Earthquake Catalogs and Their Statistical Behaviors

Seismic monitoring agencies have been continuously maintaining publicly available global and regional earthquake catalogs mainly based on the seismic data recorded on permanent global and regional networks. Building earthquake catalogs is a fundamental but challenging task, especially for microseismicity (i.e., earthquakes with relatively small magnitudes). Picking the arrival time of a seismic phase is a key initial step for this task, which can be performed manually by human experts or automatically by algorisms. A widely used classic automatic phase picker is short-time-average over long-time-average (i.e., STA/LTA (Allen, 1978; Allen, 1982)). Phase picking is typically followed by phase association (Ringdal and Kvaerna, 1989) to group phase arrivals on multiple stations to a common source (origin time and location). Finally, the earthquake magnitude (Richter, 1935; Gutenberg and Richter, 1942) can be calculated based on the waveform amplitudes and event-station distances.

Based on these earthquake catalogs, seismologists have discovered several key statistical laws of seismicity behavior. For example, the Gutenberg–Richter frequency-magnitude statistics (i.e., the G-R law (Gutenberg and Richter, 1944)) suggest that the number of earthquakes drops as a power law with the increase of earthquake magnitude, which means most earthquakes are of small magnitudes, i.e., microseismicity. Many earthquakes are clustered in space and time (Ogata, 1988; Zhuang et al., 2002), forming mainshock-aftershock sequences. The aftershock seismicity rate decays with time following the Omori law (Omori, 1894; Utsu et al., 1995). In general, a larger mainshock has larger aftershocks that cover a longer time window and a larger space (Gardner and Knopoff, 1974).

In addition to the origin time, location, and magnitude of earthquakes, the seismic moment tensor, or its double-couple component (i.e., focal mechanism), is another important piece of information describing the movement on the fault during an earthquake. The moment tensors and/or focal mechanisms are also available for some events in standard catalogs, especially for large (M>5) earthquakes such as the global Centroid Moment Tensor (GCMT) catalog (Ekström et al., 2012)). The earthquake focal mechanism is typically inverted from one or the combination of three categories of input data, including P-wave first motion polarities (Reasenberg, 1985; Hardebeck and Shearer, 2002), the P-wave and/or S-wave amplitudes and their ratios (Hardebeck and Shearer, 2003; Snoke et al., 2003), and the full waveforms (Dreger and Helmberger, 1993; Zhao and Helmberger, 1994; Zhu and Helmberger, 1996).

1.3 Catalog Incompleteness and New Detection Methods

The G-R law suggests that there are always more earthquakes of smaller magnitude. Any detection method has its detectability threshold corresponding to a noise level. Therefore, earthquake catalogs are inherently incomplete because some small events are not detected or located. The incompleteness issue of standard catalogs is significant in the noisy period during and after large earthquakes (Kagan, 2004; Peng et al., 2006; Chang et al., 2007; Enescu et al., 2007) and extreme weather events (Zhai et al., 2021c). Therefore, the analysis of microseismicity behavior during and following these Earth processes would be limited by the incompleteness of standard catalogs.

Recent studies have proposed various algorithms to improve standard earthquake catalogs provided by seismic monitoring agencies. These include template-matching (Gibbons and Ringdal, 2006; Shelly et al., 2007; Peng and Zhao, 2009) and machine-learning techniques (Ross et al., 2018b; Zhu and Beroza, 2018; Zhu et al., 2019; Mousavi et al., 2020; Zhang et al., 2022; Zhu et al., 2022). Some studies also improved the location resolution using double-difference relocation techniques (Waldhauser and Ellsworth, 2000; Trugman and Shearer, 2017; Lin, 2018). In addition, recent studies have calculated the moment-tensor/focal-mechanism solutions for newly detected earthquakes using P-wave first-motion polarities based on waveform cross-correlations (Shelly et al., 2016b) and picked by deep-learning models (Ross et al., 2018a; Hara et al., 2019; Uchide, 2020; Zhai et al., 2021c; Uchide et al., 2022). These improved earthquake catalogs can be used to improve the understanding of subsurface fault structures, earthquake interaction/nucleation, and more.

1.4 Preview of Subsequent Chapters

During my Ph.D. study, I have developed/applied machine-learning and template-matching tools to improve earthquake catalogs by detecting microearthquakes and calculating their focal mechanisms in several seismically active regions. Based on the improved high-resolution catalogs, I then perform a detailed analysis of the microseismicity behavior and their response to various Earth processes. In CHAPTER 2, I build a deep-learning network for polarity classification (NPC) to automatically determine the P-wave first-motion polarity for earthquakes. The output of NPC can be directly used to calculate the focal mechanism solution of small earthquakes and tiny laboratory acoustic emission (AE) events. In CHAPTER 3, I use template-matching and deep-learning methods to build a more complete earthquake catalog in Taiwan before and after the 2009 typhoon Morakot, which brought the highest rainfall in southern Taiwan in the past 60 years and triggered numerous landslides. I then use the new catalog to investigate the impact of this wet typhoon on microseismicity. In CHAPTER 4, I study the spatiotemporal variations of aftershock sequences between 2009-2010 in Taiwan using the high-resolution relocated template matching catalog built in CHAPTER 3. In CHAPTER 5, I perform systematic detections of intermediate-depth earthquakes (IDEQs) in the Japan subduction zone using a template-matching method. I then use the newly built IDEQ catalog to investigate the potential variations of IDEQs before and after the 2011 magnitude (M) 9 Tohoku-Oki earthquake (TOEQ) and ten M5+ IDEQ mainshocks in Japan. CHAPTER 6 is the conclusion. APPENDIX A is the supplementary material of CHAPTER 3. APPENDIX B is the supplementary material of CHAPTER 4.

CHAPTER 2. NETWORK FOR POLARITY CLASSIFICATION (NPC): P-WAVE FIRST-MOTION POLARITY DETERMINATION FOR EARTHQUAKES USING DEEP LEARNING

2.1 Summary

The results in this chapter were presented at a recent conference, the 2021 Fall American Geophysical Union Annual Meeting (Zhai et al., 2021a). The manuscript is currently in preparation. Earthquake focal mechanism provides important information about stress field and fault structure at depth. The focal mechanisms of small earthquakes are typically inferred from P-wave first-motion polarities and/or S to P amplitude ratios. Here I take advantage of recently developed deep learning techniques by computer scientists and the large volume of manually labeled polarities by seismic analysts to build an automated polarity classifier. The network for polarity classification (NPC) is based on a convolutional neural network (CNN) and an attention mechanism. I train it with global earthquake datasets of ~3.5 million first motion polarity picks. With existing P-wave arrival picks, the accuracy of the model to predict up or down polarity is 0.97. If there is a random time shift of the P-wave arrival time within 0.2 s, the accuracy is 0.93. I then explore the generalization of the model by testing its ability to predict polarities for two new datasets in Iberia and Xichang, Western China. The accuracy is about 0.85, higher than a previous model which is trained only using the Southern California dataset. Besides exploring the performance of NPC, I also use a network visualization technique to help understand which parts of the input waveform are important for the model to make a

prediction, and this technique could be used to remove false classifications. I expect that the publicly available pre-trained model can be directly applied or fine-tuned with a small dataset to determine P-wave first-motion polarity for natural earthquakes, hydraulic fracturing events, and acoustic emissions.

2.2 Introduction

Seismic moment tensor, or its double-couple component (i.e., focal mechanism), is important for studying characteristics of natural earthquakes, microseismic events during hydraulic fracturing, and acoustic emission (AE) events during laboratory rock mechanics experiments (Stein and Wysession, 2003). It is typically inverted from one or the combination of three categories of input data, such as the P-wave first motion polarities (Reasenberg, 1985; Hardebeck and Shearer, 2002), the P-wave and/or S-wave amplitudes and their ratios (Hardebeck and Shearer, 2003; Snoke et al., 2003), and the full waveforms (Dreger and Helmberger, 1993; Zhao and Helmberger, 1994; Zhu and Helmberger, 1996). The full moment tensor of large earthquakes (e.g., M>4.5) can be automatically calculated using the full waveforms recorded by regional (Yang et al., 2012; Herman et al., 2014) or global networks (Ekström et al., 2012). However, the focal mechanisms of local small earthquakes are typically calculated using polarities (and amplitudes) instead of the full waveforms because of the difficulty in modeling full waveforms at high frequencies (Reasenberg, 1985; Hardebeck and Shearer, 2003; Snoke et al., 2003). Traditionally, polarity is manually determined by human experts. As the volume of data and the number of sensors grow dramatically (Kong et al., 2019), it is increasingly difficult to determine polarity manually. To automatically determine polarity, many approaches have been proposed (Baer and Kradolfer, 1987; Nakamura, 2004; Horiuchi et al., 2009; Chen and

Holland, 2016; Pugh et al., 2016; Kim et al., 2017; Xu et al., 2019; Pei and Zhou, 2022). But the performance of these conventional algorithms is still lower than human experts (Ross et al., 2018a; Hara et al., 2019).

Machine-learning (especially its subfield, deep-learning) based algorithms can perform as well, or better, than human experts for many tasks in earth science (Bergen et al., 2019; Karpatne et al., 2019; Yu and Ma, 2021; Sun et al., 2022). Deep learning is data-hungry, especially for supervised models, which use labeled training data (Mousavi et al., 2019a). Therefore, the availability of large amounts of seismic data (e.g., manually picked P-wave and S-wave arrival times) greatly promotes the rapid development of deep learning tools in seismology (Li et al., 2018b; Ross et al., 2018b; Zhu and Beroza, 2018; Kong et al., 2019; Mousavi et al., 2019a; Zhu et al., 2019; Mousavi et al., 2020; Kuang et al., 2021; Steinberg et al., 2021; Woollam et al., 2021; Yang et al., 2021; Zhu et al., 2022).

P-wave first-motion polarity determination can be treated as a typical binary classification problem. The large volumes of manually picked polarities around the world provide great labeled datasets to solve this problem using deep learning. Recently, many studies trained convolutional neural networks (CNN) to classify P-wave first-motion polarity using a single regional earthquake dataset. For example, Ross et al. (2018a) used the Southern California dataset, Hara et al. (2019), Uchide (2020), and Uchide et al. (2022) used the Japan dataset, Zhai et al. (2021b) used the Taiwan dataset, and Tian et al. (2020) used a multiple-trace high-frequency (10-70 Hz) dataset collected in a shale gas production site in Shanxi, Western China. In addition, Mousavi et al. (2019b) tested an unsupervised approach based on CNN using the Southern California dataset. Tanaka et al. (2021) trained a CNN model using acoustic emissions datasets. These studies demonstrated that deep

learning networks (especially CNN) can pick polarities as well, or better, than human experts. However, most of these studies only focused on their own model and dataset from a limited region or at laboratory scales. A model has to be retrained when applying to a new region. For example, Baker et al. (2021) fine-tuned the model which was trained using the Southern California dataset (Ross et al., 2018a) to fit their Utah dataset, Uchide (2020) re-trained their model for datasets from different regions in Japan, and Tanaka et al. (2021) trained networks for two datasets from different laboratory samples separately. Unlike the recent development of a general phase picker called EQTransformer (Mousavi et al., 2020) which was trained with a global dataset named STEAD (Mousavi et al., 2019a), the generalization of a deep learning model for polarity classification has not been well explored.

In this study, I aim to develop a generic deep learning model for P-wave first motion polarity classification. The basic assumption is that training a more advanced model/network with a larger dataset and more powerful computational resources would generally achieve better performance (Brown et al., 2020). Following this assumption, I design a new network for polarity classification (NPC) by combining the CNN (LeCun et al., 1989) and an attention mechanism (Vaswani et al., 2017). I collect manually labeled polarity data from regions with different tectonic settings around the world to build a large training dataset. I then train a new deep-learning model with the global dataset using the Extreme Science and Engineering Discovery Environment (XSEDE) supercomputers that have multiple NVIDIA Tesla V100 GPUs. Next, I examine its performance after training with 20 epochs. I also use a network visualization technique to help understand which parts of the input waveforms are important for the model to make a prediction. Finally, I explore

its generalization by testing its ability to pick polarities of earthquakes from unseen regions. I compare its performance with the other publicly available pre-trained polarity classifier (Ross et al., 2018a) and discuss its pros and cons.

2.3 Data

2.3.1 Data Collection

One of the most time-consuming steps for building a supervised model is the construction of a training and a testing dataset (Mousavi et al., 2019a). Here I collect seven different regional and local datasets that have manually labeled P-wave first motion polarities and corresponding seismic waveforms to train and test the NPC deep-learning model. Table 2.1 shows the seven regional and local datasets around the world used in this study. Figure 2.1 shows the map of these regional and local seismic arrays. Each array (a red triangle in Figure 2.1) has tens to hundreds of seismic stations and thousands to millions of labeled polarities. The details are described below.

In Southern California, I collect seismic data recorded by the Southern California Seismic Network (SCSN) (SCEDC, 2013) and packaged by Ross et al. (2018a). Figure 2.2 shows the distribution of earthquake magnitude and event-receiver distance of this dataset. In Japan, I collect the data recorded by the High-Sensitivity Seismograph Network (Hi-net) operated by the National Research Institute for Earth Science and Disaster Resilience (NIED) in Japan (Okada et al., 2004; Obara et al., 2005). The waveforms for earthquakes since 2004 are downloaded using the HinetPy package (Tian, 2021). The polarities are from Japan Meteorological Agency (JMA) (Ueno, 2002). In Oklahoma, I collect seismic records from Oklahoma Geological Survey (OGS) seismic network (Walter et al., 2020).

In Italy, I obtain the data recorded by the Italian National Seismic Network (Centre, 2006) operated by the National Institute for Geophysics and Volcanology and packaged by Michelini et al. (2021). In Taiwan, I collect the data recorded by the Central Weather Bureau Seismic Network (CWBSN) (Shin, 1992). In Iberia, I use seismic records from the Spanish Digital Seismic Network (Instituto Geografico Nacional, 1999), the Portuguese National Seismic Network (Instituto Português Do Mar E Da Atmosfera, 2006), and the Catalan Seismic Network (Catalans, 1984). In Xichang (a city in Sichuan province, Western China), I collected the data recorded by a temporal local seismic array (Jiang et al., 2015) operated by the Institute of Geophysics, China Earthquake Administration (CEA). In total, I collect 3,540,734 traces of vertical-component waveforms and their P-wave polarities from 2004 to 2020 (Table 2.1 and Figure 2.1).

Table 2.1 Reginal and local datasets around the world used in this study.

Dataset region	Number of polarities	Time	Used	#
Southern California	2,525,947	2010-2017	Training	1
Japan	403,938	2004-2020	Training	7
Oklahoma	311,230	2010-2020	Training	2
Italy	236,388	2005-2020	Training	4
Taiwan	63,231	2008-2010	Training	6
Iberia	4,060	2007-2014	Test	3
Xichang	1,251	2018-2018	Test	5
Total	3,540,734	2004-2020		

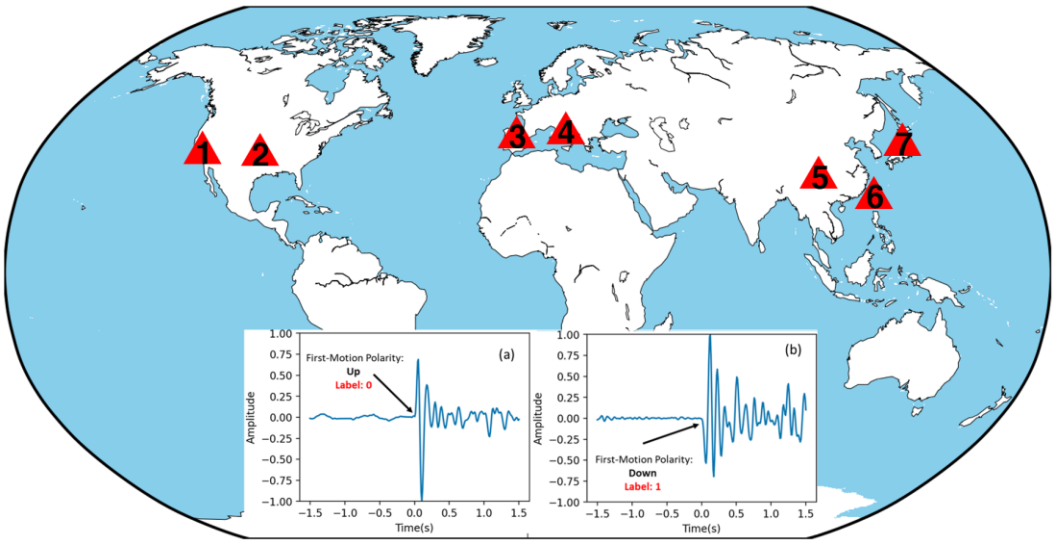

Figure 2.1 Map of regional and local seismic arrays used in this study. Inset (a) shows an example waveform that is manually labeled as 'up' P-wave first motion polarity by a human expert. Inset (b) is similar to Inset (a) but is labeled as 'down' polarity.

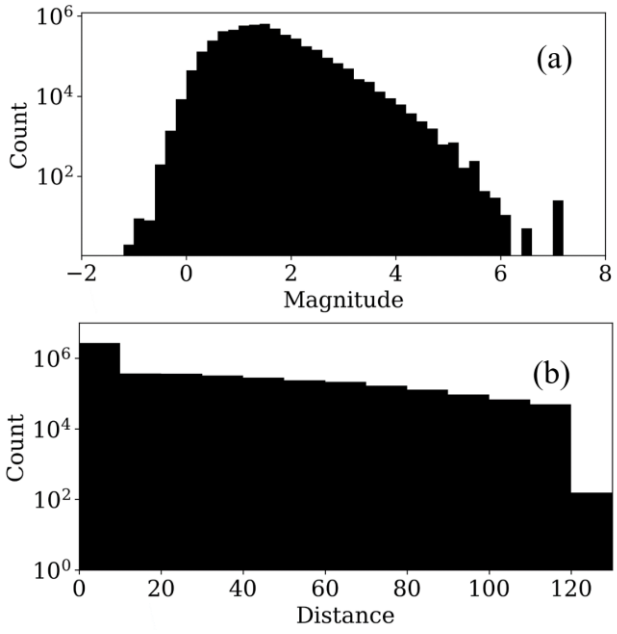

Figure 2.2 Distribution of earthquake magnitude and event-receiver distance in the Southern California Seismic Network (SCSN) dataset. (a) Distribution of earthquake magnitude. (b) Distribution of the event-receiver distance.

2.3.2 Data Preprocessing

To build datasets that can be directly used to train and test the NPC model, I preprocess the raw data of different regional and local datasets mentioned above with the following steps. I largely follow those used in a recent study (Zhai et al., 2021c) and are described as follows. First, an upward polarity is labeled by 0 and a downward polarity is labeled by 1. I only use the vertical-component waveforms associated with manually labeled P-wave first-motion polarities (upward or downward, Figure 2.1). I then band-pass filter the waveforms between 1-20 Hz (Ross et al., 2018a). I resample the waveforms to 100 Hz and then cut them between 1.5 s before and 1.5 s after their P-wave arrival times. I remove the mean and the linear trend of these 3 s long waveforms (300 data points). The amplitudes of these data points in a 3 s long waveform are normalized by their maximum absolute value. I then randomly split the dataset into three categories of datasets: training (80%), validation (10%), and testing (10%).

I then apply the following procedures to each category of data. To equalize the amount of data with upward and downward polarity, I flip the waveforms upside down (Uchide, 2020). To reduce the effects caused by the uncertainty of the arrival times, I randomly apply 20 times shift in the time domain to each waveform. Figure 2.3 shows two examples of unshifted and shifted waveforms. I only allow the shift within 0.2 s because the standard deviation of the P-wave arrival times identified by recently developed deep-learning phase pickers is smaller than or equal to 0.1 s (Ross et al., 2018b; Zhu and Beroza, 2018; Mousavi et al., 2020). Because of the flipping and time-shifting, the total number of data is augmented 40 times (Uchide, 2020).

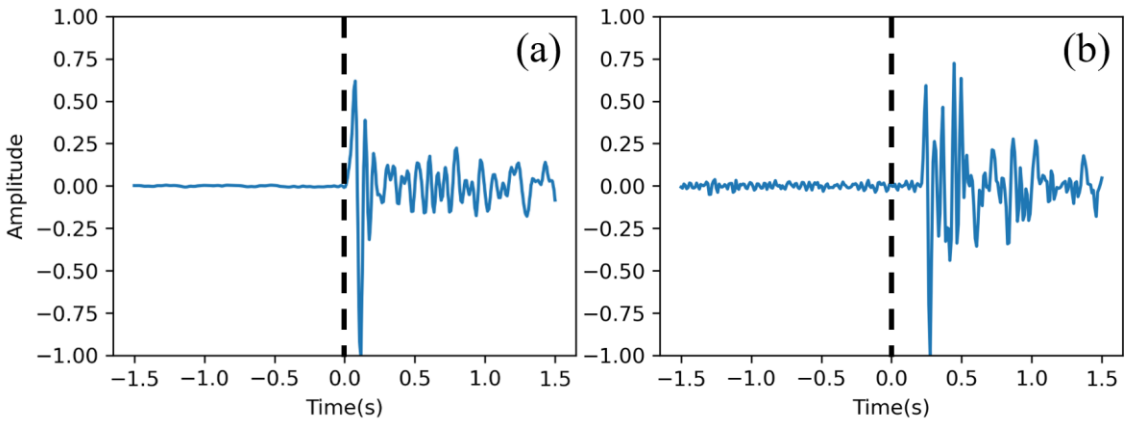

Figure 2.3 Examples of unshifted and shifted Waveforms. (a) An example of an unshifted waveform in the time domain. (b) An example of a randomly shifted waveform.

2.4 Method

2.4.1 Network Architecture

The architecture of the Network for Polarity Classification (NPC) (Figure 2.4) is modified from the CNN-based ResNet-18 (He et al., 2015) and the attention-mechanism-based Convolutional Block Attention Module (CBAM) (Woo et al., 2018) to process the 1-D time-series seismic waveform. The ResNet and CBAM are originally designed to process 2-D images (e.g., image classification: cat or dog, etc.). ResNet introduced a so-called residual connection (or shortcut connection) to overcome the vanishing gradient issue when a CNN-based network goes deeper (stacking more CNN layers) (He et al., 2015). I use CNN because previous studies show that it works well for polarity classification (Ross et al., 2018a; Hara et al., 2019; Uchide, 2020; Zhai et al., 2021c). Unlike previous studies, I add the attention module (i.e., CBAM) into a CNN-based network to mimic human experts' attention on a narrow window around the phase arrivals with high resolution while keeping track of the surrounding waveforms with low resolution.

I am somewhat inspired by the recent development of a general phase picker called EQTransformer (Mousavi et al., 2020), which is a deep network also using CNN and attention layers.

The input of NPC is a 1-D 300-data-point seismic waveform (Section 2.3.2). The outputs of NPC are two non-negative confidence scores, and their summation is 1. These two scores are considered as the probabilities of the upward and downward polarities. Unlike Ross et al. (2018a), but similar to Hara et al. (2019), Uchide (2020), Tanaka et al. (2021), and Zhai et al. (2021c), I do not classify any waveform as 'unknown' or 'unclear'. This is because I do not have plenty of polarities labeled as 'unclear'. In addition, a lack of polarity information sometimes means that this waveform was not manually analyzed by human experts for whatever reasons, but they may have clear upward or downward polarity.

There are some methods to address the potential misclassification issue of an unclear waveform. First and most importantly, such unclear waveforms can be removed by setting a signal-to-noise ratio (SNR) threshold for the input data (Zhai et al., 2021c). Second, I can set a higher threshold (e.g., 0.7 or 0.95) instead of 0.5 for the output confidence score to accept the suggested polarities when their probabilities are high enough (Uchide, 2020). Finally, this is an out-of-distribution problem and can be solved by some techniques developed in computer science such as the Out-of-DIstribution detector for Neural networks (ODIN) proposed by Liang et al. (2020).

Here I describe the details of the layers in NPC between its input and output. As mentioned above, the architecture (Figure 2.4) is modified from ResNet-18 (He et al., 2015) and CBAM (Woo et al., 2018) which are originally designed for 2-D images with 3

channels of the RGB color. In comparison, the input data is 1-D time series with 1 channel of the vertical component of the seismic sensor. Therefore, I first replace all the 2-D CNNs (LeCun et al., 1989) with 1-D CNNs (Kiranyaz et al., 2015). I also change all the max-pooling (Krizhevsky et al., 2012), average pooling (Lin et al., 2013), and batch normalization (Ioffe and Szegedy, 2015) layers from 2-D to 1-D. I leave the rectified linear unit, also known as ReLU (Nair and Hinton, 2010) unchanged. As suggested by Woo et al. (2018), I apply the CBAM to the convolution outputs in each ResBlock in ResNet-18. In ResNet-18, each ResBlock consists of two CNN layers (He et al., 2015). Next, I change the number of input channels from 3 to 1. I also modify the first CNN layer and its following pooling layers to make sure that the size of their output can fit the required input size of the following 16 stacked CNN layers. This is similar to the modification when the inputs are images with a different resolution (e.g., not 64×64). Finally, the number of classes in the fully connected layer (just before the last layer) is set as 2 (upward and downward). The last layer is a SoftMax activation function (classifier) whose outputs are the two confidence scores for upward and downward polarities mentioned above.

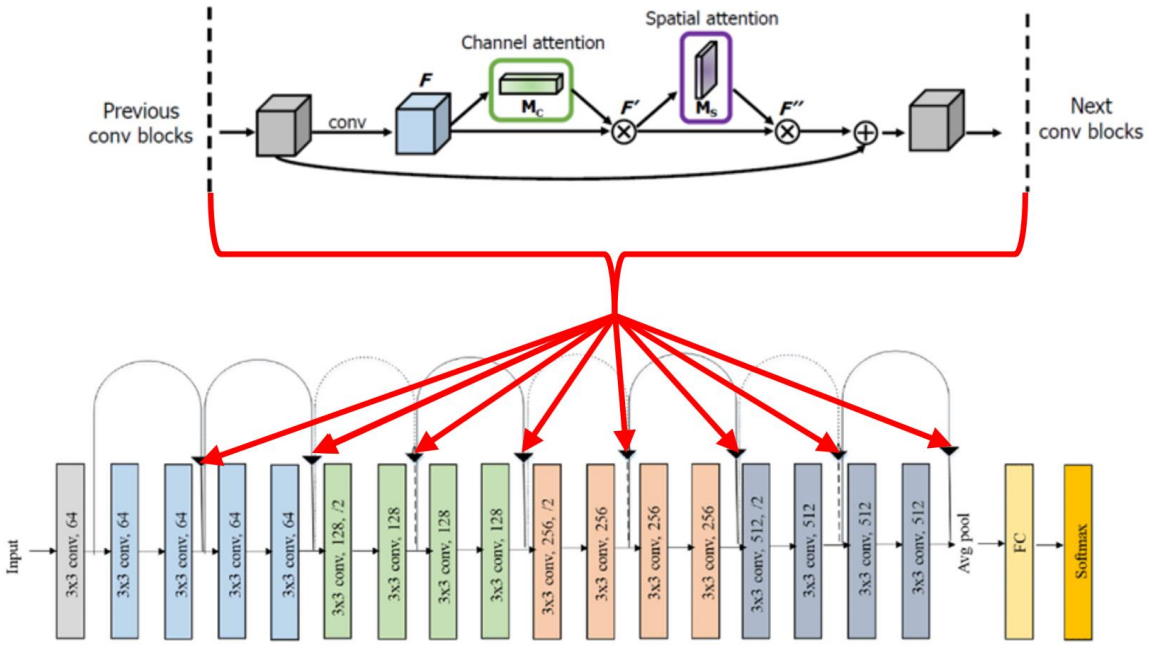

Figure 2.4 The architecture of the deep-learning network for polarity classification (NPC). The bottom half of this figure is modified from Figure 2 in Ramzan et al. (2019). It shows the original ResNet-18 architecture (He et al., 2015**). The top half of this figure is modified from Figure 3 in Woo et al. (2018). It shows the architecture of the Convolutional Block Attention Module (CBAM) which is applied to the convolution outputs in each ResBlock in the ResNet.**

2.4.2 Network Training

I add the NPC model to the open-source Yews package developed by Zhu et al. (2019) and train it with GPU-version PyTorch (Paszke et al., 2019). The training process is to minimize the cross-entropy loss function by calculating the gradient with backpropagation and iteratively updating the weights with the Adam optimization algorithm (Kingma and Ba, 2014). The learning rate is a hyperparameter for the optimization algorithm. After testing with different values, the initial value of the learning rate is set as 0.01. Its value would be automatically reduced by a factor of 10 (e.g., 0.01, 0.001, 0.0001, etc.) to fine-tune the model around a local minimum if there was no improvement in the validation loss over the previous ten epochs during the training stage.

One epoch means that the model sees every sample (a trace of waveform with its polarity) in the entire training dataset once. Due to the limitation of RAM (Random Access Memory, 512 GB in this study) of the computer, I have to use a small subset (batch size = 160000 samples) of the entire training dataset for each iteration during the training process. To monitor the performance during the training, I calculate the accuracies and losses on the training and validation datasets after each epoch. The accuracy (the same as Equation 9 in Hara et al. (2019)) is defined as:

$$accuracy = \frac{TU + TD}{TU + FU + TD + FD} \tag{2.1}$$

where T means true, F means false, U means upward polarity, and D means downward polarity. For example, TU is the number of upward polarities classified by both NPC and human experts, and FU is the number of polarities classified as downward by human experts but classified as upward by NPC. Figure 2.5 shows the accuracies and losses on the training and validation datasets as a function of epochs. The fast decay of losses in the first several epochs indicates that the learning process is efficient. I terminate the training process after 20 epochs because the trainable weights and validation losses became stable and converged. The final model is selected as the model with the best validation accuracy over all the epochs instead of the model of the last epoch (Ross et al., 2018a; Zhu et al., 2019). I follow the procedures mentioned above to train the same architecture NPC (but have different weights after training) for the unshifted and shifted datasets (Section 2.3.2), respectively.

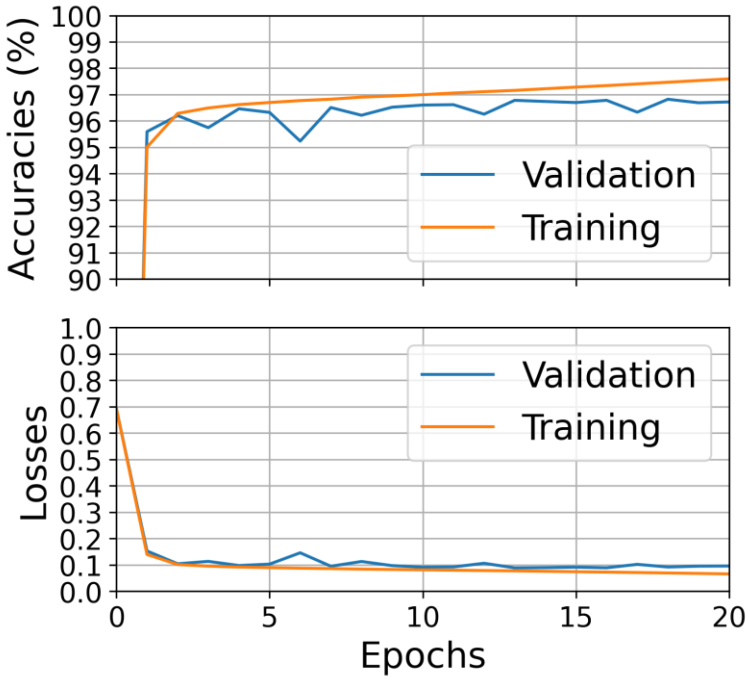

Figure 2.5 The performance of training for the unshifted datasets. (a) the classier accuracy against the number of epochs on validation and training datasets. (b) the loss function against the number of epochs on validation and training datasets.

2.4.3 Network Visualization

I use a technique called Guided Grad-CAM (Selvaraju et al., 2017) to visualize the parts of the input waveform that are important for predicting a class. Such visual explanations can make the 'black-box-like' deep-learning model more transparent and understandable. Guided Grad-CAM combines the best of GBP (Guided Backpropagation) (Springenberg et al., 2014) and Grad-CAM (Gradient-weighted Class Activation Mapping) (Selvaraju et al., 2017). GBP computes gradients for the input waveform with the high resolution and then zero-outs negative gradients to highlight the important parts of the input waveform for predictions when backpropagating through the layers (Figure 2.6b). Grad-CAM visualization is class-discriminative and highlights the important parts at the last CNN layer that has a relatively lower resolution compared to the input waveform (Figure

2.6c). Therefore, the combined Guided Grad-CAM visualization is class-discriminative and localizes the important parts of the input waveform with high-resolution (Figure 2.6d). Figure 2.6 shows the Guided Grad-CAM visualization results for an example input waveform.

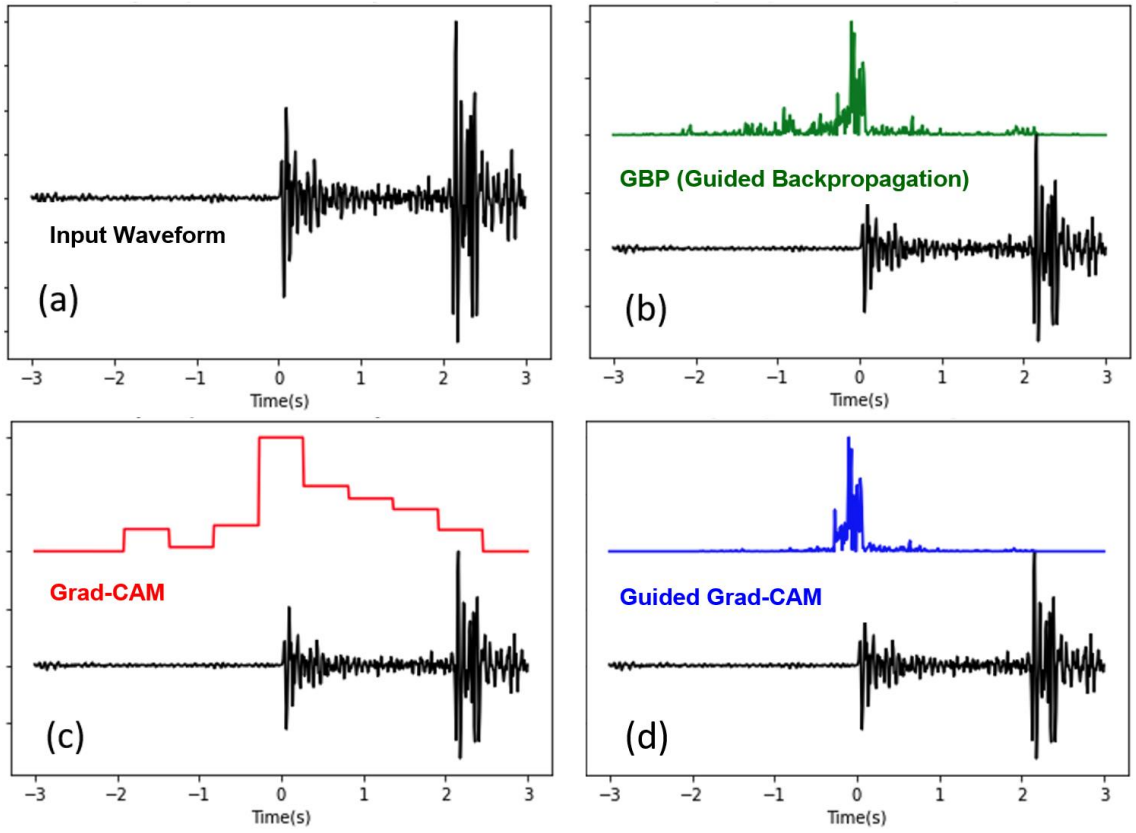

Figure 2.6 Visual Explanations from the network for the polarity classification (NPC). (a) Original waveform. (b) GBP. (c) Grad-CAM. (d) Guided Grad-CAM.

2.5 Results

2.5.1 Testing with Unseen Data from Seen Regions

I examine the performance of the trained NPC using the test dataset that has not been seen by the model during the training process. Note this test dataset is from the same regions as the training and validation datasets (Section 2.3.2). The performance is

quantified based on the standard F1 score, which is the harmonic mean of precision and recall (Zhu and Beroza, 2018; Zhu et al., 2019; Uchide, 2020; Zhai et al., 2021c). They are defined as:

$$precision = \frac{TP}{TP + FP} \tag{2.2}$$

$$recall = \frac{TP}{TP + FN} \tag{2.3}$$

$$F1\ score = \left(\frac{precision^{-1} + recall^{-1}}{2}\right)^{-1} \tag{2.4}$$

where T means true, F means false, P means positive, and N means negative. Therefore, TP is the number of true positives, FP is the number of false positives, and FN is the number of false negatives. For the class of upward polarity, $TP = TU$, $FP = FU$, and $FN = FD$. For the class of downward polarity, $TP = TD$, $FP = FD$, and $FN = FU$ (see the detailed explanation in Equation 2.1). The average F1 scores of upward and downward polarities are 97% for the NPC trained and tested with unshifted datasets, and 93% for the NPC trained and tested with shifted datasets, respectively. Note that the definition of precision and recall are the same as them in Uchide (2020), and the definition of F1 score is the same as it in Zhu et al. (2019).

2.5.2 Testing with Unseen Data from Unseen Regions

To explore the generalization of NPC, I test its ability to predict polarities for the data from two unseen regions, Iberia and Xichang, Western China. I apply the same preprocessing steps (Section 2.3.2) to build the test datasets from these two regions. Then

I use these two datasets to test the NPC model trained with a shifted global dataset and the model trained with the Southern California dataset (Ross et al., 2018a). Table 2.2 shows the comparisons of both models in terms of the average F1 scores of upward and downward polarities in these two regions. The F1 scores of NPC on both datasets are about 85%. The F1 scores of the other models are about 77% on the Xichang dataset, and about 40% on the Iberia dataset. Note that although there is no waveform manually labeled as 'unknown' by human experts in these two datasets, Ross et al. (2018a)'s model may classify a waveform as 'unknown' polarity as designed.

Table 2.2. Comparison of different models using datasets from unseen regions.

Dataset	Xichang unshifted	Xichang shifted	Iberia unshifted	Iberia shifted
F1 score of the model in Ross et al. (2018a)	76%	77%	39%	40%
F1 score of the NPC model in this study	84%	85%	86%	86%

2.6 Discussion

2.6.1 Performance of the NPC Model and the Other Model

The higher accuracy and more generic performance of NPC when compared with other existing models could be mainly due to the following two factors. The first one is that this network is deeper than previous models and is based on not only CNNs but also the attention layers (CBAM). The other one is that the training dataset is larger and consists of data from different regions around the world, somewhat similar to the better performance of the EQTransformer model when compared with other phase-picking models (Mousavi et al., 2020).

The performance of NPC on the randomly shifted data (93%) is slightly lower than the unshifted data (97%). This is because the first-motion polarity determination strongly depends on the accuracy of the first motion (arrival) time. For the unshifted dataset, the arrival time is fixed at the center of the input time window. This makes the first-motion polarity picking easier than the randomly shifted cases. The 93% F1 score is also a generally accepted value for such simple tasks. The fact that NPC can work for randomly shifted data suggests that NPC's architecture also has the potential ability to pick or refine the arrival times and to determine its polarity at the same time.

The performance of NPC on two datasets from the unseen regions (Iberia and Xichang) has the F1 scores of around 85%, higher than the model trained only on the Southern California dataset in a previous study (Ross et al., 2018a). Note that a fair and accurate comparison of different models is a challenging task (Mousavi et al., 2020; Münchmeyer et al., 2022). For example, unlike Ross et al. (2018a), in this study, no 'unknown' class is included beyond up and down polarity. This may cause some biases during the comparison. In general, I expect that training a more advanced model/network with a larger dataset using more powerful computational resources would generally achieve better performance. The results from this work and some other recent studies in seismology and computer science generally agree with this assumption (Brown et al., 2020; Mousavi et al., 2020). As mentioned in Ross et al. (2018a), future studies will build better training datasets and better models following this direction.

2.6.2 Network Visualization and Explanation

In this study, I have developed the NPC model for picking first-motion polarities with relatively high accuracy. In addition, I used the Guided Grad-CAM to understand NPC and quantify the importance of different sections of the input waveform in making a prediction (classification). The blue line in Figure 2.6d shows the normalized importance as a function of time for an example input waveform (the black line in Figure 2.6). Higher values mean greater importance for making a decision by the NPC. The results show attended parts clearly. The NPC appears to learn that the later part (on the right side) of the example waveform is not important for polarity determination even though the amplitude of this part is higher than other parts. The attended part by NPC is exactly the same as human experts because they also focus on the narrow window around the P-wave arrival time to manually determine its first-motion polarity. Recently, Kong et al. (2022) also used a similar technique (Grad-CAM) to visualize their deep-learning model designed for explosion-earthquake discrimination.

There are additional potential benefits for applying model visualization techniques (e.g., Guided Grad-CAM) in the field of machine learning application in seismology. For a straightforward problem like the polarity determination, the result of the Guided Grad-CAM can be used to verify the prediction results and remove false or not-trustable classifications. For example, if the most important part suggested by the Guided Grad-CAM is not around the P-wave arrival time for a waveform, it is likely not a reliable classification result and may need to be removed. If the target problem is not straightforward (e.g., building a model to map a complex 3-D velocity model directly from full waveforms recorded by a seismic array), human experts are not sure which parts of the

waveforms should be more important than others. Hence, I envision that seismologists may get some insights from the model visualization results and learn additional physics from machine learning models. I hope that such insights may inspire seismologists to develop better physics-based methods and achieve higher performance in the future. For example, people may discover some seismic signals or relationships between them that have not been widely used or identified in previous studies.

2.6.3 Using the Pre-trained NPC in Future Studies

The pre-trained NPC model might be directly used in future studies to automatically determine P-wave first-motion polarities for their dataset. Here I would like to highlight two points for the direct usage of the pre-trained NPC model. The first is that it is best to have waveforms pre-processed using the same procedures mentioned in Section 2.3.2. The only exception would be the flipping and shifting steps, which are only applied during the training but not deploying stages. The second is that some additional steps should be performed to obtain a solid result. For example, the input waveforms should be pre-selected by some criteria (e.g., SNR) to only keep the high-quality data with a clear P-wave signal (Zhai et al., 2021c). I do not expect that the NPC can deal with unclear signals or those with low SNRs because the training data are from labels created by human experts, and it is also a challenge for human experts to determine the polarity of noisy data. Additional steps are needed to clean up the outputs of NPC. For example, one can set a relatively high threshold (e.g., 0.7 or 0.95) for the output confidence score (Uchide, 2020; Zhai et al., 2021c) and use the ODIN technique (Liang et al., 2020) to deal with the out-of-distribution problem mentioned in Section 2.4.1. The Guided Grad-CAM network visualization

technique has the potential to be used to verify the prediction results and remove false or not-trustable classifications as mentioned in Section 2.6.2.

Besides a direct usage without any change, the pre-trained NPC can also be fine-tuned (Uchide, 2020; Baker et al., 2021) with a small training dataset to improve its performance for a special dataset of natural earthquakes, microseismic events during a hydraulic fracturing or other fluid injection procedures, and acoustic emission (AE) events during laboratory rock mechanics experiments.

2.6.4 Limitations of Current Results and Planned Future Study

In this section, I briefly summarize the limitations in the current results and planned future studies to address these potential problems. First, I will add more training data from the Chinese mainland region, the Northern California region, and the Taiwan region to build a better model. Second, I will test the model performance with a real acoustic emission dataset (Li et al., 2022b) with manually labeled polarities. I will fine-tune the model with the transfer learning technique if needed. Third, I will quantify the effects of SNR on the model performance to obtain the SNR threshold for the input data in practice. Last, I will update the visualization results of the future updated models using the Guided Grad-CAM technique to gain more insight into the models.

2.7 Conclusions

I build a generic deep-learning network (NPC) for P-wave first-motion polarity classification based on the CNN and an attention mechanism. I train it with global earthquake datasets at local to regional distances with ~3.5 million first motion polarity

picks. The accuracy of the model to predict upward or downward polarities is 0.97. If there is a random time shift of the P-wave arrival time within 0.2 s, the accuracy is 0.93. I also test on two unseen datasets from Iberia and Xichang. The accuracy is about 0.85, higher than a previous model trained only using the Southern California dataset. The network visualization results based on the Guided Grad-CAM help us to understand how the NPC makes a prediction and can be used to clean up the outputs. I expect that this publicly available pre-trained model can be directly applied or fine-tuned with a small dataset to determine P-wave first-motion polarity for natural earthquakes, hydraulic fracturing events, and acoustic emissions.

CHAPTER 3. INVESTIGATING THE IMPACTS OF A WET TYPHOON ON MICROSEISMICITY: A CASE STUDY OF THE 2009 TYPHOON MORAKOT IN TAIWAN BASED ON A TEMPLATE MATCHING CATALOG

3.1 Summary

The results presented in this chapter have been published in a peer-reviewed journal, Journal of Geophysical Research: Solid Earth, as a research article (Zhai et al., 2021c). Recent studies suggested that transient and long-term stress changes caused by Earth's surface processes (e.g., extreme weather events, annual variations on groundwater storages) can affect earthquake activities in the subsurface. However, these studies may be limited by the completeness of standard earthquake catalogs, especially during or right after extreme weather events. Here I apply the template matching method to build a more complete earthquake catalog in Taiwan spanning seven months before and twelve months after 2009 typhoon Morakot, which brought the highest rainfall in southern Taiwan in the past 60 years and triggered numerous landslides. I then use the enhanced catalog to investigate possible influences of typhoon-driven Earth's surface processes (atmospheric pressure, precipitation, and erosion) on local seismicity. I find that the seismicity rate of a 40-days-long earthquake sequence in northeastern Taiwan was reduced significantly right after the passage of typhoon Morakot's eye center. In the typhoon-triggered landslide zone in southern Taiwan, I find a slight increase in background seismicity rate in the next year after Morakot, matching the results of a recent study. However, I do not observe a clear change in the Gutenberg-Richter b-value in this zone, which is different from the recent

study. Station outages during and right after Morakot prevent us from better understanding short-term precipitation effects on local seismicity. Overall, except for a reduction in seismicity rate near the typhoon's low-pressure eye center in northeastern Taiwan, I do not observe other clear seismicity changes that can be attributed to surface changes induced by typhoon Morakot.

3.2 Introduction

Earthquakes occur in the subsurface but can also alter the Earth's surface. Examples include surface ruptures (Bonilla et al., 1984; Peltzer et al., 1998; Wesnousky, 2008), and shaking-induced landslides (Rodrıguez et al., 1999; Keefer, 2002; Khazai and Sitar, 2004; Yin et al., 2009). However, the influence of Earth's surface processes on subsurface fault slip and earthquake behaviors remains poorly understood. Previous observational and modeling studies have shown that certain surface processes are capable of generating loading/unloading stresses and modulating earthquake behaviors. These include variations in atmospheric pressures (Gao et al., 2000; Liu et al., 2009; Lin, 2013; Hsu et al., 2015; Meng et al., 2018), reservoir impoundment and fluctuations in reservoir water level (McGarr et al., 2002; Lei, 2011; Tao et al., 2015), construction (Lin, 2005; Qian et al., 2019), seasonal water storage and snow load/unload (Heki, 2001; Heki, 2003; Bettinelli et al., 2008; Johnson et al., 2017a; Johnson et al., 2017b; Johnson et al., 2020; Hsu et al., 2021), glacier load and unload (Thorson, 1996; Wu and Johnston, 2000; Grollimund and Zoback, 2001), erosion and sedimentation (Maniatis et al., 2009; Calais et al., 2010; Steer et al., 2014; Jeandet Ribes et al., 2020; Steer et al., 2020), and pore pressure changes due to rainfall and other extreme weather events (Roth et al., 1992; Hainzl et al., 2006; Kraft et al., 2006; Husen et al., 2007; Miller, 2008; Costain and Bollinger, 2010).

The time scales of these surface variations and the associated stress perturbations are broad, ranging from hours (e.g., extreme weather events), days to years (e.g., annual variations in water cycles), to hundreds to million years (e.g., long-term erosion). The stress perturbations range from a few kilopascals (KPas) (Gao et al., 2000) to a few megapascals (MPas) (Manga and Brodsky, 2006; Steer et al., 2014). While results from some studies were later confirmed by subsequent works (e.g., Kraft et al. (2006); Hainzl et al. (2006); Svejdar et al. (2011); Hainzl et al. (2013a)), there are still many open questions on the robustness of some observations and the underlying physical mechanisms. For example, Liu et al. (2009) interpreted the transient strain observed in borehole strainmeters located in eastern Taiwan as evidence for typhoon-triggered slow earthquakes. However, Hsu et al. (2015) found that the same observed strain changes are mostly associated with environmental factors such as rainfalls, rather than subsurface slip from slow earthquakes. Mouyen et al. (2017) strengthened the findings of Hsu et al. (2015) by quantifying the contributions of air pressure, ocean loading and rainfalls on surface deformation. While stress changes from long-term surface processes (e.g., seasonal water storage and snow load) generally show robust correlations with seismicity (e.g., Johnson et al. (2017b); Hsu et al. (2021)), it is still not clear whether transient stress changes from short-term events (e.g., tropical cyclones) are capable of triggering earthquake activities (Meng et al., 2018; Steer et al., 2020).

An ideal region to examine the relationship between short-term surface processes and subsurface seismic activity is Taiwan (Figure 3.1). Located at the boundary between the Eurasian and the Philippine Sea plates, Taiwan is seismically active (Tsai, 1986) and is monitored by dense and permanent seismic networks (Shin, 1992). In addition, Taiwan

frequently experiences tropical cyclones (also known as typhoons in Northwest Pacific, or hurricanes in Atlantic or Northeast Pacific). Typhoons can cause significant short-term changes such as atmospheric pressure variations (Chen, 2009) and extreme precipitation (Chien and Kuo, 2011), trigger landslides (Lin et al., 2011), and facilitate long-term erosional processes (Dadson et al., 2003). Based on historical records of these atmospheric, hydrological, and geological phenomena, Lin (2013) studied 102 typhoons that traversed or passed nearby Taiwan from 1995 to 2011 and found a 63.75% earthquake-triggering probability by a typhoon. Among them, the 2009 typhoon Morakot produced the highest rainfall in southern Taiwan in the recent 60 years (Chien and Kuo, 2011). Morakot made landfall in Taiwan on August 8 2009 (Figure 3.1), delivered up to 3 meters of rainfall in five days between August 6 and 10, 2009 (Chen, 2009; Chien and Kuo, 2011), and led to more than 20,000 landslides and subsequent erosional processes in Southern Taiwan (Lin et al., 2011; Lin et al., 2015; Hung et al., 2018; Steer et al., 2020). Therefore, I select the 19 months around typhoon Morakot in Taiwan as the target time window for the study.

In a recent study, Steer et al. (2020) found possible changes in earthquake statistics at 0-15 km depth in southern Taiwan following Typhoon Morakot. They concluded that these changes were induced by landslides and subsequent erosion driven by typhoon Morakot and lasted for at least 2.5 years. In another recent study, Hsu et al. (2021) found seasonal seismicity rate variations in western Taiwan. They proposed that these variations are driven by interannual hydrological changes in that region. Both studies utilized earthquakes listed in the Central Weather Bureau Seismic Network (CWBSN) catalog. However, standard catalogs are inherently incomplete, especially in the lower magnitude ranges, or right following large earthquakes with high background noises and overlapping

arrivals (Kagan, 2004; Peng et al., 2006; Chang et al., 2007; Enescu et al., 2007). Because extreme winds and heavy rainfalls are generally associated with wet typhoons and can generate high seismic noises, I expect that the CWBSN catalog may not be complete, at least in the time windows during and right after typhoon Morakot.

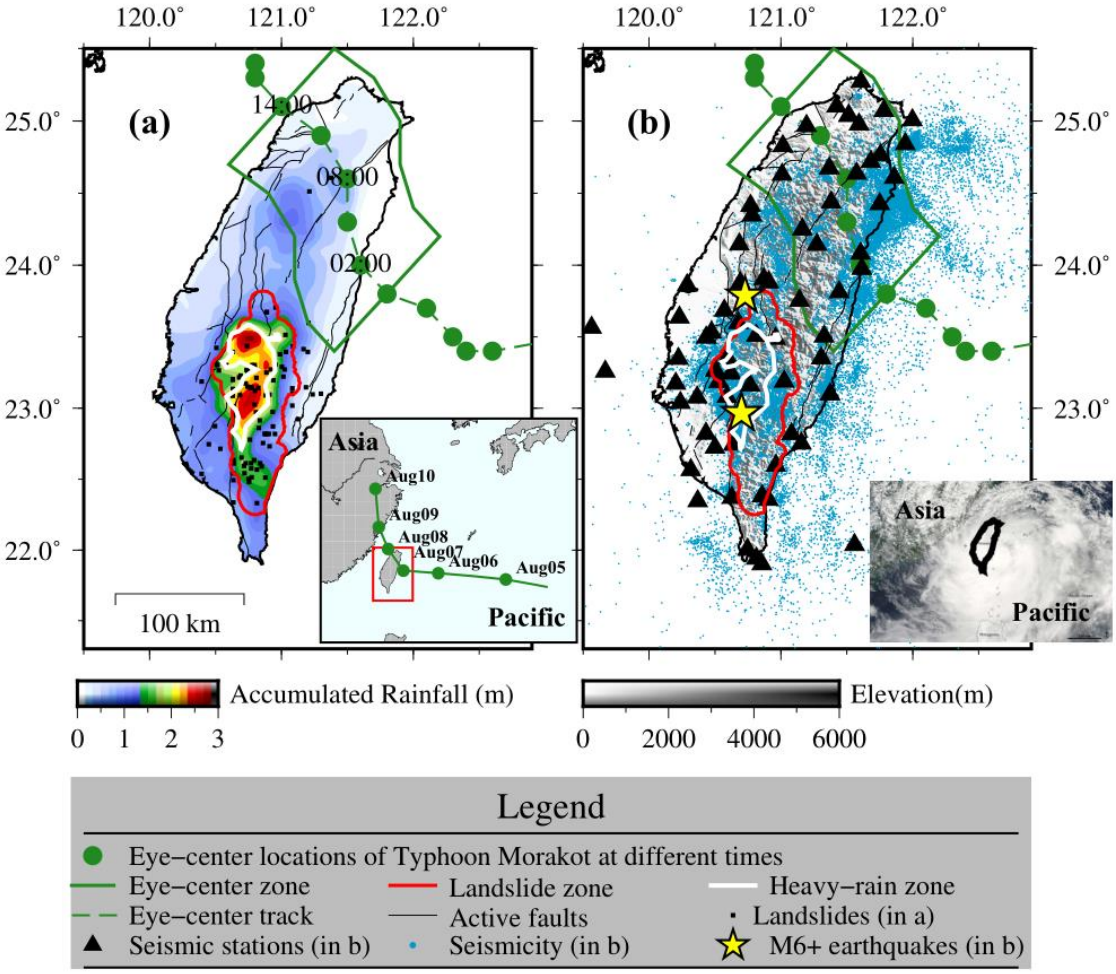

Figure 3.1 Typhoon Morakot and seismic network in Taiwan. (a) Typhoon-induced accumulated rainfall and landslides. The rainfall/precipitation data for 5 days (August 6-10 2009) are from Central Weather Bureau. The green dots on the green dashed line are the eye-center locations at different times on August 8 2009 (GMT+8). The green line marks the zone within ~60 km of the eye-center locations of Morakot, termed the eye-center zone in this study. The black squares are Morakot-induced landslides listed in Lin et al. (2015). The red line marks the zone with a high spatial density of landslides triggered by typhoon Morakot. This zone is the same as in Steer et al. (2020), termed the landslide zone in this study. The white line is the 2-meter contour of the accumulated rainfall, termed the heavy-rain zone in this study. The

black lines are active faults. In inset marks the study region (red box) and the typhoon path (green line) in a larger map of the Asia-Pacific. The blue dots mark the locations at 8 PM on these days. (b) Seismic stations of Central Weather Bureau Seismic Network (CWBSN) and seismicity in the Wu catalog (Wu et al., 2008a**) from January 1 2009 to July 31 2010. The two yellow stars are two magnitude (M) 6+ earthquakes that occurred 3 and 9 months after typhoon Morakot (North: M6.0 Nantou earthquake on November 5 2009, at 24-km depth; South: M6.4 Jiashian earthquake on March 4 2010, at 22-km depth). The colored lines are the same as in (a). The inset shows a satellite image of Morakot on August 7 2009 (adapted from a NASA image), the black line marks the coast of Taiwan's main island.**

In this study, I first build a more complete earthquake catalog for Taiwan from 7 months before to 12 months after typhoon Morakot. I use a matched filter technique (MFT, also known as template matching) (Gibbons and Ringdal, 2006; Shelly et al., 2007; Peng and Zhao, 2009) to detect possible small earthquakes that are not listed in the CWBSN catalog. I also relocate the detected events based on waveform-correlated differential times, and determine their focal mechanisms based on first-motion polarities from a deep-learning model. Finally, I use the updated catalogs to investigate the spatiotemporal properties of seismicity before and after typhoon Morakot and examine the possible influences of typhoon Morakot on local seismicity.

3.3 Data

3.3.1 Continuous Waveforms and Template Catalog

In this study, I use raw continuous waveforms recorded by CWBSN over the study period from 01/01/2009 to 07/31/2010 in Taiwan (Shin, 1992). CWBSN includes 71 three-component short-period stations with a sampling rate of 100 Hz (Figure 3.1b). I use as templates 32,802 local earthquakes within the study period and study region (latitude: 21°-26°N, longitude: 119°-124°E) listed in a 3D relocated seismicity catalog (Wu et al., 2008a), which is termed the Wu catalog in this study. I use the Wu catalog instead of the standard

CWBSN catalog that contains 33,496 events, mainly because the Wu catalog has more accurate locations based on a 3D velocity model. The Wu catalog also includes 454,055 *P* wave arrival times, 372,083 *S* wave arrival times, and 42,119 *P* wave first-motion polarities manually determined by CWBSN analysts for the template events used in this study.

3.3.2 The Number of Stations in Operation and Noise Energy Estimation

A seismic station's operational status and noise level can affect its ability to record local microseismicity. Typhoon Morakot brought strong wind and heavy rainfall to Taiwan, which increased seismic noise recorded by the CWBSN stations. In addition, some stations did not work properly during or right after such an extreme weather event due to power and communication outages, and equipment damages. In this section, I measure the daily number of operating stations and daily background noise to better understand how these changing parameters affect the subsequent analysis of seismicity rate changes.

First, I measure the daily number of operational stations. I manually check the raw 24-hour long waveforms and evaluate that are no data gaps in the raw waveforms. However, in certain time windows, all data points have exactly the same value (i.e., 0, –1, +1), indicating that the corresponding component of that station was not fully operational during these time windows. For each 24-hour long waveform, I measure the total length of the constant-value windows by counting the total number of points, in which the k^{th} derivative is equal to zero. The result is not sensitive to k, because the k^{th} derivative of a constant-value curve is always zero, regardless of the value of the positive integer k. For simplicity, I set k=10 in this study. Although the 10^{th} derivative requires plenty of data points to calculate, it is needed to identify the long constant-value window. Next, I define an

operational ratio (o-value) of a given day-long waveform by 1 minus the result of the constant-value window length divided by the total length (24 hours). I find that the distribution of o-values of all waveforms I used is clearly bimodal, either close to 0 or close to 1 (Figure A.1). Hence, I set an o-value of 0.95 as the threshold for an operational station. For each station on each day, I count the station as operational on that day if the o-values of three components are all higher than the threshold.

Next, I use the waveforms of operational stations to measure the average noise energy of each day. The daily average noise energy is defined as:

$$E_{noise}(d) = mean_s\{mean_c\{median_t[A^2(d,s,c,t)]\}_{norm}\} \quad 3.1$$

where E_{noise} is the noise energy; A^2 is the squared amplitude of the 2-16 Hz bandpass-filtered waveform at day d, station s, component c, and time t; $median_t[\,]$ is the median value over time; $mean_c\{\,\}$ is the average value of all components; $mean_s\{\,\}$ is the average value of all stations; and $norm$ is normalization. The 2-16 Hz frequency band of the filter is the same as used in the earthquake detection described in the following section. I take a median value instead of an average value of the waveform amplitude in order to reduce the effect of local transient high-noise outliers. The normalization is applied before averaging to balance the weights of different stations. Figure A.2 shows that the noise level during weekends is clearly lower than during workdays. The noise level during the Spring Festival (also known as Lunar or Chinese New Year) holidays in January 2009 and February 2010 is even lower.

3.4 Building a New Seismicity Catalog

3.4.1 Earthquake Detection

To detect possible small earthquakes that are not listed in the CWBSN catalog, I use waveforms of template events to scan through continuous waveforms with the MFT (Peng and Zhao, 2009). I use a GPU-based package developed by Meng et al. (2012) to perform this task. Figure 3.2 shows a general workflow in this study, largely following those used in several recent studies (Meng et al., 2018; Ross et al., 2019b) and is described below.

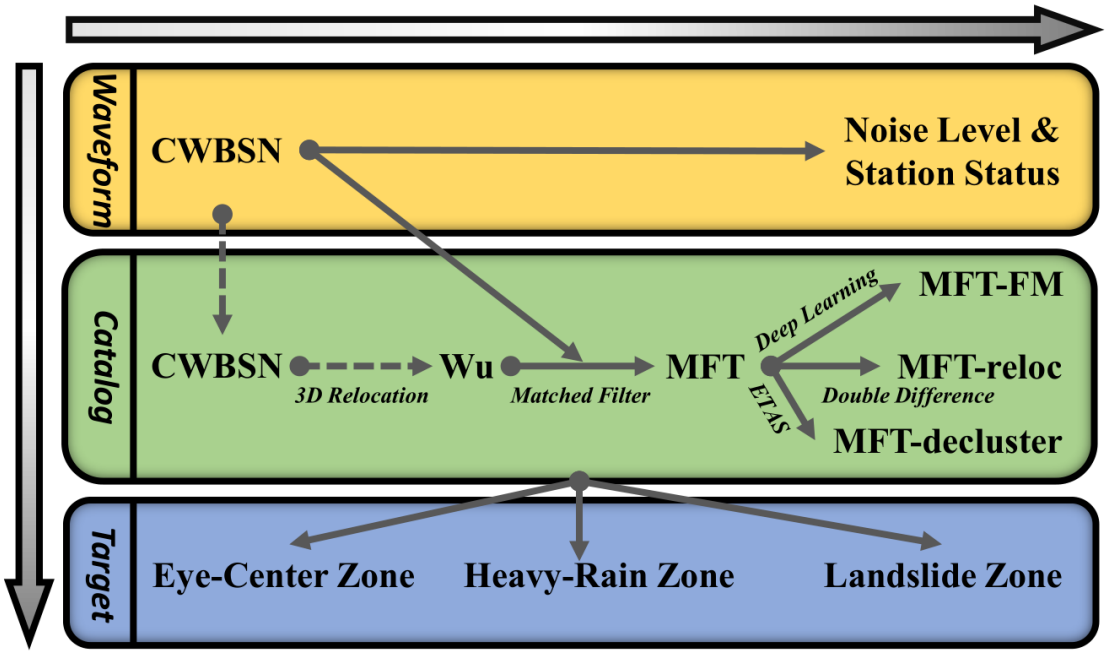

Figure 3.2 The general workflow of this study. The gray arrows mark the work done in this study and the gray dashed arrows mark the work done in previous studies. The yellow panel summarizes the continuous waveform data used in this study (Section 3.3). The green panel summarizes the catalogs used/built in this study. "CWBSN" means the CWBSN catalog used in Steer et al. (2020). "Wu" means the 3D relocated seismicity catalog (Wu et al., 2008a**), which is also the catalog of template events used in earthquake detection with matched filter technique (Section 3.3.1 & 3.3.2). The "MFT", "MFT-reloc", "MFT-FM", and "MFT-decluster" are the MFT catalogs after detection (Section 3.4.1), after relocation (Section 3.4.2 after measuring the focal mechanism (Section 3.4.3), and after declustering (Section 3.5.2), respectively. The blue panel shows three different target regions analyzed in this study with the catalogs mentioned above. The location of "Eye-Center Zone" (Section**

3.5.4 & 3.6.2), "Heavy-Rain Zone" (Section 3.5.5 & 3.6.3), and "Landslide Zone" (Section 3.5.6 & 3.6.4) can be found in Figure 3.1.

First, I down-sample all the raw continuous waveforms from 100 Hz to 50 Hz to speed up the subsequent computation. Then, I apply a bandpass filter of 2-16 Hz to these waveforms to enhance signals of local events. Template waveforms of the 32,802 local earthquakes are cut from the filtered continuous waveforms based on the phase arrival times in the Wu catalog. I compute the signal-to-noise ratio (SNR) for all template waveforms. The *P*-wave signal is 3 s or *S*–*P*+0.5 s (whichever is shorter) long starting 0.5 s before its arrival time. The *S*-wave signal is 5 s long starting 0.5 s before its arrival time. The noise window is 5 s long ending 0.5 s before the *P* arrival time. To avoid false detections by a few noisy template waveforms, I only select template events having more than 6 waveforms with SNRs greater than 5.

Next, I calculate the stacked cross-correlation (CC) functions for each day of continuous waveforms in the study period and each of these selected template events. To calculate the CC functions for each event-station pair, I use 4 s long windows for both *P*- and *S*-waves starting 0.5 s before their arrival times. All stations within 100 km of the source-receiver distances are used. I only use the vertical component for the *P* wave and horizontal components for the *S* wave. To enhance earthquake signals and suppress uncorrelated background noise, I shift CC functions to the origin time of the template with the corresponding travel times and stack the shifted CC functions. I calculate the median absolute deviation (MAD) for the stacked and normalized CC functions. An initial detection threshold is set at 9 times the MAD (Shelly et al., 2007). After repeating these

steps for all continuous waveforms and all selected template events, I obtain an initial list of detected events (detections).

I then use the following steps to refine this initial list of detections. Because a new event could be detected by multiple template events, there are many duplicated events listed in the initial catalog. To remove these duplicated events, I only keep the highest-MAD detection in each group of detections (separated by less than 2 s) and delete the other detections. Next, I measure the local magnitudes (M) of the newly detected events based on the median peak amplitude ratios between the detected and the template events (Peng and Zhao, 2009). I calculate the logarithm of the median peak amplitude ratio and assume that a factor of 1 difference in magnitude is equal to a factor of 10 difference in amplitude. To ensure that the magnitudes of the newly detected events are well-calibrated, I only use peak amplitude ratios of waveform pairs that meet the following two criteria: (1) SNR of the new detected P-wave or S-wave ≥ 4; and (2) maximum CC coefficient ≥ 0.6. The data window for the CC calculation is 1 s for P waves and 1.5 s for S waves, starting 0.25 s before the arrival time. I allow 1 s shift for P wave and 1.5 s shift for S wave, and apply it to the original data with 100 Hz. This is the same window length used later for obtaining differential travel times and relocations described in the next section.

Finally, I use the following procedure to remove events with relatively large magnitudes and relatively low CC values (but above the 9 times MAD threshold). The procedure is based on the expectation that larger earthquakes should be observed on more stations and components with high SNRs. A newly detected event with magnitude M, is kept as long as it has at least n ($n=3^{(M-1)}$) components that meet the aforementioned two criteria. Otherwise, the event is removed from the catalog. I limit the n to a value between

1 and 15. If the calculated *n* is not in this range, I set it as 1 or 15 (whichever it is closed to). This is an empirical estimation based on the visual examination of hundreds of detections, and is somewhat similar to threshold values often used in relocation programs such as hypoDD (Waldhauser and Ellsworth, 2000). For example, a magnitude 2 event would require 3 components, a magnitude 3 event would require 9 components, and a magnitude 4 (and above) would require 15 components.

The newly built catalog from MFT detection contains 218,155 earthquakes (Dataset S1 in the supporting information), which is termed the MFT catalog in this study. The number of events in the MFT catalog is a seven-fold increase compared to the Wu catalog (templates). Most of the newly detected earthquakes are below magnitude 2. In the two weeks during and after typhoon Morakot (August 6-19 2009), the number of events in the MFT catalog (2,472) is a four-fold increase compared to the Wu catalog (648). Figure 3.3 shows an example of a newly detected event on August 8 2009 (when typhoon Morakot made landfall in Taiwan) and its corresponding template event. The template event is a magnitude 1.88 earthquake that occurred on 2009-08-06T00:29:03.29. The newly detected event is a magnitude 1.90 earthquake that occurred on 2009-08-08T08:15:04.66 (~2 days after the template event). The mean CC value of this detection is 0.53, which is 25.7 times the MAD, suggesting that it occurred close to the template event.

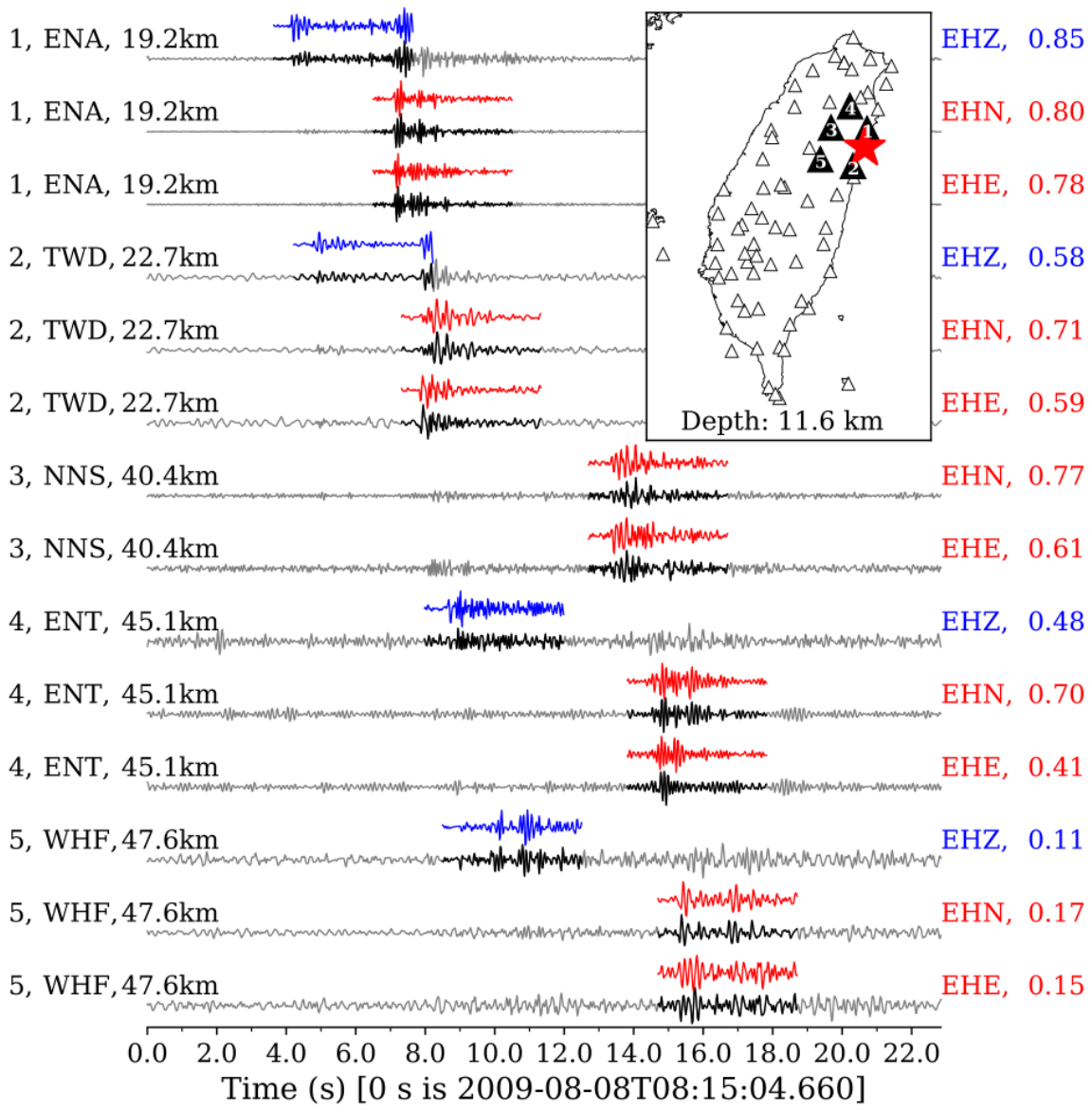

Figure 3.3 An example of a newly detected event on August 8 2009 (when typhoon Morakot made landfall in Taiwan) and its corresponding template event. The blue waveforms are the *P* wave of the template, the red waveforms are the S wave of the template, the gray colors mark the continuous waveforms, and the black sections on the gray waveforms correspond to the newly detected events. The three columns on the left are the station label, station name, and event-station epicentral distance. The two columns on the right are the component name and the CC value on this component. The location of this template (red star) is shown in the inserted map in the upper right corner. All used stations of this detection are marked as filled black triangles in the inserted map. The numbers on these black triangles are the station labels.

3.4.2 Earthquake Relocation

To improve the location accuracy, I relocate the MFT catalog obtained from the seismicity detection. The MFT catalog contains both template and newly detected events. The template events have been located individually with a 3D velocity model by Wu et al. (2008a). Here I first relocate the template events with hypoDD (Waldhauser and Ellsworth, 2000) using just the phase arrival times without the newly detected events. This improves the initial location accuracy of both template and newly detected events for the subsequent relocation process (Ross et al., 2019a). I next assign the locations, *P* and *S* travel times of newly detected events with the same locations and travel times of their best-matching template.

I relocate the MFT catalog with GrowClust, a cluster-based double-difference relocation technique (Trugman and Shearer, 2017). It defines the relative earthquake locations by fitting the observed differential times with a robust L1-norm approach. These precise differential times are measured from waveform cross-correlation (CC). For each earthquake in the MFT catalog, I apply a bandpass filter of 2-16 Hz to the 100 Hz waveforms. The data window for the CC coefficients calculation is 1 s long for *P* waves and 1.5 s long for *S* waves, starting 0.25 s before the arrival time. I allow a 1 s shift for the *P* wave and a 1.5 s shift for the *S* wave. I then perform the pairwise cross-correlation for each event with up to 1000 nearest neighbor template events within a 5-km distance. To avoid multiple crustal phases due to regional propagation, I set the maximum source-receiver distance as 100 km. I use a three-point quadratic interpolation to improve the precision of the CC function near its peak value (Shelly et al., 2016a). These differential times and their corresponding waveform similarity (CC) coefficients are the input data for

the GrowClust relocation procedure. A local 1-D velocity model (Table A.2) averaging from a 3D velocity model of Taiwan (Wu et al., 2007) is used for the relocation.

The best relocation results are produced by setting the minimum similarity coefficients as 0.6 and the minimum number of differential times as 4 (Lin, 2020). To ensure that template events are relocated before newly detected events during the GrowClust inversion process, I increase the similarity (CC) coefficients by a factor of 100 for template-template event pairs, which is the same as in Ross et al. (2019b). In the end, 63,587 (30%) earthquakes in the MFT catalog are relocated (Figure 3.4d). This relocated catalog is termed the MFT-reloc catalog in this study (Dataset S1 in the supporting information). The number of events in the MFT-reloc catalog is a two-fold increase compared to the standard CWBSN catalog or the Wu catalog.

Figure 3.5 shows the frequency-magnitude information of the newly built catalogs and the template (Wu) catalog. As expected, most of the newly detected events are in the range of magnitude 2 and smaller. Note that a small number of larger earthquakes are not successfully relocated. This is because larger earthquakes generally have more complex waveforms, so they do not cross-correlate well with other events nearby (Ross et al., 2019b; Lin, 2020).

In the following sections, I focus primarily on the temporal evolutions of earthquake statistics in the eye-center zone in northeast Taiwan, and the heavy-rain and landslide zones in southern Taiwan (Figure 3.1). Because the scale of these target zones is about several tens of kilometers, much larger than the subtle location changes between the

full MFT and MFT-reloc catalogs, I mostly use the full MFT catalog for subsequent analysis in this study.

3.4.3 Earthquake Focal Mechanisms

In the Wu catalog, only 548 events have focal mechanism solutions within the space-time windows, which are determined based on the first motions with the GaFpfit package (Wu et al., 2008b). In this study, I apply the same package to compute focal mechanism solutions for earthquakes in the MFT catalog using the polarities of *P*-wave first motions picked by a deep learning model. I develop this convolutional-neural-network (CNN) based *P*-wave first-motion polarity (CNN-Polarity) model (Figure 3.6a), which was added to the open-source Yews package developed by Zhu et al. (2019). The CNN-Polarity model is similar to those used in several recent studies (Ross et al., 2018a; Hara et al., 2019; Cheng and Ben-Zion, 2020; Uchide, 2020). The input of this model is a 300-sample-long waveform, which is 3 s long with a 100-Hz sampling rate. The outputs of this model are two non-negative confidence scores corresponding to the probabilities of the upward and downward polarities (Figure 3.6a). The sum of the two output scores is 1.

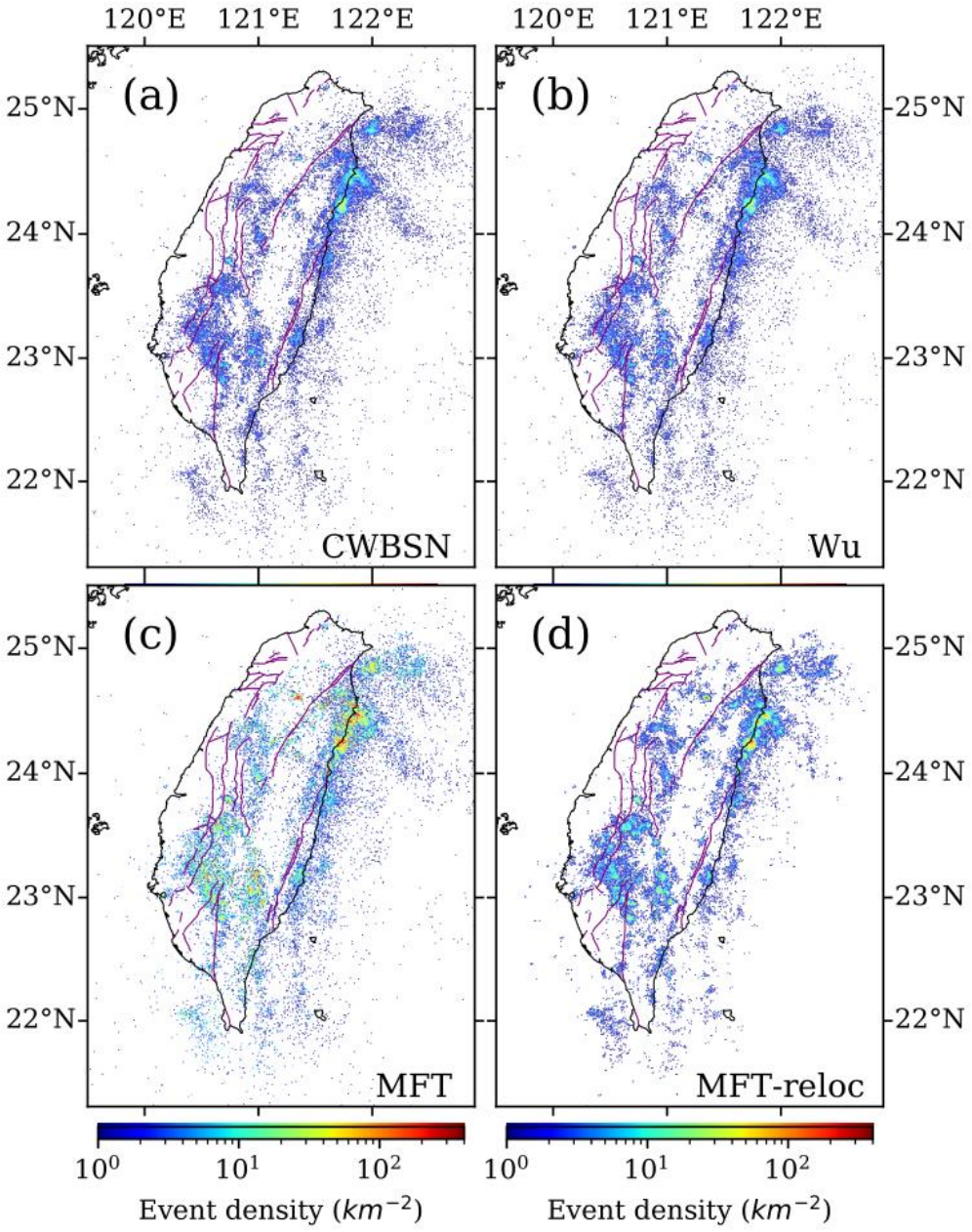

Figure 3.4 Comparison of earthquake locations listed in the four studied catalogs from January 1 2009 to July 31 2010. (a) Earthquake density map of 33,496 events in the CWBSN catalog. (b) Earthquake density map of 32,802 events in the Wu (templates) catalog. (c) Earthquake density map of 218,155 events in the MFT catalog. (d) Earthquake density map of 63,587 events in the MFT-reloc catalog. The purple lines mark active faults in all panels.

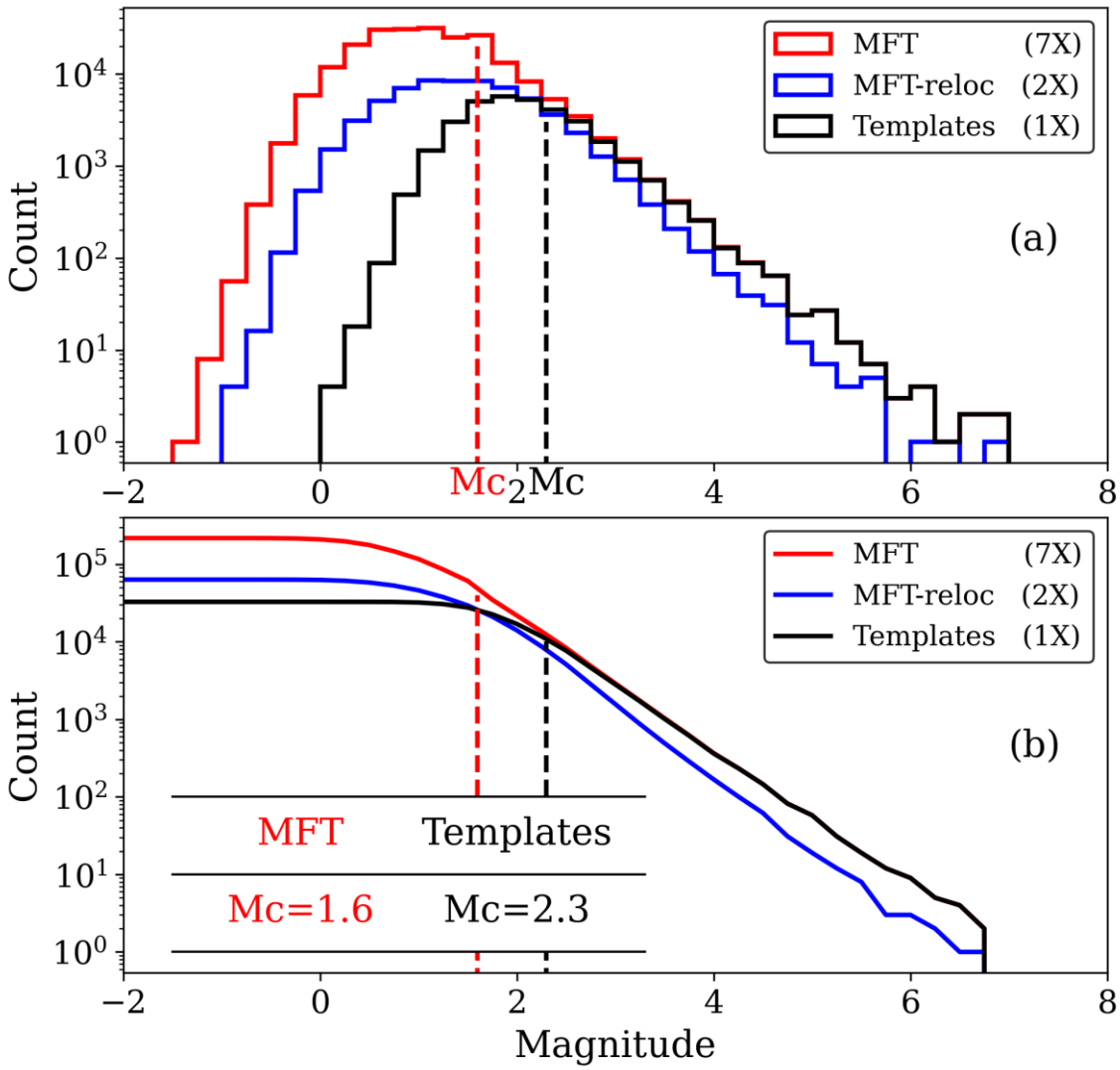

Figure 3.5 Frequency-magnitude distribution of earthquake. (a) Frequency-magnitude distribution of seismic events listed in the full detection catalog (MFT), the relocated subset of the MFT catalog (MFT-reloc), and the Wu catalog (Templates). (b) The corresponding cumulative frequency-magnitude distribution of these catalogs. The estimated magnitude of completeness (*Mc*) of the MFT catalog and the Wu catalog (Templates) are 1.6 and 2.3, respectively.

First, I build data sets to train and test this model. I use all the polarity labels (upward: 18,915; downward: 23,204) manually assigned by CWBSN analysts and listed in the Wu catalog. I randomly split the whole data set into training (80%), validation (10%), and test (10%) data sets. Upward polarities are labeled by 0 and downward polarities are

labeled by 1. The waveforms corresponding to these labels are cut 1.5 s before and 1.5 s after their arrival times from the 2-16 Hz band-pass-filtered continuous data. Each 3 s long waveform (300 data points) is normalized by its maximum absolute values. I flip the waveforms upside down to equalize the number of upward and downward polarity data (Uchide, 2020). To reduce the uncertainties in the arrival times picking, I randomly apply 100 times of time-shift within ± 1 s to each waveform. The total number of data is hence augmented 200 times by flipping and time-shifting (Uchide, 2020). Then, I train the model with the augmented training dataset. After training, I quantify the performance of the trained model based on precision, recall, and F-1 score (Zhu et al., 2019; Uchide, 2020) with the test data set (not used during the training). All of the precision, recall, and F-1 scores of the trained model on the test data set are greater or equal to 95% (Table 3.1).

Next, I deploy the trained model to the MFT dataset. I prepare the waveforms for the MFT dataset using the same preprocess as the training data set, but without flipping and time-shifting. I adopt a confidence threshold of 0.7, which is the same as it in Uchide (2020). For a quality control purpose, I require a minimum SNR of 5 for any waveform before picking its polarity. I group all the events detected by the same template event as a family (Chamberlain et al., 2017). I assume that these similar events in a family share a common focal mechanism solution with a first-order approximation (Shelly et al., 2016b). After deploying the trained model to the MFT dataset, I obtain 158,320 predicted *P*-wave first-motion polarities (upward: 63,738; downward: 94,582) for these families. This number of polarities is a four-fold increase compared to it manually assigned by CWBSN analysts and listed in the Wu catalog.

In the end, I use these predicted polarities to calculate the focal mechanisms with the GaFpfit package (Wu et al., 2008b). The minimum number of required polarities is 8 (Ross et al., 2018a; Uchide, 2020), and the maximum of the stations' coverage gap is 180° (Wu et al., 2008b). I obtain focal mechanism solutions of 1,166 families (Figure 3.6c) corresponding to 3,816 events. This focal mechanism catalog is termed the MFT-FM catalog in this study (Dataset S1 in the supporting information). This number of events in the MFT-FM catalog is a seven-fold increase compared to it (548 events, see Figure 3.6b) in the Wu catalog (Wu et al., 2008b; Wu et al., 2010) in the study period and region.

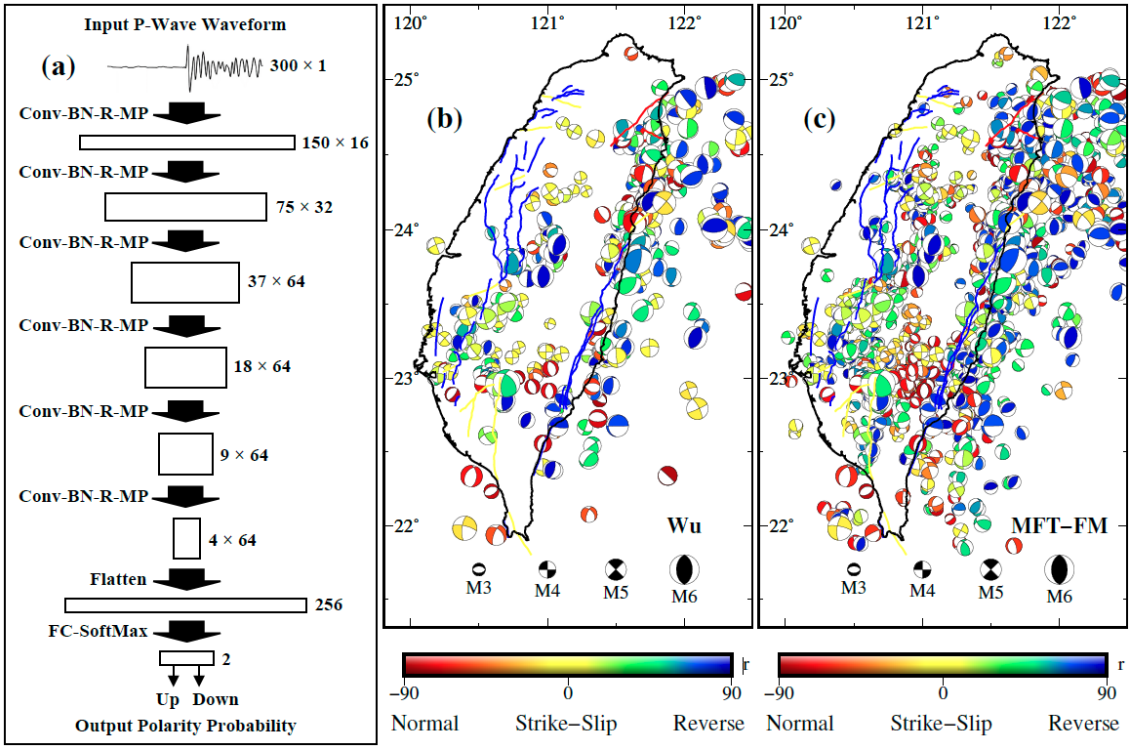

Figure 3.6 The measurement of focal mechanism solutions with a deep-learning model for polarity picking. (a) A schematic diagram of the convolutional-neural-network (CNN) based *P*-wave first-motion polarity (CNN-Polarity) model used in this study. The numbers on the right denote the size of samples and channels. There are 6 convolutional layers for feature extraction. The final layer is a fully connected layer for classification. 'Conv', 'BN', 'R', 'MP', and 'FC' on the left represent convolution, batch normalization, ReLu, max pooling, and fully connected layers, respectively. (b) Map of focal mechanism solutions in the Wu catalog (Wu et al., 2008b**; Wu et al., 2010)**

in the study period. The focal mechanisms beach balls are color-coded based on the r-value, which is a function of the rake. It can be used to determine the faulting types of earthquakes (Shearer et al., 2006**). (c) Map of focal mechanism solutions in the MFT-FM catalog built in this study. Each beach ball denotes the focal mechanism of the template event in each family. The colored lines in b and c mark the active faults in Taiwan (**Shyu et al., 2016**). Red lines are normal faults. Yellow lines are strike-slip faults. Blue lines are reverse faults.**

Table 3.1 Precision, recall, and F-1 score of the two classification categories.

Categories	Precision	Recall	F-1 score
Upward (0)	0.9563	0.9451	0.9507
Downward (1)	0.9457	0.9569	0.9513

3.5 Statistics Analysis of the Newly Built Catalogs

3.5.1 Mc and b-value Calculation

The magnitude of completeness (*Mc*) and the parameter *b* in the Gutenberg–Richter frequency-magnitude relationship (i.e., the G-R law (Gutenberg and Richter, 1944)) are commonly used to characterize statistical behaviors of an earthquake catalog. *Mc* is the minimum magnitude above which all earthquakes in a given space and time window are reliably recorded. The G-R law is defined as $N\ (\geq Mc) = 10^{a-bM}$, which describes the power-law relationship between the magnitude (M) and the total number (N) of earthquakes of at least that magnitude in a given space and time window (Gutenberg, 1956). I use a modified version of the maximum curvature method (MAXC) to calculate the *Mc* of a given catalog (Wiemer and Wyss, 2000). Specifically, *Mc* is set to 0.5 plus the maximum of the first derivative of the discrete G-R law plot (Figure 3.5b), which is the same as in Steer et al. (2020) for direct comparisons in later sections. Note the maximum of the first derivative in Figure 3.5b is the same as the maximum in Figure 3.5a. Then, I use all the events above *Mc* to compute the *b*-value and its uncertainty with the maximum

likelihood estimate method (Aki, 1965). Based on the calculation, the *Mc* of the full MFT catalog and the Wu catalog (Templates) are 1.6 and 2.3, respectively (Figure 3.5b). The *Mc* and *b*-value of the MFT-reloc catalog are not measured because some large earthquakes are not relocated. To obtain the *b*-value map, I use spatial sliding windows to further divide and sample the catalogs (Wiemer and Wyss, 2002). The radius of the sliding spatial window is set as 30 km. The minimum number of events with magnitude large or equal to *Mc* for the calculation of the *b*-value is set at 50. The sliding-window method and the two parameters are the same as in Steer et al. (2020) for direct comparisons in later sections.

3.5.2 Declustering the Seismicity Catalog

Microseismicity generally include background (i.e., driven by tectonic or external processes) and clustered (i.e., triggered by previous earthquakes) activity (Gardner and Knopoff, 1974; Zaliapin and Ben-Zion, 2021). In a typical mainshock-aftershocks cluster, aftershocks are triggered by the mainshock, and hence are not considered as independent events. To avoid over-counting these clustered/dependent events, I decluster the MFT catalog, similar to the recent studies in Taiwan (Steer et al., 2020; Hsu et al., 2021). Specifically, I calculate the probability of background seismicity for each event above *Mc* in the MFT catalog using a stochastic declustering method (Zhuang et al., 2002; Zhuang et al., 2004; Zhuang, 2006) based on the epidemic-type aftershock sequence (ETAS) model (Table A.3) (Ogata, 1988). For any given space-time window, I calculate "the number of the background seismicity" in this window by summarizing the background seismicity probability of all events above *Mc* in this window (Zhuang et al., 2005; Meng and Peng, 2014). The number of the background seismicity is then used in the analysis of the seismicity rate around typhoon Morakot. Figure 3.7 and Figure 3.8b show the cumulative

numbers and the daily numbers (seismicity rate) of the seismicity (above *Mc*) in the MFT catalog and the background seismicity in MFT-decluster catalog, respectively. As expected, the temporal clustering of seismicity due to moderate-size earthquakes in the MFT-decluster catalog are largely removed. However, it is relatively difficult to observe any clear changes in seismicity associated with typhoon Morakot in a cumulative plot for the entire space-time window (Figure 3.7). Hence, in the following sections, I focus on different space-time windows and examine the seismicity rates separately.

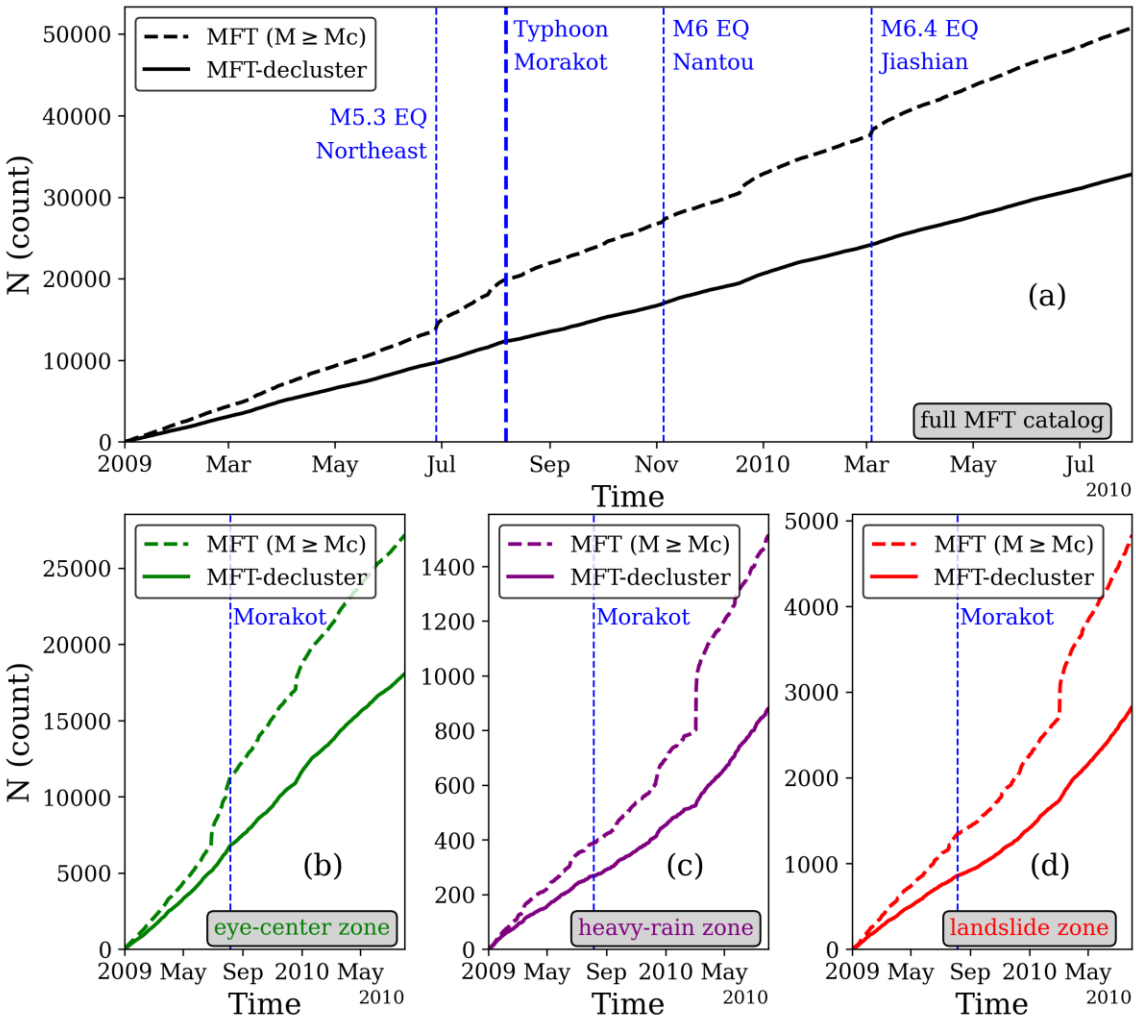

Figure 3.7 The cumulative number of seismicity (above *Mc*) in the MFT catalog and the background seismicity in MFT-decluster catalog. (a) Events in the full MFT

catalog. The vertical blue dashed lines mark a magnitude (*M*) 5.3 earthquake that occurred in Northeastern Taiwan (will be mentioned in Section 3.5.4), the typhoon Morakot, the magnitude (*M*) 6.0 Nantou earthquake (Figure 3.1b), and the magnitude (*M*) 6.4 Jiashian earthquake (Figure 3.1b). (b) Events in the eye-center zone in northeastern Taiwan. (c) Events in the heavy-rain zone in southern Taiwan. (c) Events in the landslide zone in southern Taiwan. The definition and map of these zones can be found in Figure 3.1.

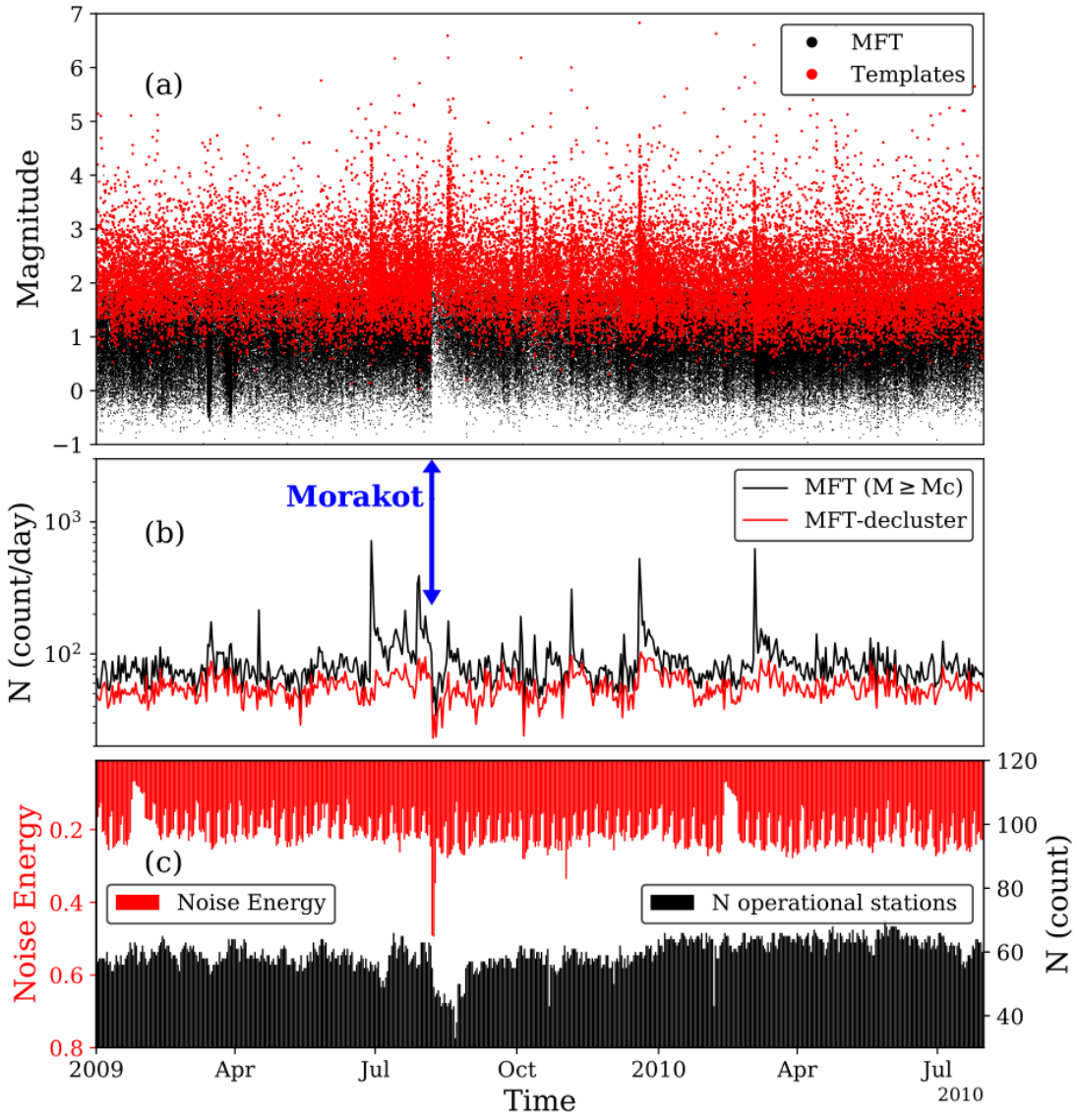

Figure 3.8 The magnitude-time distribution, seismicity rate, noise energy, and the number of operational stations in this study. (a) Magnitude-time distribution of earthquakes in Wu catalog (templates) and the MFT catalog. (b) The seismicity rate (above *Mc*) of the MFT catalog and the background seismicity rate of the MFT-decluster catalog. The blue arrows mark the day typhoon Morakot landed in Taiwan (August 8 2009). (c) The daily average noise energy (reversed red vertical axis on the

left) and the number of operational stations (see the definition in Section 3.3.2) of each day (black vertical axis on the right).

3.5.3 General Patterns of Seismicity Rate, Noise Energy, and Station Status

Based on the earthquake detection results (Figure 3.8) within the study space-time window, I observe a drop in the seismicity rate during and right after typhoon Morakot (Figure 3.8b). This seismicity-rate drop corresponds to the gap with a triangle shape between magnitude –0.5 and 1 during and right after typhoon Morakot (Figure 3.8a). The results show the number of operational stations reduced from ~70 to ~45 right after typhoon Morakot and lasted for 2-3 weeks then recovered to normal (Figure 3.8c, black bars). I also find that normalized daily average noise energy during several days of typhoon Morakot increased by about two as compared with other days (Figure 3.8c, reversed red bars).

3.5.4 Seismicity near the Eye Center of Morakot in Days before and after Morakot

Next, I analyze seismicity rate changes near Morakot's eye-center track to examine possible influences of atmospheric pressures on earthquake activities. It took about 12 hours between the landing of Morakot on Taiwan's east coast and its leaving on Taiwan's west coast (Figure 3.1a). Here I focus on the changes in the seismicity patterns within one week around typhoon Morakot (Figure 3.9). Figure 3.9b-h shows the daily seismicity density maps from 3 days before to 3 days after typhoon Morakot, respectively. Compared with the seismicity density maps of other days, I do not observe any clear increase on the day that Morakot made landfall on Taiwan island (August 8 2009). However, I do find a small zone (the red box in Figure 3.9a-h) with high seismicity density at depth of 0-15 km in northeastern Taiwan near Morakot's eye-center track during these days. The daily

seismicity number in this zone decreased with the arrival of typhoon Morakot. As expected, the atmospheric pressure recorded by the HUALIAN-CWB weather station (orange square in Figure 3.9a, inside the small zone) is lower than normal when the eye center of typhoon Morakot passed by (Figure 3.9i&j). The space-time plots of seismicity in this region (Figure 3.9k&l) show a northward migration of the sequence, which was apparently stopped at the time of typhoon Morakot's landfall.

To examine this further, I check the seismicity in this zone within the 19-month-long study period (Figure 3.10). An earthquake sequence starting 40 days before suddenly stopped at the time of typhoon Morakot's passage. Such reduction of seismicity is shown clearly in both the full MFT catalog and the declustered catalog (Figure 3.10a). This earthquake sequence includes one M5.3 reverse-faulting earthquake that occurred at 12.9-km depth on June 28 2009 (marked by the star and beachball in Figure 3.9a) and several M4 earthquakes (Figure 3.10b). A closer look reveals that the seismicity reduction started the last day before the typhoon's landfall on August 7 2009, when the atmospheric pressure inside this zone is the lowest (Figure 3.1a & Figure 3.9j). Most of the earthquakes in this zone are reverse-faulting events (Figure 3.10c).

To quantify the change in seismicity rate, I use both β-value statistic and Z-value statistic (Habermann, 1981; Habermann, 1983; Matthews and Reasenberg, 1988; Pankow and Kilb, 2020). β-value statistics is most commonly used in studies of dynamic earthquake triggering (Hill and Prejean, 2015). It measures the difference in seismic rate between a pre-window and a post-window. Therefore, it can be used to evaluate the seismicity rate changes. The β-value is defined as:

$$\beta = \frac{N_{post} - N_{pre} * (T_{post}/T_{pre})}{\sqrt{N_{pre} * (T_{post}/T_{pre})}} \quad 3.2$$

where T_{pre} and T_{post} are the lengths of time windows for counting the number of events before (N_{pre}) and after (N_{post}) the time of interest, respectively. Z-value is an alternative statistical parameter to measure the seismicity rate changes and is a more symmetric version of the β-statistic. I use it as an alternative parameter in this study. The Z-value is defined as:

$$Z = \frac{N_{post} * T_{pre} - N_{pre} * T_{post}}{\sqrt{N_{post} * {T_{pre}}^2 - N_{pre} * {T_{post}}^2}} \quad 3.3$$

where T_{pre}, T_{post}, N_{pre}, and N_{post} are defined as above. I set the window before typhoon Morakot (August 7 2009) starting from the day of the M5.3 earthquake (June 28 2009). I set the window after typhoon Morakot ended on August 15 2009 (Figure 3.10b). Then, I use the events at depth of 0-15 km above *Mc* in the MFT catalog to calculate the β-value and Z-value. I obtain a β-value of –20.45 and a Z-value of –31.42. The absolute values of both numbers are much higher than the standard significance thresholds of around 2 (Habermann, 1981; Reasenberg and Simpson, 1992; Pankow and Kilb, 2020), even considering that the threshold might vary for different times and regions (Prejean and Hill, 2018; Pankow and Kilb, 2020).

As mentioned before, some seismic stations could work well before typhoon Morakot but went down during or right after Morakot due to power and communication outages, and equipment damages. This may produce a sudden drop in detected seismicity.

To rule out this effect, I also present detection results (Figure 3.10a) that are based solely on the stations (blue triangles in Figure 3.9a) that were in operation at least 95% of days from ~1.5 months before to ~1.5 months after typhoon Morakot (July 1 2009 - September 30 2009). Although I have smaller numbers of detected events, the general patterns are similar to those based on using all available stations.

It is well known that the aftershock seismicity rate decays with time. The decay law of aftershock activity follows the Omori formula $n(t) = K(t + c)^{-1}$ or its modified form $n(t) = K(t + c)^{-p}$ (Utsu et al., 1995). To rule out the aftershock decay effect in the observed seismicity drop right after the Morakot passage, I analyze the seismicity between the last M4 event before Morakot and the first M4 event after Morakot (two gray stars in Figure 3.10b) at depth of 0-15 km inside the target zone (the red box in Figure 3.9a-h). Figure 3.10d&e show the time evolution of cumulative events number based on the events above *Mc* listed in the MFT and MFT-decluster catalog. I try to fit the data with modified Omori's law by using the AFTPOI package (Ogata, 2006), but it never converged. Nevertheless, the abrupt seismicity rate change before and after the typhoon is best explained as a reduction of rate by a factor of 3 (from 60 events/day to 20 events/day based on the MFT catalog or from 33 events/day to 13 events/day based on the MFT-decluster catalog). These two seismicity rates are calculated by using the least-squares regression to fit the data before and after typhoon Morakot, respectively (Figure 3.10d&e).

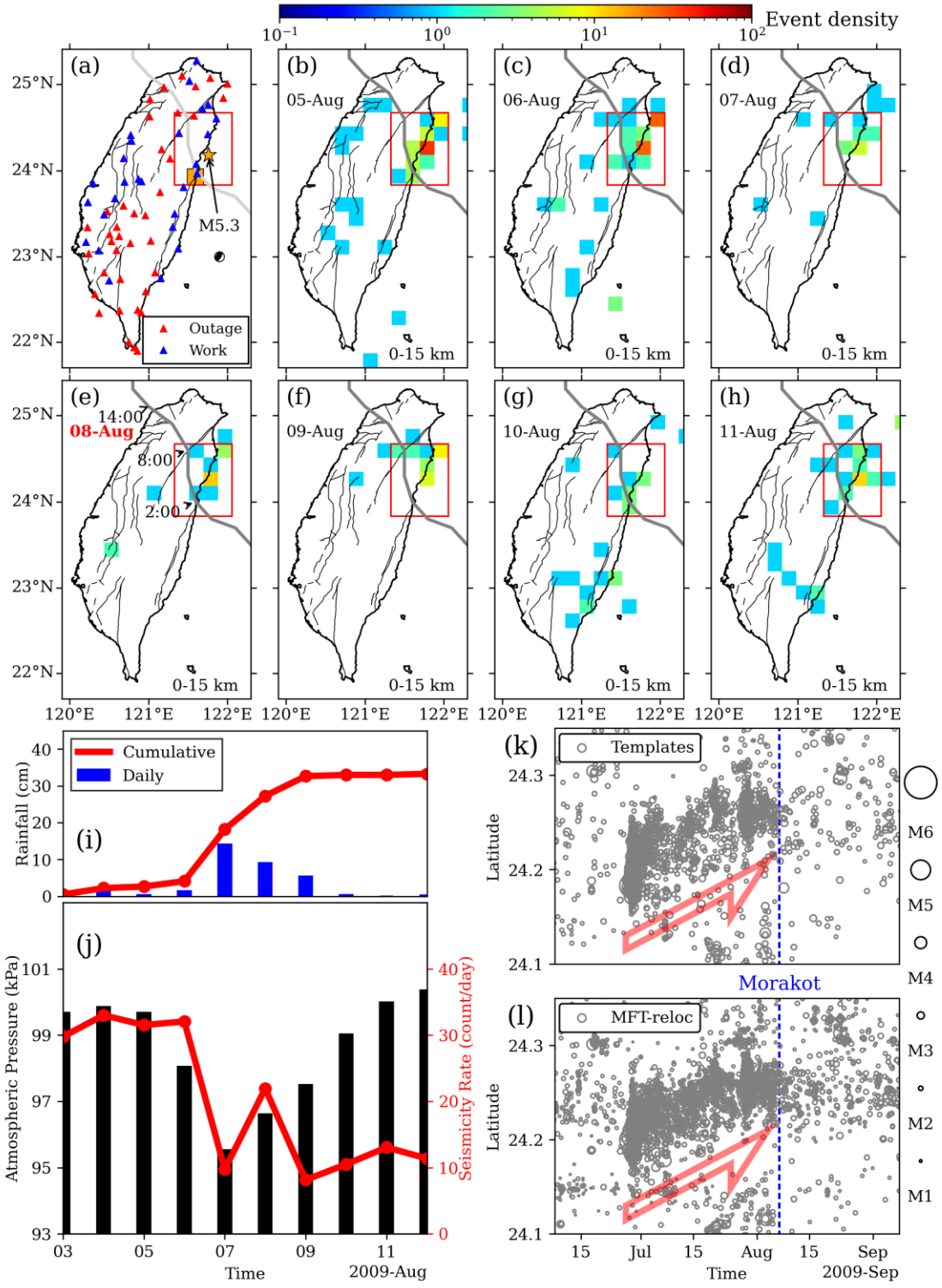

Figure 3.9 Seismicity in northeastern Taiwan around the time of typhoon Morakot. (a) Station map showing 71 CWB stations used in this study. The blue triangles are stations that were operating (see the definition in section 3.3.2) on 95% of the days between July 1 2009 and September 30 2009. The red triangles are stations not in the

well operational status in this period. The black lines are faults. The gray line is the eye-center track of typhoon Morakot (Chen, 2009**). The orange square is the HUALIAN-CWB weather station used in (j). The star and beach ball mark the location and focal mechanism solution of an M5.3 earthquake that occurred at 12.9-km depth on June 28 2009, respectively. The red box marks the zone mentioned in Section 3.5.4. (b)-(h) The daily seismicity density maps on August 5-11, respectively. The bins are 20 km × 20 km and colored by the number of events inside each bin on a day. (i) The average daily and cumulative rainfall in the target region (red box in a-h). (j) The atmospheric pressure recorded by the HUALIAN-CWB weather station (orange square in a) in these days (black bars, left vertical axis) and background seismicity rate (MFT-decluster) in the target region at depth of 0-15 km (red line, right vertical axis). (k) A zoom-in version of the latitude-time plot of seismicity in the red-box region in the Wu catalog. The full version is shown in Figure A.3. The blue dashed line marks August 7 2009. The red arrow marks the general migration of the seismicity. The open circles on the right outside mark earthquakes with different magnitudes. For example, "M1" means magnitude is equal to 1. (l) Similar to k but based on the MFT-reloc catalog.**

3.5.5 Seismicity in the Heavy-Rain Zone in Weeks before and after Morakot

To study the possible influences of rainfall brought by typhoon Morakot on seismic activities, I analyze the seismicity in the heavy-rain zone in southern Taiwan (see the white line in Figure 3.1a). This zone is defined as the 2-m contour of the accumulated rainfall map for 5 days (August 6-10 2009) during typhoon Morakot (Figure 3.1). Because previous studies show that there is a ~10-13 days delay for rain-triggered earthquakes at depth of 0-5 km after the rainfall (Kraft et al., 2006; Svejdar et al., 2011), here I focus on the time scale of weeks around typhoon Morakot and separate the seismicity into 0-5 km and 5-15 km depth range. Comparing the seismicity rate in the five weeks before (Figure 3.11), there is a lack of earthquakes a few days during and after the heavy rain associated with typhoon Morakot. In addition, the seismicity fluctuated at depth ranges of 0-5 km and 5-15 km, and I do not observe any clear changes in seismicity rates at these and larger depth ranges (Figure 3.11a-b). To rule out the influence of the way I define the heavy-rain zone, I also consider the 1.5-m contour instead of the 2-m contour. Based on the results with the 1.5-m

heavy-rain zone (Figure 3.11c-d), I still do not observe any clear change in seismicity rate in southern Taiwan after the heavy rain brought by typhoon Morakot.

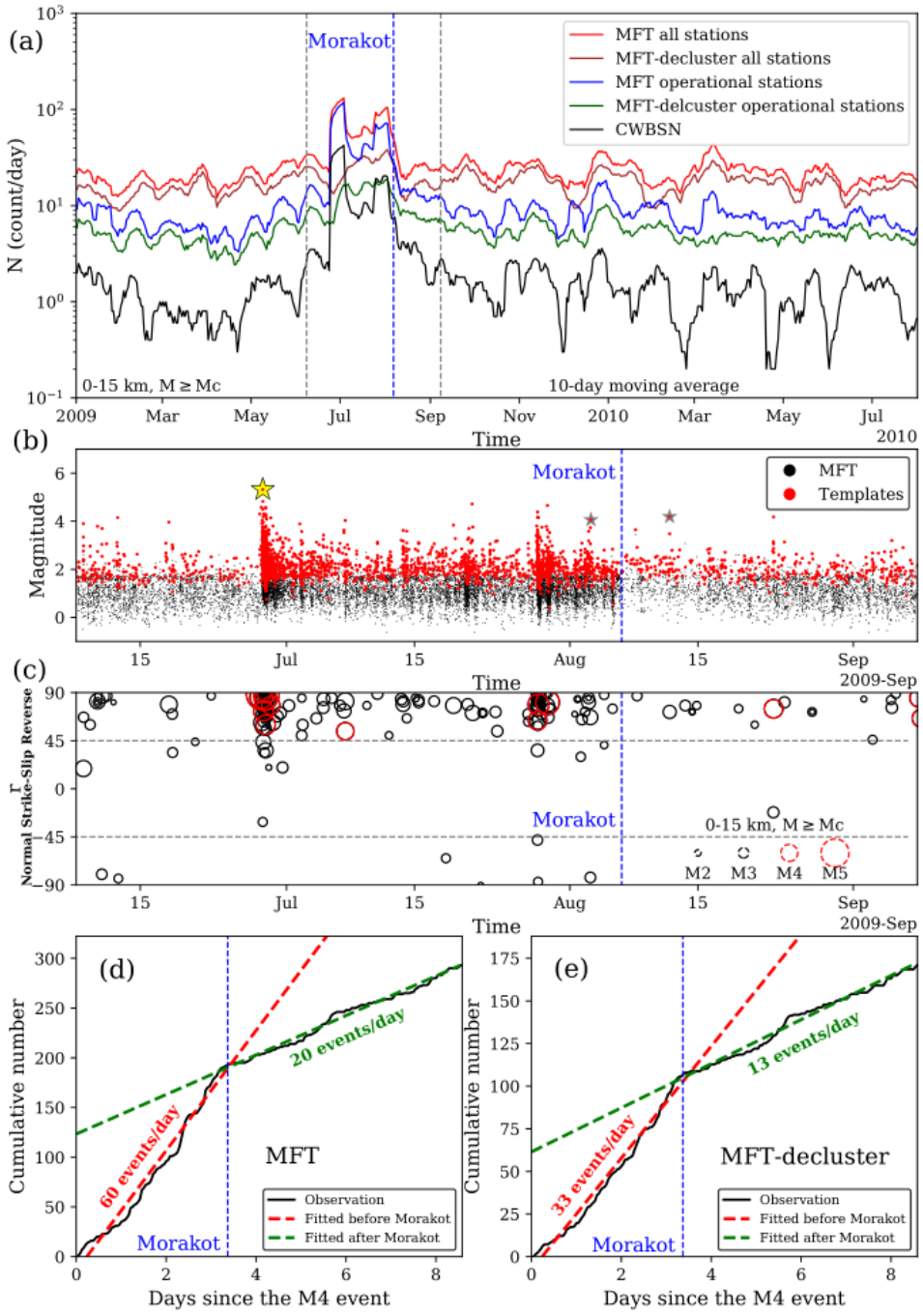

Figure 3.10 Seismicity in the zone near the eye-center track of typhoon Morakot (the red box in Figure 3.9a-h). (a) The 10-day moving average seismicity rate at depth 0-15 km inside this zone. The blue dashed line marks August 7 2009 (Figure 3.9k&l). The red and brown lines are the seismicity rate (above *Mc*) of the MFT catalog and

the background seismicity rate of the MFT-decluster catalog using all stations, respectively. The blue and green lines are based on only using the operating stations (blue triangles in Figure 3.9a) instead of all stations to perform the earthquake detection. The black line is the result of the CWBSN catalog. The two gray-dashed lines mark June 1 2009 and September 1 2009, respectively. (b) The magnitude-time distribution of seismicity at depth of 0-15 km inside the same space-time window. The yellow star marks the M5.3 earthquake, which is marked as the star and beachball in Figure 3.9a. The gray star on the left marks the last M4 earthquake in this zone before typhoon Morakot. The gray star on the right marks the first M4 earthquake in this zone after typhoon Morakot. (c) The time evolution of *r*-value of the seismicity listed in the MFT-FM catalog at depth of 0-15 km inside this zone between June 1 2009 and September 1 2009. M<4 events are marked with black circles and M≥4 events are marked with red circles. (d) The cumulative number (black line) of events in the MFT catalog above the *Mc* at depth of 0-15 km inside this zone between the last M4 event before Morakot and the first M4 event after Morakot (two gray stars in b). The blue dashed line marks August 7 2009. The red dashed line and green dashed line are the least-squares regression results only using the data before Morakot and after Morakot, respectively. (e) Similar to (d) but based on the MFT-decluster catalog.

3.5.6 Seismicity in the Landslide Zone in Months before and after Morakot

To study the possible influences of landslides driven by typhoon Morakot and subsequent erosional processes on seismicity, I analyze the seismicity in the landslide zone (see the red line in Figure 3.1a) on a longer time scale of months before and after typhoon Morakot. This zone has a high spatial density of landslides triggered by typhoon Morakot, which is the same as defined in Steer et al. (2020). Here I examine three different aspects of seismicity patterns long before and after typhoon Morakot.

First, I compare the background seismicity rate at depth of 0-15 km in the landslide zone before and after typhoon Morakot (Figure 3.12). I focus on the shallow depth of 0-15 km, mostly because stress perturbations due to surface loading/unloading processes decrease significantly at larger depths (Tao et al., 2015; Steer et al., 2020). As shown in Figure 3.12, the background seismicity rates inside and outside of the landslide zones fluctuate, but both show a minor reduction at the time of typhoon Morakot. In addition,

while the seismicity rate outside the landslide zone remains more or less stable, there is a gradual increase inside the landslide zone after typhoon Morakot.

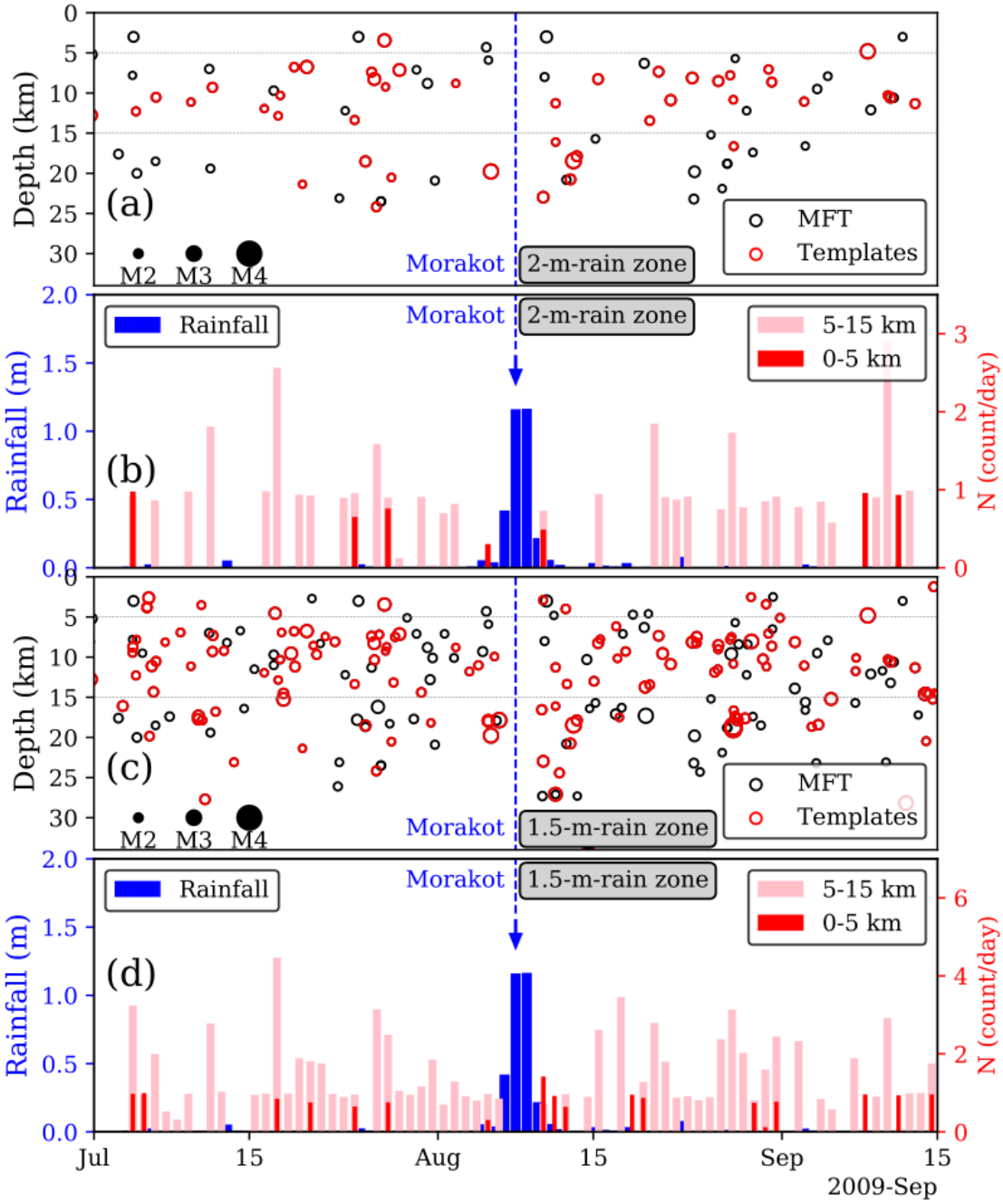

Figure 3.11 Seismicity in the heavy-rain zone from 5 weeks before to 5 weeks after typhoon Morakot. (a) The depth-time distribution of events (above *Mc*) in the MFT catalog and Wu catalog inside the heavy-rain zone, which is defined as the 2-m contour of the accumulated rainfall map (purple line in Figure 3.1). The blue dashed

line marks the day typhoon Morakot landed in Taiwan (August 8 2009). The gray dashed lines mark the depth of 5 km and 15 km used in (b). (b) The histogram of daily rainfall (blue vertical axis on the left, the bottom layer of the figure) and background seismicity rate (red vertical axis on the right, top layers of the figure) of MFT-decluster catalog at different depth ranges in the same zone and period in (a). The daily rainfall data is recorded by the ALISHAN-CWB weather station in the heavy-rain zone (latitude: 23.5082ºN; longitude: 120.8132ºE; elevation: 2413.4 m). (c) and (d) are similar to (a) and (b), respectively. but the heavy-rain zone is redefined as the 1.5-m contour instead of the 2-m contour.

Second, I examine the Gutenberg-Richter *b*-value changes at different depths before and after typhoon Morakot with both the CWBSN and the MFT catalogs (not declustered). The results based on the CWBSN catalog show a subtle *b*-value increase at depth of 0-15 km in this landslide zone after typhoon Morakot (Figure 3.13b&f). This can match the results of Steer et al. (2020), which are also based on the CWBSN catalog in the same zone. However, the results based on the newly built MFT catalog do not show a clear *b*-value increase (Figure 3.13a&e). The results at depths 15-30 km are shown in Figure A.5. The maps of *b*-value error, *Mc*, and the number of events used for computing the *b* -value map are shown in Figure A.7-Figure A.14. To examine the *b*-value results at depth 0-15 km further, I calculate the *b*-value in two additional ways. I first consider the short-term incompleteness of the catalog after typhoon Morakot (Figure 3.8), and re-calculate the *b*-values by not using the first 3 weeks of seismicity. The updated results do not show a clear *b*-value increase (Figure A.6). In addition, recently van der Elst (2021) proposed a more robust estimator of *b*-value termed *b*-positive (b^+) to reduce the effects of missing detections following a larger-magnitude event. Here I use this new method to re-calculate the *b*-values. The results with on the newly built MFT catalog still do not show a clear *b*-value increase (Figure 3.13c&d).

Finally, I check temporal variations of earthquake focal mechanism solutions in the landslide zone using the MFT-FM catalog. I find a subtle decrease in the rate and percentage of normal-faulting events at depth of 0-15 km in this landslide zone after typhoon Morakot and before the M6 Nantou Earthquake (Figure 3.14b-d). To quantify the changing rates, I compute β-value and Z-value statistics mentioned before. I set the time window before Morakot starting from January 1 2009 and the time window after Morakot ending on the day of the Nantou Earthquake (November 5 2009). Using the events at depth of 0-15 km in the landslide zone above *Mc* in the MFT-FM catalog, I obtain a β-value of −1.11 and a Z-value of −1.73. Both values are below the significance threshold of 2.

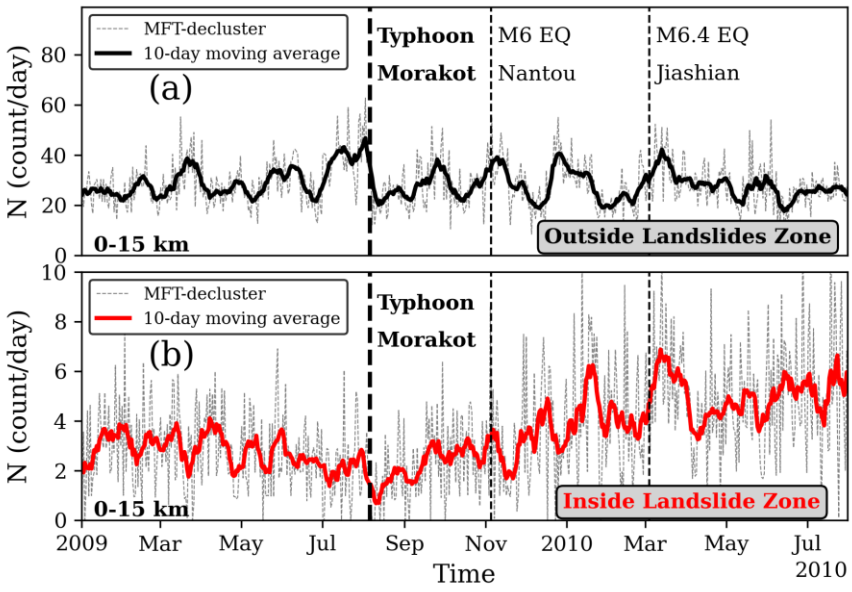

Figure 3.12 The background seismicity rate at depth of 0-15 km in the MFT-decluster catalog. (a) and (b) are the results of the events outside and inside the landslide zone (the red line in Figure 3.1a), respectively. The vertical black dashed lines mark the time of typhoon Morakot, the Nantou earthquake (outside but near the landslide zone at 24 km depth), and the Jiashian earthquake (inside the landslide zone at 22 km depth). These two M6+ earthquakes are marked as the yellow stars in Figure 3.1b. Note the depth range and the landsides zone are the same as those in Steer et al. (2020).

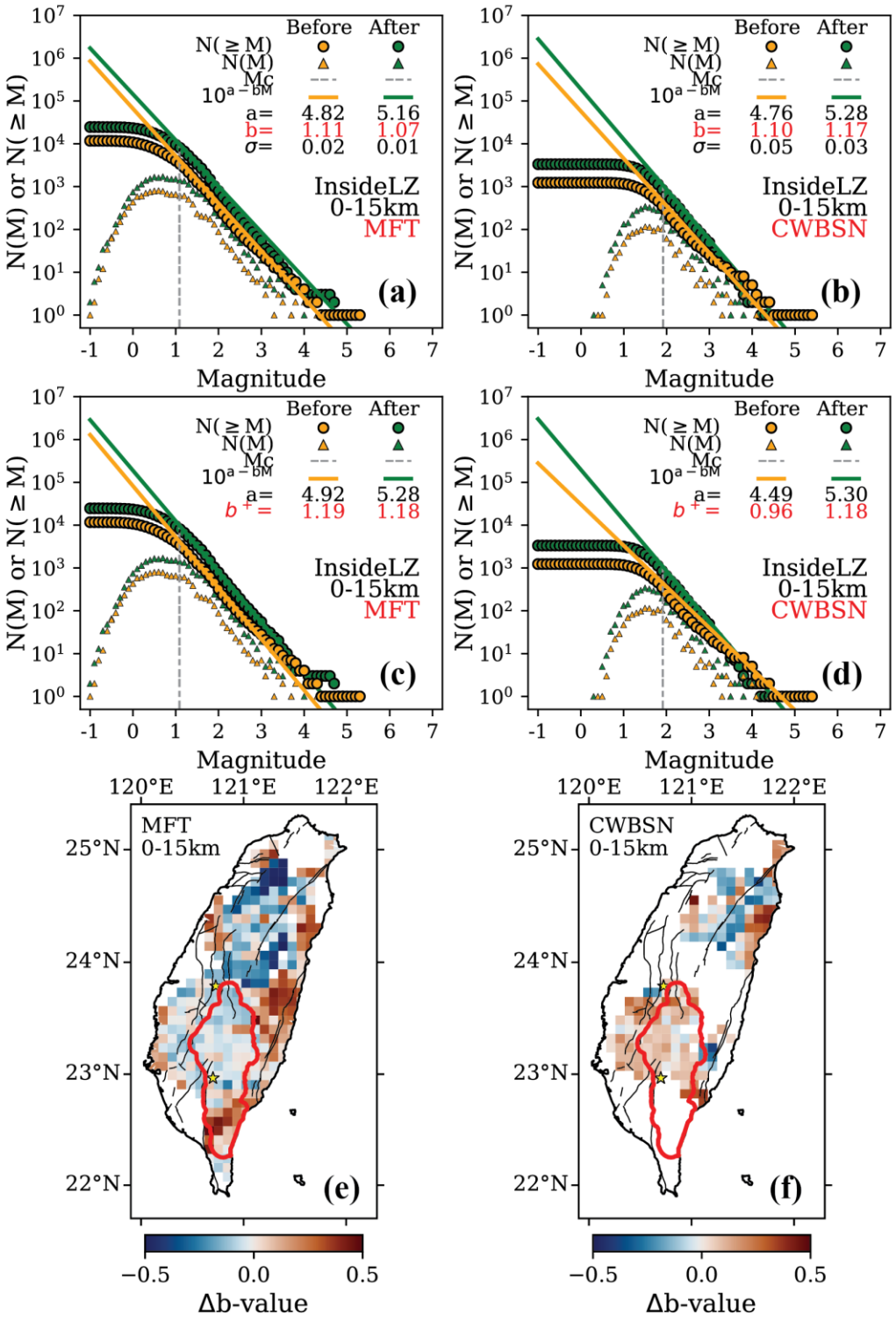

Figure 3.13 *b*-value variations by fitting the Gutenberg-Richter frequency-magnitude distribution. (a)-(b) The earthquake frequency-magnitude distribution and its corresponding *b*-value inside the landslide zone (marked by the red line in Figure 3.1a) of MFT catalog at 0-15 km depth, CWBSN catalog at 0-15 km depth,

respectively. Orange data show the results before typhoon Morakot (January 1 2009 – August 6 2009). Green data show the results after typhoon Morakot (August 7 2009 – July 31 2010). (c)-(d) Similar to (a)-(b) but the b-value is calculated by using the b-positive method. (e)-(f) Change in *b*-value, Δ*b*-value (b_{after}-b_{before}) based on the data in MFT catalog at 0-15-km depth, CWBSN catalog at 0-15 km depth, respectively. Grid steps are 10 km in both directions. The radius of the spatial window for each grid is set as 30 km. Black lines are the faults. The red line marks the boundary of the landslide zone (Figure 3.1). The two yellow stars are two magnitude (M) 6+ earthquakes (Figure 3.1) that occurred several months after typhoon Morakot (North: M6.0 Nantou earthquake on November 5 2009, at 24 km depth; South: M6.4 Jiashian earthquake on March 4 2010, at 22 km depth).

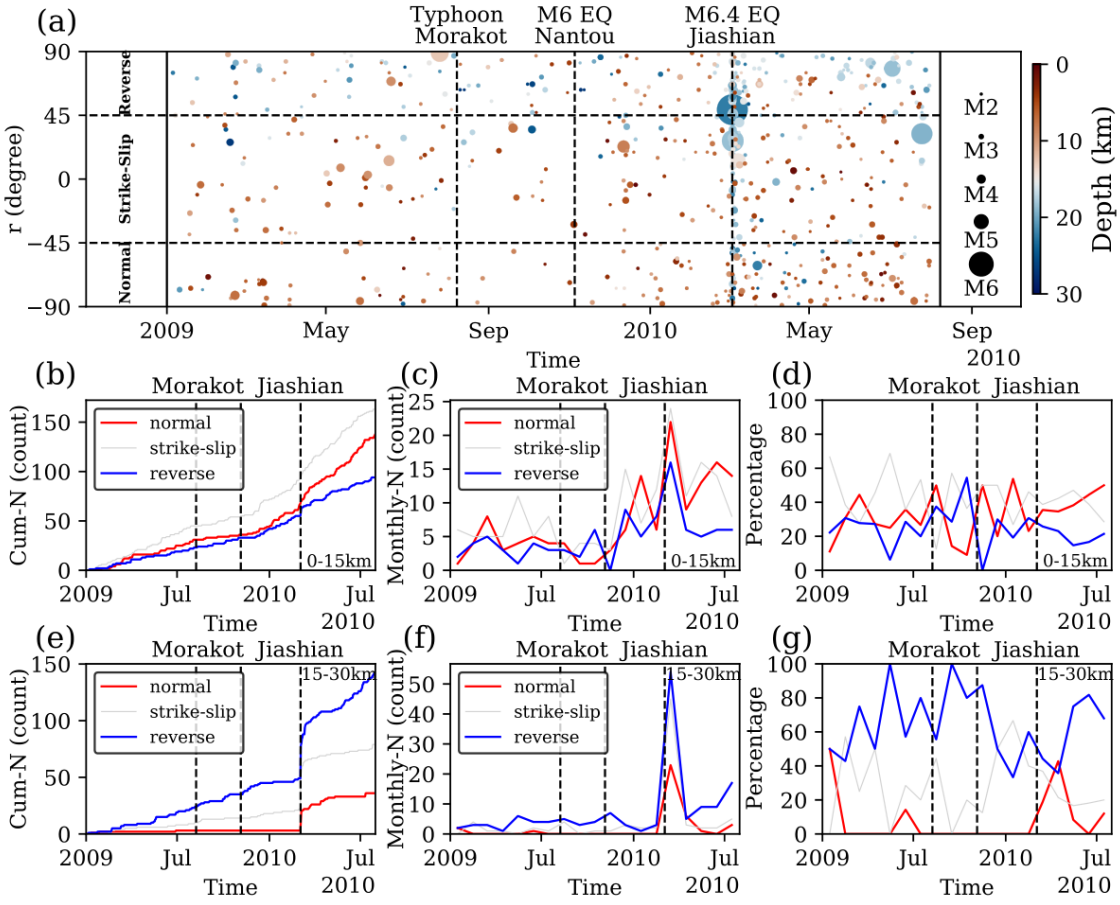

Figure 3.14 Temporal variations of earthquake focal mechanism solutions of the MFT-FM catalog inside the landslide zone. (a) The distribution of earthquakes' *r*-value over time. The *r*-value is the same as in Figure 3.6, which is used to determine the faulting types of earthquakes. Horizontal dashed lines are boundaries between different faulting types. The vertical dashed lines mark the time of typhoon Morakot, the Nantou earthquake, and the Jiashian earthquake. Each dot is an earthquake colored by its depth and scaled by its magnitude. (b)-(d) The temporal variations of the cumulative number of earthquakes (b), seismicity rate of earthquakes (c), and

percentages (d) for different types of earthquakes at depths of 0-15 km. (e), (f), and (g) are similar to (b), (c), and (d), respectively. But the depth range in (e), (f), and (f) are 15-30 km instead of 0-15 km.

3.6 Discussion

3.6.1 General Patterns of Seismicity Rate, Noise Energy, and Station Status

The number of events in the newly built MFT catalog is a seven-fold increase compared to the Wu catalog (templates) or the standard CWBSN catalog in the study period (19 months) (Figure 3.5). However, the number of detections for two weeks during and after typhoon Morakot (August 6-19 2009) is only a four-fold increase and there is a clear reduction in seismicity rate during and right after typhoon Morakot (Figure 3.8a-b). This is likely due to strong noises caused by wind and rainfall brought by typhoon Morakot. In addition, some stations were not working properly during and right after typhoon Morakot (Figure 3.8a&c). As expected, the noise level and the working status of stations have a greater impact on the detection capability of smaller earthquakes, because smaller earthquakes usually can be recorded by fewer nearby stations and have waveforms with low SNRs. This would result in the miss-detection of small events, as marked by a triangle gap between magnitude −0.5 and 1 during and right after typhoon Morakot (Figure 3.8a). Similar gaps are found right after moderate to large earthquakes (Kagan, 2004; Peng et al., 2006). Although the MFT or other waveform-based techniques can help to detect some missing events in this gap (Peng and Zhao, 2009; Yao et al., 2017; Ross et al., 2019a), they cannot completely identify all small events that are either buried by the coda of larger aftershocks or are not well recorded due to station outages.

3.6.2 Seismicity near the Eye Center of Morakot in Days before and after Morakot

As mentioned in Section 3.5.4, the results show a clear reduction of seismicity rate for a 40-days-long earthquake sequence at the time of typhoon passage in northeastern Taiwan (Figure 3.9 & Figure 3.10). This observation is likely robust for the following two reasons. The first is that the results based on only using operating stations before and after typhoon Morakot are consistent with the results based on using all stations, as well as those based on the CWBSN catalog (Figure 3.10a). In addition, if the rate reduction was caused by increasing noise levels or station outages due to typhoon Morakot, I would expect that the seismicity rate returns to the previous 40-days level right after the passage of typhoon Morakot. Instead, the seismicity rate reductions remained at the level before the 40-days-long sequence.

The results also show that the observed seismicity rate reduction cannot be simply fitted and explained by Omori's law of aftershock decay (Figure 3.10d&e). Besides interpreting this phenomenon as a pure coincidence, one possible explanation is that the sudden reduction of seismicity rate is caused by the pass-by of typhoon Morakot. The lowest atmospheric pressure of the eye center of typhoon Morakot was 95.5 kPa when it was approaching this swarm zone on August 7, 2009 (Figure 3.9j & Figure A.4). Compared to the standard atmosphere pressure (101.3 kPa), this pressure is 5.8 kPa lower, which is equivalent to the pressure caused by removing a 0.59-m thickness of water. A recent study in Taiwan shows that the average annual water thickness change in Taiwan is 0.53 m, which can result in Coulomb stress changes from 3-5 kPa on a 30°-dipping receiver thrust fault at 10-km depth in Taiwan (Hsu et al., 2020; Hsu et al., 2021). Such a level of Coulomb stress changes induced by hydrologic loading is capable of modulating seismicity in

Taiwan and other regions (Bettinelli et al., 2008; Johnson et al., 2017a; Johnson et al., 2017b; Johnson et al., 2020; Hsu et al., 2021). Therefore, changing surface atmospheric pressure at Morakot's eye center can lead to a 3-5 kPa change of Coulomb stress on faults at ~10-km depth, capable of modulating the subsurface seismicity behavior. Besides the stress change caused by atmospheric pressure, the average cumulative rainfall during Morakot in this region is about 0.3 m (Figure 3.9i), which can lead to additional Coulomb stress change on the faults likely lower than 1-3 kPa.

When Typhoon Morakot approached, a ground dilatation is expected due to atmospheric pressure drop and then followed by a larger ground compression due to rainfall loading and the recovery of ground deformation when the typhoon was away from northeastern Taiwan (Hsu et al., 2015; Mouyen et al., 2017). Therefore, reverse faulting events are prohibited by ground compression after typhoon Morakot (Figure 3.15). The focal mechanism solutions of earthquakes in this zone are diverse (Figure 3.6c), but most of them during the 40-days-long sequence are reverse-faulting events (Figure 3.9a & Figure 3.10c). The nodal planes of the M5.2 earthquake (and other M>4 events) show either an NW dipping low-angle plane or high-angle dip-slip plane, consistent with the general subduction of the Philippine Sea Plate subducting under the Eurasian Plate and the Pacific Plate. Therefore, the seismicity rate reduction in this eye-center zone may be related to the increase in atmospheric pressure after the typhoon as well as the increase in water loading.

So far there are other two cases of seismic activities directly triggered by low-pressure systems of typhoons/hurricanes. The first is the aforementioned typhoon-triggered slow earthquakes in Eastern Taiwan (Liu et al., 2009), which was later interpreted as rainfall-induced strain changes (Hsu et al., 2015). The second is a transient increase of

aftershocks following the 2011 M5.7 Virginia earthquake by Hurricane Irene (Meng et al., 2018). Here I observed a seismicity rate reduction coinciding with typhoon Morakot, which is opposite of the rate increases observed in the other two studies.

I note that the interpretation is rather speculative for the following reasons. First, this could be a pure coincidence since an earthquake sequence can stop by itself. Second, the variation in atmospheric pressure and the loading effect from the rainfall and surface water is transient (within several days). Hence, I would expect that the seismicity returns to the previous stage after days of typhoon Morakot, rather than remaining low following the typhoon. Future investigation of multiple typhoons by combining the local geodetic and seismology data, along with numerical modeling will be helpful to verify and reveal the detailed mechanism behind it. Nevertheless, compared with southern Taiwan at longer time scales, the seismicity reduction in northeastern Taiwan is the clearest seismicity rate change observed in this study.

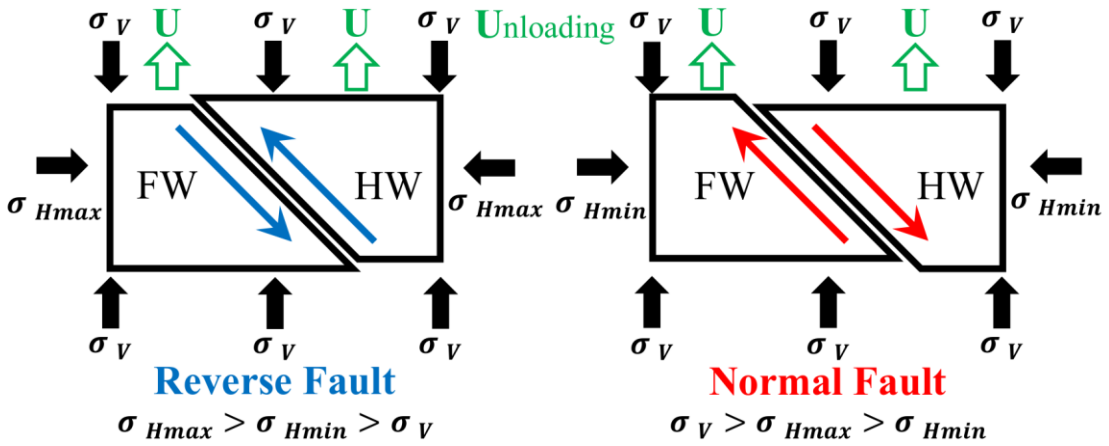

Figure 3.15 Directions and relative magnitudes of stresses for reverse fault and normal faults. FW and HW mark the footwall and hanging wall, respectively. Blue arrows and red arrows mark the direction of the slip. Green arrows and U mark unloading. Black arrows mark the three principal axes of stress: vertical (σ_V), maximum horizontal (σ_{Hmax}), and minimum horizontal (σ_{Hmin}).

3.6.3 Seismicity in the Heavy-Rain Zone in Weeks before and after Morakot

Seismicity triggered by above-average rain and the following diffusion of ground water into subsurface structure has been observed in some regions, such as Switzerland, France, and Germany (Hainzl et al., 2006; Kraft et al., 2006; Husen et al., 2007; Rigo et al., 2008; Svejdar et al., 2011). As mentioned before, typhoon Morakot produced the highest rainfall in southern Taiwan in the recent 60 years (Chien and Kuo, 2011). It delivered up to 3 meters of rainfall in the 5 days between August 6 and 10 August 2009 (Chen, 2009; Chien and Kuo, 2011). However, except for a lack of seismicity during typhoon Morakot's landfall, I did not observe any clear change in seismicity rate in the heavy-rain zone in southern Taiwan brought by typhoon Morakot (Figure 3.11).

Extreme rainfall could affect subsurface stress and seismicity in two ways. The first is an instantaneous loading effect on the surface. However, almost all seismic stations were not operating well in the several weeks during and after typhoon Morakot in the heavy-rain zone due to reasons such as power outages, equipment damages, or road damages (Figure 3.9a). Therefore, I do not have the resolution during the several days of heavy rainfall to examine the direct loading/unloading effect of rainfall on seismicity. The second possible effect of rainfall is the diffusion of rainwater into the subsurface structure, hence increasing pore pressure on active faults at seismogenic depth. I argue that this is less possible in the heavy-rain zone of this study because Miller (2008) found that the rain-triggered earthquakes occurred exclusively in karst geology where the rainwater can quickly flow into the underground karst network to induce earthquakes. In this study, the heavy-rain zone is mainly in the southern Central Ranges with primarily metamorphic rocks where its permeability is much lower than the karst areas (Ho, 1988; Wang et al., 2004; Zhang, 2016).

This is consistent with the observation that no clear changes in seismicity are observed in the following weeks in the heavy-rain zone either defined as the 2-m contour or the 1.5-m contour (Figure 3.1a and Figure 3.11). I did not try to define the heavy-rain zone as the 1-m contour because the rainfall of many regions in both north and south Taiwan is above 1-m (Figure 3.1a), resulting in a much larger area as the target zone.

3.6.4 Seismicity in the Landslide Zone in Months before and after Morakot

As mentioned in Section 3.5.6, the results based on the newly built MFT catalogs show a subtle increase in the background seismicity rate occurring in the next 12 months at depth of 0-15 km in the landslide zone after typhoon Morakot (Figure 3.12b), which match the observations of Steer et al. (2020) and Hsu et al. (2021) based on the CWBSN catalog. Steer et al. (2020) attributed this to the crustal unloading caused by the intense and prolonged sediment erosion after typhoon Morakot in the landslide zone. Hsu et al. (2021) pointed out another possible mechanism related to the interannual variation of terrestrial water storage, rather than the typhoon-associated landslides and erosions.

Steer et al. (2020) observed a clear *b*-value increase (Figure 3.13b) for seismicity at 0-15 km depth in the landslide zone over the 2.5 years after typhoon Morakot including the 1 year after typhoon Morakot in this study. However, I do not observe such a *b*-value increase in this study (Figure 3.13a). This is likely because their results are based on the standard CWBSN catalog, which misses some small earthquakes. In this study, the results are based on the newly built MFT catalog, which is more complete than the standard CWBSN catalog. A recent study shows that some catalogs based on the matched filter technique in southern California and Italy do not preserve the exponential-like magnitude-

frequency distribution toward low magnitudes (Herrmann and Marzocchi, 2021). This may lead to strong inconsistencies in *b*-values with different cutoff magnitudes. However, the study in Taiwan does not show a similar issue. For example, the *b*-values measured from the CWBSN catalog (with higher *Mc*) and the MFT catalog (with lower *Mc*) in the landslide zone before typhoon Morakot are very close: 1.11 and 1.10 (Figure 3.13a&b).

Another interesting phenomenon in the landslide zone is that the rate and percentage of normal-fault events and reverse-fault events at depths of 0-15 km moved towards two opposite trends following typhoon Morakot (Figure 3.14c&d). In particular, I found that the rate and percentage of normal-fault events decreased slightly after typhoon Morakot and before the M6 Nantou Earthquake (Figure 3.14b). This subtle change might be interpreted by the surface erosional unloading caused by the intense and rapid sediment transport in the several months right after typhoon Morakot in the landslide zone (Figure 3.15). The average erosion over the landslide zone in the following months after typhoon Morakot is about 2 cm (Chen et al., 2015; Steer et al., 2020). Steer et al. (2020) showed that 2-5 cm of average erosion can lead to about 2 kPa of Coulomb stress changes on a nearby fault at 5 km depth, which is roughly similar to the Coulomb stress changes induced by hydrologic loading/unloading that modulate seismicity in Taiwan and other regions (Bettinelli et al., 2008; Johnson et al., 2017a; Johnson et al., 2017b; Johnson et al., 2020; Hsu et al., 2021). The erosional unloading can reduce vertical stress (σ_V). For normal-fault events, this means the reduction of the difference between σ_V and σ_{Hmin}. Therefore, I expect to see fewer normal-fault events, which match the results shown in Figure 3.14. However, I note that the fluctuations of different types of events are relatively large in the entire study period (Figure 3.14c-d) and the seismicity rate change is below the significance

threshold based on both β-value and Z-value statistics. Therefore, I conclude that even if such unloading affects microseismicity in this region, its effects are too small to be clearly observed (with statistical significance).

3.6.5 Lessons Learned and Their Implications for Future Studies

In this section, I briefly summarize lessons learned in this study, which I hope could be useful for similar future studies in other regions.

I use fixed thresholds (e.g., SNR and MAD) before, during, and after typhoon Morakot. However, during typhoon Morakot's passage, the background noise level was elevated, hence requiring a signal with higher amplitudes to be detected (Figure 3.8). Such requirements reduce the ability to detect small earthquakes during these days, which prevents us from better understanding the short-term effects on local seismicity in central-southern Taiwan. In future studies, using a lower detection threshold during and right after a typhoon may help, although this may introduce events that may not be genuine earthquakes. An alternative is to use methods such as deep-learning tools (e.g., Zhu et al. (2019); Mousavi et al. (2020)) that may not depend strongly on the SNR.

Although typhoon Morakot is the wettest typhoon in the past 60 years in Taiwan, it is relatively difficult to argue for a causal link between extreme weather events and earthquake activities based solely on observational results from a single event. To rule out the possibility of pure coincidence, it is best to examine many extreme weather events in the same region, or around the globe to better establish (or reject) their triggering relationship. If there are not enough such events available, detailed modeling studies can

be helpful to interpret results from only a few cases (Steer et al., 2014; Jeandet Ribes et al., 2020).

Seismicity changes can be triggered by transient events such as another earthquake at nearby or teleseismic distances (Freed, 2005; Hill and Prejean, 2015), by both short-term (e.g., typhoons or hurricanes (Meng et al., 2018)) and long-term (e.g., annual and internal hydrological loading/unloading (Hsu et al., 2021) processes, in addition to regular tectonic loading. Hence, it is important to separate the effects from long-term changes on seismicity rate changes first, before analyzing any short-term effects due to extreme weather events.

There is an intrinsic difficulty in observing seismicity change in the presence of high seismic noises and station outages like the period during and right after typhoon Morakot. For future similar studies, focusing on regions with borehole seismic stations (e.g., the Hi-net in Japan) could help to at least suppress the recording of surface seismic noises associated with extreme weather events.

Table 3.2 Summary of the observations in this study.

Typhoon-Morakot-Driven Surface Process	Time Scale	Space Location	Observation of Changes in Seismicity
Atmospheric Pressure Variation at Eye Center	Hours-Days	Northeastern Taiwan	Yes, and statistically significant
Heavy Rainfall	Days-Weeks	Central-Southern Taiwan	Unmeasurable
Landslide Erosion	Months-Years	Central-Southern Taiwan	Yes, but not significant

3.7 Conclusions

By using the matched filter technique, I build a more complete earthquake catalog for Taiwan spanning seven months before and twelve months after the 2009 typhoon Morakot, which brought the highest rainfall in southern Taiwan in the past 60 years. The number of events in the newly built catalog is a seven-fold increase compared to the standard CWBSN catalog. I also relocate the detected events and calculate their focal mechanism solutions based on first-motion polarities from a deep-learning model. With the newly built catalogs, I analyze the possible effects of typhoon Morakot on the seismicity in Taiwan from three aspects (Table 3.2). First, I find that the seismicity rate of a 40-days-long earthquake sequence in northeastern Taiwan was reduced significantly right following the passage of typhoon Morakot's eye center. This phenomenon may be related to the increase of atmospheric pressure after the typhoon as well as the increase in water loading. Second, I do not observe any clear change in seismicity rate in the heavy-rain zone in the following five weeks after the rainfall brought by typhoon Morakot. This is likely due to strong noise and station outages during and right after typhoon Morakot. Finally, at depths of 0-15 km in the typhoon-triggered landslide zone in southern Taiwan, I find a slight increase in background seismicity rate occurring in the next 12 months after typhoon Morakot, which can match the results of a recent study (Steer et al., 2020) arguing for surface unloading due to sediment transport following typhoon Morakot. However, such a feature could also be explained by the interannual variation of terrestrial water storage (Hsu et al., 2021). I do not observe a clear change in the Gutenberg-Richter *b*-value in the landslide zone in southern Taiwan for seismicity at 0-15 km, which is different from the Steer et al. (2020) results based on a previous and less complete CWBSN catalog. However, there is a clear *b*-value reduction in southern Taiwan for seismicity at 15-30 km, which

would be difficult to interpret as surface loading/unloading effects. Overall, except for a reduction in seismicity rate near the typhoon's low-pressure eye center in northeastern Taiwan, I do not observe other clear seismicity changes that can be attributed to surface changes induced by typhoon Morakot. A systematic examination of multiple typhoons in Taiwan or extreme weather events around the globe may help us ultimately answer the question of whether extreme weather events at the surface can trigger or suppress earthquakes at seismogenic depth.

CHAPTER 4. SPATIOTEMPORAL VARIATIONS OF AFTERSHOCK SEQUENCES BETWEEN 2009-2010 IN TAIWAN REVEALED BY A HIGH-RESOLUTION RELOCATED TEMPLATE MATCHING CATALOG

4.1 Summary

This chapter is a follow-up study of CHAPTER 3 (Zhai et al., 2021c). The manuscript describing the results presented in this chapter is currently in preparation. Detailed analysis of aftershocks can provide important insights into the physical mechanisms of earthquake triggering, mainshock rupture characteristics, postseismic deformation distribution associated with the mainshock, and faults zone structure and properties at depth. In this study, I use a recently built high-resolution relocated template matching catalog to study the spatiotemporal variations of several M5+ mainshock-aftershock sequences in Taiwan. I observe clear aftershocks migrating as the logarithm of time along with depth for several mainshock-aftershock sequences in Taiwan, suggesting that these aftershocks were primarily driven by afterslip following the mainshock ruptures. In addition, I find that the minimum magnitude of early aftershocks of three M6+ events in Taiwan, including the 2010 M6.4 Jiashian earthquake, was not mainly modulated by earth tides as proposed by a recent study, but was primarily observationally limited by the daily fluctuations in the noise level. Finally, I also find a clear spatiotemporal coincidence between high-aftershock-productivity earthquake sequences and the occurrence of nearby slow slip events in northeastern Taiwan, suggesting that slow-slip events can help to further promote aftershock generation.

4.2 Introduction

Large earthquakes in the crust usually are followed by intense aftershock activities that decay with time (Omori, 1894). Previous studies based on numerical simulations and observations suggest that aftershocks can be triggered by afterslip (i.e., continuing aseismic slip on the rupture plane) following the mainshock (Ariyoshi et al., 2007; Kato, 2007; Peng and Zhao, 2009; Perfettini et al., 2018), by the direct stress change caused by the mainshock (Hardebeck et al., 1998; Stein, 1999; Cocco et al., 2000; Kilb et al., 2002), and by fluid redistribution (Miller et al., 2004; Hainzl et al., 2016; Miller, 2020). Detailed analysis of spatiotemporal variations of aftershocks and aftershock productivity can help to better understand the mechanisms of earthquake triggering (Freed, 2005). It can also provide important information on faults zone structure and properties at depth (Tajima and Kanamori, 1985; Persh and Houston, 2004; Frank et al., 2017; Ross et al., 2019a; Dascher‐Cousineau et al., 2020; Chu and Beroza, 2022), mainshock rupture characteristics (Mendoza and Hartzell, 1988; Das and Henry, 2003; Neo et al., 2020), and postseismic deformation distribution associated with the mainshock (Stein and Lisowski, 1983; Shen et al., 1994; Henry and Das, 2001; Chang et al., 2007).

Recently, several interesting behaviors of aftershocks have been reported. First, many studies showed that aftershock zones expand logarithmically with time (Peng and Zhao, 2009; Kato and Obara, 2014; Obana et al., 2014; Tang et al., 2014; Meng and Peng, 2016; Frank et al., 2017), which suggest these aftershocks were primarily driven by propagating afterslip following the mainshock ruptures (Kato, 2007; Perfettini et al., 2018; Jiang et al., 2021). However, the migration pattern along depth/dip is not as clearly

observed and less reported when compared with along-strike migration, but the physical mechanism of them is expected to be the same/similar (Perfettini et al., 2019). Second, Tang et al. (2019) observed possible Earth-tide modulations on the temporal variations of minimum aftershock magnitude based on two aftershock sequences in Taiwan. However, this potential relationship between tidal stresses and early aftershocks is rarely reported compared to the modulations of tides on the deep-tectonic tremors (Nakata et al., 2008; Rubinstein et al., 2008; Thomas et al., 2009) and large earthquakes (Berg, 1966; Wilcock, 2001; Kasahara, 2002; Tolstoy et al., 2002; Lin et al., 2003; Tanaka et al., 2004; Tanaka, 2012; Ide et al., 2016; Xie et al., 2017). A more detailed analysis is needed to understand this interesting phenomenon and to further confirm or reject the proposed interpretation. Finally, aftershock productivity (i.e., the number of aftershocks within a given space-time following a mainshock) has been found to depend strongly on the mainshock location (e.g., depth, lithosphere age, and plate boundary type) (Mogi, 1967; Singh and Suarez, 1988; Davis and Frohlich, 1991; Nyffenegger and Frohlich, 2000; Boettcher and Jordan, 2004; Persh and Houston, 2004; Page et al., 2016; Dascher‐Cousineau et al., 2020). However, temporal variations of aftershock productivity for earthquake sequences in a fixed space window are less studied when compared with the aforementioned spatial effects and source variabilities (e.g., stress drop, width, and aspect ratio) (Bouchon and Karabulut, 2008; van der Elst and Shaw, 2015; Wetzler et al., 2016; Marsan and Helmstetter, 2017; Dascher‐Cousineau et al., 2020). Recent studies about the relationship between aftershocks and slow slip events (SSEs) highlight the short-term and long-term spatiotemporal evolution of SSE may affect nearby seismicity behaviors (Ogata and Toda, 2010; Hainzl et al., 2013b; Chen

et al., 2018), suggesting the possibility that SSEs activity may affect aftershock productivity.

In this work, I focus on three topics of the spatiotemporal variations of aftershocks using a new high-resolution relocated template-matching earthquake catalog in Taiwan (Zhai et al., 2021c). The number of earthquakes in this catalog is a seven-fold increase compared to the standard CWBSN catalog. Many newly detected events in this catalog were aftershocks that were missing in the standard catalog because they were masked by overlapping arrivals of signals from the mainshocks and other aftershocks (Kagan, 2004; Peng et al., 2006; Chang et al., 2007; Enescu et al., 2007). These newly identified aftershocks provide us a great opportunity to explore detailed spatiotemporal variations of aftershocks and gain new insights into the topics mentioned above.

4.3 Earthquake Catalog

4.3.1 Catalog Building Procedure and General Patterns

A high-resolution earthquake catalog built with the matched-filter technique (MFT, also known as template matching) in Taiwan (Zhai et al., 2021c) is used in this study. This MFT catalog of Taiwan seismicity from 01/01/2009-07/31/2010 was compiled using 32,802 earthquakes listed in a 3D relocated seismicity catalog (Wu et al., 2008a) as templates for scanning the continuous waveform recorded by 71 seismic stations in Central Weather Bureau Seismic Network (CWBSN) (Shin, 1992) with the template matching technique (Gibbons and Ringdal, 2006; Shelly et al., 2007; Peng and Zhao, 2009). This process resulted in 218,155 detected earthquakes. Most of the newly detected events are below magnitude 2, beneath the M2.3 completeness threshold of the standard CWBSN

catalog. The magnitude of completeness (Mc) of the MFT catalog, is M1.6, with a seven-fold increase in the number of events compared to the CWBSN catalog. Zhai et al. (2021c) then relocated the events in this MFT catalog using waveform-correlated differential times (Waldhauser and Ellsworth, 2000; Trugman and Shearer, 2017). The relocated catalog (MFT-reloc) includes 63,587 earthquakes (~30% of the MFT catalog, a two-fold increase compared to the standard CWBSN catalog). Zhai et al. (2021c) also determined the focal mechanisms for 3816 events (a seven-fold increase compared to the 548 events in the original focal mechanism catalog (Wu et al., 2010) in the same time window using first-motion polarities (Wu et al., 2008b) measured by a deep-learning model. Figure 4.1a-b show the map of seismicity in the MFT-reloc catalog and the CWBSN catalog (the detailed profiles of Figure 4.1d a are shown in Figure B.1, Figure B.2, and Figure B.3). These seismicity relocation results show high-resolution structures of faults at depth in Taiwan (e.g., Figure B.1c-f).

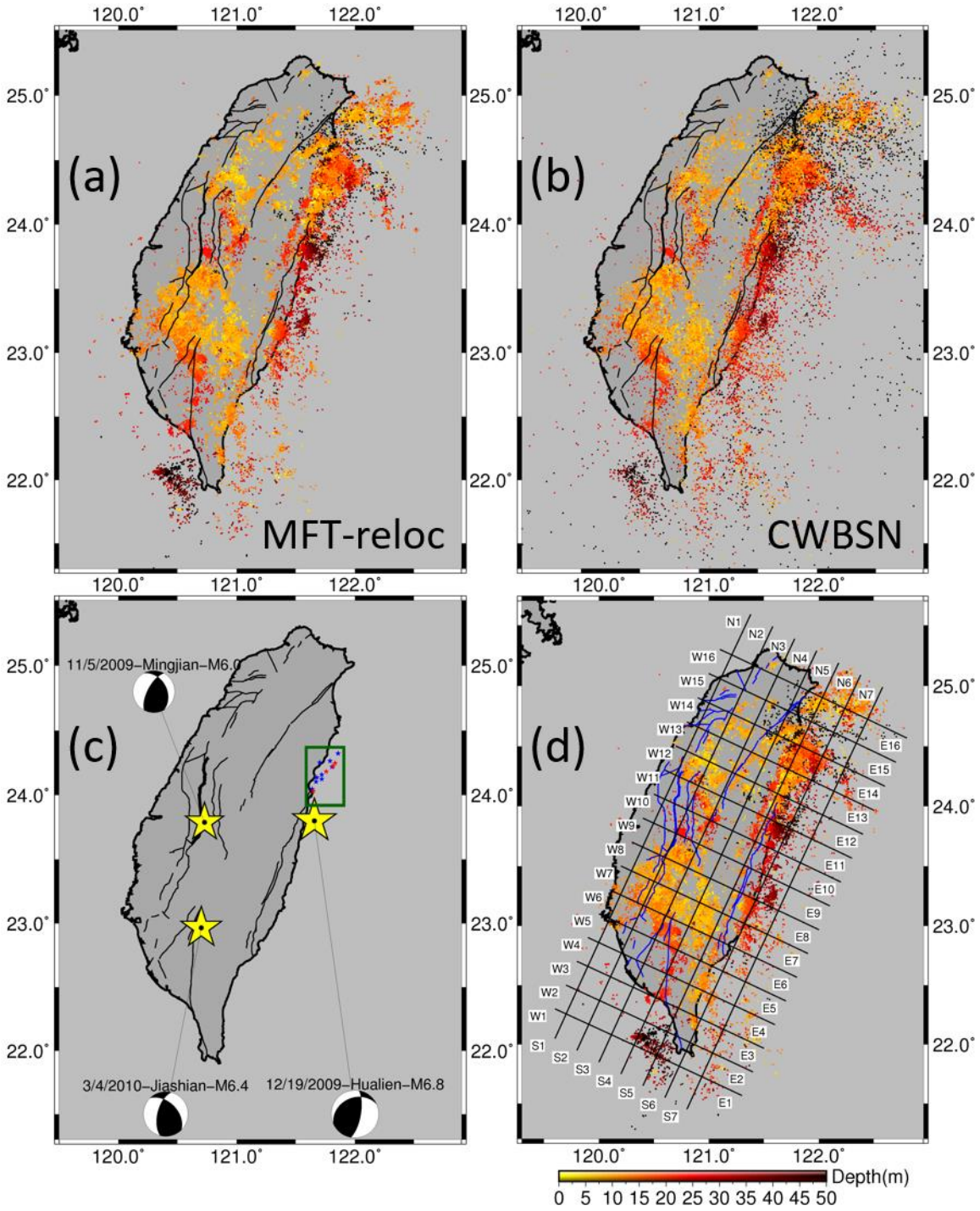

Figure 4.1 Map of seismicity in Taiwan. (a) MFT-reloc catalog. (b) CWBSN catalog. (c) The mainshocks analyzed in this study. (d) Map of the cross-sections in Figure B.1, Figure B.2, and Figure B.3.

4.3.2 Mainshock-Aftershock Sequences

Located at the convergent boundary between the Philippine Sea and Eurasian plates (Tsai, 1986), Taiwan has about one earthquake above magnitude 6 each year right beneath the main island (Shin et al., 2013; Hsu et al., 2021). In the nineteen months (01/01/2099-07/31/2010) covered by the MFT catalog, there are nine M6+ events in the original CWBSN catalog, but five of them are far away offshore. One (10/03/2009, Ml6.2, between Fengpin and Fanglin in Eastern Taiwan) of the rest four events was not successfully relocated, likely because it was located at the edge of the seismic network and had few nearby aftershocks to be paired with during the relocation process that requires waveform-correlated differential times. Finally, the rest three M6+ mainshocks were all relocated and were followed by numerous aftershocks. Figure 4.1c shows the distribution of these three M6+ mainshocks with their focal mechanism solutions. These mainshock-aftershock sequences are analyzed for their aftershock migrations in this study. Among these three M6+ mainshocks, the 2010 M6.4 Jiashian earthquake (JSEQ) (Ching et al., 2011; Hsu et al., 2011; Chan and Wu, 2012; Rau et al., 2012; Chen et al., 2013; Lee et al., 2013; Tang et al., 2014; Wen et al., 2016; Chao et al., 2017; Tang et al., 2019) is better studied than the 2009 M6.0 Mingjian earthquake (MJEQ) (Lin et al., 2014; Wen et al., 2015) and the 2009 M6.8 Hualien earthquake (HLEQ) (Lin et al., 2022). Figure 4.2 shows the spatiotemporal evolutions of the aftershocks of the JSEQ. Besides these three M6+ events, I also analyze thirteen M5+ events selected in the MFT and CWBSN catalog in northeastern Taiwan (events in the green box in Figure 4.1c) for their aftershock productivities. Three of these thirteen events have been analyzed by Chen et al. (2018) but

based on a less complete relocated CWBSN catalog (Wu et al., 2008a), rather than the MFT catalog used in this study.

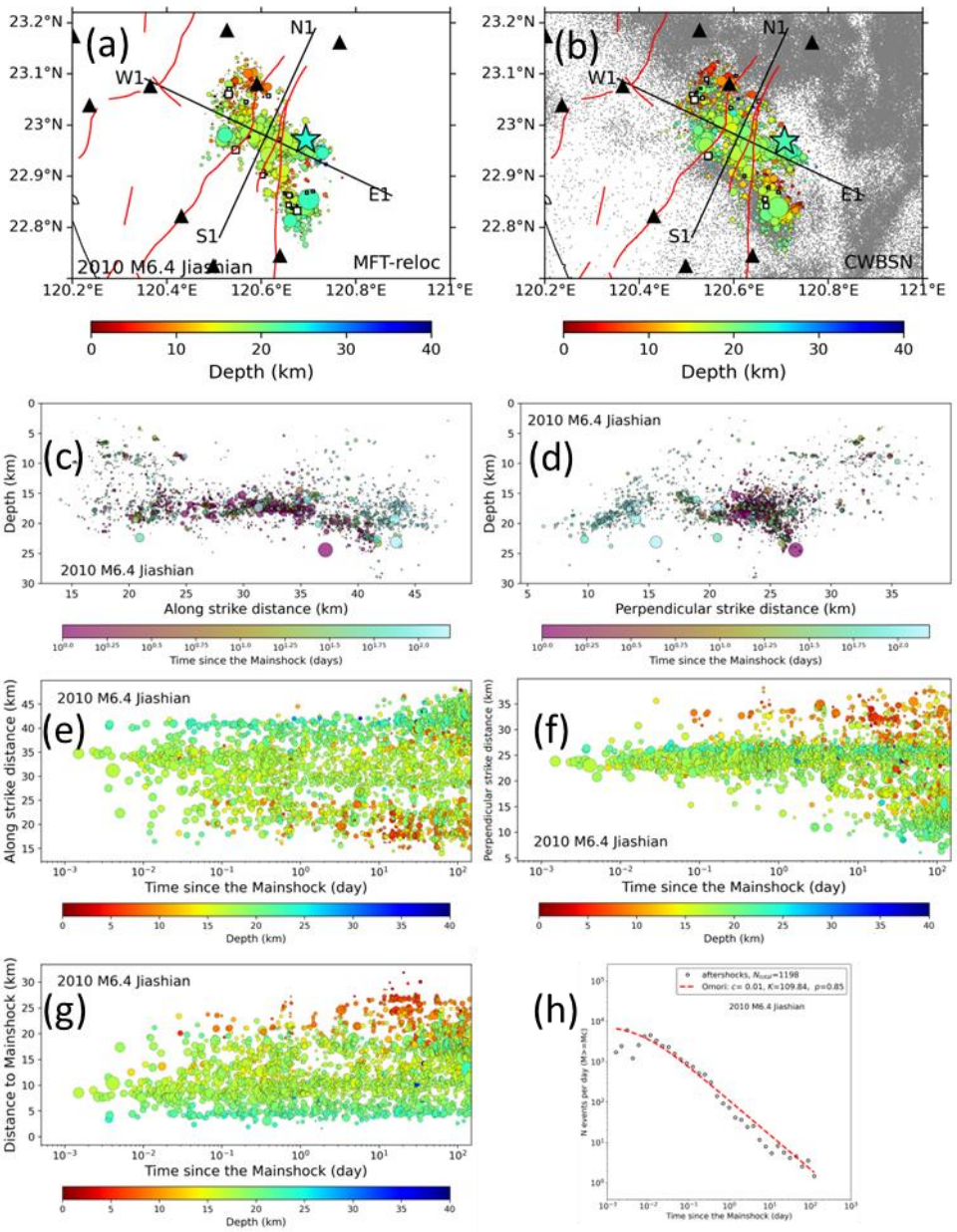

Figure 4.2 Aftershocks of the 2010-M6.4-Jiashian earthquake (JSEQ). (a) Map of aftershocks in the MFT-reloc catalog. W1-E1 is the profile along strike same as it in Tang et al. (2014). (b) Map of aftershocks in the CWBSN catalog. (c) Depth versus the along-strike distance. (d) Depth versus the perpendicular-strike distance. (e) Along-strike distance versus the occurrence times of aftershocks on a logarithmic scale. (f) Perpendicular-strike distance versus the occurrence times of aftershocks in logarithmic scale. (g) 3D distance to the mainshock versus the occurrence times of

aftershocks on a logarithmic scale. (h) Seismicity rate versus the occurrence times of aftershocks since the mainshock in logarithmic scale.

4.4 Results

4.4.1 Aftershocks Migrating as Logarithm of Time along with Depth

I observe clear along-depth aftershock migration as the logarithm of time (Figure 4.3 and Figure B.4), especially for the HLEQ aftershocks (Figure 4.3a). The HLEQ occurred at the depth of about 40 km (Lin et al., 2022). The aftershocks appear to start from about 40 km depth in the first few hours to near the Earth's surface to near the surface at ~100 days following the HLEQ. A similar expansion is shown from 40 to 50 km depth. Similar expansion patterns are shown for the 2010 JSEQ and the 2009 MJEQ, although the migration speed and spatial extent are different (Figure 4.3b-c).

Unlike the aftershocks of HLEQ and JSEQ, the upward aftershock migration of MJEQ stopped at a relatively deeper depth (19 km) because it is a blind fault inside the pre-Miocene basement beneath the Changhua fault and the Chelungpu fault, which was ruptured by the 1999 Chi-Chi earthquake (Lin et al., 2014). Note the upper boundary (19 km depth) of aftershocks shown in the MFT-reloc catalog is even deeper than in the catalog developed by Lin et al. (2014), whose upper boundary is at about 12 km depth.

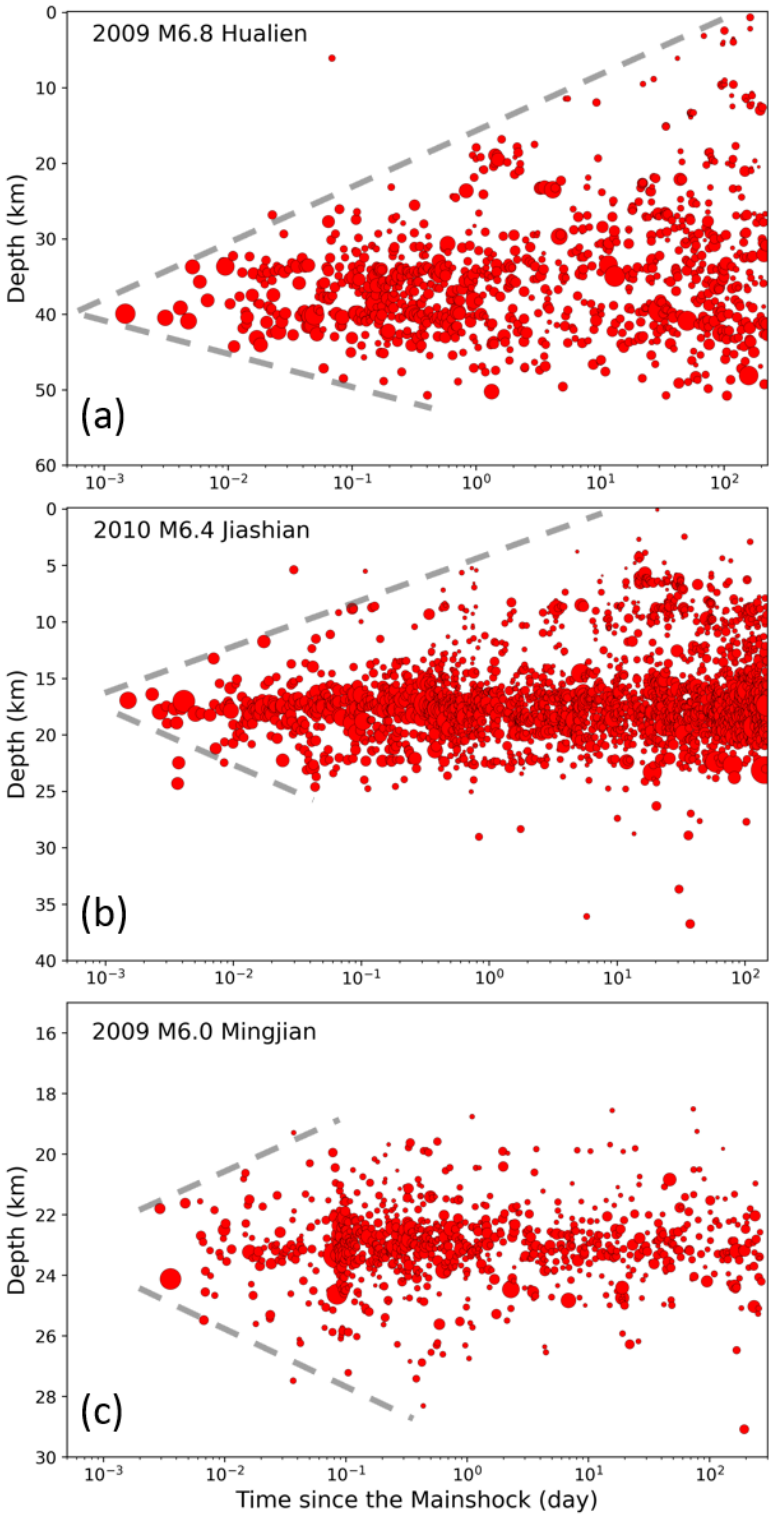

Figure 4.3 Along-depth aftershock migration of three M6+ mainshock-aftershock sequences in Taiwan. (a) Depth of aftershocks versus their occurrence times since the mainshock in logarithmic scale for the HLEQ. (b) Similar to (a) but for JSEQ. (c) Similar to (a) but for MJEQ.

4.4.2 Modulations of Early Aftershocks

To quantify the potential effects of Earth Tides and noise levels on the early aftershock magnitudes, I calculate the tidal stresses and relative noise magnitudes. The tidal stresses (normal, shear, and Coulomb stress changes with a coefficient of friction μ = 0.4 (Tang et al., 2019) resolved on the mainshock fault plane) were calculated using the GOTIC2 (Matsumoto et al., 2001) and GeoTaos (Lei and Satoh, 2007) programs. Next, I calculate the average relative noise magnitude for each hour using the continuous waveforms recorded by the seismic stations in the CWBSN. The hourly average relative noise magnitude is defined as:

$$M_{noise}(h) = mean_s\{mean_c\{median_t[log_{10}\, abs[A\,(h,s,c,t)]]\}_{norm}\} \qquad 4.1$$

where A is the amplitude of the 2-16 Hz band-pass-filtered waveform at hour h, station s, component c, and time t; abs[] is the absolute value; $median_t[\,]$ is the median value over time; $mean_c\{\,\}$ is the average value of all components; $mean_s\{\,\}$ is the average value of all stations; and $norm$ is normalization. The definition of M_{noise} (Equation 4.1) is modified from the E_{noise} (Equation 3.1) with a similar format. The 2-16 Hz filter is the same as used in earthquake detection. I take a median value instead of an average value of the waveform amplitude in order to reduce the effect of local transient high-noise outliers. The normalization is applied before averaging to balance the weights of different stations. Note the calculated noise magnitude M_{noise} is a relative magnitude similar to the earthquake magnitude scale, which means that magnitude 0 does not indicate that the amplitude/energy is 0 but a constant without special physical meaning.

Figure 4.4, Figure 4.5, and Figure 4.6 show the comparison of the temporal variations of early aftershock magnitudes, noise level (M_{noise}), and Earth-tide-induced stresses for the JSEQ, MJEQ, and HLEQ, respectively. The results suggest that the temporal variation of the minimum earthquake magnitudes of early aftershocks can match better with the noise level than with the tidal stresses, especially for the JSEQ sequence (Figure 4.4).

To verify if this result is biased by the MFT detection process, I also examine the relationship between the average number of earthquakes and the average noise level in each local hour using both the MFT and CWBSN catalogs. Figure 4.7 shows that the results based on both catalogs are very similar, suggesting that the results in Figure 4.4 - Figure 4.6 are not biased by the MFT catalog building process. The noise level during local nighttime is clearly lower than during local daytime, and there are more earthquakes detected when the noise level is lower. The local minimum value of noise level associated with a local maximum number of detected earthquakes at noon is likely due to a lunch break.

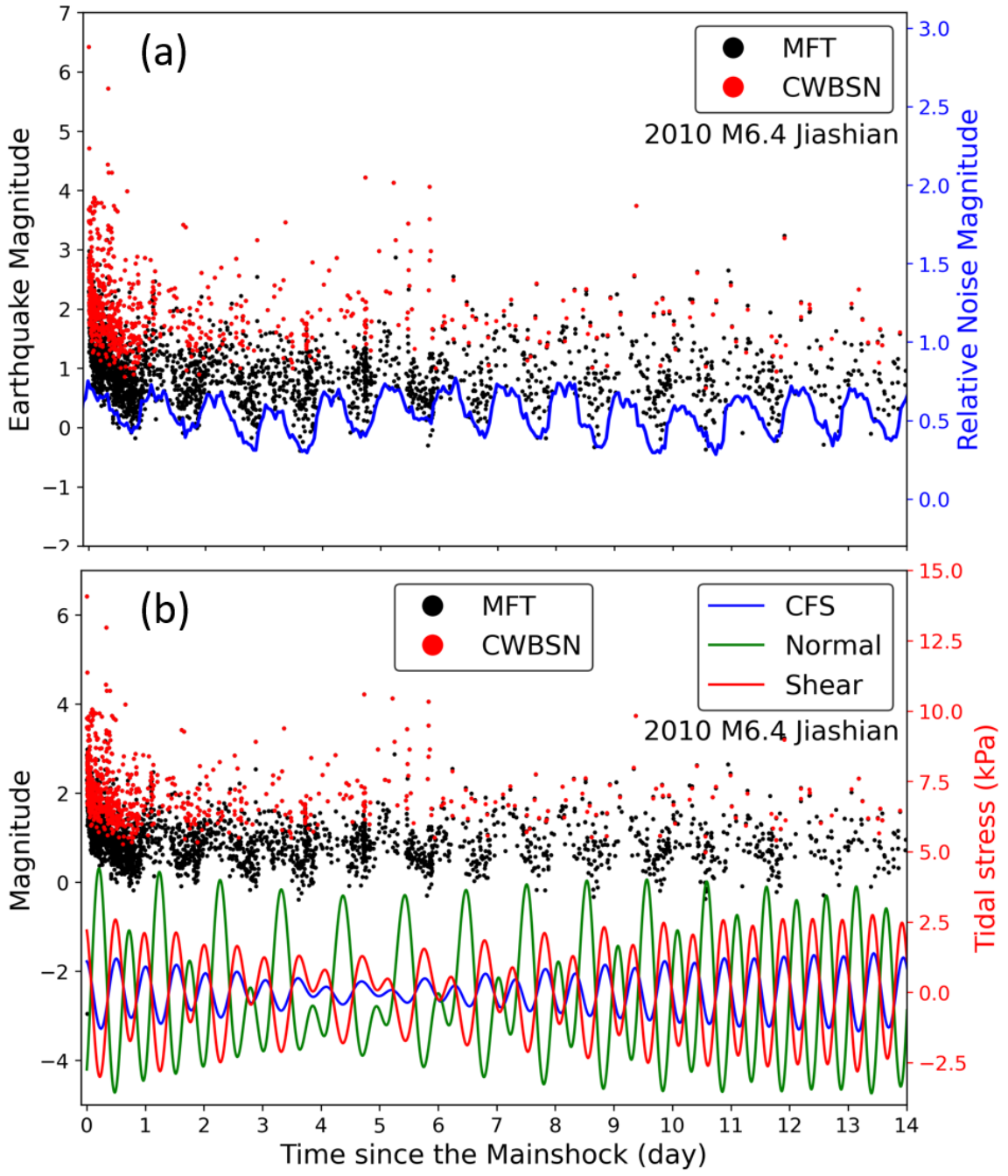

Figure 4.4 Comparison of the temporal variations of early aftershock magnitudes, noise level, and Earth-tide-induced stresses for the JSEQ. (a) Comparison of the temporal variations of early aftershock magnitudes and noise level. (b) Comparison of the temporal variations of early aftershock magnitudes and tidal stresses.

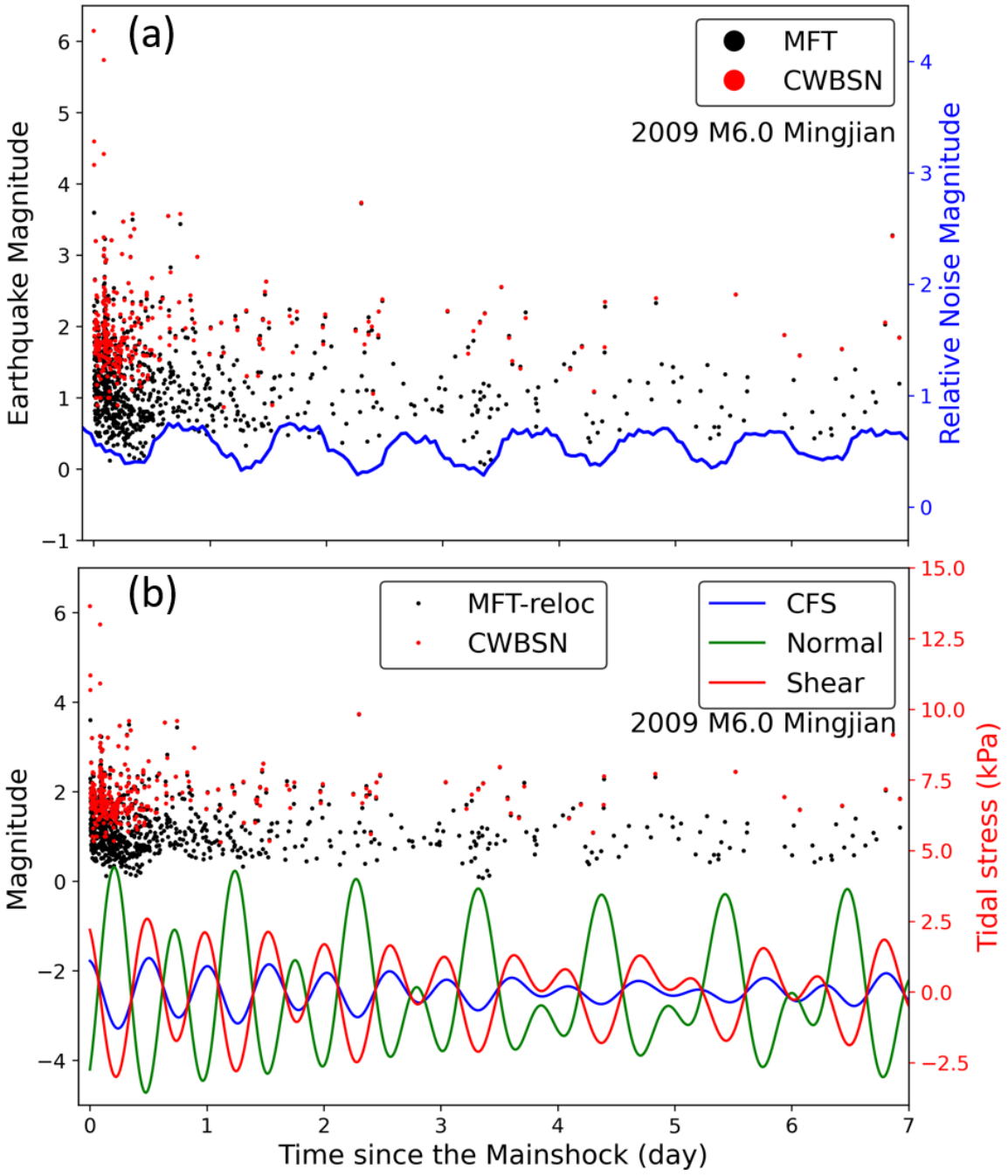

Figure 4.5 Comparison of the temporal variations of early aftershock magnitudes, noise level, and Earth-tide-induced stresses for the MJEQ. (a) Comparison of the temporal variations of early aftershock magnitudes and noise level. (b) Comparison of the temporal variations of early aftershock magnitudes and tidal stresses.

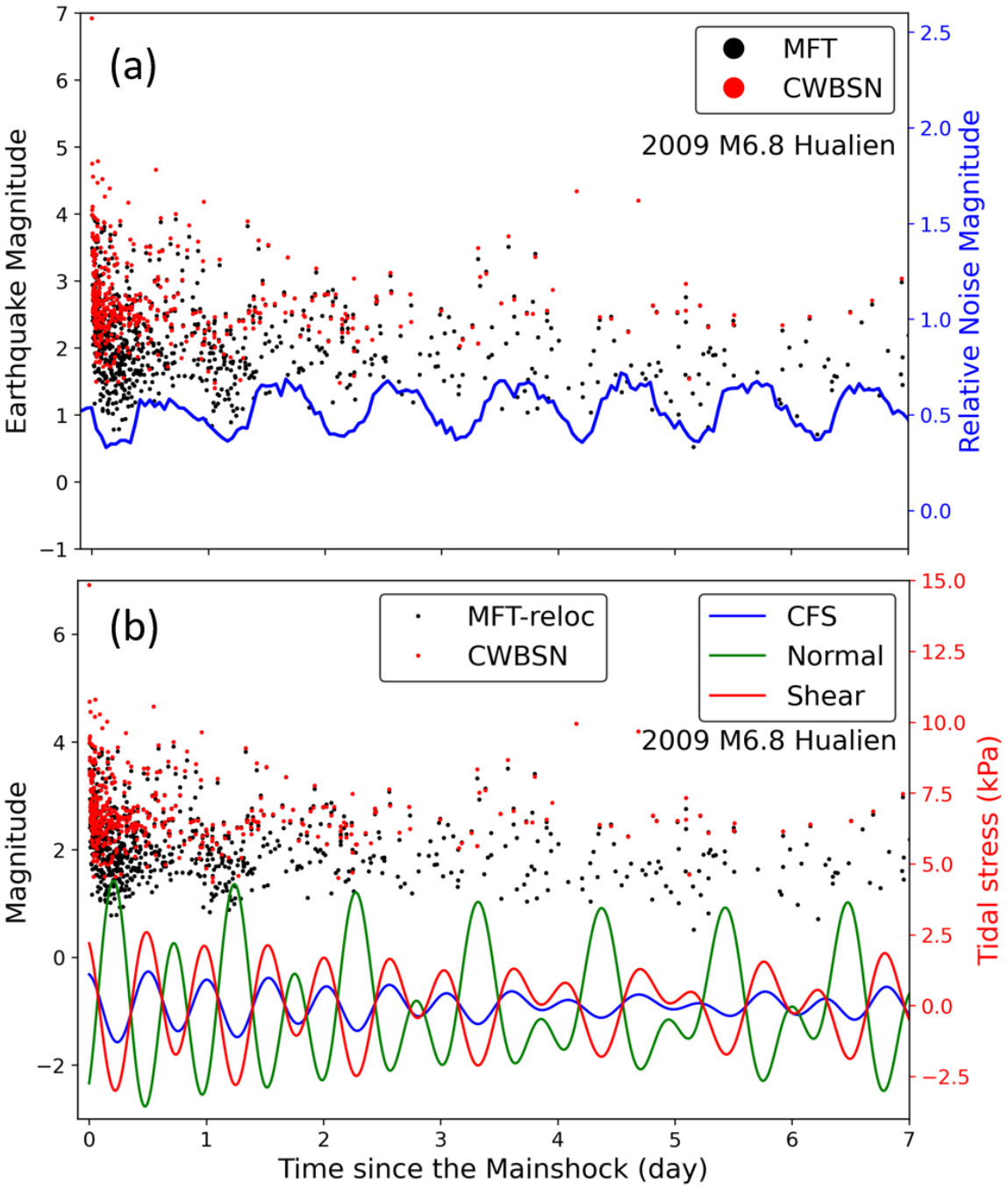

Figure 4.6 Comparison of the temporal variations of early aftershock magnitudes, noise level, and Earth-tide-induced stresses for the HLEQ. (a) Comparison of the temporal variations of early aftershock magnitudes and noise level. (b) Comparison of the temporal variations of early aftershock magnitudes and tidal stresses.

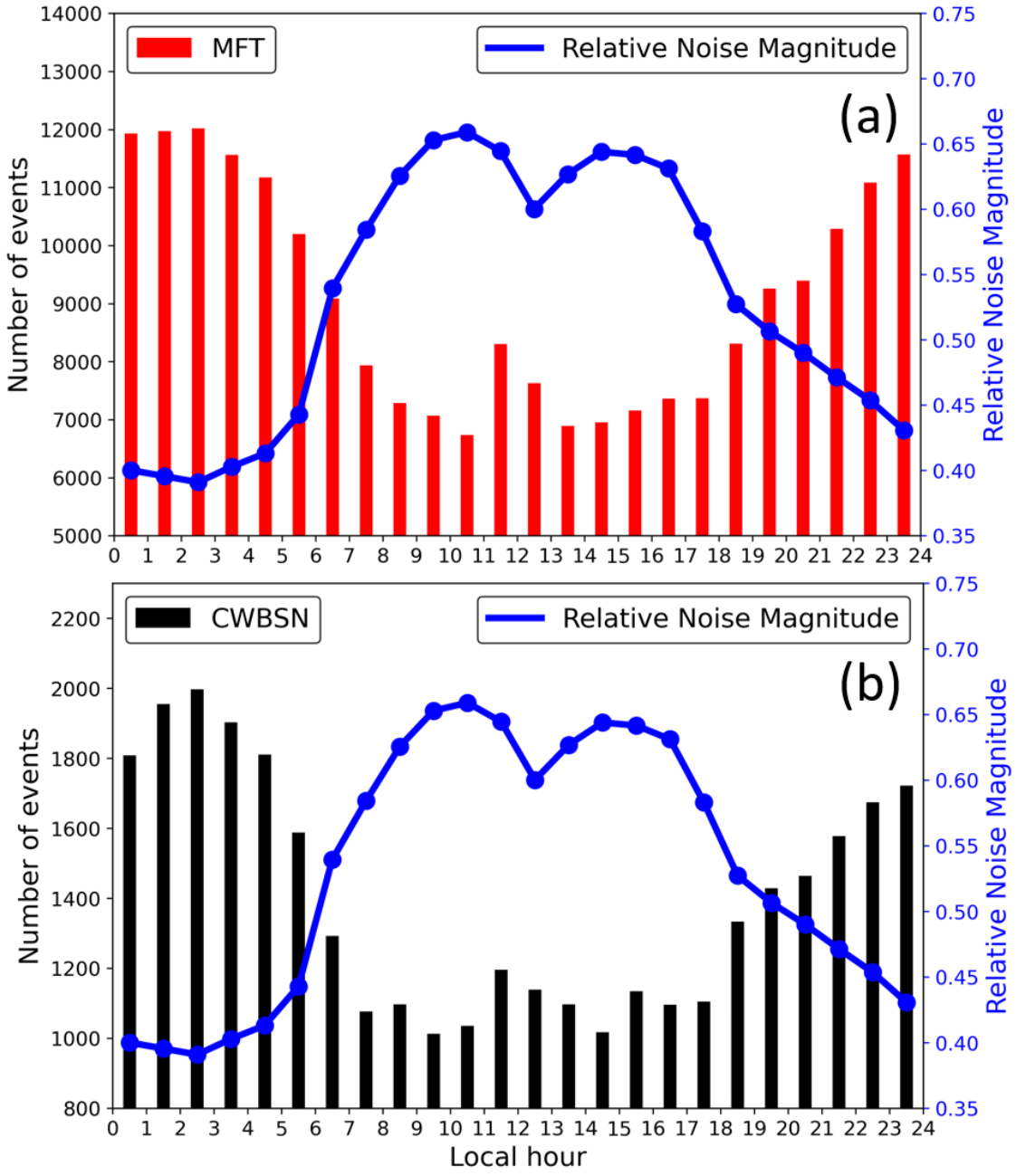

Figure 4.7 Comparison of the average number of earthquakes and average noise level in each local hour. (a) Results based on the MFT catalog. (b) Results based on the CWBSN catalog.

4.4.3 Aftershock Productivity and Slow Slip Events

Figure 4.8 shows that the 2009 M5.3 earthquake sequence occurred during a major slow slip event (SSE) in northeastern Taiwan (Chen et al., 2018). We use the Independent Component Analysis (ICA) method to separate seasonal, fault transient, and interannual signals (Figure 4.8a). Both ICA and Principal Component Analysis (PCA) are commonly used to analyze large data sets with complex signals in order to reduce the data dimension and recognize primary spatiotemporal features. The PCA aims at decomposing data into orthogonal linear transformations that maximizes the variance of a set of uncorrelated variables whereas the goal of ICA is to find a linear transformation associated with variables that are non-Gaussian and statistically independent (Hsu et al., 2020). The ICA is better in terms of separating GNSS signals with different periods. We therefore choose the ICA approach which extracts independent components (ICs) of maximum independence instead of considering the minimum correlation adopted by PCA. To extract the 2009 SSE, we removed the coseismic offsets and the long-term linear trend in the GNSS data from 2009 to 2018 and used the variational Bayesian Independent Component Analysis algorithm (vbICA, Choudrey (2002), Choudrey and Roberts (2003)) to isolate different underlying mechanisms. (Gualandi et al., 2016; Gualandi et al., 2017) The third component (vbIC3) is related to the 2009 transient event (Figure 4.8a).

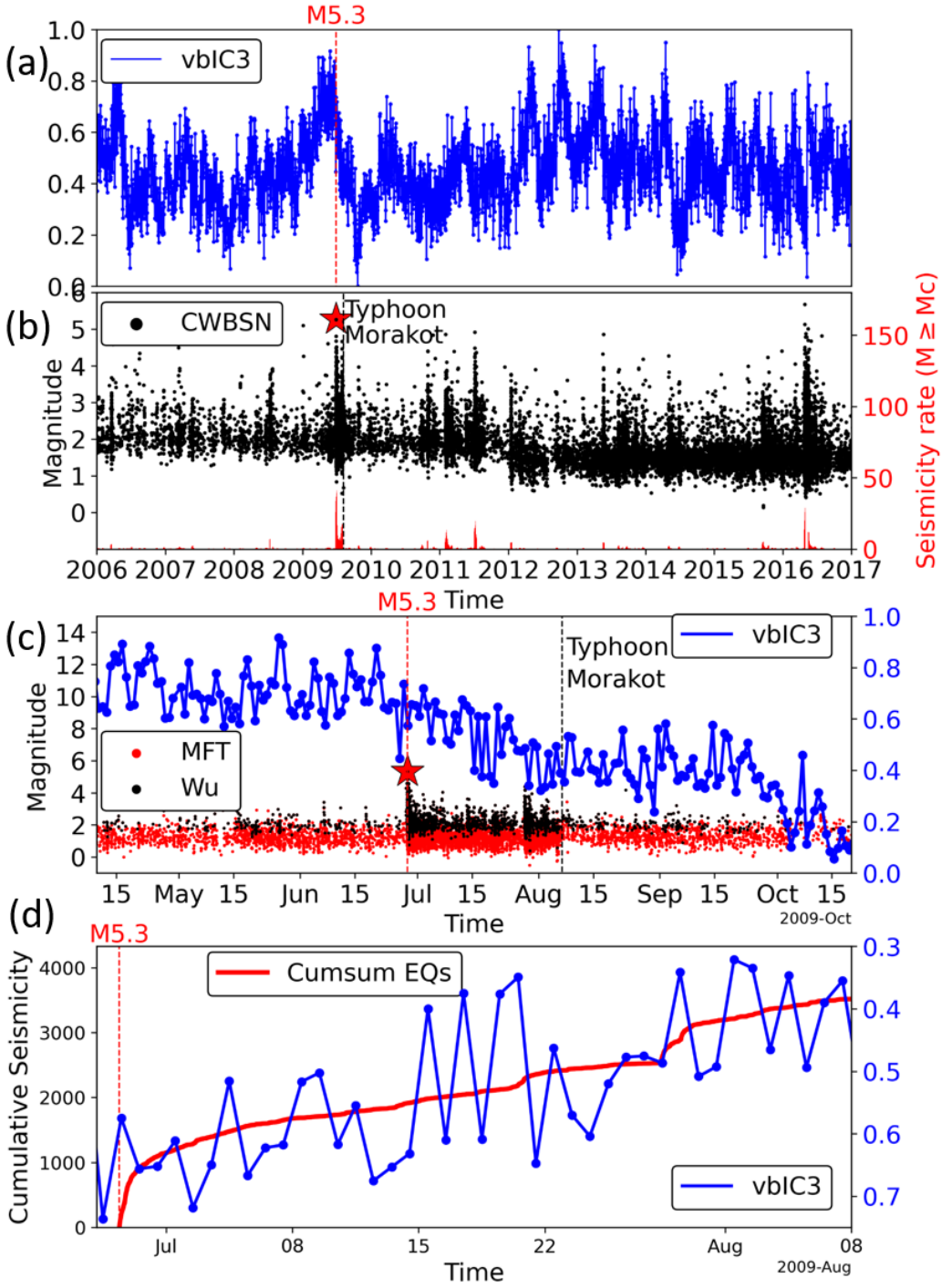

Figure 4.8 Comparision of the geodetic GNSS time series and seismicity. (a) Processed the GNSS time series. (b) Seismicity magnitude versus time in northeastern Taiwan around the 2009 M5.3 event based on the CWBSN catalog. (c) Comparison of geodetic GNSS time series and seismicity in the several months around the 2009 M5.3 event. (d)) Comparison of geodetic GNSS time series and cumulative number of earhtquakes with magnitude above Mc in the several weeks around 2009 M5.3 event.

To better quantify the spatiotemporal relations between the SSE and seismicity, we use geodetic data to invert the finite-fault slip distribution. We use a principal component analysis-based inversion method (Kositsky and Avouac, 2010) and decomposed the GNSS data into spatial and temporal components (similar to SVD). A small number of components generally can explain most of the data. The pattern of surface displacements associated with each spatial component can be inverted for the principal slip distribution. Using the product of temporal components and principal slip distributions (inverted from spatial components), we can get the whole slip history without doing inversions epoch by epoch. We choose the time interval of 27 days, but it can be any number. Note that we only used one component for this inversion (explain 70% of data variance, including more components does not produce better results). As shown in Figure 4.9 and Figure 4.10, the mainshock was followed by numerous aftershocks, and the spatial distribution of this earthquake sequence and the SSE overlapped. Based on these observations, it is a clear spatiotemporal coincidence between this relatively high-aftershock-productivity 2009 M5.3 earthquake sequence and the slow slip event in northeastern Taiwan.

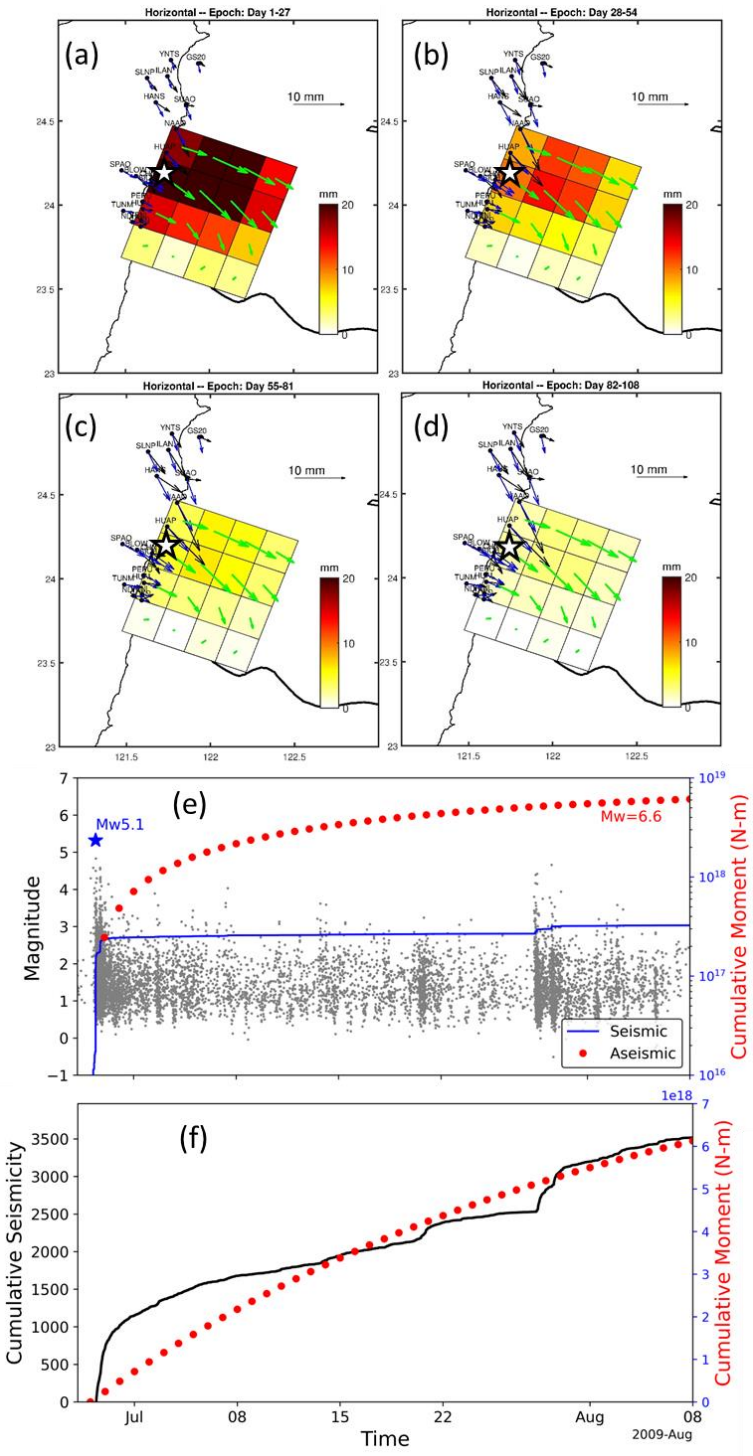

Figure 4.9 Spatiotemporal evolution of the 2009 Mw 6.6 slow slip event (SSE). (a)-(d) Integrated slip over different periods. The white stars mark the location of the 2009 M5.3 event. (e) Comparison of the temporal variation of the cumulative moment of aseismic SSE and seismic events in the M5.3 earthquake sequence. (f) Comparison of the temporal variation of the cumulative moment of aseismic SSE and cumlative number of earthquakes with magnitude above Mc in the M5.3 earthquake sequence.

To quantify the aftershock productivity of this mainshock and then compare it with the aftershock productivities of other mainshocks that have different magnitude, I use the Dascher - Cousineau et al. (2020)'s definition of relative aftershock productivity, $\Delta \log(N)$, based on the aftershock productivity law (Equation 4.2, same as Equation 1 in Dascher - Cousineau et al. (2020)) (Omori, 1894; Ogata, 1988).

$$N'(Mw) = k10^{\alpha Mw} \qquad 4.2$$

where $N'(Mw)$ is the predicted number of aftershocks above the magnitude of completeness (*Mc*) (Gutenberg and Richter, 1944) following a mainshock with moment magnitude, Mw; k is a constant that does not affect the difference of the relative aftershock productivity (Equation 4.3, same as Equation 5 in Dascher - Cousineau et al. (2020)), $\Delta \log(N)$ of two mainshocks; α is a constant set as 1 in this study based on the general observations ($\alpha \approx 1$) of many previous studies (Reasenberg and Jones, 1989; Yamanaka and Shimazaki, 1990; Tahir and Grasso, 2015; Page et al., 2016). The moment magnitude (Mw) is estimated from the local magnitude using the empirical relationship fitted using the CWBSN data in Taiwan proposed by Chen et al. (2007). The aftershock time window is defined as 60 days (Dascher - Cousineau et al., 2020) following the mainshocks. The aftershock zone size is set as two-fold of the source dimension, which is estimated from the moment magnitude using the empirical relationship fitted by Dascher - Cousineau et al. (2020). The *Mc* is determined using the maximum curvature method (Wiemer and Wyss, 2000).

$$\Delta \log(N) = \log(N) - \log\big(N'(Mw)\big) = \log\left(\frac{N}{k10^{\alpha Mw}}\right) \quad 4.3$$

where N is the observed number of aftershocks following a mainshock with moment magnitude, Mw. The $N'(Mw)$ is the predicted number of aftershocks for this mainshock using Equation 4.2. Note that the relative aftershock productivity, $\Delta \log(N)$, is magnitude independent (Dascher‐Cousineau et al., 2020). Therefore, it can be used for the comparison of mainshocks with different magnitudes.

To test if the spatiotemporal coincidence between the relatively high-aftershock-productivity earthquake sequences and the occurrence of SSEs is a general phenomenon in this region, I extend the target time window from 2009 and 2010 of the MFT catalog to a longer window using the CWBSN catalog. I first select all the M5+ events within a 25-km-radius distance from the hypocenter of the 2009 M5.3 event in northeastern Taiwan. Next, I check these selected events to make sure any event is not another event's aftershock based on the space-time distance between them (Dascher‐Cousineau et al., 2020). I get thirteen M5+ events in this target region. I then calculate the relative aftershock productivities for all of these thirteen mainshock-aftershock sequences. Table 4.1 shows the results. After comparing with the geodetic GNSS time series, I find that the top four mainshocks with the highest aftershock productivity are all associated with SSEs. Figure 4.11 shows the magnitude-time distribution of earthquakes in these four relatively high-aftershock-productivity mainshock-aftershock sequences (the other nine sequences are shown in Figure B.5 and Figure B.6). Chen et al. (2018) studies three of these four events and the associated SSEs in detail. The results shown here are generally consistent with their

observations. However, their study did not focus on aftershock productivity and did not analyze the rest ten of the thirteen events.

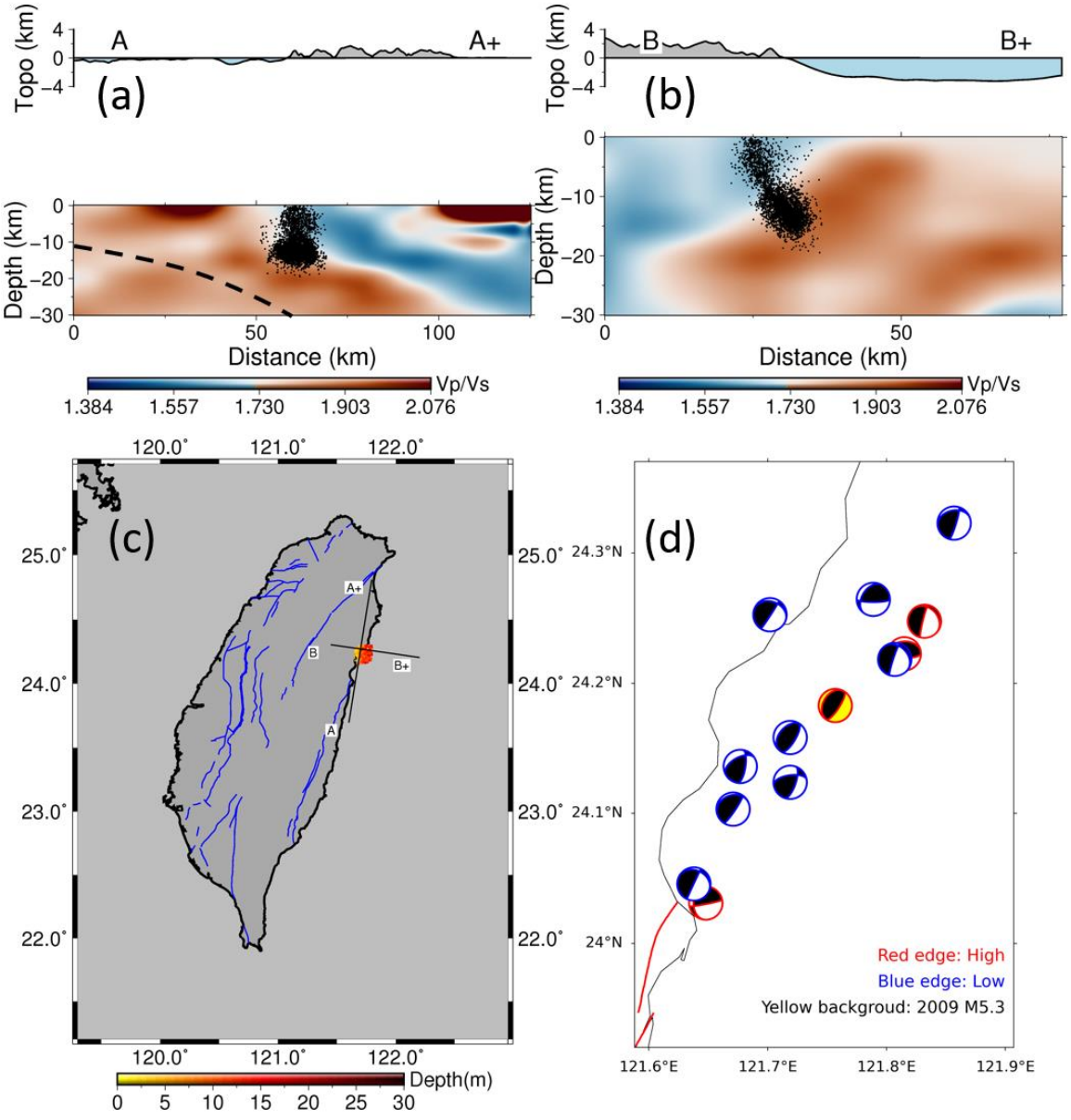

Figure 4.10 Spatial distribution of the events in the 2009 M5.3 earthquake sequence and selected thirteen M5+ mainshocks. (a)-(b) are the profile of AA+ and BB+, respectively. These dots are the earthquakes following and surrounding the 2009 M5.3 mainshock in the MFT-reloc catalog. The seismic Vp/Vs ratios along these profiles are interpolated from the 3D velocity model (Huang et al., 2014**). (c) Map of the two profiles and seismicity shown in (a)-(b). (d) Map of the selected thirteen M5+**

mainshocks in the CWBSN catalog between 2002 and 2017 around the 2009 M5.3 event. The beachball with the red edge and yellow backgroud at the center of this subfigure is the 2009 M5.3 mainshock. The four beachballs with red edge are the top #1-#4 relatively high-aftershock-productivity mainshocks shown in Table 4.1, The nine beachballs with blue edge are the #5-#13 relatively low-aftershock-productivity mainshocks shown in Table 4.1. This region is marked as the green box in Figure 4.1c.

Table 4.1 The statistics of aftershock productivity of thirteen mainshocks in northeastern Taiwan between 2002-2016. If the 'SSE' column is 'Yes' that means there was a spatiotemporal coincidence between this mainshock-aftershock sequence and an SSE event. The map of these events can be found in Figure 4.1c and Figure 4.10d.

#	Magnitude	Date	Focal Mechanism	DetLogN	SSE
1	5.32	20090628	reverse	0.31	Yes
2	5.62	20050430	reverse	0.10	Yes
3	5.69	20150915	normal	0.10	Yes
4	5.71	20160427	reverse	0.06	Yes
5	5.14	20050201	reverse	-0.05	No
6	5.46	20110201	normal	-0.14	No
7	5.27	20020403	reverse	-0.17	No
8	5.13	20110921	reverse	-0.46	No
9	5.02	20100928	reverse	-0.51	No
10	5.10	20090103	reverse	-0.64	No
11	5.41	20120419	reverse	-1.14	No
12	5.45	20150107	reverse	-1.20	No
13	5.53	20100615	normal	-1.45	No

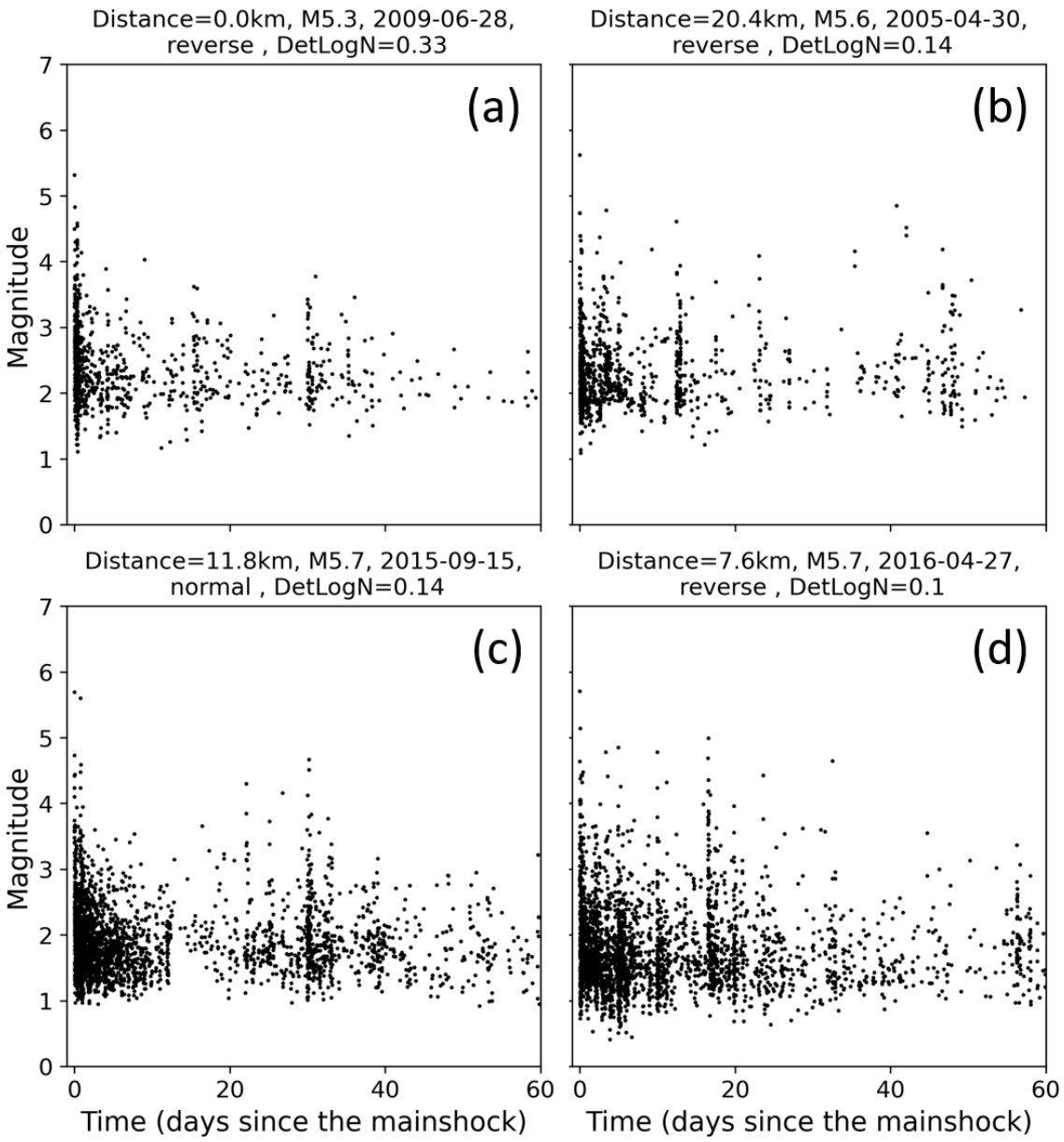

Figure 4.11 Magnitude-time distribution of earthquakes in the top #1-#4 relatively high-aftershock-productivity mainshock-aftershock sequences in Table 4.1. (a)-(d) are the #1-#4 earthquake sequences in Table 4.1, respectively.

4.5 Limitations of the Current Results and Planned Future Study

In this section, I briefly summarize the limitations in the current results and planned future studies to address these potential problems. First, I will double-check why the tidal stress calculation results of this study are slightly different from the results in Tang et al.

(2019), although it will not change the conclusion of this study. Note I use different code packages to calculate the tidal stresses and there are other packages available on the market. A detailed comparison would be helpful to make sure that the tidal stress calculation results are reproducible. Second, the accurate relative time between the earthquake sequences and the associated SSEs is not confirmed yet. In the near future, I plan to analyze the time series recorded by multiple geodetic stations to get the starting time and space distribution (at least along latitude) of these four slow slip events in Taiwan. Last, I will calculate the detailed Coulomb stress changes for these four slow slip events in Taiwan to quantify the stress change on a fault caused by a nearby slow slip event.

4.6 Discussion and Conclusions

Using the high-resolution relocated template matching catalog in Taiwan (Zhai et al., 2021c), I observed clear aftershocks migration as the logarithm of time along with the hypocentral depth for several mainshock-aftershock sequences in Taiwan. This result is similar to previous studies that showed similar logarithmic along-strike migration of aftershocks (Peng and Zhao, 2009; Kato and Obara, 2014; Obana et al., 2014; Tang et al., 2014; Meng and Peng, 2016; Frank et al., 2017), suggesting that these aftershocks were primarily driven by afterslip following the mainshock ruptures (Kato, 2007; Perfettini et al., 2018). This result is also consistent with a recent study (Lin et al., 2022) that proposed that the aftershocks of HLEQ were primarily driven by afterslip based on local geodetic strainmeter data. In addition, I found that the minimum magnitude and number of early aftershocks of three M6+ events in Taiwan, including the 2010 M6.4 Jiashian earthquake, were not mainly modulated by earth tides as proposed by Tang et al. (2019). Instead, they were primarily limited by the daily fluctuations in the local noise level. Finally, I also found

a clear spatiotemporal coincidence between high-aftershock-productivity earthquake sequences and the occurrence of nearby SSEs in northeastern Taiwan, suggesting that SSEs can help to further promote aftershock generation. These results suggest that SSEs may temporally increase the productivity of nearby aftershock sequences, and hence potential seismic hazard in a region that host both SSEs.

CHAPTER 5. SYSTEMATIC DETECTIONS OF INTERMEDIATE-DEPTH EARTHQUAKES IN THE JAPAN SUBDUCTION ZONE

5.1 Summary

The results in this chapter have been presented at several recent conferences, such as the 2021 Fall American Geophysical Union Annual Meeting (Zhai et al., 2021b) and the 2022 Seismological Society of America Annual Meeting (Zhai et al., 2022). The manuscript is currently in preparation. Intermediate-depth earthquakes (IDEQs), defined as between ~70 and 350 km depths, dominate in the number of all deep earthquakes below 70 km and pose seismic hazards in certain regions. However, the physical mechanisms of IDEQs are still in debate. With well-resolved double seismic layers and subducting slab geometry, and dense seismic instrumentation, Central and Northeastern Japan is an ideal region to study IDEQs. I investigate the responses of IDEQs on double seismic layers to the Magnitude (*M*) 9 Tohoku-Oki earthquake (TOEQ) and several *M*5+ IDEQs listed in the JMA catalog between 2004 and 2018. Because standard catalogs are inherently incomplete in the lower magnitude ranges, particularly right after large earthquakes when the background noises are high, I perform a systematic search for possible missing IDEQs with a matched filter technique (MFT). Specifically, I use 69,225 IDEQs listed in the Japan Meteorological Agency (JMA) catalog between 2004 and 2018 as templates to scan through the continuous waveforms recorded by ~800 borehole stations of the High-Sensitivity Seismograph Network (Hi-net). The time window is one year before and after the 2011 *M*9 TOEQ, and ten days around each one of ten *M*5+ IDEQs. The number of

events in the newly built catalog (48,882) is a 3.5-fold increase compared to the JMA catalog in the two years around the TOEQ. The newly built MFT catalog does not show a significant anomalous precursory increase in IDEQs in the two months prior to the TOEQ, as reported in a previous study. However, the newly built MFT catalog shows a significant increase in the rate of IDEQs following the TOEQ in both upper and lower planes beneath 70 km depth, but without a significant increase in the upper-to-lower ratio. I also observe a spatial separation of postseismic slips of TOEQ and the triggered IDEQs activity following the TOEQ. For the ten *M*5+ IDEQ mainshocks, I detect more foreshocks and aftershocks, but I do not have any clear pattern on which sequences are more productive than others. In addition, the results show that the JMA catalog is relatively complete above the magnitude two except right following the 2011 *M*9 TOEQ, and hence can be directly used to analyze the aftershock productivity of IDEQs in Central and Northeastern Japan.

5.2 Introduction

The occurrence of intermediate-depth earthquakes (IDEQs) at a depth between 70-350 km is still an enigma because the high pressure and temperature conditions should favor ductile deformation over brittle failure. At present, the physical mechanisms of IDEQs are still under debate (Zhan, 2020). Three leading proposed mechanisms are dehydration embrittlement (Kirby et al., 1996; Peacock and Wang, 1999; Peacock, 2001; Dobson et al., 2002; Jung et al., 2004; Yamasaki and Seno, 2005; Chernak and Hirth, 2011; Barcheck et al., 2012; Proctor and Hirth, 2015; Okazaki and Hirth, 2016; Ferrand et al., 2017; Chen et al., 2019), phase transformational faulting (Kirby, 1987; Green and Burnley, 1989; Burnley et al., 1991; Kirby et al., 1991; Green and Houston, 1995; Kao and Liu, 1995; Kirby et al., 1996; Schubnel et al., 2013; Shi et al., 2022), and thermal shear

instability (Ogawa, 1987; Hobbs and Ord, 1988; Karato et al., 2001; Kelemen and Hirth, 2007; John et al., 2009; Ohuchi et al., 2017). Although IDEQs have been documented globally (Fujita and Kanamori, 1981; Nyffenegger and Frohlich, 2000; Brudzinski et al., 2007; Florez and Prieto, 2019) since about one century ago (Wadati, 1928), finding direct and solid seismic evidence to confirm/reject a proposed mechanism is still a challenge (Zhan, 2020).

Previous studies have shown that aftershock productivities of deep earthquakes including IDEQs are significantly lower than shallow earthquakes on average (Kagan and Knopoff, 1980; Prozorov and Dziewonski, 1982; Frohlich, 1987; Nyffenegger and Frohlich, 2000; Wiens, 2001; Persh and Houston, 2004). However, at least some IDEQs had abundant aftershocks (Wiens et al., 1997; Takahashi and Hirata, 2003; Li et al., 2018a) that decayed following the Omori's Law (Omori, 1894). In addition, recent studies have attempted to investigate how IDEQs and deep-focus earthquakes (depths between 350 and 700 km) respond to dynamic stresses from earthquakes at long-range distances (Price and Wiens, 2018; Jia et al., 2020; Luo and Wiens, 2020).

Recently, Chu and Beroza (2022) systematically analyzed the aftershock productivity of large IDEQs in Japan using the Japan Meteorological Agency (JMA) earthquake catalog (Ueno, 2002; Tamaribuchi et al., 2016). They found that the productive events occurred at a higher Vp-Vs ratio (mean ratio 1.79 and 1.75 for productive events and unproductive events, respectively), suggesting fluids may enable IDEQ aftershock activity in this region. However, the JMA catalog may not be complete right before or following large mainshocks (Enescu et al., 2007; Peng et al., 2007; Lengliné et al., 2012). It is important to detect these potential missing earthquakes, because they may provide a

new perspective on fault properties, stress environment, and the physical mechanism of IDEQs (Li et al., 2018a).

In this study, I investigate the behavior of small-magnitude IDEQs before and after the 2011 *M*9 Tohoku-Oki earthquake and ten moderate-size IDEQ mainshocks in Central and Northeastern Japan. I use a matched filter technique (MFT, also known as template matching) (Gibbons and Ringdal, 2006; Shelly et al., 2007; Peng and Zhao, 2009) to detect missing IDEQs that are not reported in the JMA catalog. After building a more complete catalog, I use it to investigate the seismicity rate changes before and after the *M*9 Tohoku earthquake and ten moderate IDEQ mainshocks. By systematically detecting IDEQs around these mainshocks, I hope to gain some insight into the physical mechanism of IDEQs and their responses to external stress perturbations.

5.3 Study Region and the 2011 Tohoku-Oki Earthquake

In Central and Northeastern Japan, the Pacific Plate is subducting west-northwestward along the Japan Trench (Figure 5.1). The convergence rate is about 8.5 cm/yr and the subducting Pacific is about 130-Ma old (Ruff and Kanamori, 1980; Demets et al., 1994). This region is an ideal region to study IDEQs (Figure 5.1) for the following reasons. It is seismically active with IDEQs extending to the mantle transition zone, and well-resolved double seismic layers (Umino, 1975; Hasegawa et al., 1978b; Hasegawa et al., 1978a; Kawakatsu, 1986; Kosuga et al., 1996; Igarashi et al., 2001; Kita et al., 2010; Nishitsuji and Mori, 2014; Warren et al., 2015; Chu et al., 2019), and well-defined slab geometry delineated by seismic tomography and other imaging methods (Zhao et al., 1992; Miura et al., 2005; Hayes et al., 2018; Chen et al., 2021). In addition, this region has been

well monitored by dense seismic networks such as the High-Sensitivity Seismograph Network (Hi-net) (Section 5.4) and the Seafloor Observation Network for Earthquakes and Tsunamis along the Japan Trench (S-net) in the past two decades (Okada et al., 2004; Obara et al., 2005; Kaneda et al., 2015; Kanazawa et al., 2016).

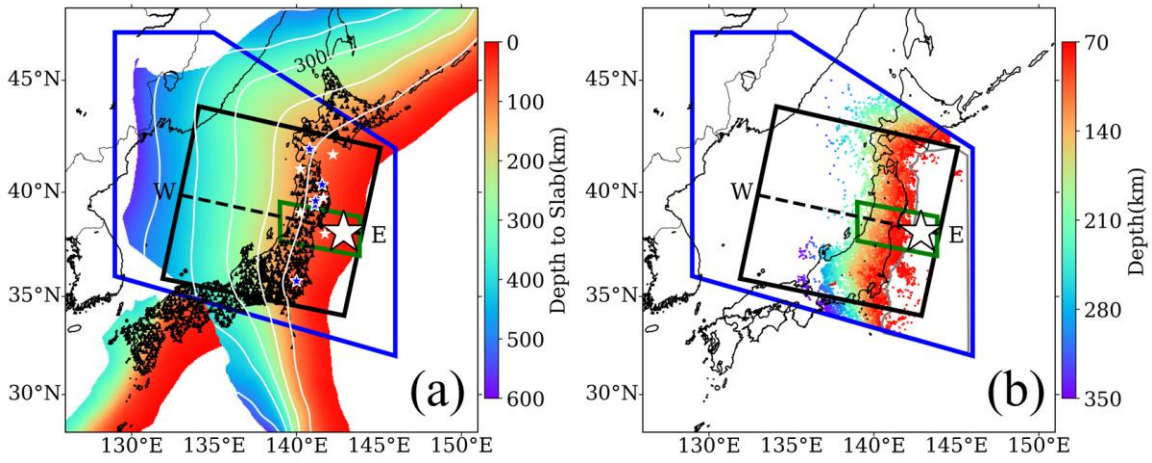

Figure 5.1 Map of the study region. (a) Black triangles are the ~800 borehole stations of Hi-net operated by NIED. The large white star is the 2011 M9 Tohoku-Oki earthquake; The small white stars are five M5+ mainshocks on the upper plane. The small blue stars are five M5+ mainshocks on the lower plane. The data of the depth of the slab is from the Slab2 model (Hayes et al., 2018**). (b) The colored dots are template intermediate-depth earthquakes (IDEQs) used in the template matching procedure. The blue-line zone is the zone I perform the template matching, termed the template-matching zone in this study. The black-line zone is termed the wide-target zone in this study. The green-line zone is termed the narrow-target zone in this study. This narrow-target zone is the same as in Delbridge et al. (2017). The gray-line zone is termed the not-double-seismic zone in this study.**

The largest earthquake in this region is the magnitude (*M*) 9 Tohoku-Oki earthquake (TOEQ), which occurred along the shallow plate boundary on March 11, 2011 (Figure 5.1). The rupture area is about 300 × 200 km (Iinuma et al., 2011; Iinuma et al., 2012; Uchida and Burgmann, 2021), the co-seismic rupture extended from the trench to about 50 km depth (Iinuma et al., 2011; Iinuma et al., 2012; Ozawa et al., 2012), and the post-seismic slip reached about 90 km depth (Shirzaei et al., 2014; Iinuma et al., 2016).

Many aftershocks occurred right after the mainshock, including three M7+ aftershocks within 40 minutes (Asano et al., 2011; Hirose et al., 2011; Lengliné et al., 2012; Shinohara et al., 2012). These aftershocks can reach about 70 km in depth (Shinohara et al., 2012), covering an area of 500 × 200 km (Hirose et al., 2011).

In the past decade, some studies focused on changes in seismic and other geophysical properties right before the TOEQ and were summarized in Uchida and Burgmann (2021) briefly described as follows. Kato et al. (2012) reported two foreshock sequences at shallow depth migrated toward the TOEQ, including a magnitude 7.3 earthquake that occurred 3 days before the mainshock. Panet et al. (2018) reported large-scale gravity and mass changes starting a few months before the mainshock. Heki (2011) and Heki and Enomoto (2015) found ionospheric electron enhancement preceding the mainshock. Bedford et al. (2020) showed that the TOEQ is preceded by months of surface displacement variations that spanned thousands of kilometers with the GPS data. However, other studies argue the significance of these precursory observations. For example, Wang and Burgmann (2019) suggest the preseismic gravity variations reported by Panet et al. (2018) are not statistically unique, either in space or in time. Kamogawa and Kakinami (2013), Masci et al. (2015), and Ikuta et al. (2020) showed that the proposed preseismic variations of total electron content reported by Heki (2011) and Heki and Enomoto (2015) are likely contaminated by artifacts. Additional studies are needed to critically evaluate these preseismic changes and better understand the physical mechanisms behind them (Kato and Ben-Zion, 2020; Pritchard et al., 2020; Uchida and Burgmann, 2021).

Several studies also focused on the seismicity changes of IDEQs before and after the TOEQ. Bouchon et al. (2016) reported synchronous bursts of both shallow seismicity

and IDEQs in the subducting slab prior to the mainshock. They suggested the slab started to plunge into the mantle before massive megathrust earthquakes. However, Delbridge et al. (2017) argued from a long-term JMA catalog analysis that the precursory acceleration of IDEQs reported by Bouchon et al. (2016) is not statistically significant. In addition, Delbridge et al. (2017) observed a significant rate increase of IDEQs in the upper plane of the double seismic zone following the TOEQ. Both studies are based on the JMA catalog, which is likely not complete, especially right following the *M*9 TOEQ (Kato et al., 2012; Lengliné et al., 2012; Gardonio et al., 2019). Here I plan to use the MFT to detect additional IDEQs around the TOEQ and use them to better understand how the double seismic zone changed their patterns before and after the TOEQ.

5.4 Data

I use continuous seismic recordings and template events to build a more complete IDEQ catalog in Central and Northeastern Japan with the matched filter technique. For the continuous waveforms, I take the raw data recorded by the entire High-Sensitivity Seismograph Network (Hi-net) operated by the National Research Institute for Earth Science and Disaster Resilience (NIED) in Japan (Figure 5.1a) (Okada et al., 2004; Obara et al., 2005). Hi-net consists of ~800 three-component borehole stations with a sampling rate of 100 Hz. The time windows of continuous waveforms used in this study are two years starting from one year before the 03/11/2011 M9 Tohoku-Oki earthquake (Section 5.6.1), and ten days starting from three days before each of the selected ten *M*5+ IDEQ mainshocks in the study region between 2004 and 2018 (Section 5.6.2). The continuous waveforms are downloaded using the HinetPy package (Tian, 2021). For the templates, I use 90,214 IDEQs between 70 and 350 km depth listed in the JMA catalog. These events

are all the IDEQs between 04/01/2004 and 12/31/2018 in the study region (Figure 5.1b). The time window starts on 04/01/2004 because it is the first day of the Hi-net continuous waveforms that can be directly accessed using the HinetPy package, although the Hi-net started its service on 10/01/2000. These templates in the JMA catalog include 800,375 *P* wave arrival times and 723,432 *S* wave arrival times manually picked by local analysts. Figure 5.2b and Figure 5.2c show the magnitude and depth distribution of the templates in Figure 5.1b, respectively.

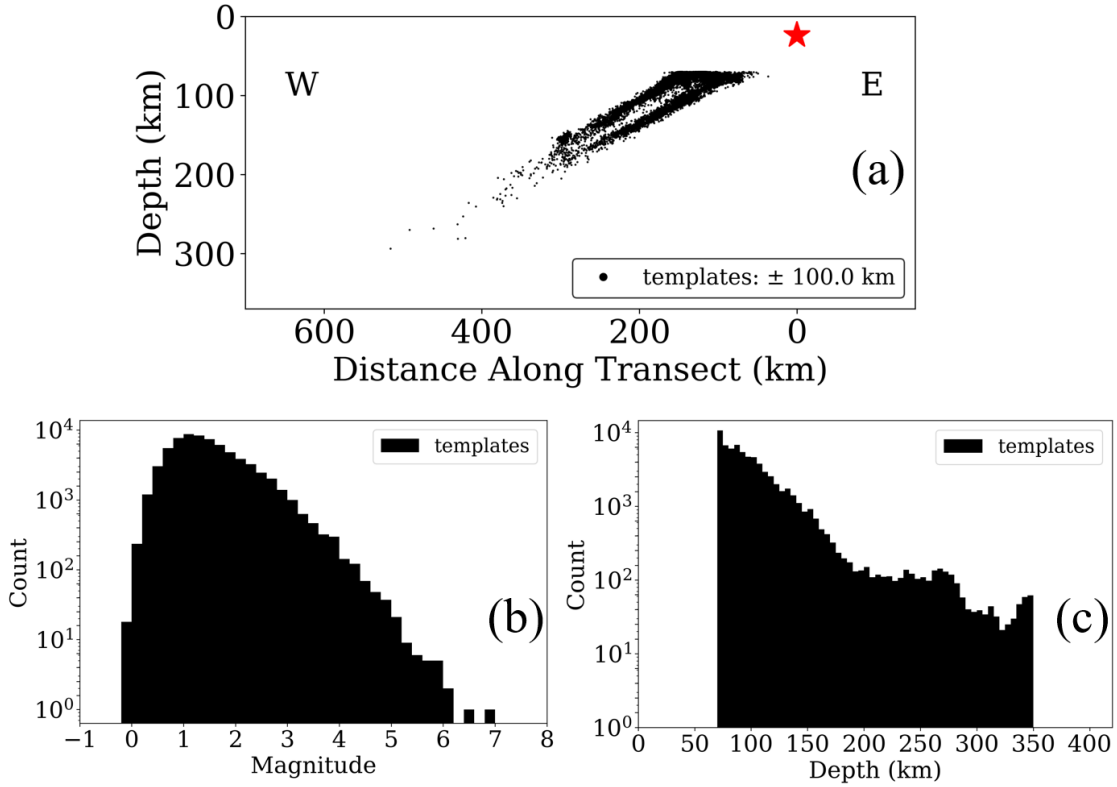

Figure 5.2 Template intermediate-depth earthquakes distributions. (a) The 'W-E' cross-section in Figure 5.1b. Seismicity are within ±100 km of the black dashed line. (b) The magnitude distribution of all IDEQs in Figure 5.1b. (c) The depth distribution of all IDEQs in Figure 5.1b.

5.5 Method

5.5.1 Distinguishing the Upper and Lower Planes in the Double Seismic Zone

An important task is to decide whether an IDEQ is on the upper or lower plane of the double seismic zone before analyzing the seismicity rate changes. Here I use the following procedure to define a boundary between the upper and lower planes. First, I use a 2D plane to fit the Slab2 model in the wide-target zone with the least-squares method. Figure 5.3a and Figure 5.3b show the real Slab2 model and the fitted 2D plane, respectively. The geometry of the slab in the wide-target zone is relatively simple and can be well represented by a 2D plane, termed the slab interface in this study. I then calculate the distances from the slab interface to all the template IDEQs, termed plate-interface depth in this study. Figure 5.3c shows the plate-interface depth distribution of all templates. There are two clear groups of IDEQs with the minimum distribution at 35 km plate-interface depth. Therefore, I take the plate-interface depth of this point as the boundary between the upper and lower plane in this study. IDEQs with plate-interface depths between 0-35 km and 35-70 km are labeled as in the upper and lower planes, respectively (Figure 5.3d). In addition, some offshore events with poor depth constraints could be mistakenly labeled as events in the lower planes. Therefore, I manually set up a zone off-shore (the not-double-seismic zone marked with gray lines in Figure 5.1b) based on the distribution of template IDEQs. When analyzing the IDEQ behaviors on the upper plane or the lower plane before and after the mainshocks in the following sections, I remove all the events that are inside this off-shore not-double-seismic zone. I also remove all the events that are outside the wide-target zone (black lines in Figure 5.1b).

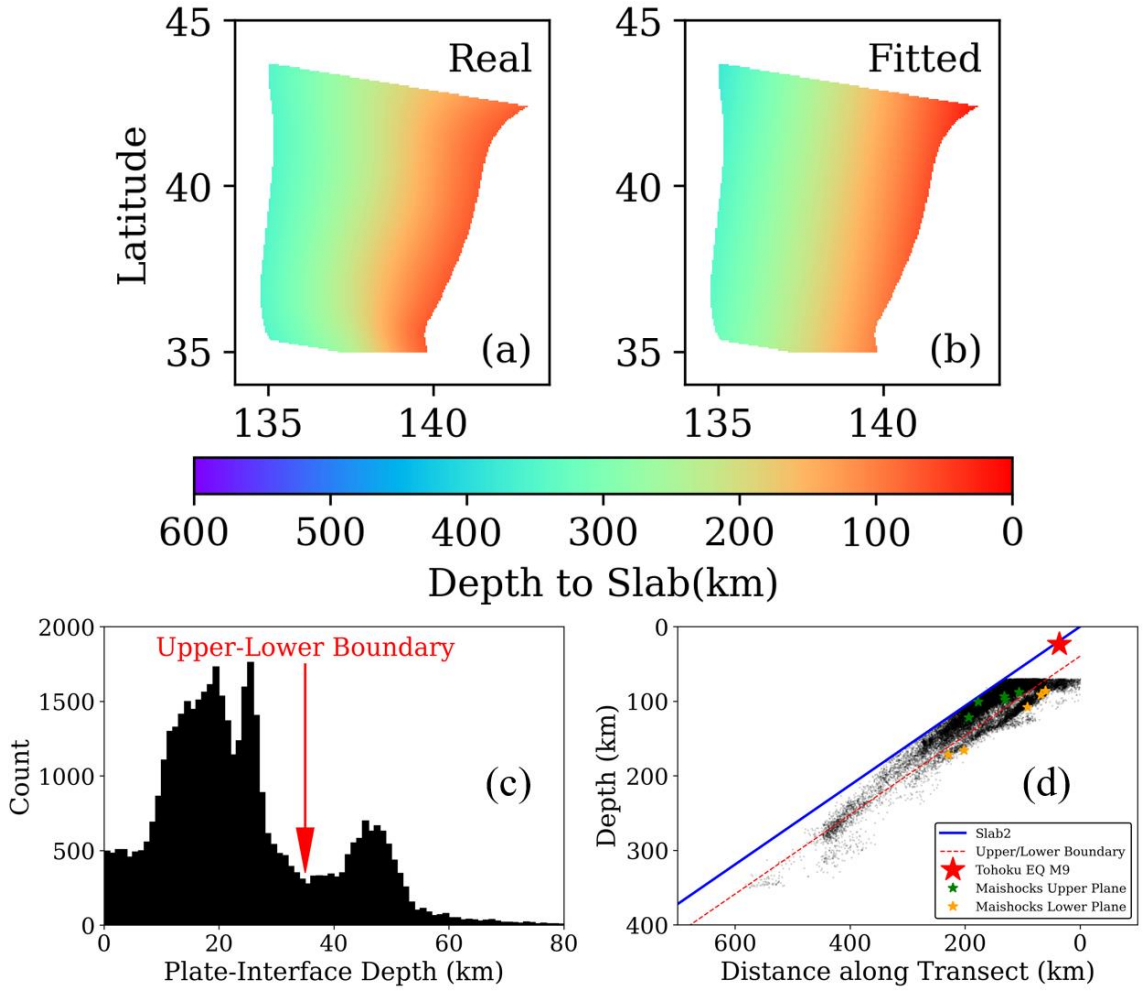

Figure 5.3 The boundary between the upper and lower plane. (a) The map of the depth of the Slab2 model in the wide-target zone (black-line zone in Figure 5.1a). (b) A 2D plane in 3D space by fitting the data in (a) with the least-squares method. (c) The plate-interface depth distribution of template events in the wide-target zone (Figure 5.1b). Plate-interface depth is the distance between the slab surface (the fitted 2D plane in b) and the earthquake hypocenter. The red arrow pointing at 35 km is the same upper-lower boundary as shown in (d). (d) Templates distribution in the slab in the wide-target zone.

5.5.2 Building a New IDEQ Catalog with MFT

To detect more small-magnitude IDEQs that are not recorded in the JMA catalog, I use the matched-filter technique (MFT) to scan the continuous seismic waveform recordings. The workflow of MFT in this study generally follows it in the Zhai et al. (2021c)

and Li et al. (2018a). I slightly modify the EQcorrscan (Chamberlain et al., 2017) and FMF (Fast-Matched-Filter) (Beaucé et al., 2017) packages to perform the MFT scan in this study. To efficiently process such a big dataset and perform heavy MFT calculations, I take advantage of the Extreme Science and Engineering Discovery Environment (XSEDE) supercomputers with GPU resources. It took about 33,000 NVIDIA Tesla V100 GPU hours to finish the MFT detection performed in this study. Detailed steps and parameters to build the new catalog are described below.

First, I pre-process the raw waveforms before the cross-correlation (CC) detection. Both day-long continuous waveforms and template events' waveforms are demeaned, detrended, down-sampled as 40 Hz to reduce computation cost, and filtered between 2-16 Hz to enhance the signal of small IDEQs. For the template waveforms, I trim them to 6 s long starting from 1 s before the *P* wave arrival, and 12 s long starting from 1 s before *S* wave arrival (Li et al., 2018a). I take all the three components of available stations for both *P* and *S* waves (Li et al., 2018a). I then remove any template waveform if its signal-to-noise ratio (SNR) is below 5. I use the default definition of SNR in EQcorrscan, which is the ratio of the maximum absolute amplitude in the signal window of *P* or *S* to the root-mean-squared (RMS) of 100 s before the signal window. Then, I remove any template IDEQs containing fewer than twelve traces of waveforms. These constraints can reduce false detections from a few noisy template waveforms. The number of IDEQs in the selected template list used for further computation is 69,225.

Next, I compute the stack of zero-normalized cross-correlation (CC) functions (Meng et al., 2012) between the selected template IDEQs and the continuous waveforms using the GPU-based FMF package. Note I modify the original version of FMF (Beaucé et

al., 2017) to fit the need in this study. The first modification is to remove the mean of the two waveforms when computing the cross-correlation between them. This is slightly slower than the original version of FMF but is more accurate for template matching CC calculation (Chamberlain et al., 2021). The second is to modify the package so that it can work for the dataset with different window lengths of *P* and *S* waveforms. I stack the CC functions after shifting them with corresponding travel times at different stations. Then, I compute the median absolute deviation (MAD) of the network-wide stacked CC function. An initial list of detections is made by setting the threshold at ten times MAD (Chamberlain et al., 2021). I then remove the duplicate events which are detected by multiple templates. Only the detection with the highest MAD is retained if more than one detection occurred within 12 s (same as the length of S waveforms) of each other. As was done before, I assign the same travel times and location of their best-matching template to these newly detected events.

Finally, I take the following procedures to calculate the magnitude for newly detected events and refine the initial catalog. I compute the magnitude for the newly detected events following the method used in Zhai et al. (2021c). I assume a factor of 1 difference in magnitude between the newly detected event and its template is equal to a ratio of 10 difference in the median value of peak absolute amplitudes (Peng and Zhao, 2009). Before calculating the median value, I remove the amplitude ratios of waveform pairs that do not meet these two criteria: (1) the maximum CC coefficient greater or equal to 0.5; and (2) the SNR of the newly detected *P* or *S* wave greater or equal to 4. To compute the CC value, I use a 2 s window starting from 0.5 s before the *P* wave and allowing 1 s shift, and a 2.5 s window starting 0.5s before the *S* wave and allowing a 1.25 s shift. The

window length is narrower than it in the previous step of MFT detection but is somewhat similar to it in a relocation (e.g. HypoDD (Waldhauser and Ellsworth, 2000)) when measuring differential travel times and CC coefficient. Last, I further clean up the initial catalog based on the magnitude and their SNR and CC coefficient. For any newly detected event with magnitude M and best-matching template with magnitude M_{temp}, I remove it if it does not have at least n ($n=3(M-M_{temp}+1)$ and $n\geq1$) stations with clear waveforms that satisfy the two criteria mentioned above (Zhai et al., 2021c). This is because if a newly detected event was much larger than its template, it should be observed on more stations with clear waveforms. Otherwise, it should be already in the standard catalog or a false detection (Ross et al., 2019b). This criterion is based on the visual examination of hundreds of newly detected events in the initial catalog. For example, a newly detected event with a factor of 1 in magnitude larger than its template requires 6 stations; a factor of 2 difference in magnitude requires 9 stations; a factor of 3 difference in magnitude requires 12 stations. Figure 5.4 shows an example of a newly detected M0.9 event on April 20, 2008, and its best-matching template, an M1.9 event occurring at 103 km depth on August 30, 2005. The stacked CC value is 0.26, corresponding to 36.9 times MAD. This suggests that the newly detected event is likely a true IDEQ occurring at nearly the same region.

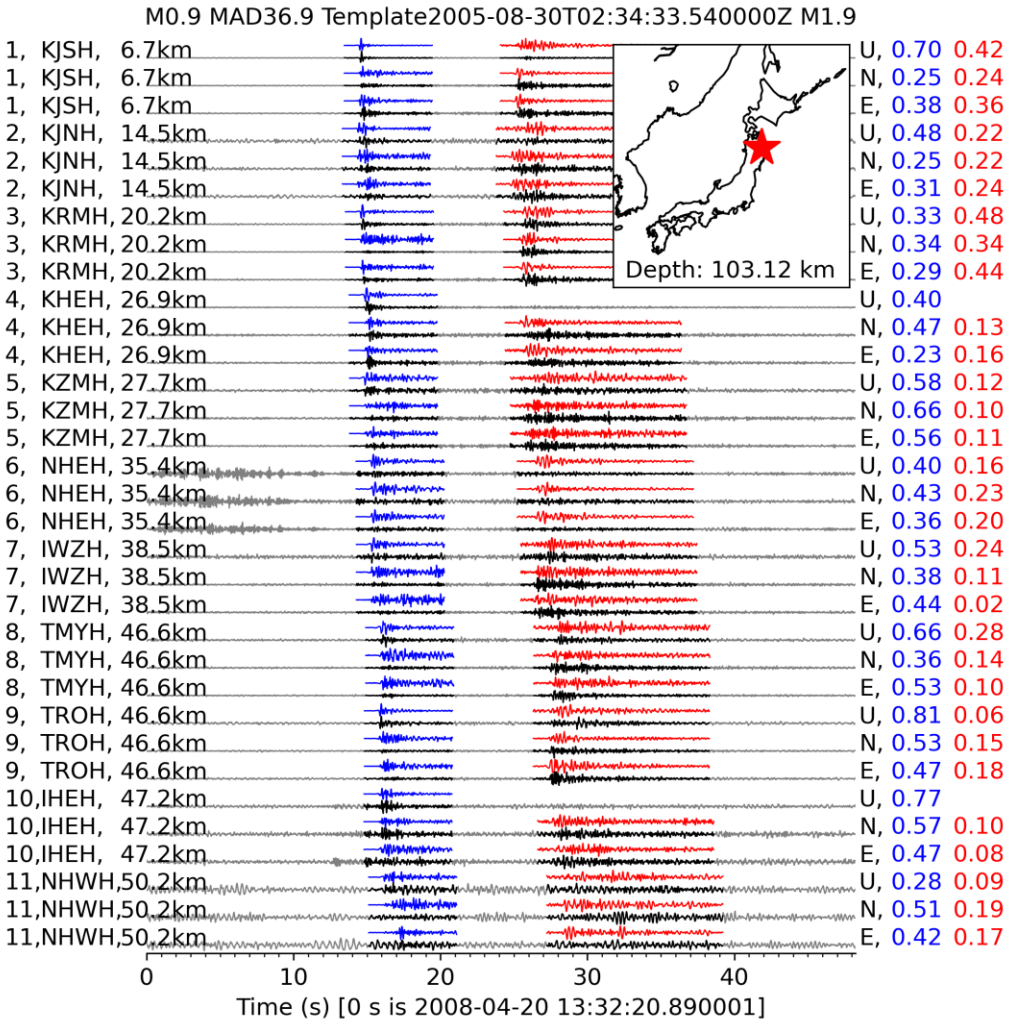

Figure 5.4 An example of a newly detected IDEQ on April 20, 2008, and its template event occurred on August 30, 2005. The blue and red waveforms are the *P* wave and *S* wave of the template, respectively. The black sections on the gray continuous waveforms are the newly detected events. The station label, station name, and event-station epicentral distance are on the left of this figure. The component name and the cross-correlation (CC) values on this component of the *P* wave and *S* wave are on the right of this figure. The inserted map at the upper right corner shows the location of this template (red star).

5.6 Results

5.6.1 Analysis of IDEQs Before and After the 2011 M9 TOEQ

I obtain the final MFT catalog following the steps mentioned above. This MFT catalog consists of 48,882 IDEQs including the newly detected event and the templates in the wide-target zone (Figure 5.1) between one year before the one year after the 2011 TOEQ. This number is about a 3.5-fold increase compared to the standard JMA catalog (14,030) in the same time window. Most of the newly detected IDEQs are after the TOEQ in the low-magnitude range (Figure 5.6). As shown in Figure 5.6a, there is a clear lack of low-magnitude events (e.g., between magnitude 0-1) in the JMA catalog within several months following the TOEQ. However, the MFT catalog only misses events in magnitude 0-1 in about one month right following the mainshock (Figure 5.6a). The total number of IDEQs for all magnitudes in the MFT catalog is about a two-fold and a four-fold increase compared to the JMA catalog in the one year before and after the TOEQ (Figure 5.6b), respectively. At the larger magnitude range ($M2+$) where the catalogs are more complete (Figure 5.5), the MFT catalog shows about a two-fold increase in the one year after the TOEQ, and the increase decayed with time (Figure 5.6c). In comparison, except for a small spike in late April 2011, the JMA catalog did not show a clear increase of IDEQs following the TOEQ for seismicity below 70 km depth.

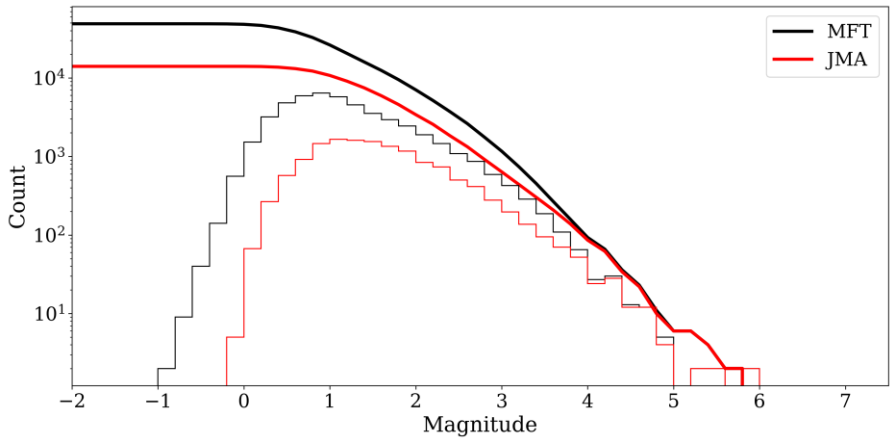

Figure 5.5 Frequency-magnitude distribution of IDEQs listed in the JMA (templates) catalog and the matched filter technique (MFT) catalog inside the wide-target zone (Figure 5.1).The bold smooth curves on the top are the cumulative frequency-magnitude distribution.

Figure 5.7 and Figure 5.8 show the location of IDEQs before and after the TOEQ in the JMA catalog and the MFT catalog. The seismicity rate of IDEQs increased after the TOEQ between the latitude range of N35-N39 in both upper and lower planes (Figure 5.7). The majority of the IDEQs in the upper plane occurred at a relative shallower depth (e.g., 70-100 km) between the latitude range of N36^o-N39^o (Figure 5.8a-b). In the lower plane, most of the relatively shallow IDEQs occurred in the area north of N37^o. Note there was a cluster of IDEQs beneath 200 km around N36^o (Figure 5.8). Based on the depth distribution of IDEQs shown in Figure 5.2a, the IDEQs in upper and lower planes merge together beneath about 180 km depth. Therefore, it is a challenge to distinguish the upper-plane and lower-plane IDEQs in this cluster. Nevertheless, I simply use the boundary (i.e., the plate-interface depth of 35 km, Figure 5.3) to show them separately in the Figure 5.7-Figure 5.9.

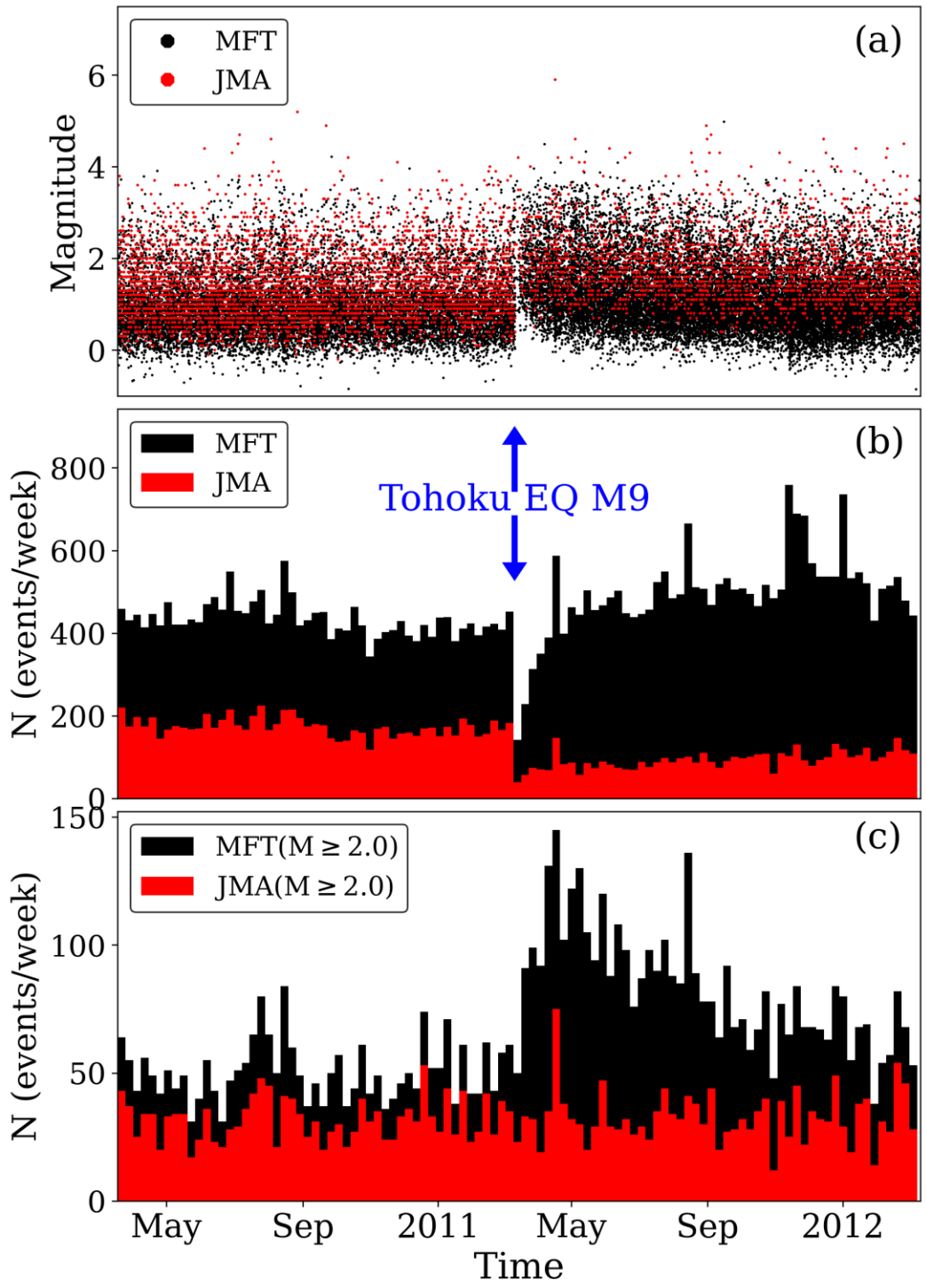

Figure 5.6 The magnitude-time distribution and seismicity rate of IDEQs before and after TOEQ inside the wide-target zone. (a) Magnitude-time distribution of IDEQs in the JMA catalog (templates) and the matched filter technique (MFT) catalog. The red and black dots represent the JMA catalog and the MFT catalog, respectively. (b) Seismicity rate of all the IDEQs with any magnitude. (c) Seismicity rate of the IDEQs with a magnitude above 2.

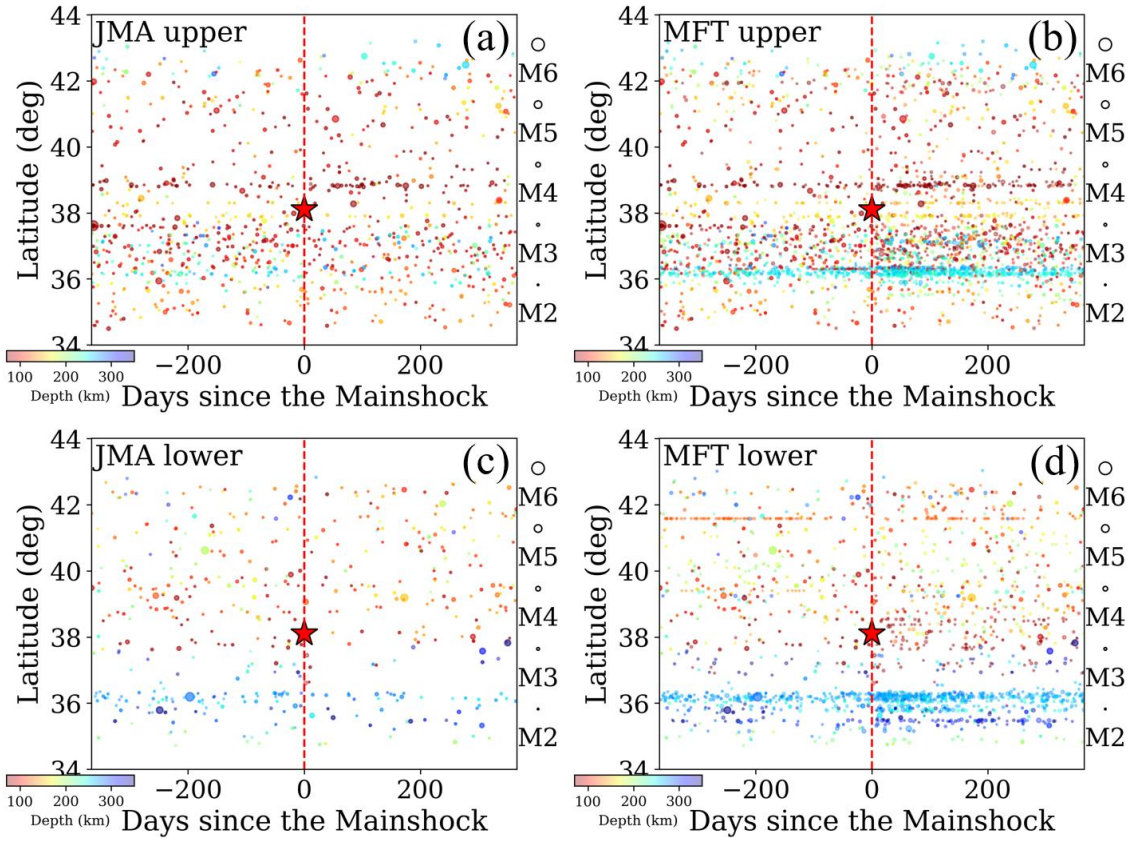

Figure 5.7 Earthquake location distribution one year before and one year after the 2011 M9 TOEQ. (a) IDEQs in the upper plane in the JMA catalog. (b) IDEQs in the upper plane in the MFT catalog. (c) IDEQs in the lower plane in the JMA catalog. (d) IDEQs in the lower plane in the MFT catalog. The red star and dashed line mark the TOEQ.

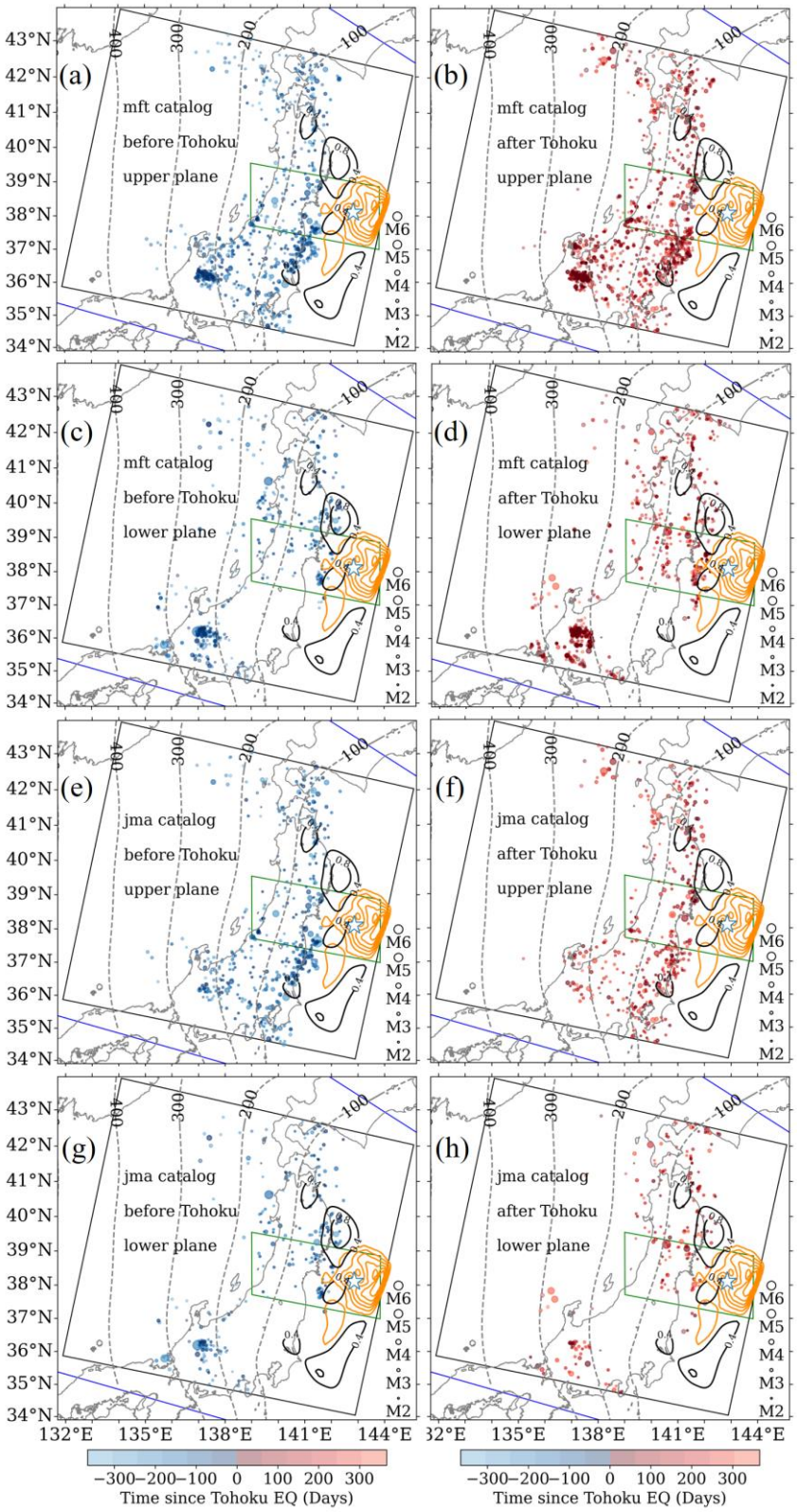

Figure 5.8 Map of IDEQs one year before and one year after the 2011 M9 TOEQ. (a) IDEQs before the TOEQ in the upper plane in the MFT catalog. (b) Similar to (a) but

after the TOEQ. (c)-(d) Similar to (a)-(b) but in the lower plane. (e)-(h) Similar to (a)-(d) but in the JMA catalog. All the dots in this figure are the IDEQs sized by their magnitudes and colored by their time. The dashed gray lines are the contours of the depth in the Slab2 model. The black-line zone the wide-target zone in this study same as it in Figure 5.1. The green-line zone is the narrow-target same as it in Figure 5.1. The orange and black lines are the contours of coseismic slip from Iinuma et al. (2012) and postseismic slip from Iinuma et al. (2016), respectively.

Next, I use the β-value statistic (Matthews and Reasenberg, 1988; Pankow and Kilb, 2020) to quantify the seismicity rate change of IDEQs before and after the TOEQ. This method is commonly used to study dynamic earthquake triggering (Hill and Prejean, 2015). A typical significance threshold of the absolute β-value is around 2 (Habermann, 1981; Reasenberg and Simpson, 1992; Pankow and Kilb, 2020), although this threshold might slightly vary in different regions and time windows (Prejean and Hill, 2018; Pankow and Kilb, 2020; Fan et al., 2021; Li et al., 2022a). Because this method can measure the seismicity rate change between a pre-window and a post-window, it fits this study well. In this study, the pre-window and the post-window are the one year before and after the TOEQ, respectively. The β-value is calculated as:

$$\beta = \frac{N_{post} - N_{pre} * (T_{post}/T_{pre})}{\sqrt{N_{pre} * (T_{post}/T_{pre})}} \qquad 5.1$$

where T_{pre} and T_{post} are the window lengths for counting the number of earthquakes in the pre-mainshock window (N_{pre}) and the post-mainshock window (N_{post}), respectively. Because the pre-mainshock and post-mainshock windows are the same, equation 5.1 can be further simplified as:

$$\beta = \frac{N_{post} - N_{pre}}{\sqrt{N_{pre}}} \qquad 5.2$$

I divide the wide-target zone (Figure 5.1) into 40 × 40 km grids. For each grid, I compute its β-value for the IDEQs in the upper plane and lower plane, respectively. Figure 5.9 shows the β-value maps using the JMA catalog and the MFT catalog. The β-values of some grids are higher than the threshold of 2 mentioned above. Note the color scale shown in Figure 5.9 is clipped at the maximum absolute value of 8 for plotting purposes. These β-value maps again show that the increase of IDEQs after the TOEQ is in both the upper and lower planes in the wide-target zone (Figure 5.9b&d, see the definition of different zones in Figure 5.1). When compared with the JMA catalog results, the MFT catalog shows a more widespread seismicity rate increase zone (red region, see the color map in Figure 5.9). The absolute value and total area of the seismicity rate increase in the upper plane are larger than that in the lower plane (Figure 5.9 and Figure 5.10). There are some isolated spots with a seismicity rate increase in the lower plane (Figure 5.9d). Comparing the distribution of IDEQs in the upper plane after the TOEQ (Figure 5.9b) and the postseismic slip distribution in Iinuma et al. (2016), I observe a spatial separation of postseismic slips of TOEQ and the increasing IDEQs activity following the TOEQ. For example, the significant seismicity rate increase zone (red region in Figure 5.9b) at latitude ranges of N36^{o}-N37.5^{o} and N38^{o}-N39^{o} at shallow depth (70-100 km) in this study can match the gap of the postseismic slip distribution in Iinuma et al. (2016) in the same regions.

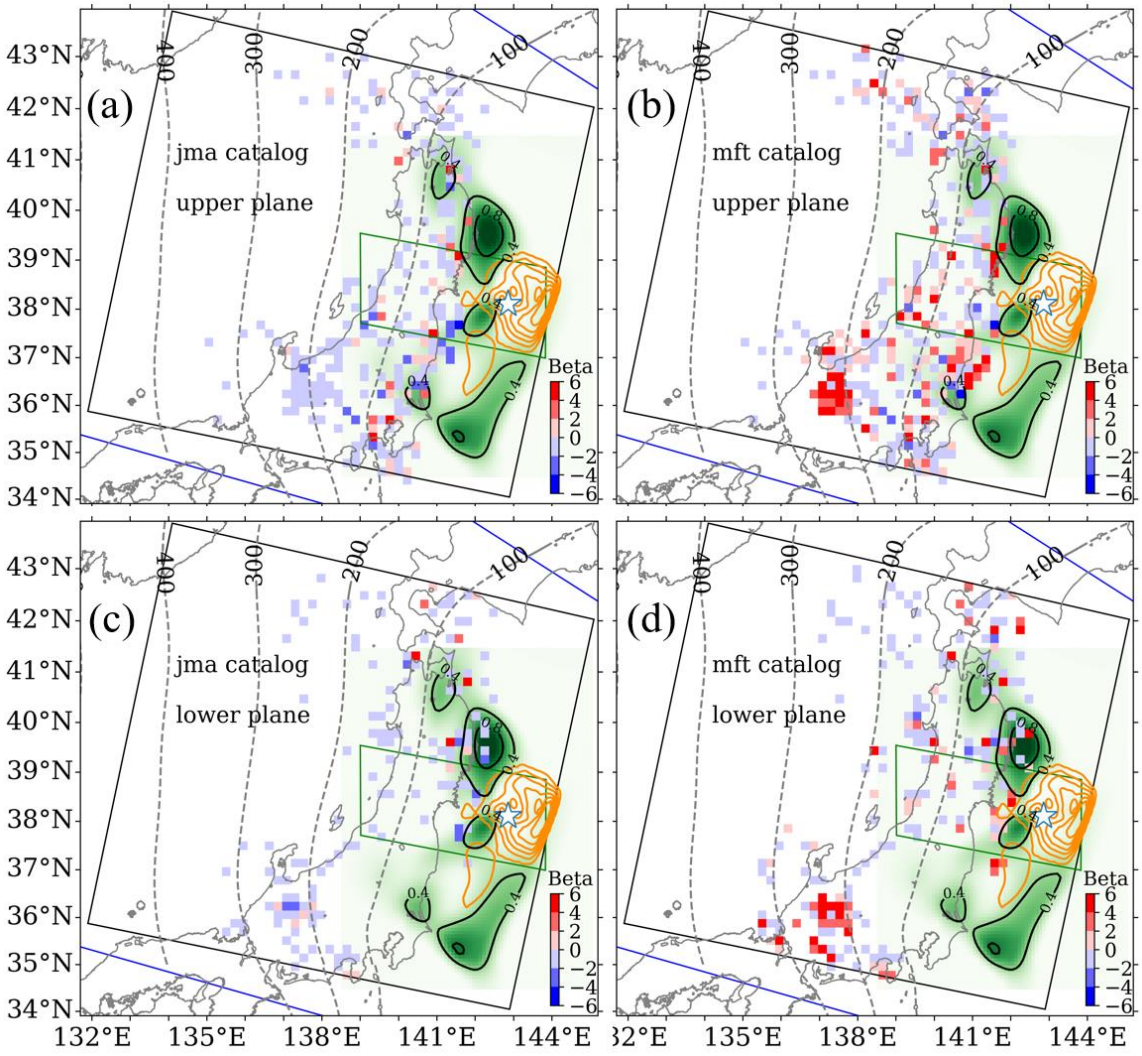

Figure 5.9 Beta map of IDEQs comparing one year after to one year before the 2011 M9 TOEQ. (a) Beta map of IDEQs in the upper plane in the JMA catalog. Red and blue mean increase and decrease of IDEQs after the TOEQ, respectively. (b) Similar to (a) but in the MFT catalog. (c)-(d) Similar to (a)-(b) but in the lower plane. The dashed gray lines are the contours of the depth in the Slab2 model. The black-line zone the wide-target zone in this study same as it in Figure 5.1. The green-line zone is the narrow-target same as it in Figure 5.1. The orange lines are the contours of coseismic slip from Iinuma et al. (2012). The black lines are the contours of the green-colored postseismic slip from Iinuma et al. (2016).

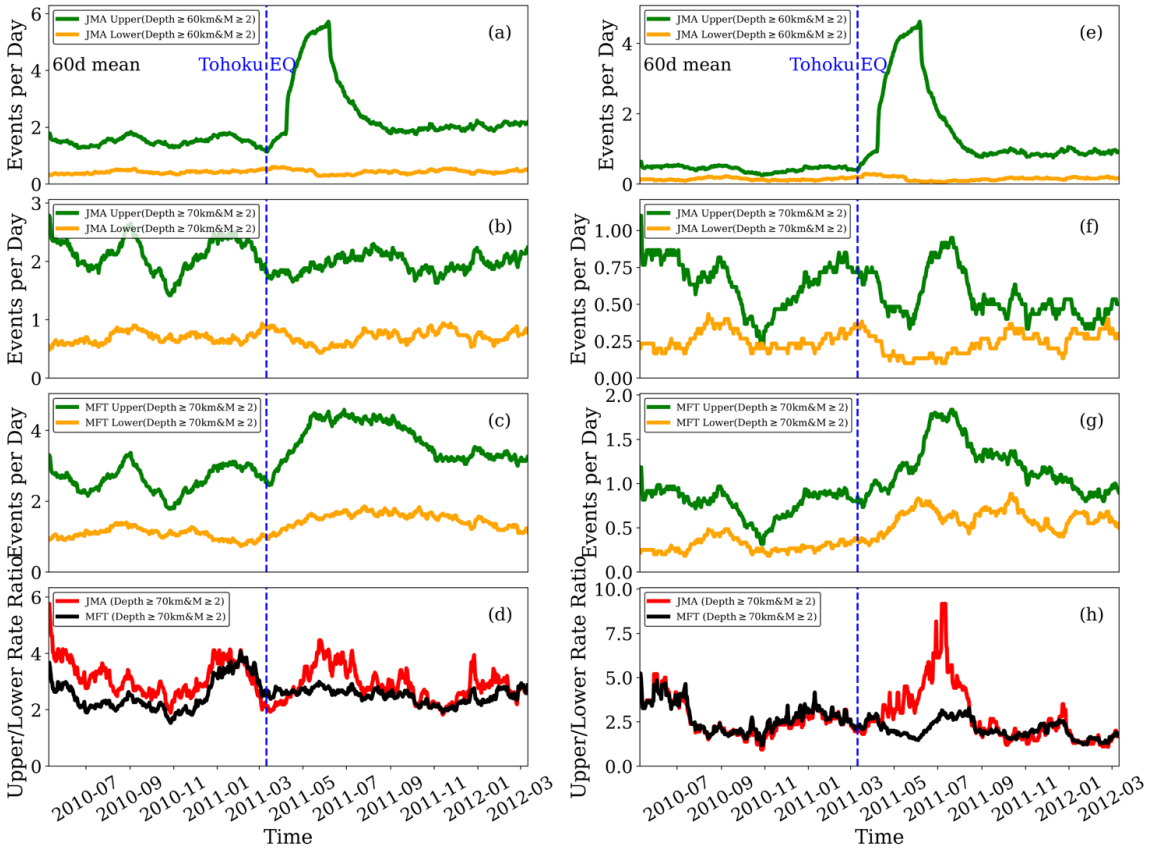

Figure 5.10 Seismicity rate of IDEQs before and after the TOEQ. (a) Seismicity rate of IDEQs inside the wide-target zone (Figure 5.1) with magnitude above 2 between 60 and 180 km depth in the JMA catalog. The green and orange curves represent the upper plane and the lower plane, respectively. (b) Similar to (a) but based on the JMA catalog beneath 70-km depth. (c) Similar to (a) but based on the MFT catalog beneath 70-km depth. (d) The ratio of the seismicity rates of the upper and lower planes, termed the upper-to-lower ratio. The red and black curves represent the JMA and the MFT catalog, respectively. (e) Seismicity rate of IDEQs inside the narrow-target zone (Figure 5.1) with magnitude above 2 between 60 and 180 km depth in the JMA catalog. (e) -(h) are similar to (a)-(d). (e)-(h) are the IDEQs inside the narrow-target zone, but (a)-(e) are the IDEQs inside the wide-target zone (Figure 5.1).

Figure 5.10 show that the newly built MFT catalog does not contain a significant increase in the rate of IDEQs prior to the TOEQ. Following the TOEQ, analysis based on the MFT catalog shows a significant increase in the rate of IDEQs in both upper and lower planes beneath 70 km depth, but without a significant increase in the upper-to-lower ratio. Similar results of the increase in the upper plane seismicity rate have been reported in

Delbridge et al. (2017) based on the JMA catalog. To directly compare the results with the results in Delbridge et al. (2017), I also show the results in the narrow-target zone (Figure 5.8, Figure 5.9, and Figure 5.10g) which is the same as the zone in Delbridge et al. (2017). There are two key differences in the results between Delbridge et al. (2017) and this study. The first one is the depth range of the increase of the seismicity rate. I can reproduce the rate increase in the upper plane reported in Delbridge et al. (2017) using the IDEQs in the JMA catalog depth beneath 60 km (Figure 5.10e). But if I exclude the IDEQs between 60 and 70 km in the JMA catalog, I cannot observe any significant increase (Figure 5.10f). This means that the depth range most responsible for the change reported in their study is only at 60-70 km depth. Based on the newly built MFT catalog, I can also observe a clear seismicity rate increase after the TOEQ beneath 70 km depth. Another key difference is the upper-to-lower ratio of seismicity rate following the Tohoku earthquake. I do not find any increase in the upper-to-lower ratio of seismicity rate reported in their study using the MFT catalog.

5.6.2 Analysis of IDEQs around Ten M5+ IDEQ Mainshocks

To obtain more detailed information on the foreshock and aftershock properties of IDEQs in the study region, I perform the MFT detection to build a new catalog for each of the ten M5+ IDEQ mainshocks between 2004-2018 at 70-350 km depth. These ten mainshocks are selected by following these criteria. First, I find a spatial range where an IDEQ mainshock should clearly belong to either the upper plane or the lower plane. Based on the visual assessment of the distribution in the study region (Figure 5.2a), I set the depth range as 80-180 km and the distance from an IDEQ to the boundary between the upper and lower planes (i.e., the plate-interface depth of 35 km) greater than 5 km (Figure 5.3). Next,

I sort the IDEQs in the JMA catalog between 2004 and 2018 by their magnitudes on the upper and lower planes, respectively. Finally, I select the five largest IDEQs on each plane (Figure 5.1a, Figure 5.3c, and Table 5.1). Note I also check these selected events to make sure any event is not another event's aftershock based on the space-time distance between them (Chu and Beroza, 2022). Note that the time and location information in Table 5.1 is from the JMA catalog, but the *Mw* is from the U.S. Geological Survey (USGS). The minimum magnitude of selected mainshocks on both planes is the same, *Mw*5.1. After selecting these ten *M*5+, I follow the steps mentioned in Section 5.5.2 to build the MFT catalog for the ten days starting from three days before to seven days after each mainshock.

The aftershocks of a given IDEQ mainshock in this section are defined as the IDEQs occurring within the mainshock's aftershock radial extent and time duration. I take the empirical relations of the aftershock radial extent and time duration in Chu and Beroza (2022), which are fitted using the IDEQs listed in the JMA catalog in Japan. The aftershock radial extent and time duration are functions of the mainshock's magnitude. For example, they are 5 km and 26 days for the magnitude 5 IDEQ mainshock; they are 14 km and 141 days for a magnitude 6 IDEQ mainshock.

Figure 11 shows the magnitude-time distributions for the ten target sequences. The MFT catalog shows that there are two types of mainshocks in terms of aftershock productivity on both upper and lower planes. One type has relatively high aftershock productivity (e.g., Figure 5.11b on the upper plane and Figure 5.11h on the lower plane). The other has relatively low aftershock productivity (e.g., Figure 5.11d on the upper plane and Figure 5.11i on the lower plane). For the first type which already shows its high aftershock productivity in the JMA catalog, I do detect more foreshocks and aftershocks in

the MFT catalog. However, for the second type which shows its low aftershock productivity in the JMA catalog, I detect few additional foreshocks and aftershocks in the MFT catalog.

Table 5.1 Ten *M*5+ IDEQ mainshocks.

Plane	Mw	Time	Latitude	Longitude	Depth	Label
Upper	5.5	2015-07-10T03:32:51.270	40.35	141.56	88.01	a
Upper	5.5	2014-06-15T02:31:42.150	39.40	141.11	93.90	b
Upper	5.1	2018-05-07T05:00:48.420	39.60	141.16	98.11	c
Upper	5.1	2006-02-01T20:35:53.060	35.76	140.00	101.02	d
Upper	5.6	2007-08-22T16:26:23.420	41.97	140.80	121.81	e
Lower	5.1	2008-10-30T00:48:40.720	38.05	141.73	86.30	f
Lower	5.1	2009-10-10T17:42:48.490	41.72	142.23	91.83	g
Lower	6.8	2008-07-24T00:26:19.690	39.73	141.64	108.08	h
Lower	5.8	2008-04-17T04:19:36.800	39.04	140.23	165.86	i
Lower	5.3	2009-08-24T14:26:16.690	41.06	140.24	171.90	J

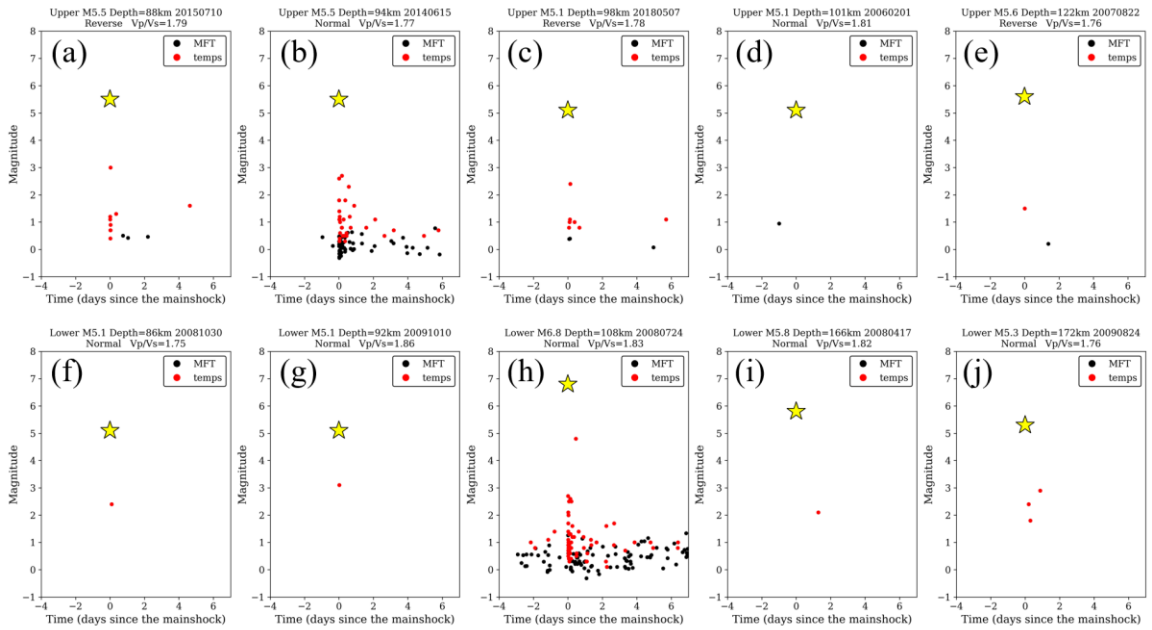

Figure 5.11 Magnitude-time distribution around the ten M5+ IDEQ mainshocks. Their locations are shown in Figure 5.1a and Figure 5.3d. (a)-(e) are the five mainshocks in the upper plane. They are sorted by depth. (f)-(j) are the five mainshocks in the lower plane. They are also sorted by depth. In this figure, the yellow stars are the mainshocks. The red dots and black dots represent the JMA (templates) catalog and the MFT catalog, respectively. The Vp-Vs ratio data is from the 3D velocity model in Matsubara et al. (2019).

5.7 Discussion

5.7.1 IDEQs Before and After the 2011 M9 TOEQ

In this study, I detected several times more IDEQs that are not listed in the JMA catalog, especially in the one year following the *M*9 TOEQ. However, it is still challenging to fill in the small triangle-shaped gap between the magnitude 0-1 range in a few weeks right following the TOEQ (Figure 5.6a). Such a gap exists because small events were buried by the coda of the TOEQ and its large aftershocks at shallow depth (Kagan, 2004; Peng et al., 2006; Peng and Zhao, 2009; Yao et al., 2017; Ross et al., 2019a). The MFT helps to improve the detection capability of those small-magnitude IDEQs, but it cannot

detect all of them shortly following the TOEQ. As aftershocks of TOEQ decayed with time following Omori's law (Omori, 1894), the detection capability of small-magnitude IDEQs also improved (Figure 5.6).

The newly built MFT catalog does not show a significant increase in IDEQs prior to the TOEQ. This observation is different from the results in Bouchon et al. (2016) but matches the finding of a follow-up study (Delbridge et al., 2017). Based on the observed precursory signal, Bouchon et al. (2016) proposed the deep part of the slab was stretched and started to plunge into the mantle before the TOEQ. Such a plunge implies an increase in the downdip tensional normal stress on both the upper and lower planes of the double seismic zone (Delbridge et al., 2017). It is well known that the background stress state in the Japan subduction zone is downdip compression in the upper plane and downdip extension in the lower plane, respectively (Hasegawa et al., 1978b; Fujita and Kanamori, 1981). The opposite stress state in the upper plane and the lower plane is caused by the unbending of the slab at this intermediate-depth range (Engdahl and Scholz, 1977). Given the opposite stress state, a decrease in the rate of IDEQs in the upper plane and an increase in the rate of IDEQs in the lower plane would be expected if there was an increase in downdip tensional normal stress in the double seismic zone (Delbridge et al., 2017). But neither the MFT catalog nor the JMA catalog shows any statistically significant changes in seismicity in both planes before the TOEQ.

Following the TOEQ, the newly built MFT catalog shows a significant increase in the rate of IDEQs in both upper and lower planes beneath 70 km depth, but without a significant increase in the upper-to-lower ratio. The TOEQ was a megathrust event occurring on the slab surface. Therefore, I expect an increase in downdip compressional

shear stress at depth after the TOEQ (about 10-100 kPa reported in Hu et al. (2016)), which is exactly the opposite of the downdip tensional normal stress caused by the possible slab plunge at depth prior to the TOEQ (Bouchon et al., 2016). I expect the downdip compressional stress at the slab interface would result in an increase in both the compressional stress in the upper plane and the tensional stress in the lower plane of the double seismic zone. The opposite effects are somehow similar to the effects caused by the unbending process which results in the opposite stress state in both planes. Therefore, I expect an increase in the rate of IDEQs following the TOEQ in both planes, although they have opposite background stress states. I also expect the upper-to-lower ratio of IDEQs would not show a significant change following the TOEQ. The observations based on the newly built MFT catalog can match these expectations well.

As mentioned in Section 5.6.1, an increase in the upper plane seismicity rate was reported in Delbridge et al. (2017) based on the JMA catalog. However, there are two key differences in the results between Delbridge et al. (2017) and this study. Their proposed increase in the upper-to-lower ratio cannot match the expectation mentioned above. In addition, even with an assumption of an opposite stress response (a decrease in the tensional stress instead of an increase) in the lower plane after the TOEQ, I should expect to observe a significant decrease in the seismicity rate in the lower plane following the TOEQ. However, such a significant decrease is not reported either in their study with the JMA catalog or the study with the MFT catalog. As mentioned in Section 5.6.1, I observed a spatial separation of postseismic slips of the TOEQ and the promoted IDEQs activity following the TOEQ. This result is somewhat similar to the anti-correlation between afterslip and aftershock locations on the subduction zone interface following the 2012 M7.6

Nicoya, Costa Rica earthquake (Hobbs et al., 2017). However, it is worth noting that the inverted afterslip following the TOEQ was mostly resolved on the subduction zone interface, while most of the IDEQs occurred within the subduction slab, rather than on the interface. Hence, their exact relationship is still not clear. A detailed Coulomb stress analysis is needed to better understand the spatial distribution and triggering relationship between the TOEQ mainshock rupture, its afterslip, and the IDEQs.

5.7.2 IDEQs around Ten M5+ IDEQ Mainshocks

The aftershock deficiency of IDEQs has been reported in previous studies (Kagan and Knopoff, 1980; Prozorov and Dziewonski, 1982; Frohlich, 1987; Nyffenegger and Frohlich, 2000; Wiens, 2001; Persh and Houston, 2004). In addition, Chu and Beroza (2022) reported that over half of the IDEQs, but only 3 percent of shallow earthquakes, have no aftershocks in Japan, including the study region. Chu and Beroza (2022) also systematically analyzed several possible parameters contributing to the aftershock productivity of IDEQs in Japan using the JMA catalog. Therefore, I did not perform the same detailed statistical analysis using the newly built catalog, which only consists of ten mainshocks in a spatially limited region. Instead, I focus on whether the reported lack of aftershocks is real, or due to the aforementioned completeness issue in the JMA catalog. A case study of the 2015 *Mw* 7.5 Hindu Kush earthquake at 213 km depth highlights such concerns (Li et al., 2018a). In that study, more than 15 times more aftershocks than listed in the standard global catalog are detected using the MFT. Based on the results mentioned in Section 5.6.2, the conclusion is the JMA catalog is relatively complete above the magnitude two except right following the 2011 *M*9 TOEQ. Hence it can be directly used to analyze the aftershock productivity of IDEQs in Central and Northeastern Japan.

5.7.3 Limitations of Current Results and Planned Future Study

In this section, I briefly summarize the limitations in the current results and planned future studies to address these potential problems. First, a well-known limitation of the template matching method used in this study is that it can only detect events that are spatially close to the templates. This means that if the spatial coverage of templates is limited, the detection results based on these templates could be biased or incomplete. To address this potential issue, I do not only use aftershocks of these mainshocks as templates. Instead, I use all the 90,214 IDEQs listed in the JMA catalog between 2004 and 2018 in the entire study region as the templates. Second, the results shown in this study are based on the original MFT catalog, which consists of both background IDEQs and clustered events (i.e., triggered by previous IDEQs). In the future, I will decluster the MFT catalog first, and then analyze the behavior of background IDEQs before and after the TOEQ. Third, I plan to compute the Coulomb stress change on the upper and lower plans following the TOEQ to quantify its static stress perturbations on the IDEQs. Last, I only analyze ten *M*5+ IDEQ mainshocks in this study. In the future, I may perform the MFT detection for more IDEQ mainshocks with slightly lower magnitude in the study region.

5.8 Conclusions

I build a more complete earthquake catalog of IDEQs in Central and Northeastern Japan for the two years starting the one year before the 2011 *M*9 TOEQ and ten days starting from three days before each of ten *M*5+ IDEQ mainshocks. For the TOEQ, the number of IDEQs in the newly built MFT catalog is a 3.5-fold increase compared to the standard JMA catalog. The newly built MFT catalog does not show any significant increase

in IDEQs in the two months prior to the TOEQ. Following the TOEQ, the newly built MFT catalog shows a significant increase in the rate of IDEQs in both upper and lower planes beneath 70 km depth, but without a significant increase in the upper-to-lower seismicity ratio. I also observe a spatial separation of postseismic slips of the TOEQ and the promoted IDEQs activity following the TOEQ. These results suggest that like seismic activity at shallow depth, IDEQs in the double seismic zone also respond to stress perturbations generated by the 2011 M9 TOEQ, highlighting a sustained seismic hazard associated with these intraslab events in the next decades. In the future, I will decluster the MFT catalog first, and then analyze the behavior of background IDEQs before and after the TOEQ. For the ten $M5+$ IDEQ mainshocks, I detect more foreshocks and aftershocks, but I do not have any clear pattern on which sequences are more productive than others. In addition, the results show that the JMA catalog is relatively complete above the magnitude two except right following the 2011 $M9$ TOEQ, and hence can be directly used to analyze the aftershock productivity of IDEQs in Central and Northeastern Japan.

CHAPTER 6. CONCLUSION

In my Ph.D. work, I developed/applied machine-learning and template-matching techniques in several regions to improve earthquake catalogs by detecting microearthquakes directly from continuous seismic waveforms and calculating their focal mechanisms. Using the improved high-resolution catalogs, I then analyzed the microseismicity behavior and their responses to a super wet typhoon in Taiwan and a large megathrust earthquake in Japan. Here I briefly summarized the conclusions of the previous chapters.

In CHAPTER 2, I developed a generic deep-learning network (NPC) for P-wave first-motion polarity classification based on CNN and attention mechanism. I trained it with global earthquake datasets of ~3.5 million first motion polarity picks. I also applied the Guided Grad-CAM tool to help visualize how the NPC makes a prediction, which can be used to further clean up the picking results. Based on its performance on test datasets, I expect the pre-trained model can be used in future studies to determine P-wave first-motion polarity for natural earthquakes, hydraulic fracturing events, and acoustic emissions.

In CHAPTER 3, I built a more complete template-matching earthquake catalog for Taiwan spanning seven months before and twelve months after the 2009 typhoon Morakot, which brought the highest rainfall in southern Taiwan in the past 60 years. The number of events in the newly built catalog is a seven-fold increase compared to the standard CWBSN catalog. I observe no significant seismicity changes that can be attributed to surface changes induced by typhoon Morakot, but a clear reduction in seismicity rate near the typhoon's low-pressure eye center in northeastern Taiwan during the typhoon passed by.

Additional study is needed to verify whether such a drop was by random chance or caused by a stress perturbation due to the low-pressure typhoon system.

In CHAPTER 4, using the high-resolution relocated template matching catalog built in CHAPTER 3, I observed clear aftershocks migrating as the logarithm of time along with depth for several mainshock-aftershock sequences in Taiwan. This result is similar to previous studies that showed similar logarithmic along-strike migration of aftershocks, suggesting that these aftershocks were primarily driven by afterslip following the mainshock ruptures. In addition, I found that the minimum magnitude of early aftershocks of the 2010 M6.4 Jiashian earthquake (as well as two other M6+ events) was not mainly modulated by earth tides but was observationally limited by the daily fluctuations in the noise level. Finally, I also found a clear spatiotemporal coincidence between high-aftershock-productivity earthquake sequences and the occurrence of nearby SSEs in northeastern Taiwan, suggesting that SSEs can help to further promote aftershock generation. These results suggest that SSEs may temporally increase the productivity of nearby aftershock sequences, and hence potential seismic hazard in a region that host both SSEs.

In CHAPTER 5, I build a more complete template-matching intermediate-depth earthquakes (IDEQs) catalog in the Central and Northeastern Japan subduction zone before and after the 2011 magnitude (M) 9 Tohoku-Oki earthquake (TOEQ) and ten. M>5 mainshocks along the double seismic zones. The number of IDEQs in the newly built catalog is a 3.5-fold increase compared to the standard JMA catalog. I did not find any significant increase in IDEQs in the two months prior to the TOEQ. However, I found a significant increase in the rate of IDEQs in both upper and lower planes of the double

seismic zone beneath 70 km depth following the TOEQ. These results suggest that similar to seismic activity at shallow depth, IDEQs in the double seismic zone also respond to stress perturbations generated by the 2011 M9 TOEQ, highlighting a sustained seismic hazard associated with these intraslab events in the next decades.

APPENDIX A. INVESTIGATING THE IMPACTS OF A WET TYPHOON ON MICROSEISMICITY: A CASE STUDY OF THE 2009 TYPHOON MORAKOT IN TAIWAN BASED ON A TEMPLATE MATCHING CATALOG

This appendix provides additional detailed information for CHAPTER 3, including how to access some datasets, one earthquake catalog, three tables, and fourteen figures to support the main text. Table A.1 shows the format of a matched-filter detected earthquake catalog in Taiwan from January 1, 2009, to July 31, 2010. Latitude: 21°-26°N, Longitude: 119°-124°E. This catalog (MFT catalog) includes its subsets, the relocation catalog (MFT-reloc catalog), and the focal mechanism catalog (MFT-FM catalog).

The earthquake catalogs (MFT, MFT-reloc, and MFT-FM catalogs) used in this study are available through the Mendeley Data (https://dx.doi.org/10.17632/cgys3svzrp.1 (Zhai et al., 2021)). The original Wu earthquake catalogs (Wu et al., 2008a; Wu et al., 2008b) and the 3D velocity model of Taiwan (Wu et al., 2007) used in this study are archived in the Seismological Lab at National Taiwan University (http://seismology.gl.ntu.edu.tw/download.htm, last accessed November 2021). Some figures are plotted by using the Generic Mapping Tools (Wessel et al., 2013), Version 5.4.1 (https://www.generic-mapping-tools.org/, last accessed November 2021). Seismic waveform data are archived at the Central Weather Bureau Seismic Network (https://gdmsn.cwb.gov.tw/signup.php, last accessed November 2021), which is open to all researchers after signing up an account. Weather data can be freely accessed through https://e-service.cwb.gov.tw/HistoryDataQuery/ (e.g., The weather data including the daily

atmospheric pressure in August 2009 at #466910 station can be accessed through https://e-service.cwb.gov.tw/HistoryDataQuery/MonthDataController.do?command=viewMain&station=466910&stname=%25E9%259E%258D%25E9%2583%25A8&datepicker=2009-08, last accessed November 2021). The satellite image is archived in the National Aeronautics and Space Administration (NASA, https://earthobservatory.nasa.gov/images/39720/typhoon-morakot, last accessed November 2021).

Table A.1 Data format of the earthquake catalog.

Column	Information
1	EventTime
2	EventID
3	Latitude
4	Longitude
5	Depth
6	Magnitude
7	TemplateID
8	TemplateLatitude
9	TemplateLongitude
10	TemplateDepth
11	StackCC
12	MAD
13	Relocated?
14	Strike
15	Dip
16	Rake
17	R
18	FocalMechanism

Table A.2 1-D velocity used for the relocation.

Depth(km)	Vp(km/s)	Vs(km/s)	Vp/Vs
0	3.9064	2.0965	1.8633
2	4.5886	2.5934	1.7694
4	5.0475	2.9278	1.7240
6	5.1987	3.0280	1.7169
9	5.6216	3.2536	1.7278
13	5.9705	3.4506	1.7303
17	6.2501	3.6046	1.7339
21	6.5251	3.7527	1.7388
25	6.7240	3.8623	1.7409
30	7.0582	4.0494	1.7430
35	7.4786	4.2848	1.7454
50	7.9449	4.5829	1.7336
70	8.1601	4.6826	1.7426
90	8.2660	4.7950	1.7239
110	8.3696	4.8298	1.7329
140	8.4063	4.8302	1.7404
200	8.6999	5.0000	1.7400

Table A.3 Estimated Parameters of the ETAS model used in this study.

mu	A	c	alfa	p	d	q	gamma
1.00	2.16	5.79E-04	6.97E-01	1.05	6.79E-06	1.26	7.66E-01

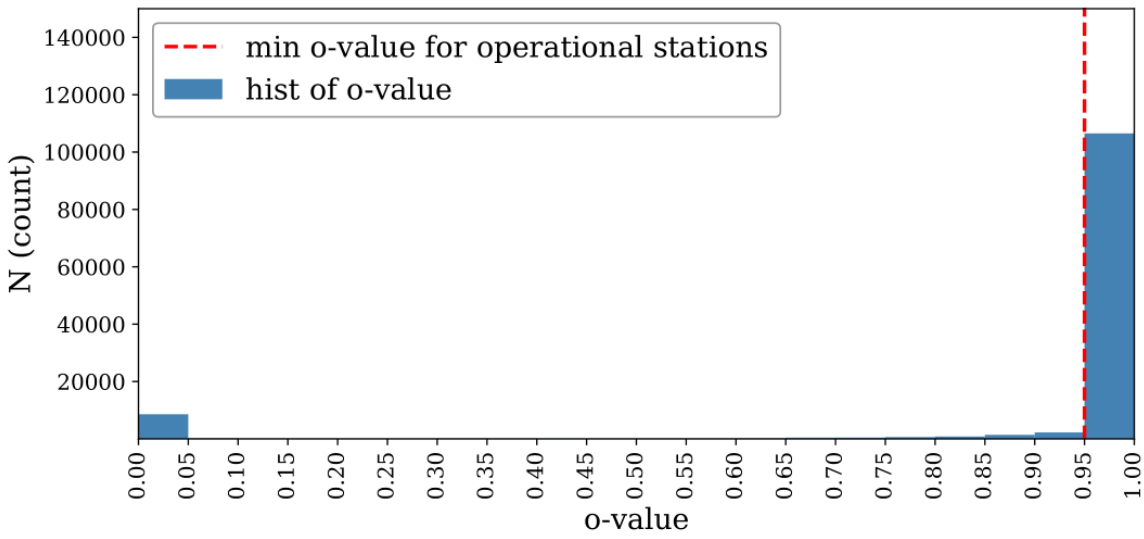

Figure A.1 The hist of o-values of all the one-day-long raw waveforms used in this study. The red dashed line is the threshold for operational stations. This is the result of *k*=10. Based on the test, the result of *k*=8 is almost the same.

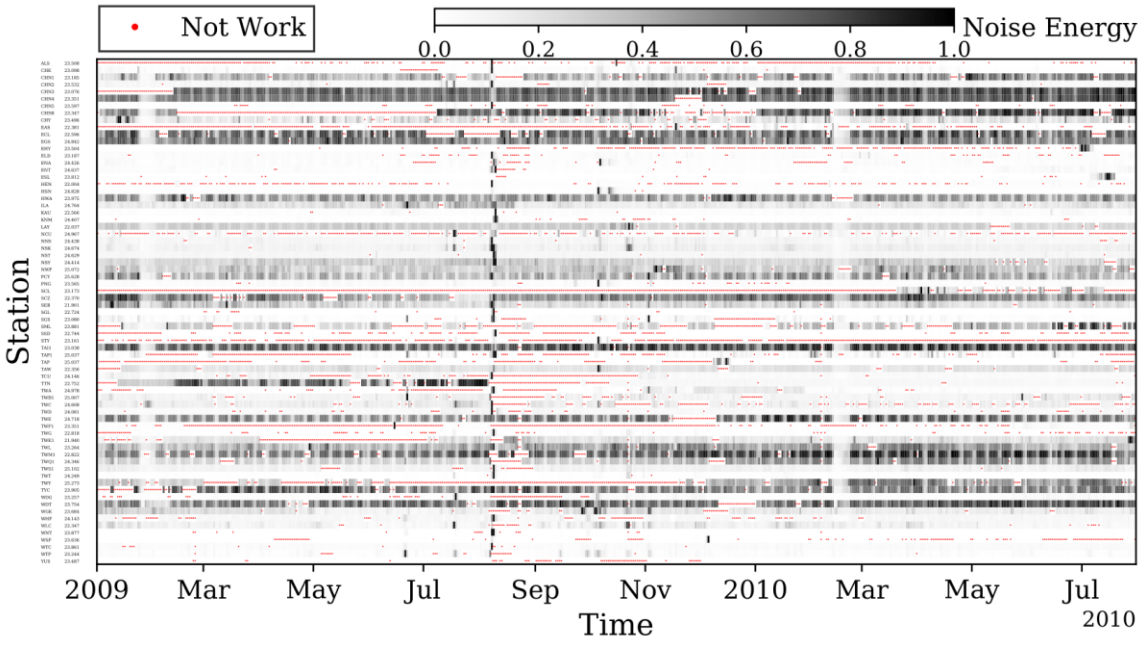

Figure A.2 The noise energy and operational status of all stations used in this study. Stations are sorted by their latitudes. The northern stations are on the top and the southern stations are on the bottom.

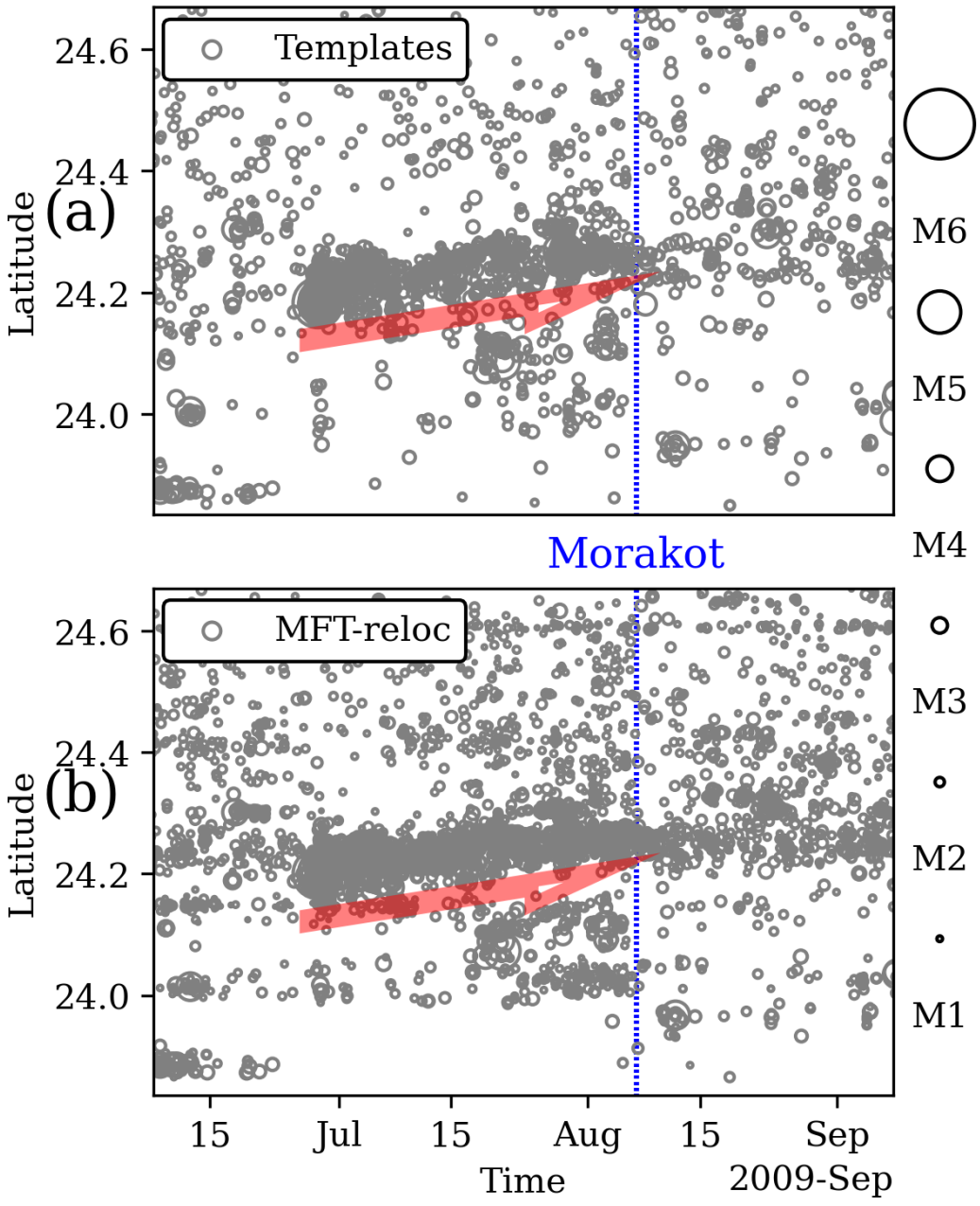

Figure A.3 The latitude-time plot of seismicity in the red-box region. (a) The full version of the latitude-time plot of seismicity in the red-box region in the Wu catalog (A zoom-in version is shown in Figure 3.9k). The blue dashed line marks August 7 2009. The red arrow marks the general migration of the seismicity. The open circles on the right outside mark earthquakes with different magnitudes. For example, "M1" means magnitude is equal to 1. (l) Similar to a but based on the MFT-reloc catalog.

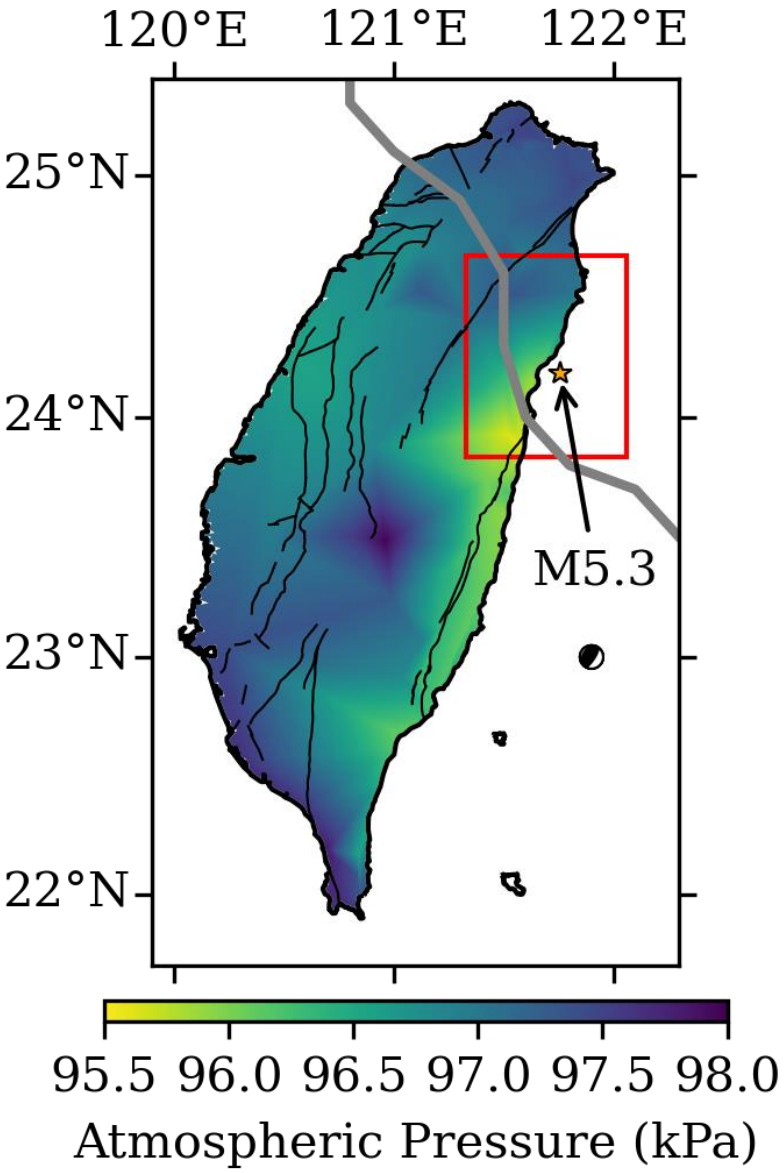

Figure A.4 The map of atmospheric pressure on August 7 2009 in Taiwan. The data is from CWB and the effect of the altitude variation is removed. The star and beach ball mark the location and focal mechanism solution of the same M5.3 earthquake in Figure 3.9a. The red box marks the zone mentioned in Section 3.5.4.

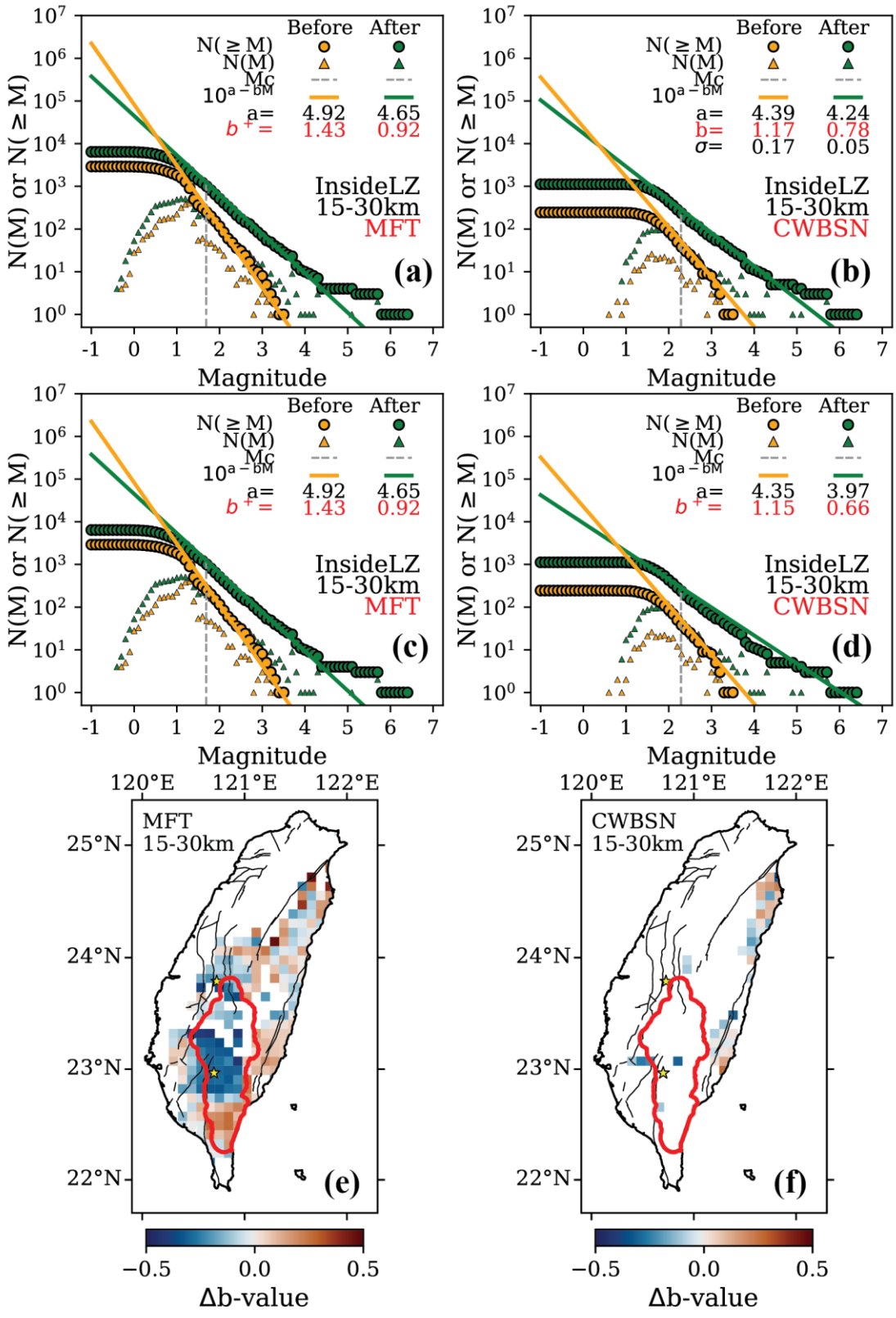

Figure A.5 Similar to Figure 3.13 but at 15-30 km depth.

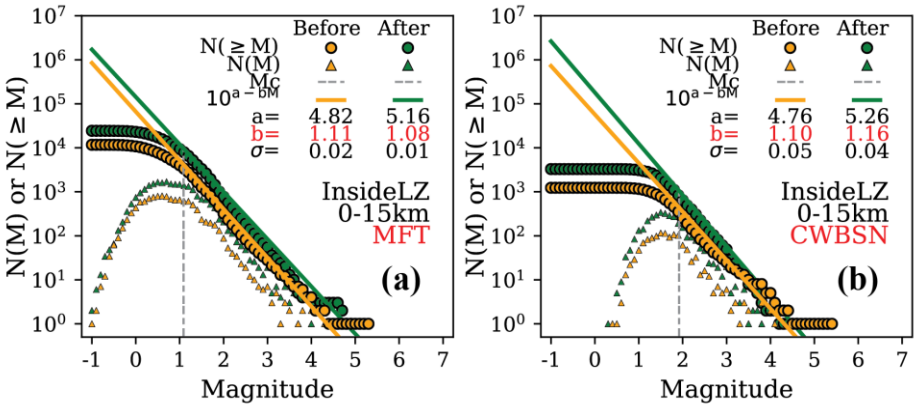

Figure A.6 Similar to Figure 3.13a&b but neglects the first 3 weeks after typhoon Morakot.

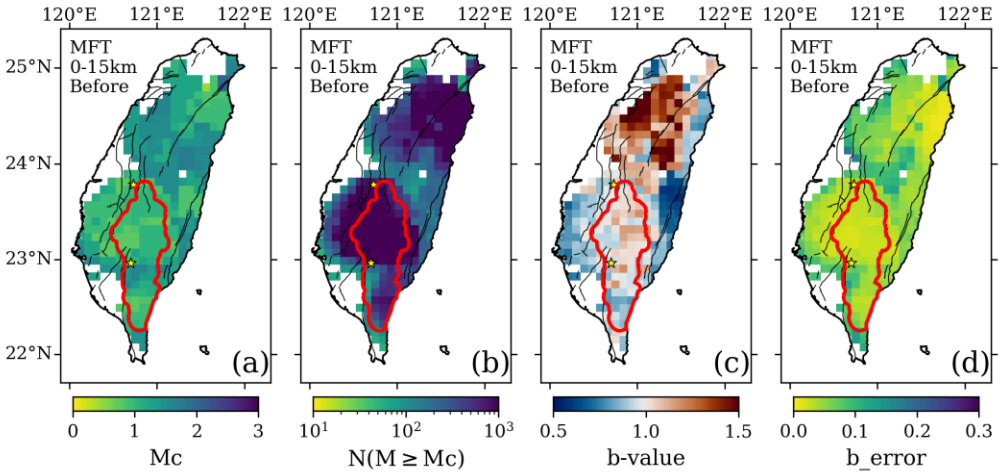

Figure A.7 The maps of *Mc* (a), number of events with M ≥ *Mc* (b), *b*-value (c), and *b*-value error (d) based on the earthquakes before typhoon Morakot (January 1 2009 – August 6 2009) at depth of 0-15 km in the MFT catalog. Black lines are the faults. The red line marks the boundary of the landslide zone (Figure 3.1). The two yellow stars are two magnitude (M) 6+ earthquakes (Figure 3.1) that occurred several months after typhoon Morakot (North: M6.0 Nantou earthquake on November 5 2009, at 24 km depth; South: M6.4 Jiashian earthquake on March 4 2010, at 22 km depth).

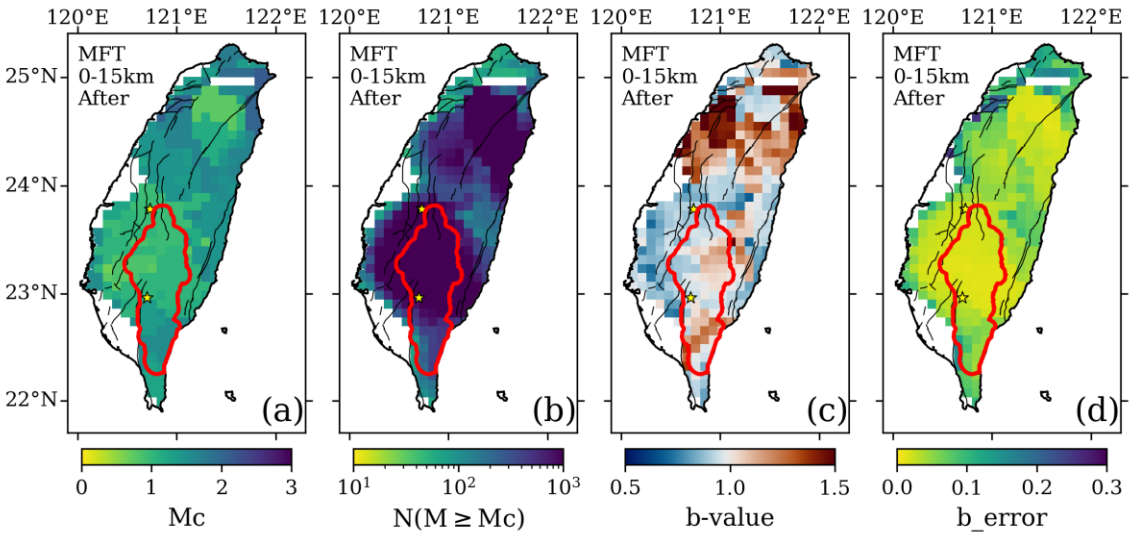

Figure A.8 Similar to Figure A.7 but this is based on the earthquakes <u>after</u> typhoon Morakot (August 6 2009 – July 31 2010) at depth of <u>0-15 km</u> in the <u>MFT</u> catalog.

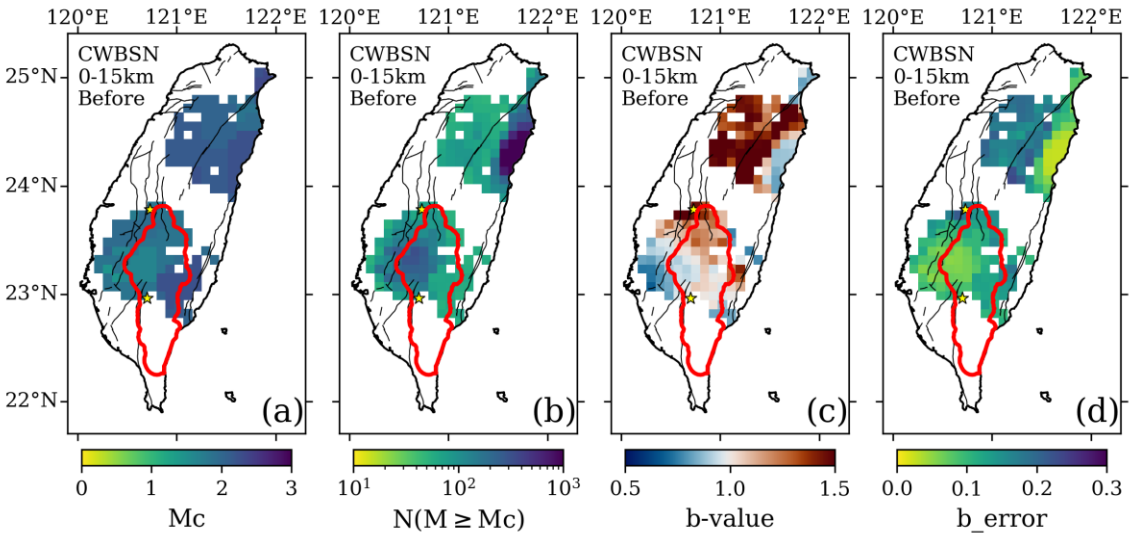

Figure A.9 Similar to Figure A.7 but this is based on the earthquakes <u>before</u> typhoon Morakot at depth of <u>0-15 km</u> in the <u>CWBSN</u> catalog.

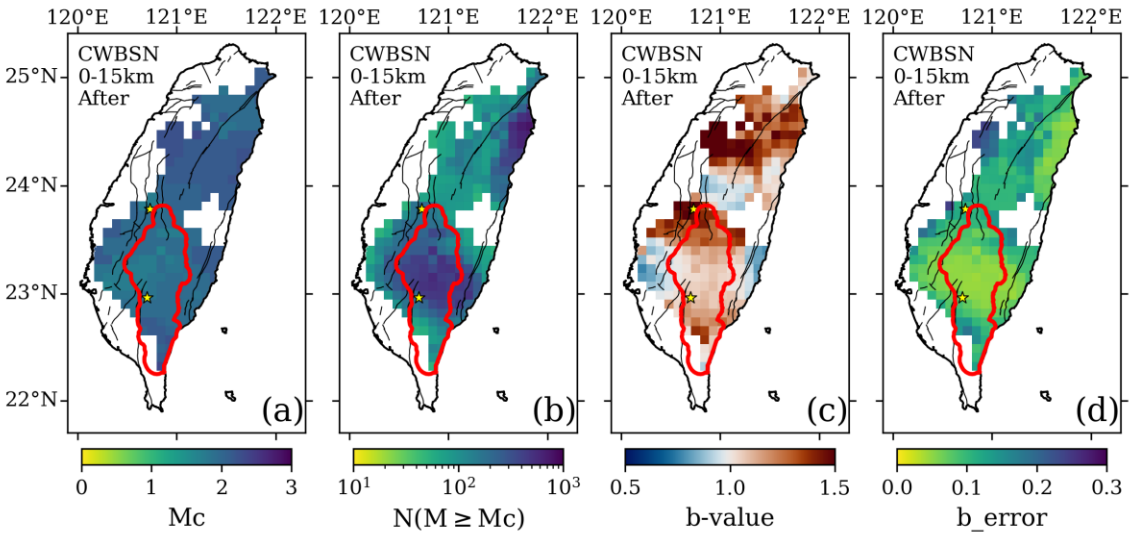

Figure A.10 Similar to Figure A.7 but this is based on the earthquakes <u>after</u> typhoon Morakot at depth of <u>0-15 km</u> in the <u>CWBSN</u> catalog.

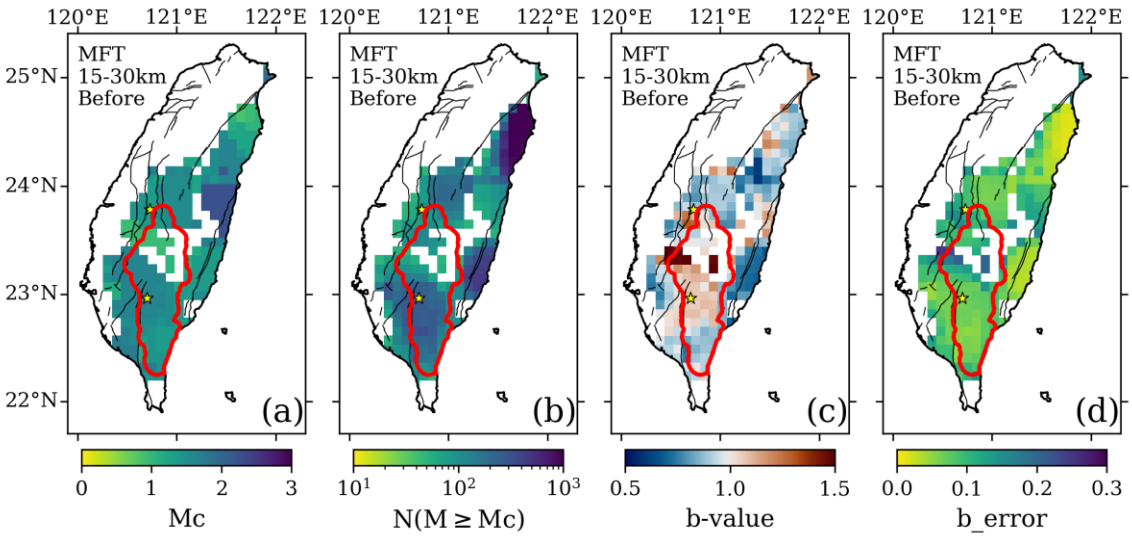

Figure A.11 Similar to Figure A.7 but this is based on the earthquakes <u>before</u> typhoon Morakot at depth of <u>15-30 km</u> in the <u>MFT</u> catalog.

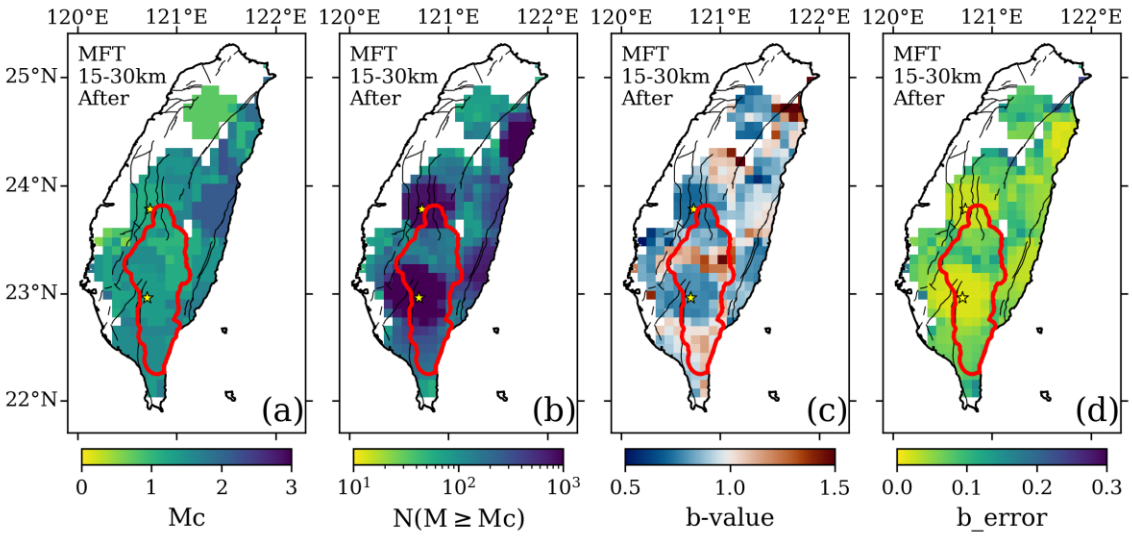

Figure A.12 Similar to Figure A.7 but this is based on the earthquakes <u>after</u> typhoon Morakot at depth of <u>15-30 km</u> in the <u>MFT</u> catalog.

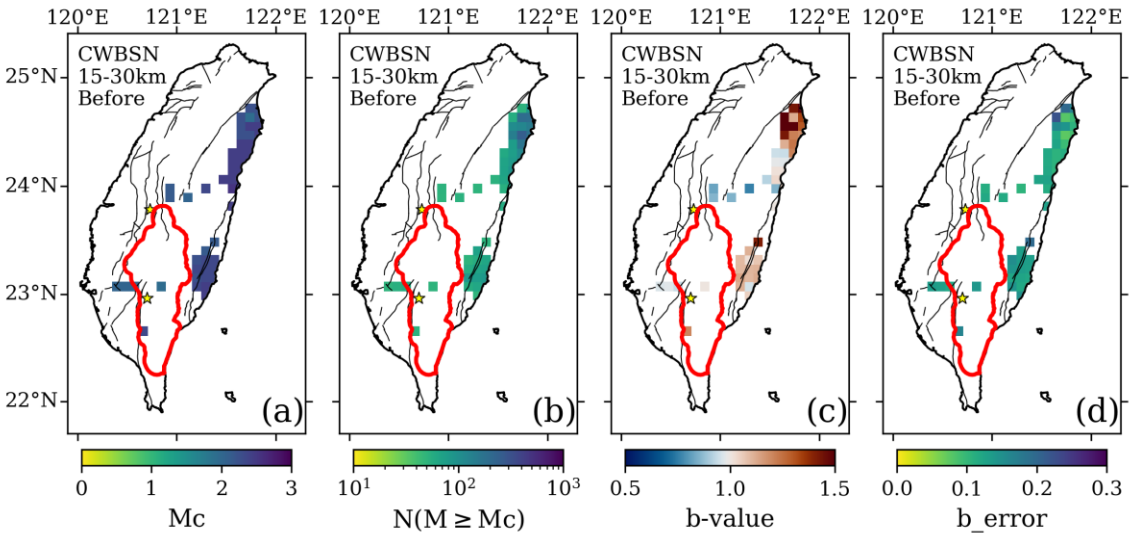

Figure A.13 Similar to Figure A.7 but this is based on the earthquakes <u>before</u> typhoon Morakot at depth of <u>15-30 km</u> in the <u>CWBSN</u> catalog.

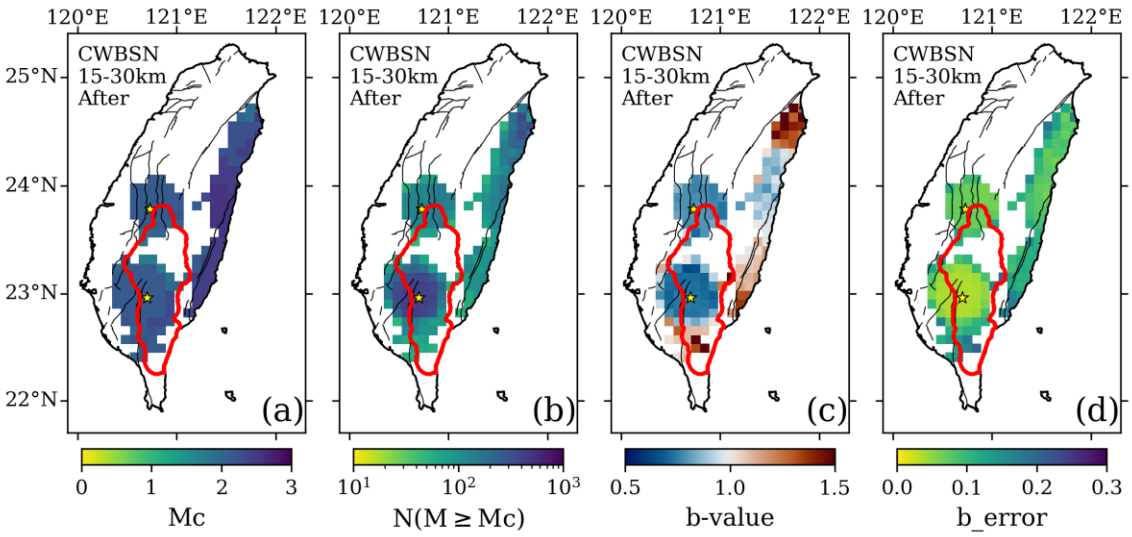

Figure A.14 Similar to Figure A.7 but this is based on the earthquakes <u>after</u> typhoon Morakot at depth of <u>15-30 km</u> in the <u>CWBSN</u> catalog.

APPENDIX B. SPATIOTEMPORAL VARIATIONS OF AFTERSHOCK SEQUENCES BETWEEN 2009-2010 IN TAIWAN REVEALED BY A HIGH-RESOLUTION RELOCATED TEMPLATE MATCHING CATALOG

This appendix provides additional information on detailed spatiotemporal variations of seismicity for CHAPTER 4.

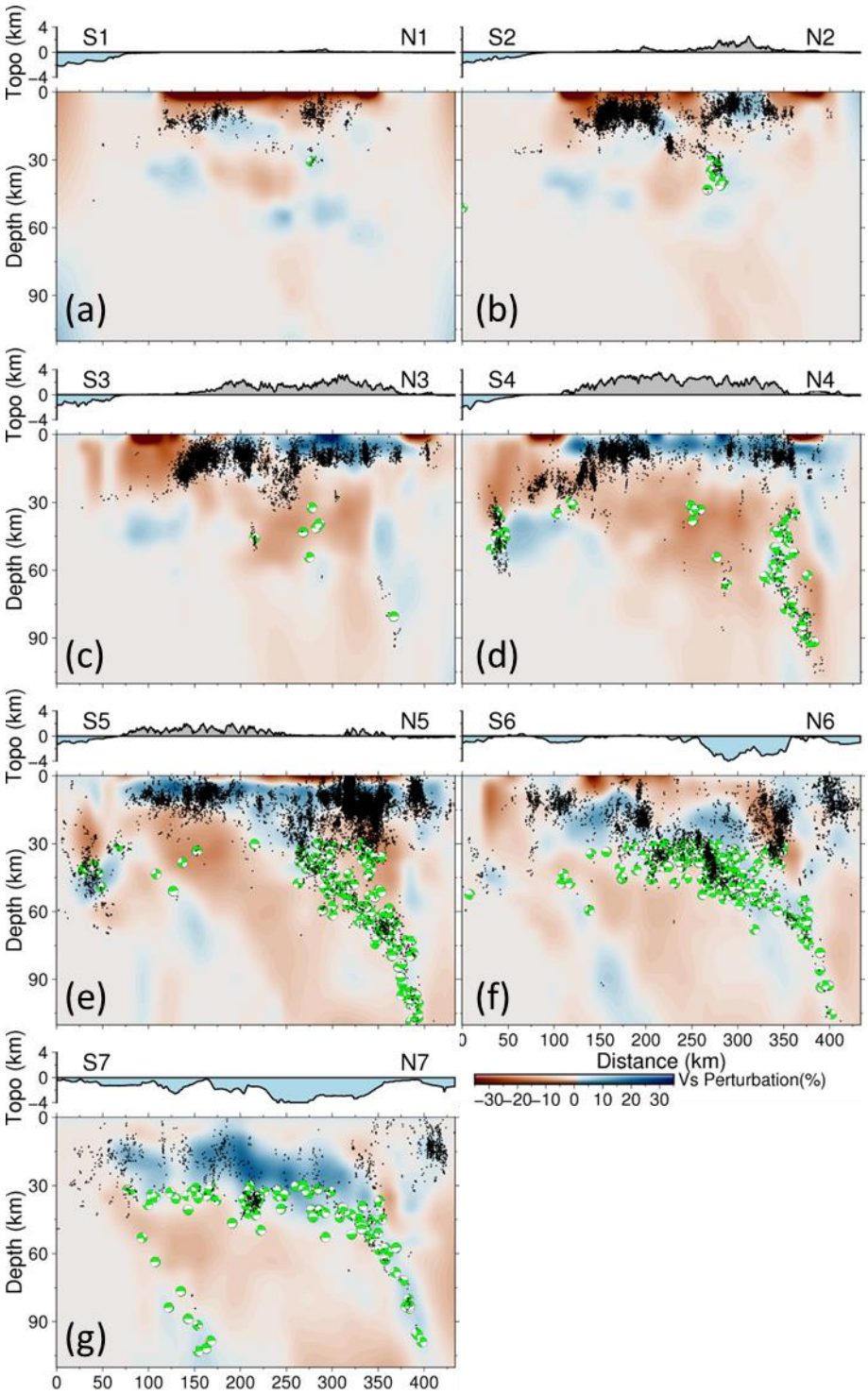

Figure B.1 MFT-reloc catalog seismicity south-north cross-sections in Taiwan as shown in Figure 4.1d. (a)-(g) are the profiles from S1-N1 to S7-N7.

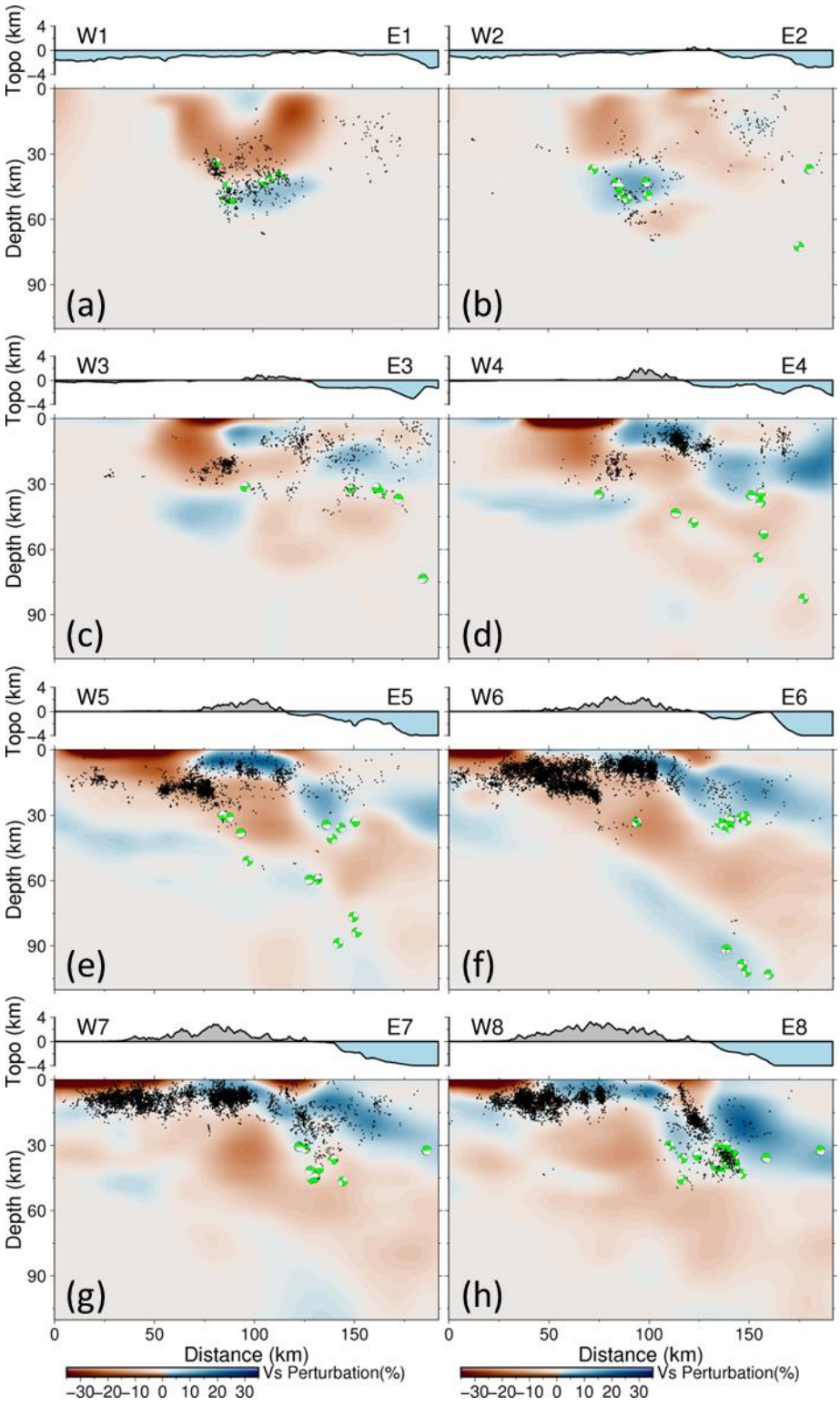

Figure B.2 MFT-reloc catalog seismicity west-east cross-sections in Taiwan as shown in Figure 4.1d. (a)-(h) are the profiles from W1-E1 to W8-E8.

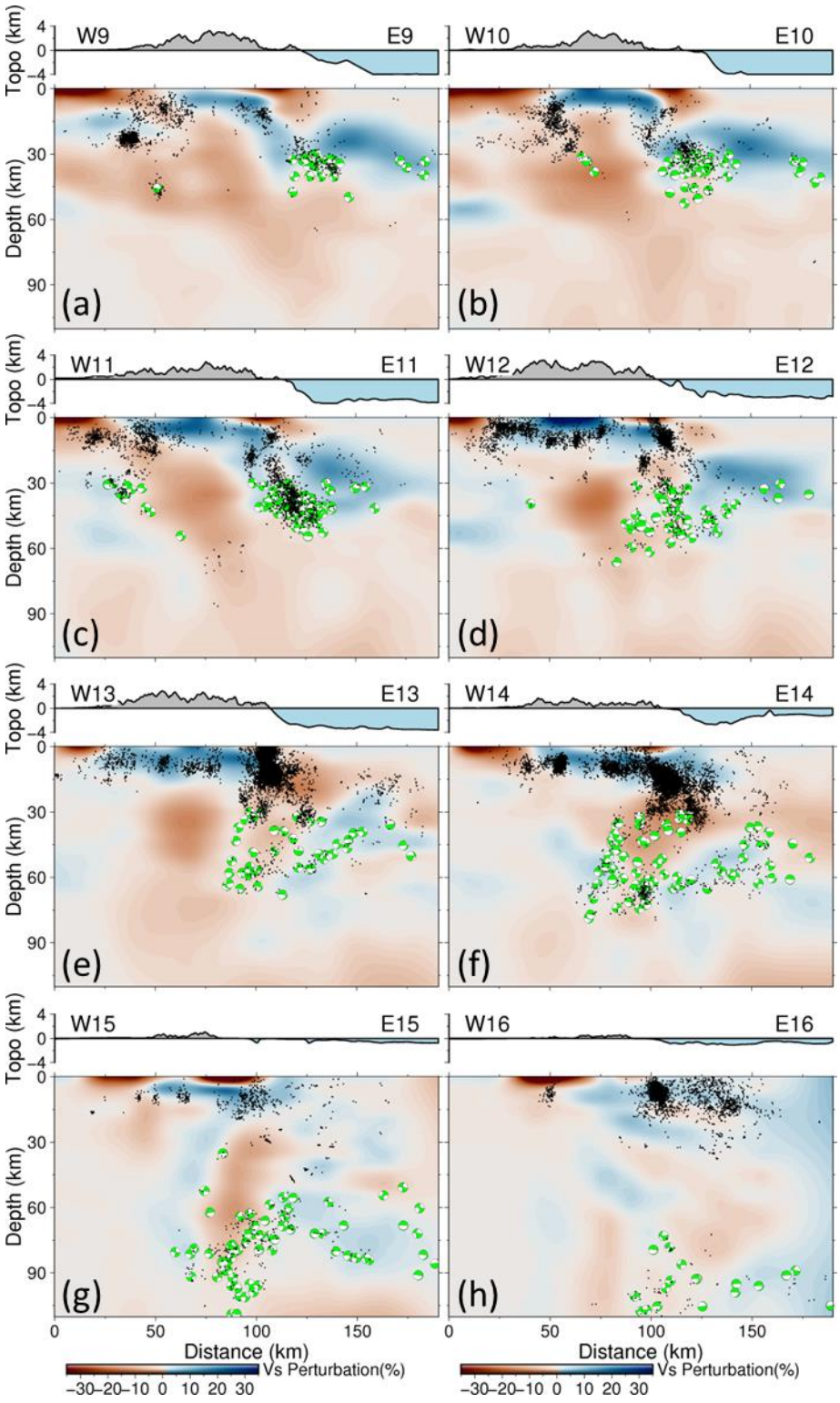

Figure B.3 MFT-reloc catalog seismicity west-east cross-sections in Taiwan as shown in Figure 4.1d. (a)-(h) are the profiles from W9-E9 to W16-E16.

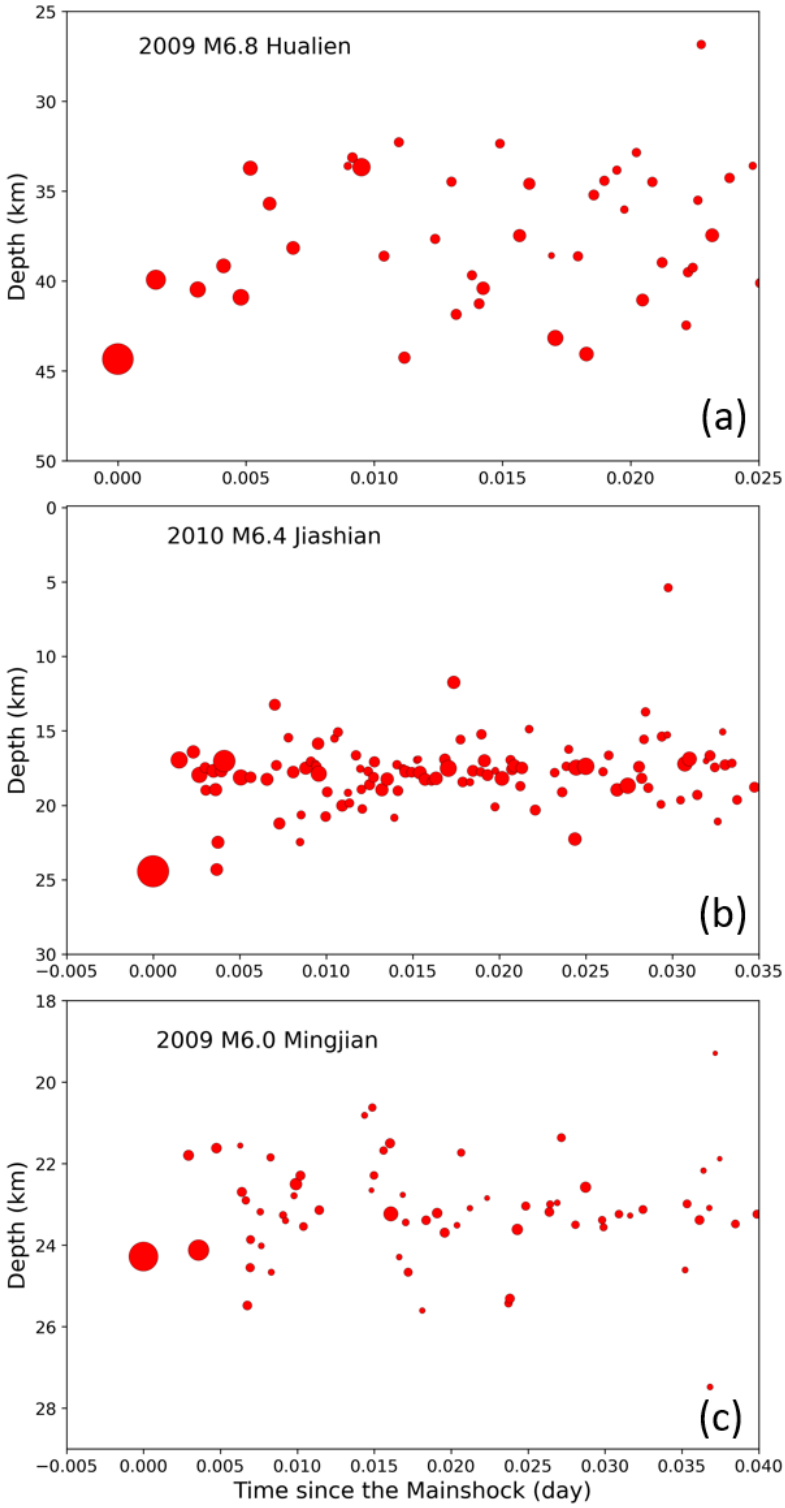

Figure B.4 Along-depth aftershock migration of three M6+ mainshock-aftershock sequences in Taiwan in linear time scale. (a) Depth of aftershocks versus their occurrence times since the mainshock in linear scale for the HLEQ. (b) Similar to (a) but for JSEQ. (c) Similar to (a) but for MJEQ.

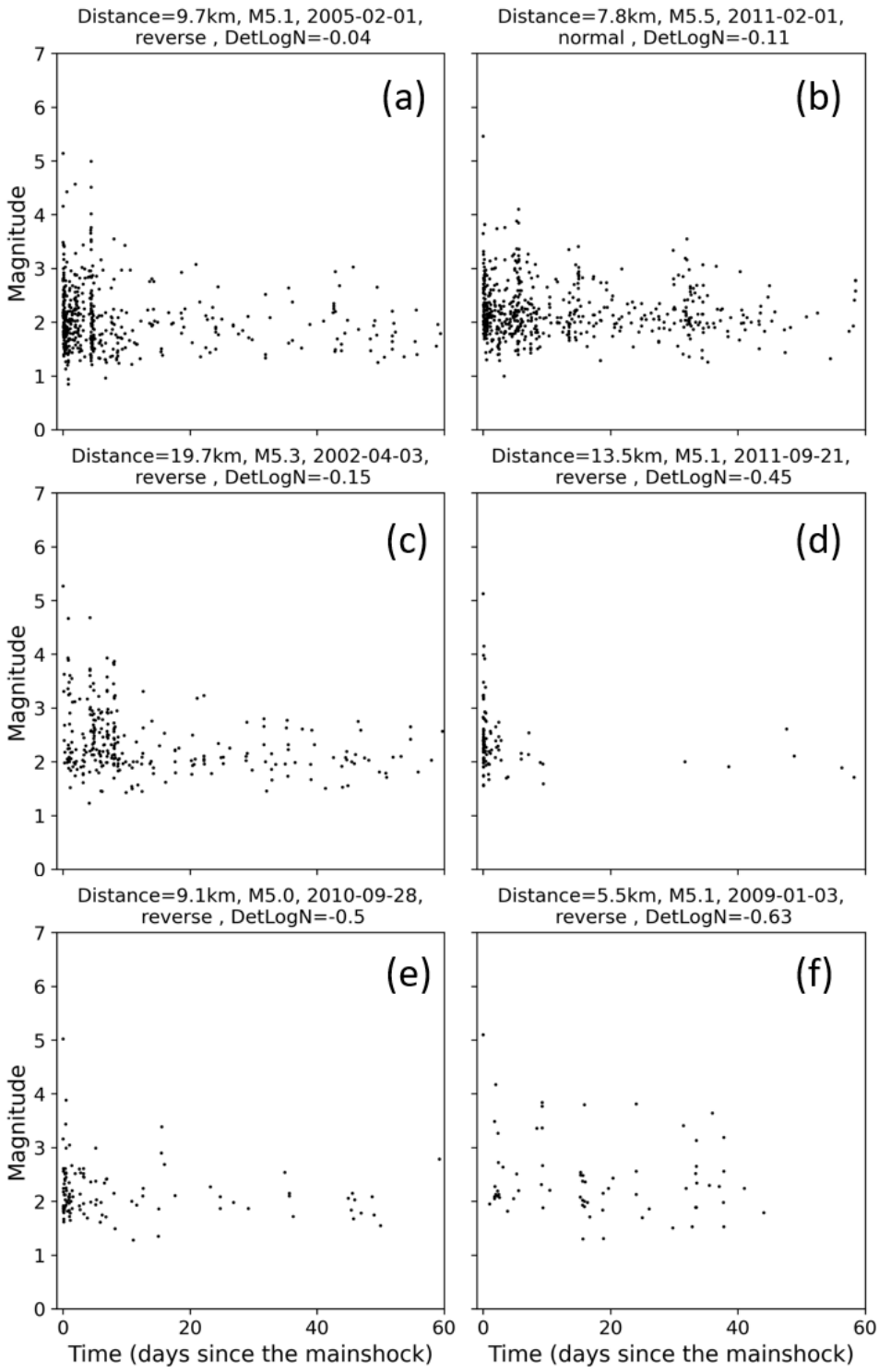

Figure B.5 Magnitude-time distribution of earthquakes in the top #5-#10 relatively high-aftershock-productivity mainshock-aftershock sequences in Table 4.1. (a)-(f) are the #5-#10 earthquake sequences in Table 4.1, respectively.

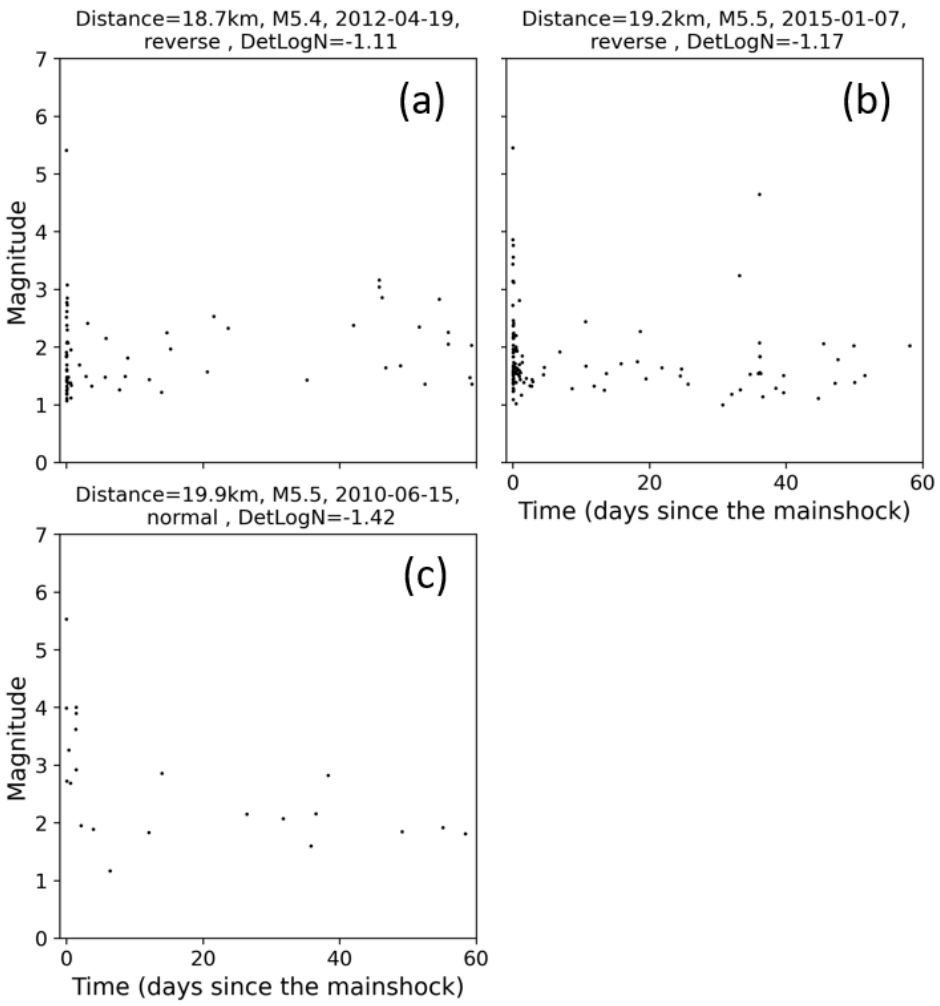

Figure B.6 Magnitude-time distribution of earthquakes in the top #11-#13 relatively high-aftershock-productivity mainshock-aftershock sequences in Table 4.1. (a)-(c) are the #11-#13 earthquake sequences in Table 4.1, respectively.

REFERENCES

Aki, K. (1965). Maximum Likelihood Estimate of b in the Formula logN= a-bM and its Confidence Limits. *Bull Earthq Res Inst Univ Tokyo, 43*(2), 237-239.

Allen, R. (1982). Automatic Phase Pickers - Their Present Use and Future-Prospects. *Bulletin of the Seismological Society of America, 72*(6), S225-S242. https://doi.org/10.1785/bssa07206b0225

Allen, R. V. (1978). Automatic Earthquake Recognition and Timing from Single Traces. *Bulletin of the Seismological Society of America, 68*(5), 1521-1532. https://doi.org/10.1785/bssa0680051521

Ariyoshi, K., Matsuzawa, T., & Hasegawa, A. (2007). The key frictional parameters controlling spatial variations in the speed of postseismic-slip propagation on a subduction plate boundary. *Earth and Planetary Science Letters, 256*(1-2), 136-146. https://doi.org/10.1016/j.epsl.2007.01.019

Asano, Y., Saito, T., Ito, Y., Shiomi, K., Hirose, H., Matsumoto, T., et al. (2011). Spatial distribution and focal mechanisms of aftershocks of the 2011 off the Pacific coast of Tohoku Earthquake. *Earth Planets and Space, 63*(7), 669-673. https://doi.org/10.5047/eps.2011.06.016

Baer, M., & Kradolfer, U. (1987). An Automatic Phase Picker for Local and Teleseismic Events. *Bulletin of the Seismological Society of America, 77*(4), 1437-1445. https://doi.org/10.1785/bssa0770041437

Baker, B., Holt, M. M., Pankow, K. L., Koper, K. D., & Farrell, J. (2021). Monitoring the 2020 Magna, Utah, Earthquake Sequence with Nodal Seismometers and Machine Learning. *Seismological Research Letters, 92*(2), 787-801. https://doi.org/10.1785/0220200316

Barcheck, C. G., Wiens, D. A., van Keken, P. E., & Hacker, B. R. (2012). The relationship of intermediate- and deep-focus seismicity to the hydration and dehydration of subducting slabs. *Earth and Planetary Science Letters, 349*, 153-160. https://doi.org/10.1016/j.epsl.2012.06.055

Beaucé, E., Frank, W. B., & Romanenko, A. (2017). Fast Matched Filter (FMF): An Efficient Seismic Matched-Filter Search for Both CPU and GPU Architectures. *Seismological Research Letters, 89*(1), 165-172. https://doi.org/10.1785/0220170181

Bedford, J. R., Moreno, M., Deng, Z., Oncken, O., Schurr, B., John, T., et al. (2020). Months-long thousand-kilometre-scale wobbling before great subduction earthquakes. *Nature, 580*(7805), 628-635. https://doi.org/10.1038/s41586-020-2212-1

Ben-Zion, Y., & Sammis, C. G. (2003). Characterization of fault zones. *Pure and Applied Geophysics, 160*(3-4), 677-715. https://doi.org/Doi 10.1007/Pl00012554

Berg, E. (1966). Triggering of Alaskan Earthquake of March 28 1964 and Major Aftershocks by Low Ocean Tide Loads. *Nature, 210*(5039), 893-&. Article. https://doi.org/DOI 10.1038/210893a0

Bergen, K. J., Johnson, P. A., de Hoop, M. V., & Beroza, G. C. (2019). Machine learning for data-driven discovery in solid Earth geoscience. *Science, 363*(6433), eaau0323. https://doi.org/10.1126/science.aau0323

Bettinelli, P., Avouac, J. P., Flouzat, M., Bollinger, L., Ramillien, G., Rajaure, S., & Sapkota, S. (2008). Seasonal variations of seismicity and geodetic strain in the Himalaya induced by surface hydrology. *Earth and Planetary Science Letters, 266*(3-4), 332-344. https://doi.org/10.1016/j.epsl.2007.11.021

Boettcher, M. S., & Jordan, T. H. (2004). Earthquake scaling relations for mid-ocean ridge transform faults. *Journal of Geophysical Research-Solid Earth, 109*(B12), 21. Review. https://doi.org/10.1029/2004jb003110

Bonilla, M. G., Mark, R. K., & Lienkaemper, J. J. (1984). Statistical Relations among Earthquake Magnitude, Surface Rupture Length, and Surface Fault Displacement. *Bulletin of the Seismological Society of America, 74*(6), 2379-2411.

Bouchon, M., & Karabulut, H. (2008). The aftershock signature of supershear earthquakes. *Science, 320*(5881), 1323-1325. Article. https://doi.org/10.1126/science.1155030

Bouchon, M., Marsan, D., Durand, V., Campillo, M., Perfettini, H., Madariaga, R., & Gardonio, B. (2016). Potential slab deformation and plunge prior to the Tohoku,

Iquique and Maule earthquakes. *Nature Geoscience, 9*(5), 380-+. https://doi.org/10.1038/Ngeo2701

Brown, T., Mann, B., Ryder, N., Subbiah, M., Kaplan, J. D., Dhariwal, P., et al. (2020). Language models are few-shot learners. *Advances in neural information processing systems, 33*, 1877-1901.

Brudzinski, M. R., Thurber, C. H., Hacker, B. R., & Engdahl, E. R. (2007). Global prevalence of double Benioff zones. *Science, 316*(5830), 1472-1474. https://doi.org/10.1126/science.1139204

Burnley, P. C., Green, H. W., & Prior, D. J. (1991). Faulting associated with the olivine to spinel transformation in Mg2GeO4and its implications for deep-focus earthquakes. *Journal of Geophysical Research, 96*(B1), 425. https://doi.org/10.1029/90jb01937

Calais, E., Freed, A. M., Van Arsdale, R., & Stein, S. (2010). Triggering of New Madrid seismicity by late-Pleistocene erosion. *Nature, 466*(7306), 608-611. https://doi.org/10.1038/nature09258

Catalans, I. C. f. I. G. D. C.-I. D. E. (1984). *Catalan Seismic Network.*

Centre, I. N. d. G. e. V. S. D. (2006). *Rete sismica nazionale (RSN)*.

Chamberlain, C. J., Frank, W. B., Lanza, F., Townend, J., & Warren-Smith, E. (2021). Illuminating the Pre-, Co-, and Post-Seismic Phases of the 2016 M7.8 Kaikoura Earthquake With 10 Years of Seismicity. *Journal of Geophysical Research-Solid Earth, 126*(8). https://doi.org/10.1029/2021JB022304

Chamberlain, C. J., Hopp, C. J., Boese, C. M., Warren-Smith, E., Chambers, D., Chu, S. X., et al. (2017). EQcorrscan: Repeating and Near-Repeating Earthquake Detection and Analysis in Python. *Seismological Research Letters, 89*(1), 173-181. https://doi.org/10.1785/0220170151

Chan, C.-H., & Wu, Y.-M. (2012). A seismicity burst following the 2010M 6.4 Jiashian earthquake – Implications for short-term seismic hazards in southern Taiwan. *Journal of Asian Earth Sciences, 59*, 231-239. https://doi.org/10.1016/j.jseaes.2012.08.011

Chang, C. H., Wu, Y. M., Zhao, L., & Wu, F. T. (2007). Aftershocks of the 1999 Chi-Chi, Taiwan, earthquake: The first hour. *Bulletin of the Seismological Society of America, 97*(4), 1245-1258. https://doi.org/10.1785/0120060184

Chao, K., Peng, Z. G., Hsu, Y. J., Obara, K., Wu, C. Q., Ching, K. E., et al. (2017). Temporal variation of tectonic tremor activity in southern Taiwan around the 2010 M(L)6.4 Jiashian earthquake. *Journal of Geophysical Research-Solid Earth, 122*(7), 5417-5434. https://doi.org/10.1002/2016jb013925

Chen, C.-H., Wen, S., Yeh, T.-K., Wang, C.-H., Yen, H.-Y., Liu, J.-Y., et al. (2013). Observation of surface displacements from GPS analyses before and after the Jiashian earthquake (M=6.4) in Taiwan. *Journal of Asian Earth Sciences, 62*, 662-671. https://doi.org/10.1016/j.jseaes.2012.11.016

Chen, C., & Holland, A. A. (2016). PhasePApy: A Robust Pure Python Package for Automatic Identification of Seismic Phases. *Seismological Research Letters, 87*(6), 1384-1396. https://doi.org/10.1785/0220160019

Chen, K.-C., Huang, W.-G., & Wang, J.-H. (2007). Relationships among magnitudes and seismic moment of earthquakes in the Taiwan region. *TAO: Terrestrial, Atmospheric and Oceanic Sciences, 18*(5), 9.

Chen, M., Manea, V. C., Niu, F. L., Wei, S. S., & Kiser, E. (2019). Genesis of Intermediate-Depth and Deep Intraslab Earthquakes beneath Japan Constrained by Seismic Tomography, Seismicity, and Thermal Modeling. *Geophysical Research Letters, 46*(4), 2025-2036. https://doi.org/10.1029/2018gl080025

Chen, Q. F., Wang, X., Jiang, J. Z., & Li, T. J. (2021). The Northwest Pacific subduction zone and its deep earthquake activity. *Chinese Journal of Geophysics-Chinese Edition, 64*(12), 4394-4405. https://doi.org/10.6038/cjg2021P0038

Chen, S. K., Wu, Y. M., & Chan, Y. C. (2018). Episodic Slow Slip Events and Overlying Plate Seismicity at the Southernmost Ryukyu Trench. *Geophysical Research Letters, 45*(19), 10369-10377. https://doi.org/10.1029/2018gl079740

Chen, Y. (2009). Report on Typhoon Morakot (0908) of 2009. *Weather Forecast Center Central Weather Bureau. Ministry of Interior*.

Chen, Y. C., Chang, K. T., Lee, H. Y., & Chiang, S. H. (2015). Average landslide erosion rate at the watershed scale in southern Taiwan estimated from magnitude and

frequency of rainfall. *Geomorphology, 228*, 756-764. https://doi.org/10.1016/j.geomorph.2014.07.022

Cheng, Y. F., & Ben-Zion, Y. (2020). Variations of Earthquake Properties Before, During, and After the 2019 M7.1 Ridgecrest, CA, Earthquake. *Geophysical Research Letters, 47*(18). https://doi.org/10.1029/2020GL089650

Chernak, L. J., & Hirth, G. (2011). Syndeformational antigorite dehydration produces stable fault slip. *Geology, 39*(9), 847-850. https://doi.org/10.1130/G31919.1

Chien, F. C., & Kuo, H. C. (2011). On the extreme rainfall of Typhoon Morakot (2009). *Journal of Geophysical Research-Atmospheres, 116*(D5). https://doi.org/10.1029/2010jd015092

Ching, K. E., Johnson, K. M., Rau, R. J., Chuang, R. Y., Kuo, L. C., & Leu, P. L. (2011). Inferred fault geometry and slip distribution of the 2010 Jiashian, Taiwan, earthquake is consistent with a thick-skinned deformation model. *Earth and Planetary Science Letters, 301*(1-2), 78-86. https://doi.org/10.1016/j.epsl.2010.10.021

Choudrey, R. A. (2002). *Variational methods for Bayesian independent component analysis.* University of Oxford Oxford, UK,

Choudrey, R. A., & Roberts, S. J. (2003). Variational mixture of Bayesian independent component analyzers. *Neural Comput, 15*(1), 213-252. https://doi.org/10.1162/089976603321043766

Chu, S. N., Beroza, G. C., & Ellsworth, W. L. (2019). Source Parameter Variability of Intermediate-Depth Earthquakes in Japanese Subduction Zones. *Journal of Geophysical Research-Solid Earth, 124*(8), 8704-8725. https://doi.org/10.1029/2019jb017592

Chu, S. X., & Beroza, G. C. (2022). Aftershock productivity of intermediate-depth earthquakes in Japan. *Geophysical Journal International, 230*(1), 448-463. https://doi.org/10.1093/gji/ggac024

Cocco, M., Nostro, C., & Ekstrom, G. (2000). Static stress changes and fault interaction during the 1997 Umbria-Marche earthquake sequence. *Journal of Seismology, 4*(4), 501-516. https://doi.org/Doi 10.1023/A:1026507917308

Costain, J. K., & Bollinger, G. A. (2010). Review: Research Results in Hydroseismicity from 1987 to 2009. *Bulletin of the Seismological Society of America, 100*(5a), 1841-1858. https://doi.org/10.1785/0120090288

Dadson, S. J., Hovius, N., Chen, H., Dade, W. B., Hsieh, M. L., Willett, S. D., et al. (2003). Links between erosion, runoff variability and seismicity in the Taiwan orogen. *Nature, 426*(6967), 648-651. https://doi.org/10.1038/nature02150

Das, S., & Henry, C. (2003). Spatial relation between main earthquake slip and its aftershock distribution. *Reviews of Geophysics, 41*(3). https://doi.org/10.1029/2002rg000119

Dascher-Cousineau, K., Brodsky, E. E., Lay, T., & Goebel, T. H. W. (2020). What Controls Variations in Aftershock Productivity? *Journal of Geophysical Research: Solid Earth, 125*(2). https://doi.org/10.1029/2019jb018111

Davis, S. D., & Frohlich, C. (1991). Single-Link Cluster-Analysis of Earthquake Aftershocks - Decay Laws and Regional Variations. *Journal of Geophysical Research-Solid Earth and Planets, 96*(B4), 6335-6350. https://doi.org/Doi 10.1029/90jb02634

Delbridge, B. G., Kita, S., Uchida, N., Johnson, C. W., Matsuzawa, T., & Buergmann, R. (2017). Temporal variation of intermediate-depth earthquakes around the time of the M9.0 Tohoku-oki earthquake. *Geophysical Research Letters, 44*(8), 3580-3590. https://doi.org/10.1002/2017gl072876

Demets, C., Gordon, R. G., Argus, D. F., & Stein, S. (1994). Effect of Recent Revisions to the Geomagnetic Reversal Time-Scale on Estimates of Current Plate Motions. *Geophysical Research Letters, 21*(20), 2191-2194. https://doi.org/Doi 10.1029/94gl02118

Dieterich, J. (1994). A Constitutive Law for Rate of Earthquake Production and Its Application to Earthquake Clustering. *Journal of Geophysical Research-Solid Earth, 99*(B2), 2601-2618. https://doi.org/Doi 10.1029/93jb02581

Dieterich, J. H. (1992). Earthquake nucleation on faults with rate-and state-dependent strength. *Tectonophysics, 211*(1-4), 115-134. https://doi.org/10.1016/0040-1951(92)90055-b

Dobson, D. P., Meredith, P. G., & Boon, S. A. (2002). Simulation of subduction zone seismicity by dehydration of serpentine. *Science, 298*(5597), 1407-1410. https://doi.org/10.1126/science.1075390

Dreger, D. S., & Helmberger, D. V. (1993). Determination of source parameters at regional distances with three-component sparse network data. *Journal of Geophysical Research: Solid Earth, 98*(B5), 8107-8125. https://doi.org/10.1029/93jb00023

Eberhart-Phillips, D., & Michael, A. J. (1993). Three-dimensional velocity structure, seismicity, and fault structure in the Parkfield Region, central California. *Journal of Geophysical Research, 98*(B9), 15737. https://doi.org/10.1029/93jb01029

Ekström, G., Nettles, M., & Dziewoński, A. (2012). The global CMT project 2004–2010: Centroid-moment tensors for 13,017 earthquakes. *Physics of the Earth and Planetary Interiors, 200*, 1-9.

Enescu, B., Mori, J., & Miyazawa, M. (2007). Quantifying early aftershock activity of the 2004 mid-Niigata Prefecture earthquake (Mw6.6). *Journal of Geophysical Research: Solid Earth, 112*(B4). https://doi.org/10.1029/2006jb004629

Engdahl, E. R., & Scholz, C. H. (1977). A double Benioff Zone beneath the central Aleutians: An unbending of the lithosphere. *Geophysical Research Letters, 4*(10), 473-476. https://doi.org/10.1029/GL004i010p00473

Fan, W. Y., Barbour, A. J., Cochran, E. S., & Lin, G. Q. (2021). Characteristics of Frequent Dynamic Triggering of Microearthquakes in Southern California. *Journal of Geophysical Research-Solid Earth, 126*(1). https://doi.org/10.1029/2020JB020820

Ferrand, T. P., Hilairet, N., Incel, S., Deldicque, D., Labrousse, L., Gasc, J., et al. (2017). Dehydration-driven stress transfer triggers intermediate-depth earthquakes. *Nat Commun, 8*(1), 15247. https://doi.org/10.1038/ncomms15247

Florez, M. A., & Prieto, G. A. (2019). Controlling Factors of Seismicity and Geometry in Double Seismic Zones. *Geophysical Research Letters, 46*(8), 4174-4181. https://doi.org/10.1029/2018gl081168

Frank, W. B., Poli, P., & Perfettini, H. (2017). Mapping the rheology of the Central Chile subduction zone with aftershocks. *Geophysical Research Letters, 44*(11), 5374-5382. https://doi.org/10.1002/2016gl072288

Freed, A. M. (2005). Earthquake triggering by static, dynamic, and postseismic stress transfer. *Annual Review of Earth and Planetary Sciences, 33*(1), 335-367. https://doi.org/10.1146/annurev.earth.33.092203.122505

Frohlich, C. (1987). Aftershocks and Temporal Clustering of Deep Earthquakes. *Journal of Geophysical Research-Solid Earth and Planets, 92*(B13), 13944-13956. https://doi.org/DOI 10.1029/JB092iB13p13944

Fujita, K., & Kanamori, H. (1981). Double Seismic Zones and Stresses of Intermediate Depth Earthquakes. *Geophysical Journal of the Royal Astronomical Society, 66*(1), 131-156. https://doi.org/DOI 10.1111/j.1365-246X.1981.tb05950.x

Gao, S. S., Silver, P. G., Linde, A. T., & Sacks, I. S. (2000). Annual modulation of triggered seismicity following the 1992 Landers earthquake in California. *Nature, 406*(6795), 500-504. https://doi.org/10.1038/35020045

Gardner, J., & Knopoff, L. (1974). Is the sequence of earthquakes in Southern California, with aftershocks removed, Poissonian? *Bulletin of the Seismological Society of America, 64*(5), 1363-1367.

Gardonio, B., Campillo, M., Marsan, D., Lecointre, A., Bouchon, M., & Letort, J. (2019). Seismic Activity Preceding the 2011 Mw 9.0 Tohoku Earthquake, Japan, Analyzed With Multidimensional Template Matching. *Journal of Geophysical Research: Solid Earth, 124*(7), 6815-6831. https://doi.org/10.1029/2018jb016751

Gerstenberger, M. C., Wiemer, S., Jones, L. M., & Reasenberg, P. A. (2005). Real-time forecasts of tomorrow's earthquakes in California. *Nature, 435*(7040), 328-331. https://doi.org/10.1038/nature03622

Gibbons, S. J., & Ringdal, F. (2006). The detection of low magnitude seismic events using array-based waveform correlation. *Geophysical Journal International, 165*(1), 149-166. https://doi.org/10.1111/j.1365-246X.2006.02865.x

Green, H. W., & Burnley, P. C. (1989). A New Self-Organizing Mechanism for Deep-Focus Earthquakes. *Nature, 341*(6244), 733-737. https://doi.org/DOI 10.1038/341733a0

Green, H. W., & Houston, H. (1995). The Mechanics of Deep Earthquakes. *Annual Review of Earth and Planetary Sciences, 23*(1), 169-213. https://doi.org/DOI 10.1146/annurev.ea.23.050195.001125

Grollimund, B., & Zoback, M. D. (2001). Did deglaciation trigger intraplate seismicity in the New Madrid seismic zone? *Geology, 29*(2), 175-178.

Gualandi, A., Avouac, J.-P., Galetzka, J., Genrich, J. F., Blewitt, G., Adhikari, L. B., et al. (2017). Pre-and post-seismic deformation related to the 2015, Mw7. 8 Gorkha earthquake, Nepal. *Tectonophysics, 714*, 90-106.

Gualandi, A., Serpelloni, E., & Belardinelli, M. E. (2016). Blind source separation problem in GPS time series. *Journal of Geodesy, 90*(4), 323-341. https://doi.org/10.1007/s00190-015-0875-4

Gutenberg, B. (1956). The energy of earthquakes. *Quarterly Journal of the Geological Society, 112*(1-4), 1-14.

Gutenberg, B., & Richter, C. F. (1942). Earthquake magnitude, intensity, energy, and acceleration*. *Bulletin of the Seismological Society of America, 32*(3), 163-191. https://doi.org/10.1785/bssa0320030163

Gutenberg, B., & Richter, C. F. (1944). Frequency of earthquakes in California. *Bulletin of the Seismological Society of America, 34*(4), 185-188.

Habermann, R. (1981). Precursory seismicity patterns: stalking the mature seismic gap. *Earthquake prediction: An international review, 4*, 29-42.

Habermann, R. E. (1983). Teleseismic Detection in the Aleutian Island-Arc. *Journal of Geophysical Research, 88*(Nb6), 5056-5064. https://doi.org/DOI 10.1029/JB088iB06p05056

Hainzl, S., Ben-Zion, Y., Cattania, C., & Wassermann, J. (2013a). Testing atmospheric and tidal earthquake triggering at Mt. Hochstaufen, Germany. *Journal of Geophysical Research-Solid Earth, 118*(10), 5442-5452. https://doi.org/10.1002/jgrb.50387

Hainzl, S., Fischer, T., Cermakova, H., Bachura, M., & Vlcek, J. (2016). Aftershocks triggered by fluid intrusion: Evidence for the aftershock sequence occurred 2014 in West Bohemia/Vogtland. *Journal of Geophysical Research-Solid Earth, 121*(4), 2575-2590. https://doi.org/10.1002/2015jb012582

Hainzl, S., Kraft, T., Wassermann, J., Igel, H., & Schmedes, E. (2006). Evidence for rainfall-triggered earthquake activity. *Geophysical Research Letters, 33*(19). https://doi.org/10.1029/2006gl027642

Hainzl, S., Zakharova, O., & Marsan, D. (2013b). Impact of Aseismic Transients on the Estimation of Aftershock Productivity Parameters. *Bulletin of the Seismological Society of America, 103*(3), 1723-1732. https://doi.org/10.1785/0120120247

Hara, S., Fukahata, Y., & Iio, Y. (2019). P-wave first-motion polarity determination of waveform data in western Japan using deep learning. *Earth Planets and Space, 71*(1). https://doi.org/10.1186/s40623-019-1111-x

Hardebeck, J. L., Nazareth, J. J., & Hauksson, E. (1998). The static stress change triggering model: Constraints from two southern California aftershock sequences. *Journal of Geophysical Research-Solid Earth, 103*(B10), 24427-24437. https://doi.org/Doi 10.1029/98jb00573

Hardebeck, J. L., & Shearer, P. M. (2002). A new method for determining first-motion focal mechanisms. *Bulletin of the Seismological Society of America, 92*(6), 2264-2276. https://doi.org/Doi 10.1785/0120010200

Hardebeck, J. L., & Shearer, P. M. (2003). Using S/P amplitude ratios to constrain the focal mechanisms of small earthquakes. *Bulletin of the Seismological Society of America, 93*(6), 2434-2444. https://doi.org/Doi 10.1785/0120020236

Hasegawa, A., Umino, N., & Takagi, A. (1978a). Double-planed deep seismic zone and upper-mantle structure in the Northeastern Japan Arc. *Geophysical Journal International, 54*(2), 281-296. https://doi.org/10.1111/j.1365-246X.1978.tb04260.x

Hasegawa, A., Umino, N., & Takagi, A. (1978b). Double-planed structure of the deep seismic zone in the northeastern Japan arc. *Tectonophysics, 47*(1-2), 43-58.

Hayes, G. P., Moore, G. L., Portner, D. E., Hearne, M., Flamme, H., Furtney, M., & Smoczyk, G. M. (2018). Slab2, a comprehensive subduction zone geometry model. *Science, 362*(6410), 58-61. https://doi.org/10.1126/science.aat4723

He, K., Zhang, X., Ren, S., & Sun, J. (2015). Deep Residual Learning for Image Recognition.

Heki, K. (2001). Seasonal modulation of interseismic strain buildup in northeastern Japan driven by snow loads. *Science, 293*(5527), 89-92. https://doi.org/10.1126/science.1061056

Heki, K. (2003). Snow load and seasonal variation of earthquake occurrence in Japan. *Earth and Planetary Science Letters, 207*(1-4), 159-164. https://doi.org/10.1016/S0012-821x(02)01148-2

Heki, K. (2011). Ionospheric electron enhancement preceding the 2011 Tohoku-Oki earthquake. *Geophysical Research Letters, 38*(17), n/a-n/a. https://doi.org/10.1029/2011gl047908

Heki, K., & Enomoto, Y. (2015). Mw dependence of the preseismic ionospheric electron enhancements. *Journal of Geophysical Research: Space Physics, 120*(8), 7006-7020. https://doi.org/10.1002/2015ja021353

Henry, C., & Das, S. (2001). Aftershock zones of large shallow earthquakes: fault dimensions, aftershock area expansion and scaling relations. *Geophysical Journal International, 147*(2), 272-293. https://doi.org/DOI 10.1046/j.1365-246X.2001.00522.x

Herman, M. W., Herrmann, R. B., Benz, H. M., & Furlong, K. P. (2014). Using regional moment tensors to constrain the kinematics and stress evolution of the 2010-2013 Canterbury earthquake sequence, South Island, New Zealand. *Tectonophysics, 633*, 1-15. https://doi.org/10.1016/j.tecto.2014.06.019

Herrmann, M., & Marzocchi, W. (2021). Inconsistencies and Lurking Pitfalls in the Magnitude-Frequency Distribution of High-Resolution Earthquake Catalogs. *Seismological Research Letters, 92*(2), 909-922. https://doi.org/10.1785/0220200337

Hill, D. P., & Prejean, S. G. (2015). Dynamic Triggering. In *Treatise on Geophysics* (pp. 273-304): Elsevier.

Hirose, F., Miyaoka, K., Hayashimoto, N., Yamazaki, T., & Nakamura, M. (2011). Outline of the 2011 off the Pacific coast of Tohoku Earthquake (M-w 9.0) -Seismicity: foreshocks, mainshock, aftershocks, and induced activity. *Earth Planets and Space, 63*(7), 513-518. https://doi.org/10.5047/eps.2011.05.019

Ho, C.-S. (1988). An introduction to the geology of Taiwan, explanatory text of the geologic map of Taiwan. *Central Geological Survey*, 151-152.

Hobbs, B. E., & Ord, A. (1988). Plastic Instabilities - Implications for the Origin of Intermediate and Deep-Focus Earthquakes. *Journal of Geophysical Research-Solid Earth and Planets*, *93*(B9), 10521-10540. https://doi.org/DOI 10.1029/JB093iB09p10521

Hobbs, T. E., Kyriakopoulos, C., Newman, A. V., Protti, M., & Yao, D. (2017). Large and primarily updip afterslip following the 2012 Mw 7.6 Nicoya, Costa Rica, earthquake. *Journal of Geophysical Research: Solid Earth, 122*(7), 5712-5728. https://doi.org/10.1002/2017jb014035

Horiuchi, S., Horiuchi, Y., Iio, Y., Nakamura, H., & Hasemi, A. (2009). *Automatic arrival time picking as accurate as picking by a seismologist. 2009 Abst Jpn Geosci Uni Meet S150-001 http://www2. jpgu. org/meeting/2009/program/session/pdf/S150.* Paper presented at the S150-001_e. pdf Accessed.

Hsu, Y. J., Chang, Y. S., Liu, C. C., Lee, H. M., Linde, A. T., Sacks, S. I., et al. (2015). Revisiting borehole strain, typhoons, and slow earthquakes using quantitative estimates of precipitation-induced strain changes. *Journal of Geophysical Research-Solid Earth, 120*(6), 4556-4571. https://doi.org/10.1002/2014jb011807

Hsu, Y. J., Fu, Y. N., Burgmann, R., Hsu, S. Y., Lin, C. C., Tang, C. H., & Wu, Y. M. (2020). Assessing seasonal and interannual water storage variations in Taiwan using geodetic and hydrological data. *Earth and Planetary Science Letters, 550*, 116532. https://doi.org/10.1016/j.epsl.2020.116532

Hsu, Y. J., Kao, H., Burgmann, R., Lee, Y. T., Huang, H. H., Hsu, Y. F., et al. (2021). Synchronized and asynchronous modulation of seismicity by hydrological loading: A case study in Taiwan. *Sci Adv*, *7*(16), eabf7282. https://doi.org/10.1126/sciadv.abf7282

Hsu, Y. J., Yu, S. B., Kuo, L. C., Tsai, Y. C., & Chen, H. Y. (2011). Coseismic deformation of the 2010 Jiashian, Taiwan earthquake and implications for fault activities in southwestern Taiwan. *Tectonophysics*, *502*(3-4), 328-335. https://doi.org/10.1016/j.tecto.2011.02.005

Hu, Y., Burgmann, R., Uchida, N., Banerjee, P., & Freymueller, J. T. (2016). Stress-driven relaxation of heterogeneous upper mantle and time-dependent afterslip following

the 2011 Tohoku earthquake. *Journal of Geophysical Research-Solid Earth, 121*(1), 385-411. https://doi.org/10.1002/2015jb012508

Huang, H. H., Wu, Y. M., Song, X. D., Chang, C. H., Lee, S. J., Chang, T. M., & Hsieh, H. H. (2014). Joint Vp and Vs tomography of Taiwan: Implications for subduction-collision orogeny. *Earth and Planetary Science Letters, 392*, 177-191. https://doi.org/10.1016/j.epsl.2014.02.026

Hung, C., Lin, G. W., Kuo, H. L., Zhang, J. M., Chen, C. W., & Chen, H. (2018). Impact of an Extreme Typhoon Event on Subsequent Sediment Discharges and Rainfall-Driven Landslides in Affected Mountainous Regions of Taiwan. *Geofluids, 2018*, 1-11. https://doi.org/10.1155/2018/8126518

Husen, S., Bachmann, C., & Giardini, D. (2007). Locally triggered seismicity in the central Swiss Alps following the large rainfall event of August 2005. *Geophysical Journal International, 171*(3), 1126-1134. https://doi.org/10.1111/j.1365-246X.2007.03561.x

Ide, S., Yabe, S., & Tanaka, Y. (2016). Earthquake potential revealed by tidal influence on earthquake size-frequency statistics. *Nature Geoscience, 9*(11), 834-+. https://doi.org/10.1038/Ngeo2796

Igarashi, T., Matsuzawa, T., Umino, N., & Hasegawa, A. (2001). Spatial distribution of focal mechanisms for interplate and intraplate earthquakes associated with the subducting Pacific plate beneath the northeastern Japan arc: A triple-planed deep seismic zone. *Journal of Geophysical Research-Solid Earth, 106*(B2), 2177-2191. https://doi.org/Doi 10.1029/2000jb900386

Iinuma, T., Hino, R., Kido, M., Inazu, D., Osada, Y., Ito, Y., et al. (2012). Coseismic slip distribution of the 2011 off the Pacific Coast of Tohoku Earthquake (M9.0) refined by means of seafloor geodetic data. *Journal of Geophysical Research-Solid Earth, 117*(B7), n/a-n/a. https://doi.org/10.1029/2012jb009186

Iinuma, T., Hino, R., Uchida, N., Nakamura, W., Kido, M., Osada, Y., & Miura, S. (2016). Seafloor observations indicate spatial separation of coseismic and postseismic slips in the 2011 Tohoku earthquake. *Nat Commun, 7*(1), 13506. https://doi.org/10.1038/ncomms13506

Iinuma, T., Ohzono, M., Ohta, Y., & Miura, S. (2011). Coseismic slip distribution of the 2011 off the Pacific coast of Tohoku Earthquake (M 9.0) estimated based on GPS

data— Was the asperity in Miyagi-oki ruptured? *Earth, Planets and Space, 63*(7), 643-648. https://doi.org/10.5047/eps.2011.06.013

Ikuta, R., Hisada, T., Karakama, G., & Kuwano, O. (2020). Stochastic Evaluation of Pre-Earthquake TEC Enhancements. *Journal of Geophysical Research-Space Physics, 125*(11). https://doi.org/10.1029/2020JA027899

Instituto Geografico Nacional, S. (1999). *Spanish digital seismic network*.

Instituto Português Do Mar E Da Atmosfera, I. (2006). *Portuguese national seismic network [Data set]*.

Ioffe, S., & Szegedy, C. (2015). *Batch normalization: Accelerating deep network training by reducing internal covariate shift.* Paper presented at the International conference on machine learning.

Ishii, M., Shearer, P. M., Houston, H., & Vidale, J. E. (2005). Extent, duration and speed of the 2004 Sumatra-Andaman earthquake imaged by the Hi-Net array. *Nature, 435*(7044), 933-936. https://doi.org/10.1038/nature03675

Jeandet Ribes, L., Cubas, N., Bhat, H. S., & Steer, P. (2020). The Impact of Large Erosional Events and Transient Normal Stress Changes on the Seismicity of Faults. *Geophysical Research Letters, 47*(22). https://doi.org/10.1029/2020gl087631

Jia, Z., Shen, Z., Zhan, Z., Li, C., Peng, Z., & Gurnis, M. (2020). The 2018 Fiji Mw 8.2 and 7.9 deep earthquakes: One doublet in two slabs. *Earth and Planetary Science Letters, 531*, 115997.

Jiang, C. S., Fang, L. H., Han, L. B., Wang, W. L., & Guo, L. J. (2015). Assessment of earthquake detection capability for the seismic array : A case study of the Xichang seismic array. *Chinese Journal of Geophysics-Chinese Edition, 58*(3), 832-843. https://doi.org/10.6038/cjg20150313

Jiang, J., Bock, Y., & Klein, E. (2021). Coevolving early afterslip and aftershock signatures of a San Andreas fault rupture. *Sci Adv, 7*(15), eabc1606. https://doi.org/10.1126/sciadv.abc1606

John, T., Medvedev, S., Rupke, L. H., Andersen, T. B., Podladchikov, Y. Y., & Austrheim, H. (2009). Generation of intermediate-depth earthquakes by self-localizing thermal runaway. *Nature Geoscience, 2*(2), 137-140. https://doi.org/10.1038/Ngeo419

Johnson, C. W., Fu, Y., & Burgmann, R. (2017a). Seasonal water storage, stress modulation, and California seismicity. *Science, 356*(6343), 1161-1164. https://doi.org/10.1126/science.aak9547

Johnson, C. W., Fu, Y. N., & Burgmann, R. (2017b). Stress Models of the Annual Hydrospheric, Atmospheric, Thermal, and Tidal Loading Cycles on California Faults: Perturbation of Background Stress and Changes in Seismicity. *Journal of Geophysical Research-Solid Earth, 122*(12), 10605-10625. https://doi.org/10.1002/2017jb014778

Johnson, C. W., Fu, Y. N., & Burgmann, R. (2020). Hydrospheric modulation of stress and seismicity on shallow faults in southern Alaska. *Earth and Planetary Science Letters, 530*, 115904. https://doi.org/10.1016/j.epsl.2019.115904

Jung, H., Green, I. H., & Dobrzhinetskaya, L. F. (2004). Intermediate-depth earthquake faulting by dehydration embrittlement with negative volume change. *Nature, 428*(6982), 545-549. https://doi.org/10.1038/nature02412

Kagan, Y. Y. (2004). Short-term properties of earthquake catalogs and models of earthquake source. *Bulletin of the Seismological Society of America, 94*(4), 1207-1228. https://doi.org/Doi 10.1785/012003098

Kagan, Y. Y., & Knopoff, L. (1980). Dependence of Seismicity on Depth. *Bulletin of the Seismological Society of America, 70*(5), 1811-1822.

Kamogawa, M., & Kakinami, Y. (2013). Is an ionospheric electron enhancement preceding the 2011 Tohoku-Oki earthquake a precursor? *Journal of Geophysical Research: Space Physics, 118*(4), 1751-1754. https://doi.org/10.1002/jgra.50118

Kanamori, H., & Brodsky, E. E. (2004). The physics of earthquakes. *Reports on Progress in Physics, 67*(8), 1429.

Kanazawa, T., Uehira, K., Mochizuki, M., Shinbo, T., Fujimoto, H., Noguchi, S., et al. (2016). S-net project, cabled observation network for earthquakes and tsunamis. *Dubai: Suboptic*.

Kaneda, Y., Kawaguchi, K., Araki, E., Matsumoto, H., Nakamura, T., Kamiya, S., et al. (2015). Development and application of an advanced ocean floor network system for megathrust earthquakes and tsunamis. In *Seafloor Observatories* (pp. 643-662): Springer Berlin Heidelberg.

Kao, H., & Liu, L. G. (1995). A Hypothesis for the Seismogenesis of a Double Seismic Zone. *Geophysical Journal International, 123*(1), 71-84. https://doi.org/DOI 10.1111/j.1365-246X.1995.tb06662.x

Karato, S., Riedel, M. R., & Yuen, D. A. (2001). Rheological structure and deformation of subducted slabs in the mantle transition zone: implications for mantle circulation and deep earthquakes. *Physics of the Earth and Planetary Interiors, 127*(1-4), 83-108. https://doi.org/Doi 10.1016/S0031-9201(01)00223-0

Karpatne, A., Ebert-Uphoff, I., Ravela, S., Babaie, H. A., & Kumar, V. (2019). Machine Learning for the Geosciences: Challenges and Opportunities. *IEEE Transactions on Knowledge and Data Engineering, 31*(8), 1544-1554. https://doi.org/10.1109/Tkde.2018.2861006

Kasahara, J. (2002). Geophysics. Tides, earthquakes, and volcanoes. *Science, 297*(5580), 348-349. Editorial Material. https://doi.org/10.1126/science.1074601

Kato, A., & Ben-Zion, Y. (2020). The generation of large earthquakes. *Nature Reviews Earth & Environment, 2*(1), 26-39. https://doi.org/10.1038/s43017-020-00108-w

Kato, A., & Obara, K. (2014). Step-like migration of early aftershocks following the 2007 Mw 6.7 Noto-Hanto earthquake, Japan. *Geophysical Research Letters, 41*(11), 3864-3869. https://doi.org/10.1002/2014gl060427

Kato, A., Obara, K., Igarashi, T., Tsuruoka, H., Nakagawa, S., & Hirata, N. (2012). Propagation of slow slip leading up to the 2011 M(w) 9.0 Tohoku-Oki earthquake. *Science, 335*(6069), 705-708. https://doi.org/10.1126/science.1215141

Kato, N. (2007). Expansion of aftershock areas caused by propagating post-seismic sliding. *Geophysical Journal International, 168*(2), 797-808. https://doi.org/10.1111/j.1365-246X.2006.03255.x

Kawakatsu, H. (1986). Double Seismic Zones - Kinematics. *Journal of Geophysical Research-Solid Earth and Planets, 91*(B5), 4811-4825. https://doi.org/DOI 10.1029/JB091iB05p04811

Keefer, D. K. (2002). Investigating landslides caused by earthquakes - A historical review. *Surveys in Geophysics, 23*(6), 473-510. https://doi.org/Doi 10.1023/A:1021274710840

Kelemen, P. B., & Hirth, G. (2007). A periodic shear-heating mechanism for intermediate-depth earthquakes in the mantle. *Nature, 446*(7137), 787-790. https://doi.org/10.1038/nature05717

Khazai, B., & Sitar, N. (2004). Evaluation of factors controlling earthquake-induced landslides caused by Chi-Chi earthquake and comparison with the Northridge and Loma Prieta events. *Engineering Geology, 71*(1-2), 79-95. https://doi.org/10.1016/S0013-7952(03)00127-3

Kilb, D., Gomberg, J., & Bodin, P. (2002). Aftershock triggering by complete Coulomb stress changes. *Journal of Geophysical Research-Solid Earth, 107*(B4), ESE 2-1-ESE 2-1. https://doi.org/10.1029/2001jb000202

Kim, J., Woo, J. U., Rhie, J., & Kang, T. S. (2017). Automatic determination of first-motion polarity and its application to focal mechanism analysis of microseismic events. *Geosciences Journal, 21*(5), 695-702. https://doi.org/10.1007/s12303-017-0022-8

Kingma, D. P., & Ba, J. (2014). Adam: A method for stochastic optimization. *arXiv preprint arXiv:1412.6980*.

Kiranyaz, S., Ince, T., Hamila, R., & Gabbouj, M. (2015, 2015-08-01). *Convolutional Neural Networks for patient-specific ECG classification.* Paper presented at the 2015 37th Annual International Conference of the IEEE Engineering in Medicine and Biology Society (EMBC).

Kirby, S., Engdahl, R. E., & Denlinger, R. (1996). Intermediate-depth intraslab earthquakes and arc volcanism as physical expressions of crustal and uppermost mantle metamorphism in subducting slabs. *Washington DC American Geophysical Union Geophysical Monograph Series, 96*, 195-214.

Kirby, S. H. (1987). Localized Polymorphic Phase-Transformations in High-Pressure Faults and Applications to the Physical-Mechanism of Deep Earthquakes. *Journal of Geophysical Research-Solid Earth and Planets, 92*(B13), 13789-13800. https://doi.org/DOI 10.1029/JB092iB13p13789

Kirby, S. H., Durham, W. B., & Stern, L. A. (1991). Mantle phase changes and deep-earthquake faulting in subducting lithosphere. *Science, 252*(5003), 216-225. https://doi.org/10.1126/science.252.5003.216

Kita, S., Okada, T., Hasegawa, A., Nakajima, J., & Matsuzawa, T. (2010). Existence of interplane earthquakes and neutral stress boundary between the upper and lower planes of the double seismic zone beneath Tohoku and Hokkaido, northeastern Japan. *Tectonophysics, 496*(1-4), 68-82. https://doi.org/10.1016/j.tecto.2010.10.010

Kong, Q., Wang, R., Walter, W. R., Pyle, M., Koper, K., & Schmandt, B. (2022). Combining Deep Learning with Physics Based Features in Explosion-Earthquake Discrimination. *arXiv preprint arXiv:2203.06347*.

Kong, Q. K., Trugman, D. T., Ross, Z. E., Bianco, M. J., Meade, B. J., & Gerstoft, P. (2019). Machine Learning in Seismology: Turning Data into Insights. *Seismological Research Letters, 90*(1), 3-14. https://doi.org/10.1785/0220180259

Kositsky, A. P., & Avouac, J. P. (2010). Inverting geodetic time series with a principal component analysis-based inversion method. *Journal of Geophysical Research-Solid Earth, 115*(B3). https://doi.org/10.1029/2009jb006535

Kosuga, M., Sato, T., Hasegawa, A., Matsuzawa, T., Suzuki, S., & Motoya, Y. (1996). Spatial distribution of intermediate-depth earthquakes with horizontal or vertical nodal planes beneath northeastern Japan. *Physics of the Earth and Planetary Interiors, 93*(1-2), 63-89. https://doi.org/Doi 10.1016/0031-9201(95)03089-1

Kraft, T., Wassermann, J., & Igel, H. (2006). High-precision relocation and focal mechanism of the 2002 rain-triggered earthquake swarms at Mt Hochstaufen, SE Germany. *Geophysical Journal International, 167*(3), 1513-1528. https://doi.org/10.1111/j.1365-246X.2006.03171.x

Krizhevsky, A., Sutskever, I., & Hinton, G. E. (2012). Imagenet classification with deep convolutional neural networks. *Advances in neural information processing systems, 25*.

Kuang, W., Yuan, C., & Zhang, J. (2021). Real-time determination of earthquake focal mechanism via deep learning. *Nat Commun, 12*(1), 1432. https://doi.org/10.1038/s41467-021-21670-x

LeCun, Y., Boser, B., Denker, J., Henderson, D., Howard, R., Hubbard, W., & Jackel, L. (1989). Handwritten digit recognition with a back-propagation network. *Advances in neural information processing systems, 2*.

Lee, S.-J., Mozziconacci, L., Liang, W.-T., Hsu, Y.-J., Huang, W.-G., & Huang, B.-S. (2013). Source complexity of the 4 March 2010 Jiashian, Taiwan, Earthquake determined by joint inversion of teleseismic and near field data. *Journal of Asian Earth Sciences, 64*, 14-26. https://doi.org/10.1016/j.jseaes.2012.11.018

Lei, X. L. (2011). Possible roles of the Zipingpu Reservoir in triggering the 2008 Wenchuan earthquake. *Journal of Asian Earth Sciences, 40*(4), 844-854. https://doi.org/10.1016/j.jseaes.2010.05.004

Lei, X. L., & Satoh, T. (2007). Indicators of critical point behavior prior to rock failure inferred from pre-failure damage. *Tectonophysics, 431*(1-4), 97-111. https://doi.org/10.1016/j.tecto.2006.04.023

Lengliné, O., Enescu, B., Peng, Z., & Shiomi, K. (2012). Decay and expansion of the early aftershock activity following the 2011, Mw9.0 Tohoku earthquake. *Geophysical Research Letters, 39*(18), n/a-n/a. https://doi.org/10.1029/2012gl052797

Li, C., Peng, Z., Yao, D., Guo, H., Zhan, Z., & Zhang, H. (2018a). Abundant aftershock sequence of the 2015 Mw7.5 Hindu Kush intermediate-depth earthquake. *Geophysical Journal International, 213*(2), 1121-1134. https://doi.org/10.1093/gji/ggy016

Li, C., Peng, Z., Yao, D., Meng, X., & Zhai, Q. (2022a). Temporal Changes of Seismicity in Salton Sea Geothermal Field due to distant earthquakes and geothermal productions. *Geophysical Journal International, submitted*.

Li, Z., Zhu, L., Officer, T., Shi, F., Yu, T., & Wang, Y. (2022b). A machine-learning-based method of detecting and picking the first P-wave arrivals of acoustic emission events in laboratory experiments. *Geophysical Journal International, 230*(3), 1818-1823. https://doi.org/10.1093/gji/ggac148

Li, Z. F., Meier, M. A., Hauksson, E., Zhan, Z. W., & Andrews, J. (2018b). Machine Learning Seismic Wave Discrimination: Application to Earthquake Early Warning. *Geophysical Research Letters, 45*(10), 4773-4779. https://doi.org/10.1029/2018gl077870

Liang, S., Li, Y., & Srikant, R. (2020). Enhancing The Reliability of Out-of-distribution Image Detection in Neural Networks.

Lin, C. H. (2005). Seismicity increase after the construction of the world's tallest building: An active blind fault beneath the Taipei 101. *Geophysical Research Letters, 32*(22). https://doi.org/10.1029/2005gl024223

Lin, C. H., Jan, J. C., Pu, H. C., Tu, Y., Chen, C. C., & Wu, Y. M. (2015). Landslide seismic magnitude. *Earth and Planetary Science Letters, 429*, 122-127. https://doi.org/10.1016/j.epsl.2015.07.068

Lin, C. H., Yeh, Y. H., Chen, Y. I., Liu, J. Y., & Chen, K. J. (2003). Earthquake clustering relative to lunar phases in Taiwan. *Terrestrial Atmospheric and Oceanic Sciences, 14*(3), 289-298. https://doi.org/Doi 10.3319/Tao.2003.14.3.289(T)

Lin, C. M., Chang, T. M., Wen, K. L., Kuo, C. H., & Hsieh, H. H. (2014). Seismogenic Structure Beneath Decollement Inferred from 2009/11/5 M-L 6.2 Mingjian Earthquake in Central Taiwan. *Terrestrial Atmospheric and Oceanic Sciences, 25*(1), 27-38. https://doi.org/10.3319/Tao.2013.09.23.01(T)

Lin, C. W., Chang, W. S., Liu, S. H., Tsai, T. T., Lee, S. P., Tsang, Y. C., et al. (2011). Landslides triggered by the 7 August 2009 Typhoon Morakot in southern Taiwan. *Engineering Geology, 123*(1-2), 3-12. https://doi.org/10.1016/j.enggeo.2011.06.007

Lin, G. Q. (2018). The Source-Specific Station Term and Waveform Cross-Correlation Earthquake Location Package and Its Applications to California and New Zealand. *Seismological Research Letters, 89*(5), 1877-1885. https://doi.org/10.1785/0220180108

Lin, G. Q. (2020). Waveform Cross-Correlation Relocation and Focal Mechanisms for the 2019 Ridgecrest Earthquake Sequence. *Seismological Research Letters, 91*(4), 2055-2061. https://doi.org/10.1785/0220190277

Lin, H. F., Hsu, Y. F., & Canitano, A. (2022). Source Modeling of the 2009 Fengpin-Hualien Earthquake Sequence, Taiwan, Inferred From Static Strain Measurements. *Pure and Applied Geophysics*. https://doi.org/10.1007/s00024-022-03068-y

Lin, J. W. (2013). An empirical correlation between the occurrence of earthquakes and typhoons in Taiwan: a statistical multivariate approach. *Natural Hazards, 65*(1), 605-634. https://doi.org/10.1007/s11069-012-0382-3

Lin, M., Chen, Q., & Yan, S. (2013). Network in network. *arXiv preprint arXiv:1312.4400*.

Liu, C., Linde, A. T., & Sacks, I. S. (2009). Slow earthquakes triggered by typhoons. *Nature, 459*(7248), 833-836. https://doi.org/10.1038/nature08042

Luo, Y. T., & Wiens, D. A. (2020). High Rates of Deep Earthquake Dynamic Triggering in the Thermal Halos of Subducting Slabs. *Geophysical Research Letters, 47*(8). https://doi.org/10.1029/2019GL086125

Manga, M., & Brodsky, E. (2006). Seismic triggering of eruptions in the far field: Volcanoes and geysers. *Annual Review of Earth and Planetary Sciences, 34*(1), 263-291. https://doi.org/10.1146/annurev.earth.34.031405.125125

Maniatis, G., Kurfess, D., Hampel, A., & Heidbach, O. (2009). Slip acceleration on normal faults due to erosion and sedimentation - Results from a new three-dimensional numerical model coupling tectonics and landscape evolution. *Earth and Planetary Science Letters, 284*(3-4), 570-582. https://doi.org/10.1016/j.epsl.2009.05.024

Marsan, D., & Helmstetter, A. (2017). How variable is the number of triggered aftershocks? *Journal of Geophysical Research: Solid Earth, 122*(7), 5544-5560. Article. https://doi.org/10.1002/2016jb013807

Masci, F., Thomas, J. N., Villani, F., Secan, J. A., & Rivera, N. (2015). On the onset of ionospheric precursors 40 min before strong earthquakes. *Journal of Geophysical Research-Space Physics, 120*(2), 1383-1393. https://doi.org/10.1002/2014ja020822

Matsubara, M., Sato, H., Uehira, K., Mochizuki, M., Kanazawa, T., Takahashi, N., et al. (2019). Seismic Velocity Structure in and around the Japanese Island Arc Derived from Seismic Tomography Including NIED MOWLAS Hi-net and S-net Data. In *Seismic Waves - Probing Earth System*: IntechOpen.

Matsumoto, K., Sato, T., Takanezawa, T., & Ooe, M. (2001). GOTIC2: A program for computation of oceanic tidal loading effect. *Journal of the Geodetic Society of Japan, 47*(1), 243-248.

Matthews, M. V., & Reasenberg, P. A. (1988). Statistical-Methods for Investigating Quiescence and Other Temporal Seismicity Patterns. *Pure and Applied Geophysics, 126*(2-4), 357-372. https://doi.org/Doi 10.1007/Bf00879003

McGarr, A., Simpson, D., Seeber, L., & Lee, W. (2002). Case histories of induced and triggered seismicity. *International Geophysics Series, 81*(A), 647-664.

Mendoza, C., & Hartzell, S. H. (1988). Aftershock Patterns and Main Shock Faulting. *Bulletin of the Seismological Society of America, 78*(4), 1438-1449.

Meng, X., & Peng, Z. (2014). Seismicity rate changes in the Salton Sea Geothermal Field and the San Jacinto Fault Zone after the 2010 Mw 7.2 El Mayor-Cucapah earthquake. *Geophysical Journal International, 197*(3), 1750-1762. https://doi.org/10.1093/gji/ggu085

Meng, X., Yu, X., Peng, Z., & Hong, B. (2012). Detecting Earthquakes around Salton Sea Following the 2010 Mw7.2 El Mayor-Cucapah Earthquake Using GPU Parallel Computing. *Procedia Computer Science, 9*, 937-946. https://doi.org/10.1016/j.procs.2012.04.100

Meng, X. F., & Peng, Z. G. (2016). Increasing lengths of aftershock zones with depths of moderate-size earthquakes on the San Jacinto Fault suggests triggering of deep creep in the middle crust. *Geophysical Journal International, 204*(1), 250-261. https://doi.org/10.1093/gji/ggv445

Meng, X. F., Yang, H. F., & Peng, Z. G. (2018). Foreshocks, b Value Map, and Aftershock Triggering for the 2011 M-w 5.7 Virginia Earthquake. *Journal of Geophysical Research-Solid Earth, 123*(6), 5082-5098. https://doi.org/10.1029/2017jb015136

Michelini, A., Cianetti, S., Gaviano, S., Giunchi, C., Jozinovic, D., & Lauciani, V. (2021). INSTANCE - the Italian seismic dataset for machine learning. *Earth System Science Data, 13*(12), 5509-5544. https://doi.org/10.5194/essd-13-5509-2021

Miller, S. A. (2008). Note on rain-triggered earthquakes and their dependence on karst geology. *Geophysical Journal International, 173*(1), 334-338. https://doi.org/10.1111/j.1365-246X.2008.03735.x

Miller, S. A. (2020). Aftershocks are fluid-driven and decay rates controlled by permeability dynamics. *Nat Commun, 11*(1), 5787. https://doi.org/10.1038/s41467-020-19590-3

Miller, S. A., Collettini, C., Chiaraluce, L., Cocco, M., Barchi, M., & Kaus, B. J. (2004). Aftershocks driven by a high-pressure CO2 source at depth. *Nature, 427*(6976), 724-727. https://doi.org/10.1038/nature02251

Miura, S., Takahashi, N., Nakanishi, A., Tsuru, T., Kodaira, S., & Kaneda, Y. (2005). Structural characteristics off Miyagi forearc region, the Japan Trench seismogenic zone, deduced from a wide-angle reflection and refraction study. *Tectonophysics, 407*(3-4), 165-188. https://doi.org/10.1016/j.tecto.2005.08.001

Mogi, K. (1967). Earthquakes and Fractures. *Tectonophysics, 5*(1), 35-&. Article. https://doi.org/Doi 10.1016/0040-1951(67)90043-1

Mousavi, S. M., Ellsworth, W. L., Zhu, W., Chuang, L. Y., & Beroza, G. C. (2020). Earthquake transformer-an attentive deep-learning model for simultaneous earthquake detection and phase picking. *Nat Commun, 11*(1), 3952. https://doi.org/10.1038/s41467-020-17591-w

Mousavi, S. M., Sheng, Y. X., Zhu, W. Q., & Beroza, G. C. (2019a). STanford EArthquake Dataset (STEAD): A Global Data Set of Seismic Signals for AI. *IEEE Access, 7*, 179464-179476. https://doi.org/10.1109/Access.2019.2947848

Mousavi, S. M., Zhu, W. Q., Ellsworth, W., & Beroza, G. (2019b). Unsupervised Clustering of Seismic Signals Using Deep Convolutional Autoencoders. *Ieee Geoscience and Remote Sensing Letters, 16*(11), 1693-1697. https://doi.org/10.1109/Lgrs.2019.2909218

Mouyen, M., Canitano, A., Chao, B. F., Hsu, Y. J., Steer, P., Longuevergne, L., & Boy, J. P. (2017). Typhoon-Induced Ground Deformation. *Geophysical Research Letters, 44*(21), 11004-11011. https://doi.org/10.1002/2017gl075615

Münchmeyer, J., Woollam, J., Rietbrock, A., Tilmann, F., Lange, D., Bornstein, T., et al. (2022). Which Picker Fits My Data? A Quantitative Evaluation of Deep Learning Based Seismic Pickers. *Journal of Geophysical Research: Solid Earth, 127*(1). https://doi.org/10.1029/2021jb023499

Nair, V., & Hinton, G. E. (2010). *Rectified linear units improve restricted boltzmann machines.* Paper presented at the Icml.

Nakamura, M. (2004). Automatic determination of focal mechanism solutions using initial motion polarities of P and S waves. *Physics of the Earth and Planetary Interiors, 146*(3-4), 531-549. https://doi.org/10.1016/j.pepi.2004.05.009

Nakata, R., Suda, N., & Tsuruoka, H. (2008). Non-volcanic tremor resulting from the combined effect of Earth tides and slow slip events. *Nature Geoscience, 1*(10), 676-678. https://doi.org/10.1038/ngeo288

Neo, J. C., Huang, Y., Yao, D., & Wei, S. (2020). Is the Aftershock Zone Area a Good Proxy for the Mainshock Rupture Area? *Bulletin of the Seismological Society of America, 111*(1), 424-438. https://doi.org/10.1785/0120190200

Nishitsuji, Y., & Mori, J. (2014). Source parameters and radiation efficiency for intermediate-depth earthquakes in Northeast Japan. *Geophysical Journal International, 196*(2), 1247-1259. https://doi.org/10.1093/gji/ggt458

Nyffenegger, P., & Frohlich, C. (2000). Aftershock occurrence rate decay properties for intermediate and deep earthquake sequences. *Geophysical Research Letters, 27*(8), 1215-1218. https://doi.org/Doi 10.1029/1999gl010371

Obana, K., Takahashi, T., No, T., Kaiho, Y., Kodaira, S., Yamashita, M., et al. (2014). Distribution and migration of aftershocks of the 2010 Mw 7.4 Ogasawara Islands intraplate normal-faulting earthquake related to a fracture zone in the Pacific plate. *Geochemistry Geophysics Geosystems, 15*(4), 1363-1373. https://doi.org/10.1002/2014gc005246

Obara, K. (2002). Nonvolcanic deep tremor associated with subduction in southwest Japan. *Science, 296*(5573), 1679-1681. https://doi.org/10.1126/science.1070378

Obara, K., Kasahara, K., Hori, S., & Okada, Y. (2005). A densely distributed high-sensitivity seismograph network in Japan:Hi-net by National Research Institute for Earth Science and DisasterPrevention. *Review of Scientific Instruments, 76*(2), 021301. https://doi.org/10.1063/1.1854197

Ogata, Y. (1988). Statistical-Models for Earthquake Occurrences and Residual Analysis for Point-Processes. *Journal of the American Statistical Association, 83*(401), 9-27. https://doi.org/Doi 10.1080/01621459.1988.10478560

Ogata, Y. (2006). Statistical analysis of seismicity: updated version (SASeis2006): Institute of Statistical Mathematics.

Ogata, Y. (2017). Statistics of Earthquake Activity: Models and Methods for Earthquake Predictability Studies. *Annual Review of Earth and Planetary Sciences, Vol 45, 45*(1), 497-527. https://doi.org/10.1146/annurev-earth-063016-015918

Ogata, Y., & Toda, S. (2010). Bridging great earthquake doublets through silent slip: On- and off-fault aftershocks of the 2006 Kuril Island subduction earthquake toggled by a slow slip on the outer rise normal fault of the 2007 great earthquake. *Journal of Geophysical Research-Solid Earth, 115*(B6). https://doi.org/10.1029/2009jb006777

Ogawa, M. (1987). Shear Instability in a Viscoelastic Material as the Cause of Deep-Focus Earthquakes. *Journal of Geophysical Research-Solid Earth and Planets, 92*(B13), 13801-13810. https://doi.org/DOI 10.1029/JB092iB13p13801

Ohuchi, T., Lei, X. L., Ohfuji, H., Higo, Y. J., Tange, Y., Sakai, T., et al. (2017). Intermediate-depth earthquakes linked to localized heating in dunite and harzburgite. *Nature Geoscience, 10*(10), 771-+. https://doi.org/10.1038/Ngeo3011

Okada, Y., Kasahara, K., Hori, S., Obara, K., Sekiguchi, S., Fujiwara, H., & Yamamoto, A. (2004). Recent progress of seismic observation networks in Japan - Hi-net, F-net, K-NET and KiK-net. *Earth Planets and Space, 56*(8), Xv-Xxviii. https://doi.org/Doi 10.1186/Bf03353076

Okazaki, K., & Hirth, G. (2016). Dehydration of lawsonite could directly trigger earthquakes in subducting oceanic crust. *Nature, 530*(7588), 81-84. https://doi.org/10.1038/nature16501

Omori, F. (1894). On after-shocks of earthquakes. *J. Fact. Sci. Univ. Tokyo, 7*, 111-120.

Ozawa, S., Nishimura, T., Munekane, H., Suito, H., Kobayashi, T., Tobita, M., & Imakiire, T. (2012). Preceding, coseismic, and postseismic slips of the 2011 Tohoku earthquake, Japan. *Journal of Geophysical Research-Solid Earth, 117*(B7), n/a-n/a. https://doi.org/10.1029/2011jb009120

Page, M. T., van der Elst, N., Hardebeck, J., Felzer, K., & Michael, A. J. (2016). Three Ingredients for Improved Global Aftershock Forecasts: Tectonic Region, Time-Dependent Catalog Incompleteness, and Intersequence Variability. *Bulletin of the Seismological Society of America, 106*(5), 2290-2301. Article. https://doi.org/10.1785/0120160073

Panet, I., Bonvalot, S., Narteau, C., Remy, D., & Lemoine, J. M. (2018). Migrating pattern of deformation prior to the Tohoku-Oki earthquake revealed by GRACE data. *Nature Geoscience, 11*(5), 367-373. https://doi.org/10.1038/s41561-018-0099-3

Pankow, K. L., & Kilb, D. (2020). Going Beyond Rate Changes as the Sole Indicator for Dynamic Triggering of Earthquakes. *Sci Rep, 10*(1), 4120. https://doi.org/10.1038/s41598-020-60988-2

Paszke, A., Gross, S., Massa, F., Lerer, A., Bradbury, J., Chanan, G., et al. (2019). PyTorch: An Imperative Style, High-Performance Deep Learning Library. *Advances in Neural Information Processing Systems 32 (Nips 2019), 32*.

Peacock, S. M. (2001). Are the lower planes of double seismic zones caused by serpentine dehydration in subducting oceanic mantle? *Geology, 29*(4), 299-302.

Peacock, S. M., & Wang, K. (1999). Seismic consequences of warm versus cool subduction metamorphism: examples from southwest and northeast japan. *Science, 286*(5441), 937-939. https://doi.org/10.1126/science.286.5441.937

Pei, W. L., & Zhou, S. Y. (2022). Automatic P-wave polarity determination and focal mechanism inversion based on maximum order statistics and its application in Xiaojiang Fault Zone, Yunnan. *Chinese Journal of Geophysics-Chinese Edition, 65*(3), 992-1005. https://doi.org/10.6038/cjg2022P0313

Peltzer, G., Rosen, P., Rogez, F., & Hudnut, K. (1998). Poroelastic rebound along the Landers 1992 earthquake surface rupture. *Journal of Geophysical Research: Solid Earth, 103*(B12), 30131-30145. https://doi.org/10.1029/98jb02302

Peng, Z. G., Vidale, J. E., & Houston, H. (2006). Anomalous early aftershock decay rate of the 2004 Mw6.0 Parkfield, California, earthquake. *Geophysical Research Letters, 33*(17). https://doi.org/10.1029/2006gl026744

Peng, Z. G., Vidale, J. E., Ishii, M., & Helmstetter, A. (2007). Seismicity rate immediately before and after main shock rupture from high-frequency waveforms in Japan. *Journal of Geophysical Research-Solid Earth, 112*(B3). https://doi.org/10.1029/2006jb004386

Peng, Z. G., & Zhao, P. (2009). Migration of early aftershocks following the 2004 Parkfield earthquake. *Nature Geoscience, 2*(12), 877-881. https://doi.org/10.1038/ngeo697

Perfettini, H., Frank, W. B., Marsan, D., & Bouchon, M. (2018). A Model of Aftershock Migration Driven by Afterslip. *Geophysical Research Letters, 45*(5), 2283-2293. https://doi.org/10.1002/2017gl076287

Perfettini, H., Frank, W. B., Marsan, D., & Bouchon, M. (2019). Updip and Along-Strike Aftershock Migration Model Driven by Afterslip: Application to the 2011 Tohoku-Oki Aftershock Sequence. *Journal of Geophysical Research-Solid Earth, 124*(3), 2653-2669. https://doi.org/10.1029/2018jb016490

Persh, S. E., & Houston, H. (2004). Strongly depth-dependent aftershock production in deep earthquakes. *Bulletin of the Seismological Society of America, 94*(5), 1808-1816. https://doi.org/Doi 10.1785/012003191

Prejean, S. G., & Hill, D. P. (2018). The influence of tectonic environment on dynamic earthquake triggering: A review and case study on Alaskan volcanoes. *Tectonophysics, 745*, 293-304. https://doi.org/10.1016/j.tecto.2018.08.007

Price, A. C., & Wiens, D. (2018). *Dynamic triggering of remote, intermediate-depth earthquakes in the Mariana subduction zone following the 2012 Indian Ocean earthquakes.* Paper presented at the AGU Fall Meeting Abstracts.

Pritchard, M. E., Allen, R. M., Becker, T. W., Behn, M. D., Brodsky, E. E., Burgmann, R., et al. (2020). New Opportunities to Study Earthquake Precursors. *Seismological Research Letters, 91*(5), 2444-2447. https://doi.org/10.1785/0220200089

Proctor, B., & Hirth, G. (2015). Role of pore fluid pressure on transient strength changes and fabric development during serpentine dehydration at mantle conditions: Implications for subduction-zone seismicity. *Earth and Planetary Science Letters, 421*, 1-12. https://doi.org/10.1016/j.epsl.2015.03.040

Prozorov, A. G., & Dziewonski, A. M. (1982). A Method of Studying Variations in the Clustering Property of Earthquakes - Application to the Analysis of Global Seismicity. *Journal of Geophysical Research, 87*(Nb4), 2829-2839. https://doi.org/DOI 10.1029/JB087iB04p02829

Pugh, D. J., White, R. S., & Christie, P. A. F. (2016). Automatic Bayesian polarity determination. *Geophysical Journal International, 206*(1), 275-291. https://doi.org/10.1093/gji/ggw146

Qian, Y. Y., Chen, X. F., Luo, H., Wei, S. J., Wang, T., Zhang, Z. G., & Luo, X. Y. (2019). An Extremely Shallow M(w)4.1 Thrust Earthquake in the Eastern Sichuan Basin (China) Likely Triggered by Unloading During Infrastructure Construction. *Geophysical Research Letters, 46*(23), 13775-13784. https://doi.org/10.1029/2019gl085199

Ramzan, F., Khan, M. U. G., Rehmat, A., Iqbal, S., Saba, T., Rehman, A., & Mehmood, Z. (2019). A Deep Learning Approach for Automated Diagnosis and Multi-Class Classification of Alzheimer's Disease Stages Using Resting-State fMRI and Residual Neural Networks. *J Med Syst, 44*(2), 37. https://doi.org/10.1007/s10916-019-1475-2

Rau, R. J., Lee, J. C., Ching, K. E., Lee, Y. H., Byrne, T. B., & Chen, R. Y. (2012). Subduction-continent collision in southwestern Taiwan and the 2010 Jiashian earthquake sequence. *Tectonophysics, 578*, 107-116. https://doi.org/10.1016/j.tecto.2011.09.013

Reasenberg, P. A. (1985). FPFIT, FPPLOT, and FPPAGE: Fortran computer programs for calculating and displaying earthquake fault-plane solutions. *US Geol. Surv. Open-File Rep.*, 85-739.

Reasenberg, P. A., & Jones, L. M. (1989). Earthquake hazard after a mainshock in california. *Science, 243*(4895), 1173-1176. Article. https://doi.org/10.1126/science.243.4895.1173

Reasenberg, P. A., & Simpson, R. W. (1992). Response of regional seismicity to the static stress change produced by the loma prieta earthquake. *Science, 255*(5052), 1687-1690. https://doi.org/10.1126/science.255.5052.1687

Richter, C. F. (1935). An instrumental earthquake magnitude scale*. *Bulletin of the Seismological Society of America, 25*(1), 1-32. https://doi.org/10.1785/bssa0250010001

Rigo, A., Bethoux, N., Masson, F., & Ritz, J. F. (2008). Seismicity rate and wave-velocity variations as consequences of rainfall: the case of the catastrophic storm of September 2002 in the Nimes Fault region (Gard, France). *Geophysical Journal International, 173*(2), 473-482. https://doi.org/10.1111/j.1365-246X.2008.03718.x

Ringdal, F., & Kvaerna, T. (1989). A Multi-Channel Processing Approach to Real-Time Network Detection, Phase Association, and Threshold Monitoring. *Bulletin of the Seismological Society of America, 79*(6), 1927-1940.

Rodrıguez, C., Bommer, J., & Chandler, R. (1999). Earthquake-induced landslides: 1980–1997. *Soil Dynamics and Earthquake Engineering, 18*(5), 325-346.

Ross, Z. E., Idini, B., Jia, Z., Stephenson, O. L., Zhong, M., Wang, X., et al. (2019a). Hierarchical interlocked orthogonal faulting in the 2019 Ridgecrest earthquake sequence. *Science, 366*(6463), 346-351. https://doi.org/10.1126/science.aaz0109

Ross, Z. E., Meier, M. A., & Hauksson, E. (2018a). P Wave Arrival Picking and First-Motion Polarity Determination With Deep Learning. *Journal of Geophysical Research-Solid Earth, 123*(6), 5120-5129. https://doi.org/10.1029/2017jb015251

Ross, Z. E., Meier, M. A., Hauksson, E., & Heaton, T. H. (2018b). Generalized Seismic Phase Detection with Deep Learning. *Bulletin of the Seismological Society of America, 108*(5a), 2894-2901. https://doi.org/10.1785/0120180080

Ross, Z. E., Trugman, D. T., Hauksson, E., & Shearer, P. M. (2019b). Searching for hidden earthquakes in Southern California. *Science, 364*(6442), 767-771. https://doi.org/10.1126/science.aaw6888

Roth, P., Pavoni, N., & Deichmann, N. (1992). Seismotectonics of the Eastern Swiss Alps and Evidence for Precipitation-Induced Variations of Seismic Activity. *Tectonophysics, 207*(1-2), 183-197. https://doi.org/Doi 10.1016/0040-1951(92)90477-N

Rubinstein, J. L., La Rocca, M., Vidale, J. E., Creager, K. C., & Wech, A. G. (2008). Tidal modulation of nonvolcanic tremor. *Science, 319*(5860), 186-189. Article. https://doi.org/10.1126/science.1150558

Ruff, L., & Kanamori, H. (1980). Seismicity and the Subduction Process. *Physics of the Earth and Planetary Interiors, 23*(3), 240-252. https://doi.org/Doi 10.1016/0031-9201(80)90117-X

SCEDC. (2013). *Southern California Earthquake Data Center. Caltech. Dataset*.

Schubnel, A., Brunet, F., Hilairet, N., Gasc, J., Wang, Y., & Green, H. W., 2nd. (2013). Deep-focus earthquake analogs recorded at high pressure and temperature in the laboratory. *Science, 341*(6152), 1377-1380. https://doi.org/10.1126/science.1240206

Selvaraju, R. R., Cogswell, M., Das, A., Vedantam, R., Parikh, D., & Batra, D. (2017). *Grad-cam: Visual explanations from deep networks via gradient-based localization.* Paper presented at the Proceedings of the IEEE international conference on computer vision.

Shearer, P. M., Prieto, G. A., & Hauksson, E. (2006). Comprehensive analysis of earthquake source spectra in southern California. *Journal of Geophysical Research-Solid Earth, 111*(B6). https://doi.org/10.1029/2005jb003979

Shelly, D. R., Beroza, G. C., & Ide, S. (2007). Non-volcanic tremor and low-frequency earthquake swarms. *Nature, 446*(7133), 305-307. https://doi.org/10.1038/nature05666

Shelly, D. R., Ellsworth, W. L., & Hill, D. P. (2016a). Fluid-faulting evolution in high definition: Connecting fault structure and frequency-magnitude variations during the 2014 Long Valley Caldera, California, earthquake swarm. *Journal of Geophysical Research-Solid Earth, 121*(3), 1776-1795. https://doi.org/10.1002/2015jb012719

Shelly, D. R., Hardebeck, J. L., Ellsworth, W. L., & Hill, D. P. (2016b). A new strategy for earthquake focal mechanisms using waveform-correlation-derived relative polarities and cluster analysis: Application to the 2014 Long Valley Caldera earthquake swarm. *Journal of Geophysical Research-Solid Earth, 121*(12), 8622-8641. https://doi.org/10.1002/2016jb013437

Shen, Z. K., Jackson, D. D., Feng, Y. J., Cline, M., Kim, M., Fang, P., & Bock, Y. (1994). Postseismic Deformation Following the Landers Earthquake, California, 28 June 1992. *Bulletin of the Seismological Society of America, 84*(3), 780-791. https://doi.org/10.1785/bssa0840030780

Shi, F., Wang, Y., Wen, J., Yu, T., Zhu, L., Huang, T., & Wang, K. (2022). Metamorphism-facilitated faulting in deforming orthopyroxene: Implications for global intermediate-depth seismicity. *Proc Natl Acad Sci U S A, 119*(11), e2112386119. https://doi.org/10.1073/pnas.2112386119

Shin, T. (1992). Some implications of Taiwan tectonic features from the data collected by the Central Weather Bureau Seismic Network. *Meteorol. Bull, 38*, 23-48 (in Chinese).

Shin, T. C., Chang, C. H., Pu, H. C., Lin, H. W., & Leu, P. L. (2013). The Geophysical Database Management System in Taiwan. *Terrestrial Atmospheric and Oceanic Sciences, 24*(1), 11-18. https://doi.org/10.3319/Tao.2012.09.20.01(T)

Shinohara, M., Machida, Y., Yamada, T., Nakahigashi, K., Shinbo, T., Mochizuki, K., et al. (2012). Precise aftershock distribution of the 2011 off the Pacific coast of Tohoku Earthquake revealed by an ocean-bottom seismometer network. *Earth Planets and Space, 64*(12), 1137-1148. https://doi.org/10.5047/eps.2012.09.003

Shirzaei, M., Burgmann, R., Uchida, N., Hu, Y., Pollitz, F., & Matsuzawa, T. (2014). Seismic versus aseismic slip: Probing mechanical properties of the northeast Japan subduction zone. *Earth and Planetary Science Letters, 406*, 7-13. https://doi.org/10.1016/j.epsl.2014.08.035

Shyu, J. B. H., Chuang, Y. R., Chen, Y. L., Lee, Y. R., & Cheng, C. T. (2016). A New On-Land Seismogenic Structure Source Database from the Taiwan Earthquake Model (TEM) Project for Seismic Hazard Analysis of Taiwan. *Terrestrial Atmospheric and Oceanic Sciences, 27*(3), 311-323. https://doi.org/10.3319/Tao.2015.11.27.02(Tem)

Sibson, R. H. (1982). Fault Zone Models, Heat-Flow, and the Depth Distribution of Earthquakes in the Continental-Crust of the United-States. *Bulletin of the Seismological Society of America, 72*(1), 151-163.

Singh, S. K., & Suarez, G. (1988). Regional Variation in the Number of Aftershocks (Mb Greater-Than-or-Equal-to 5) of Large, Subduction-Zone Earthquakes (Mw Greater-Than-or-Equal-to 7.0). *Bulletin of the Seismological Society of America, 78*(1), 230-242. Article.

Snoke, J. A., Lee, W., Kanamori, H., Jennings, P., & Kisslinger, C. (2003). FOCMEC: Focal mechanism determinations. *International handbook of earthquake and engineering seismology, 85*, 1629-1630.

Springenberg, J. T., Dosovitskiy, A., Brox, T., & Riedmiller, M. (2014). Striving for simplicity: The all convolutional net. *arXiv preprint arXiv:1412.6806*.

Steer, P., Jeandet, L., Cubas, N., Marc, O., Meunier, P., Simoes, M., et al. (2020). Earthquake statistics changed by typhoon-driven erosion. *Sci Rep, 10*(1), 10899. https://doi.org/10.1038/s41598-020-67865-y

Steer, P., Simoes, M., Cattin, R., & Shyu, J. B. (2014). Erosion influences the seismicity of active thrust faults. *Nat Commun, 5*(1), 5564. https://doi.org/10.1038/ncomms6564

Stein, R. S. (1999). The role of stress transfer in earthquake occurrence. *Nature, 402*(6762), 605-609. https://doi.org/Doi 10.1038/45144

Stein, R. S., & Lisowski, M. (1983). The 1979 Homestead Valley Earthquake Sequence, California - Control of Aftershocks and Postseismic Deformation. *Journal of Geophysical Research, 88*(Nb8), 6477-6490. https://doi.org/DOI 10.1029/JB088iB08p06477

Stein, S., & Wysession, M. (2003). An introduction to seismology. *Earthquakes, and Earth, 7*(9), 10.

Steinberg, A., Vasyura-Bathke, H., Gaebler, P., Ohrnberger, M., & Ceranna, L. (2021). Estimation of Seismic Moment Tensors Using Variational Inference Machine Learning. *Journal of Geophysical Research-Solid Earth, 126*(10). https://doi.org/10.1029/2021JB022685

Sun, Z. H., Sandoval, L., Crystal-Ornelas, R., Mousavi, S. M., Wang, J. B., Lin, C., et al. (2022). A review of Earth Artificial Intelligence. *Computers & Geosciences, 159*, 105034. https://doi.org/10.1016/j.cageo.2022.105034

Svejdar, V., Kuchenhoff, H., Fahrmeir, L., & Wassermann, J. (2011). External forcing of earthquake swarms at Alpine regions: example from a seismic meteorological network at Mt. Hochstaufen SE-Bavaria. *Nonlinear Processes in Geophysics, 18*(6), 849-860. https://doi.org/10.5194/npg-18-849-2011

Tahir, M., & Grasso, J. R. (2015). Faulting Style Controls for the Space-Time Aftershock Patterns. *Bulletin of the Seismological Society of America, 105*(5), 2480-2497. Article. https://doi.org/10.1785/0120140336

Tajima, F., & Kanamori, H. (1985). Global Survey of Aftershock Area Expansion Patterns. *Physics of the Earth and Planetary Interiors, 40*(2), 77-134. https://doi.org/Doi 10.1016/0031-9201(85)90066-4

Takahashi, H., & Hirata, K. (2003). The 2000 Nemuro-Hanto-Oki earthquake, off eastern Hokkaido, Japan, and the high intraslab seismic activity in the southwestern Kuril

Trench. *Journal of Geophysical Research-Solid Earth, 108*(B4). https://doi.org/10.1029/2002jb001813

Tamaribuchi, K., Moriwaki, K., Ueno, H., & Tsukada, S. (2016). Automatic hypocenter determination for the Seismological Bulletin of Japan using Bayesian estimation. *Quart J Seis, 79*, 1-13.

Tanaka, R., Naoi, M., Chen, Y. Q., Yamamoto, K., Imakita, K., Tsutsumi, N., et al. (2021). Preparatory acoustic emission activity of hydraulic fracture in granite with various viscous fluids revealed by deep learning technique. *Geophysical Journal International, 226*(1), 493-510. https://doi.org/10.1093/gji/ggab096

Tanaka, S. (2012). Tidal triggering of earthquakes prior to the 2011 Tohoku-Oki earthquake (Mw9.1). *Geophysical Research Letters, 39*(7), n/a-n/a. https://doi.org/10.1029/2012gl051179

Tanaka, S., Ohtake, M., & Sato, H. (2004). Tidal triggering of earthquakes in Japan related to the regional tectonic stress. *Earth Planets and Space, 56*(5), 511-515. Article. https://doi.org/Doi 10.1186/Bf03352510

Tang, C.-C., Lin, C.-H., & Peng, Z. (2014). Spatial-temporal evolution of early aftershocks following the 2010 ML 6.4 Jiashian earthquake in southern Taiwan. *Geophysical Journal International, 199*(3), 1772-1783. https://doi.org/10.1093/gji/ggu361

Tang, C. C., Lin, L. C., Luo, Y. H., Liu, S. J., Xu, R., & Lin, C. H. (2019). Possible Earth-Tide Modulations of Early Aftershocks in Southern Taiwan. *Bulletin of the Seismological Society of America, 109*(4), 1571-1577. https://doi.org/10.1785/0120170381

Tao, W., Masterlark, T., Shen, Z. K., & Ronchin, E. (2015). Impoundment of the Zipingpu reservoir and triggering of the 2008 Mw 7.9 Wenchuan earthquake, China. *J Geophys Res Solid Earth, 120*(10), 7033-7047. https://doi.org/10.1002/2014JB011766

Thomas, A. M., Nadeau, R. M., & Burgmann, R. (2009). Tremor-tide correlations and near-lithostatic pore pressure on the deep San Andreas fault. *Nature, 462*(7276), 1048-1051. Article. https://doi.org/10.1038/nature08654

Thorson, R. M. (1996). Earthquake recurrence and glacial loading in western Washington. *Geological Society of America Bulletin, 108*(9), 1182-1191. https://doi.org/Doi 10.1130/0016-7606(1996)108<1182:Eragli>2.3.Co;2

Tian, D. (2021). Seisman/HinetPy: 0.6. 9 (0.6. 9). Zenodo. In.

Tian, X., Zhang, W., Zhang, X., Zhang, J., Zhang, Q. S., Wang, X. T., & Guo, Q. S. (2020). Comparison of Single-Trace and Multiple-Trace Polarity Determination for Surface Microseismic Data Using Deep Learning. *Seismological Research Letters, 91*(3), 1794-1803. https://doi.org/10.1785/0220190353

Tolstoy, M., Vernon, F. L., Orcutt, J. A., & Wyatt, F. K. (2002). Breathing of the seafloor: Tidal correlations of seismicity at Axial volcano. *Geology, 30*(6), 503-506. Article. https://doi.org/Doi 10.1130/0091-7613(2002)030<0503:Botstc>2.0.Co;2

Trugman, D. T., & Shearer, P. M. (2017). GrowClust: A Hierarchical Clustering Algorithm for Relative Earthquake Relocation, with Application to the Spanish Springs and Sheldon, Nevada, Earthquake Sequences. *Seismological Research Letters, 88*(2), 379-391. https://doi.org/10.1785/0220160188

Tsai, Y. B. (1986). Seismotectonics of Taiwan. *Tectonophysics, 125*(1-3), 17-&. https://doi.org/10.1016/0040-1951(86)90005-3

Uchida, N., & Burgmann, R. (2021). A Decade of Lessons Learned from the 2011 Tohoku-Oki Earthquake. *Reviews of Geophysics, 59*(2). https://doi.org/10.1029/2020RG000713

Uchide, T. (2020). Focal mechanisms of small earthquakes beneath the Japanese islands based on first-motion polarities picked using deep learning. *Geophysical Journal International, 223*(3), 1658-1671. https://doi.org/10.1093/gji/ggaa401

Uchide, T., Shiina, T., & Imanishi, K. (2022). Stress Map of Japan: Detailed Nationwide Crustal Stress Field Inferred From Focal Mechanism Solutions of Numerous Microearthquakes. *Journal of Geophysical Research: Solid Earth, 127*(6). https://doi.org/10.1029/2022jb024036

Ueno, S. (2002). Improvement of hypocenter determination method by Japan Meteorological Agency. *Kenshinjiho, 65*, 123-134.

Umino, N. (1975). On the two-layered structure of a deep seismic plane in the northeastern Japan arc. *J. Seismol. Soc. Japan., 28*, 125-139.

Utsu, T., Ogata, Y., & Matsuura, R. S. (1995). The Centenary of the Omori Formula for a Decay Law of Aftershock Activity. *Journal of Physics of the Earth, 43*(1), 1-33. https://doi.org/DOI 10.4294/jpe1952.43.1

van der Elst, N. J. (2021). B-Positive: A Robust Estimator of Aftershock Magnitude Distribution in Transiently Incomplete Catalogs. *Journal of Geophysical Research: Solid Earth, 126*(2). https://doi.org/10.1029/2020jb021027

van der Elst, N. J., & Shaw, B. E. (2015). Larger aftershocks happen farther away: Nonseparability of magnitude and spatial distributions of aftershocks. *Geophysical Research Letters, 42*(14), 5771-5778. Article. https://doi.org/10.1002/2015gl064734

Vaswani, A., Shazeer, N., Parmar, N., Uszkoreit, J., Jones, L., Gomez, A. N., et al. (2017). Attention Is All You Need. *Advances in Neural Information Processing Systems 30 (Nips 2017), 30*.

Wadati, K. (1928). Shallow and deep earthquakes. *Geophys. Mag., 1*, 162-202.

Waldhauser, F., & Ellsworth, W. L. (2000). A double-difference earthquake location algorithm: Method and application to the northern Hayward fault, California. *Bulletin of the Seismological Society of America, 90*(6), 1353-1368. https://doi.org/Doi 10.1785/0120000006

Walter, J. I., Ogwari, P., Thiel, A., Ferrer, F., Woelfel, I., Chang, J. C., et al. (2020). The Oklahoma Geological Survey Statewide Seismic Network. *Seismological Research Letters, 91*(2), 611-621. https://doi.org/10.1785/0220190211

Wang, C.-y., Wang, C.-H., & Manga, M. (2004). Coseismic release of water from mountains: Evidence from the 1999 (Mw = 7.5) Chi-Chi, Taiwan, earthquake. *Geology, 32*(9), 769. https://doi.org/10.1130/g20753.1

Wang, L., & Burgmann, R. (2019). Statistical Significance of Precursory Gravity Changes Before the 2011 Mw 9.0 Tohoku-Oki Earthquake. *Geophysical Research Letters, 46*(13), 7323-7332. https://doi.org/10.1029/2019gl082682

Warren, L. M., Baluyut, E. C., Osburg, T., Lisac, K., & Kokkinen, S. (2015). Fault plane orientations of intermediate-depth and deep-focus earthquakes in the Japan-Kuril-Kamchatka subduction zone. *Journal of Geophysical Research-Solid Earth, 120*(12), 8366-8382. https://doi.org/10.1002/2015jb012463

Wen, S., Chen, C. H., Ji, Y. J., Chang, Y. Z., & Chen, C. H. (2015). The seismogenic deformation and Qp temporal variation before the M6.2 Mingjen earthquake, Taiwan. *Journal of Asian Earth Sciences, 114*, 403-413. https://doi.org/10.1016/j.jseaes.2015.06.011

Wen, Y.-Y., Chen, C.-C., Wu, Y.-H., Chan, C.-H., Wang, Y.-J., & Yeh, Y.-L. (2016). Spatiotemporal investigation of seismicity and Coulomb stress variations prior to the 2010ML6.4 Jiashian, Taiwan earthquake. *Geophysical Research Letters, 43*(16), 8451-8457. https://doi.org/10.1002/2016gl070633

Wesnousky, S. G. (2008). Displacement and geometrical characteristics of earthquake surface ruptures: Issues and implications for seismic-hazard analysis and the process of earthquake rupture. *Bulletin of the Seismological Society of America, 98*(4), 1609-1632. https://doi.org/10.1785/0120070111

Wetzler, N., Brodsky, E. E., & Lay, T. (2016). Regional and stress drop effects on aftershock productivity of large megathrust earthquakes. *Geophysical Research Letters, 43*(23), 12012-12020. https://doi.org/10.1002/2016gl071104

Wiemer, S., & Wyss, M. (2000). Minimum magnitude of completeness in earthquake catalogs: Examples from Alaska, the western United States, and Japan. *Bulletin of the Seismological Society of America, 90*(4), 859-869. https://doi.org/Doi 10.1785/0119990114

Wiemer, S., & Wyss, M. (2002). Mapping spatial variability of the frequency-magnitude distribution of earthquakes. In *Advances in Geophysics Volume 45* (pp. 259-V): Elsevier.

Wiens, D. A. (2001). Seismological constraints on the mechanism of deep earthquakes: temperature dependence of deep earthquake source properties. *Physics of the Earth and Planetary Interiors, 127*(1-4), 145-163. https://doi.org/Doi 10.1016/S0031-9201(01)00225-4

Wiens, D. A., Gilbert, H. J., Hicks, B., Wysession, M. E., & Shore, P. J. (1997). Aftershock sequences of moderate-sized intermediate and deep earthquakes in the Tonga

subduction zone. *Geophysical Research Letters, 24*(16), 2059-2062. https://doi.org/Doi 10.1029/97gl01957

Wilcock, W. S. D. (2001). Tidal triggering of micro earthquakes on the Juan de Fuca Ridge. *Geophysical Research Letters, 28*(20), 3999-4002. Article. https://doi.org/Doi 10.1029/2001gl013370

Woo, S. H., Park, J., Lee, J. Y., & Kweon, I. S. (2018). CBAM: Convolutional Block Attention Module. *Computer Vision - Eccv 2018, Pt Vii, 11211*, 3-19. https://doi.org/10.1007/978-3-030-01234-2_1

Woollam, J., M\"unchmeyer, J., Tilmann, F., Rietbrock, A., Lange, D., Bornstein, T., et al. (2021). SeisBench -- A Toolbox for Machine Learning in Seismology.

Wu, P., & Johnston, P. (2000). Can deglaciation trigger earthquakes in N. America? *Geophysical Research Letters, 27*(9), 1323-1326. https://doi.org/10.1029/1999gl011070

Wu, Y. M., Chang, C. H., Zhao, L., Shyu, J. B. H., Chen, Y. G., Sieh, K., & Avouac, J. P. (2007). Seismic tomography of Taiwan: Improved constraints from a dense network of strong motion stations. *Journal of Geophysical Research-Solid Earth, 112*(B8). https://doi.org/10.1029/2007jb004983

Wu, Y. M., Chang, C. H., Zhao, L., Teng, T. L., & Nakamura, M. (2008a). A comprehensive relocation of earthquakes in Taiwan from 1991 to 2005. *Bulletin of the Seismological Society of America, 98*(3), 1471-1481. https://doi.org/10.1785/0120070166

Wu, Y. M., Hsu, Y. J., Chang, C. H., Teng, L. S., & Nakamura, M. (2010). Temporal and spatial variation of stress field in Taiwan from 1991 to 2007: Insights from comprehensive first motion focal mechanism catalog. *Earth and Planetary Science Letters, 298*(3-4), 306-316. https://doi.org/10.1016/j.epsl.2010.07.047

Wu, Y. M., Zhao, L., Chang, C. H., & Hsu, Y. J. (2008b). Focal-mechanism determination in Taiwan by genetic algorithm. *Bulletin of the Seismological Society of America, 98*(2), 651-661. https://doi.org/10.1785/0120070115

Xie, C. D., Lei, X. L., Zhao, X. Y., Ma, Q. B., Yang, S. M., & Wang, Y. N. (2017). Tidal triggering of earthquakes in the Ning'er area of Yunnan Province, China. *Journal*

of Asian Earth Sciences, 138, 477-483. Article. https://doi.org/10.1016/j.jseaes.2017.02.029

Xu, J., Zhang, W., Chen, X., & Guo, Q. (2019). Minimum semblance weighted stacking with polarity correction for surface microseismic data processing. *The Leading Edge, 38*(8), 630-636.

Yamanaka, Y., & Shimazaki, K. (1990). Scaling Relationship between the Number of Aftershocks and the Size of the Main Shock. *Journal of Physics of the Earth, 38*(4), 305-324. Article. https://doi.org/DOI 10.4294/jpe1952.38.305

Yamasaki, T., & Seno, T. (2005). High strain rate zone in central Honshu resulting from the viscosity heterogeneities in the crust and mantle. *Earth and Planetary Science Letters, 232*(1-2), 13-27. https://doi.org/10.1016/j.epsl.2005.01.015

Yang, W. Z., Hauksson, E., & Shearer, P. M. (2012). Computing a Large Refined Catalog of Focal Mechanisms for Southern California (1981-2010): Temporal Stability of the Style of Faulting. *Bulletin of the Seismological Society of America, 102*(3), 1179-1194. https://doi.org/10.1785/0120110311

Yang, Y., Gao, A. F., Castellanos, J. C., Ross, Z. E., Azizzadenesheli, K., & Clayton, R. W. (2021). Seismic Wave Propagation and Inversion with Neural Operators. *The Seismic Record, 1*(3), 126-134. https://doi.org/10.1785/0320210026

Yao, D. D., Walter, J. I., Meng, X. F., Hobbs, T. E., Peng, Z. G., Newman, A. V., et al. (2017). Detailed spatiotemporal evolution of microseismicity and repeating earthquakes following the 2012 M-w 7.6 Nicoya earthquake. *Journal of Geophysical Research-Solid Earth, 122*(1), 524-542. https://doi.org/10.1002/2016jb013632

Yao, H. J., & van der Hilst, R. D. (2009). Analysis of ambient noise energy distribution and phase velocity bias in ambient noise tomography, with application to SE Tibet. *Geophysical Journal International, 179*(2), 1113-1132. https://doi.org/10.1111/j.1365-246X.2009.04329.x

Yin, Y. P., Wang, F. W., & Sun, P. (2009). Landslide hazards triggered by the 2008 Wenchuan earthquake, Sichuan, China. *Landslides, 6*(2), 139-152. https://doi.org/10.1007/s10346-009-0148-5

Yu, S. W., & Ma, J. W. (2021). Deep Learning for Geophysics: Current and Future Trends. *Reviews of Geophysics, 59*(3). https://doi.org/10.1029/2021RG000742

Zaliapin, I., & Ben-Zion, Y. (2021). Perspectives on Clustering and Declustering of Earthquakes. *Seismological Research Letters, 93*(1), 386-401. https://doi.org/10.1785/0220210127

Zhai, Q., Mach, P., Peng, Z., Matsubara, M., Obara, K., & Wang, Y. (2022). *Systematic detections of intermediate-depth earthquakes in the subduction zone of Japan before and after the M9 Tohoku-Oki Earthquake and M5+ intermediate-depth earthquakes.* Paper presented at the 2022 SSA Annual Meeting.

Zhai, Q., Peng, Z., Heidary, R., Williams, J., Howard, S., Dai, S., et al. (2021a). *P-wave first-motion polarity determination using deep learning.* Paper presented at the AGU Fall Meeting 2021.

Zhai, Q., Peng, Z., Matsubara, M., Obara, K., & Wang, Y. (2021b). *Investigating spatiotemporal variations of intermediate-depth earthquakes in the subduction zone of Japan before and after M9 Tohoku-Oki Earthquake.* Paper presented at the AGU Fall Meeting 2021.

Zhai, Q. S., Peng, Z. G., Chuang, L. Y., Wu, Y. M., Hsu, Y. J., & Wdowinski, S. (2021c). Investigating the Impacts of a Wet Typhoon on Microseismicity: A Case Study of the 2009 Typhoon Morakot in Taiwan Based on a Template Matching Catalog. *Journal of Geophysical Research-Solid Earth, 126*(12). https://doi.org/10.1029/2021JB023026

Zhan, Z. W. (2020). Mechanisms and Implications of Deep Earthquakes. *Annual Review of Earth and Planetary Sciences, Vol 48, 2020, 48*(1), 147-174. https://doi.org/10.1146/annurev-earth-053018-060314

Zhang, H. J., & Thurber, C. (2006). Development and applications of double-difference seismic tomography. *Pure and Applied Geophysics, 163*(2-3), 373-403. https://doi.org/10.1007/s00024-005-0021-y

Zhang, M., Liu, M., Feng, T., Wang, R., & Zhu, W. (2022). LOC-FLOW: An End-to-End Machine Learning-Based High-Precision Earthquake Location Workflow. *Seismological Research Letters*.

Zhang, Z.-X. (2016). Rock Fracture and Rock Strength. In *Rock Fracture and Blasting* (pp. 69-88): Elsevier.

Zhao, D. P., Hasegawa, A., & Horiuchi, S. (1992). Tomographic Imaging of P-Wave and S-Wave Velocity Structure beneath Northeastern Japan. *Journal of Geophysical Research-Solid Earth, 97*(B13), 19909-19928. https://doi.org/Doi 10.1029/92jb00603

Zhao, L.-S., & Helmberger, D. V. (1994). Source estimation from broadband regional seismograms. *Bulletin of the Seismological Society of America, 84*(1), 91-104.

Zhu, L. J., Peng, Z. G., McClellan, J., Li, C. Y., Yao, D. D., Li, Z. F., & Fang, L. H. (2019). Deep learning for seismic phase detection and picking in the aftershock zone of 2008 M(w)7.9 Wenchuan Earthquake. *Physics of the Earth and Planetary Interiors, 293*. https://doi.org/10.1016/j.pepi.2019.05.004

Zhu, L. P., & Helmberger, D. V. (1996). Advancement in source estimation techniques using broadband regional seismograms. *Bulletin of the Seismological Society of America, 86*(5), 1634-1641. https://doi.org/10.1785/bssa0860051634

Zhu, W., & Beroza, G. C. (2018). PhaseNet: A Deep-Neural-Network-Based Seismic Arrival Time Picking Method. *Geophysical Journal International*. https://doi.org/10.1093/gji/ggy423

Zhu, W. Q., Tai, K. S., Mousavi, S. M., Bailis, P., & Beroza, G. C. (2022). An End-To-End Earthquake Detection Method for Joint Phase Picking and Association Using Deep Learning. *Journal of Geophysical Research-Solid Earth, 127*(3). https://doi.org/10.1029/2021JB023283

Zhuang, J., Ogata, Y., & Vere-Jones, D. (2002). Stochastic declustering of space-time earthquake occurrences. *Journal of the American Statistical Association, 97*(458), 369-380. https://doi.org/Doi 10.1198/016214502760046925

Zhuang, J. C. (2006). Second-order residual analysis of spatiotemporal point processes and applications in model evaluation. *Journal of the Royal Statistical Society Series B-Statistical Methodology, 68*(4), 635-653. https://doi.org/DOI 10.1111/j.1467-9868.2006.00559.x

Zhuang, J. C., Chang, C. P., Ogata, Y., & Chen, Y. I. (2005). A study on the background and clustering seismicity in the Taiwan region by using point process models.

Journal of Geophysical Research-Solid Earth, 110(B5). https://doi.org/10.1029/2004jb003157

Zhuang, J. C., Ogata, Y., & Vere-Jones, D. (2004). Analyzing earthquake clustering features by using stochastic reconstruction. *Journal of Geophysical Research-Solid Earth, 109*(B5). https://doi.org/10.1029/2003jb002879